Protection of Future Power Systems with High Amounts of Power Electronic Converters

Di Liu

A thesis submitted for the degree of Doctor of Philosophy to the Department of Electronic and Electrical Engineering University of Strathclyde

April 20, 2023

This thesis is the result of the author's original research. It has been composed by the author and has not been previously submitted for examination which has led to the award of a degree.

Signed: _____Di_Liu_____ Date: _____20/04/2023_____

Abstract

In recent decades, power systems worldwide have seen a significant increase in power electronic converters to facilitate the integration of renewable energy, e.g., solar and wind energy, and also for the transmission of electrical power between different areas, e.g., High-Voltage Direct Current (HVDC) links. Unlike Synchronous Generators (SGs), Converter-based Resources (CBRs) cannot generate high-magnitude fault currents and their fault characteristics are dependent on implemented control strategies, which are governed by the associated grid codes. Those features of CBRs can pose severe challenges to the reliable operation of protection systems designed based on the fault characteristic of SGs. Two typical application scenarios with high penetrations of CBRs are investigated in this thesis, which includes the HVDC system connected to the transmission system and the low-voltage (LV) microgrid connected to the distribution system.

In this thesis, the performance of distance protection is evaluated systematically using the Hardware-in-the-Loop (HIL) approach on two commercially available relays. Based on HIL test results and further supported by the theoretical analysis, it was found that the performance of the distance relay is compromised significantly after the connection of CBRs such as HVDC systems. The observed issues include the distance under/over-reach, incorrect faulted phase selection, problematic impedance measurement and oscillating impedance locus. A novel sequence component-based distance measuring element is proposed in this thesis to accurately reflect the fault distance and thus address the under/over-reach issue of the conventional impedance-based distance algorithm, whose performance is verified by the simulation conducted using the Real-Time Digital Simulator (RTDS) under a wide range of system and fault conditions including varied fault types, fault resistances, fault positions, system fault levels and protected line length. Based on simulation results, the proposed algorithm can measure the fault distance accurately and trip faults within the time required by the GB grid code.

Except for HVDC systems in the transmission system, significant amounts of inverter-interfaced distributed generators (IIDGs) are also connected to the distribution system, which poses severe challenges to the existing overcurrent protection relays

because of the reduced fault contribution of IIDGs and the bi-directional power flow. Therefore, some solutions must be designed to protect the future distribution system. As an emerging type of distribution system, the microgrid, a compact network comprising generators, loads and storage devices, is selected in this thesis to investigate the protection challenges of the future distribution system and demonstrate the development of a new energy-based protection scheme. In normal conditions, a microgrid is typically connected to the main grid, i.e., grid-connected microgrid, but when severe disturbances occur, e.g., loss of major generation or faults, it can be safely disconnected from the main grid and run as an independent islanded system, i.e., islanded microgrid. This dual mode capability results in the dynamic variation of fault levels in different operating modes, where the fault level is reduced substantially in the islanded mode due to the loss of the fault infeed from the main network and the limited fault current contribution from IIDGs. Additionally, different fault responses of IIDGs in a microgrid, governed by embedded controllers of inverters, also increase the risk of protection failure. To address issues of fault level variation of two operating modes, reduced fault current infeed in the islanded mode, and non-uniform fault characteristics of CBRs, an energy-based protection scheme is designed in this thesis to protect LV microgrids, where the energy of high-frequency transients resulting from the reflections of travelling waves are extracted using the Maximal Overlap Discrete Wavelet Transform (MODWT) algorithm, and relays in microgrids are coordinated by a developed algorithm. The performance of the proposed protection algorithm is evaluated using a 400-V CIGRE benchmark microgrid implemented in MATLAB/SIMULINK.

In summary, this thesis evaluates the challenges of conventional distance and overcurrent protection in transmission and distribution systems (i.e., microgrids) where high amounts of CBRs/IIDGs are expected. Solutions proposed in the literature are reviewed, along with a comprehensive discussion of their benefits and limitations. Additionally, a sequence components-based distance protection algorithm and a novel high-frequency transient-based protection scheme are developed in this thesis to protect transmission lines connected to CBRs and microgrids dominated by IIDGs.

Acknowledgements

I would like to thank my supervisor, Dr Adam Dyśko, for his tremendous support of my PhD research. He started to supervise me in 2017, firstly for the undergraduate final-year project and then for the PhD study. I am grateful for his trust in providing me with a precious opportunity to conduct my PhD research. His enthusiasm and rigorous attitude toward academic research encourages me to overcome the difficulties during the research period. I would also express my thanks to my second supervisor, Professor Campbell Booth, who provided significant academic guidance and resources during my PhD.

I would like to express my thanks to Dr Qiteng Hong, who taught me a lot of skills in conducting research and projects. He provides valuable opportunities for me to communicate and share ideas with people from industries and other research institutions, which is essential for my PhD and future career development.

I would also like to express my thanks to Dr Dimitrios Tzelepis, Dr Agusti Egea Alvarez and Professor Lie Xu. They all give me strong support and valuable guidance during this study period. I would like to extend thanks to all my colleagues in the Advanced Electrical System Group at the University of Strathclyde for their memorable friendship and helps during the study time, especially to Dr Md Asif Uddin Khan, Dr Lei Shi, Weijie Yan, Zhenkun Yang, Hengqing Tian, Jiabin Fan, Xufei Ge, Yang Teng and Shiyao Yu.

I am grateful to my wife, Qi Dong, for her continuous support over those years, which help me significantly to overcome the difficulties in my PhD. Finally, I would like to share my gratitude to my parents for their support and understanding. This thesis is dedicated to them.

Table of Contents

List of Figures

List of Tables

List of Abbreviations and Symbols

The abbreviations and symbols are used throughout this thesis.

Abbreviations:

AG	Phase-A-to-Ground Fault
AB	Phase-A-to-Phase-B Fault
ABG	Phase-A-to-Phase-B-to-Ground Fault
ABC	Three-Phase Fault
ABCG	Three-Phase-to-Ground Fault
AC	Alternating Current
BC	Phase-B-to-Phase-C Fault
BCG	Phase-B-to-Phase-C-to-Ground Fault
BECCS	Bioenergy with Carbon Capture and Storage
BG	Phase-B-to-Ground Fault
BI	Balanced Current Controller
CA	Phase-C-to-Phase-A Fault
CAG	Phase-C-to-Phase-A-to-Ground Fault
CB	Circuit Breaker
CBRs	Converter-based Resources
CG	Phase-C-to-Ground Fault

CNN	Convolutional Neural Network
CP	Constant Active Power Controller
CQ	Constant Reactive Power Controller
CT	Current Transformer
CWT	Continuous Wavelet Transform
DC	Direct Current
DERs	Distributed Energy Resources
DGs	Distributed Generators
DOCRs	Directional Overcurrent Relays
DR1	Distance Relay 1
DR2	Distance Relay 2
DWT	Discrete Wavelet Transform
EU	European Union
FFCI	Fast Fault Current Injection
FFT	Fast Fourier Transform
FIA	Fault Inception Angle
FIR	Finite Impulse Response
FT	Fourier Transform
FFT	Fast Fourier Transform
GB	Great Britain

GC	Grid Code
GFL	Grid-Following Converter
GFM	Grid-Forming Converter
HIFs	High-Impedance Faults
HIL	Hardware-in-the-Loop
HV	High-Voltage
HVDC	High-Voltage Direct Current
IDMT	Inverse Definite Minimum Time
IIDG	Inverter-Interfaced Distributed Generation
KCL	Kirchhoff's Current Law
KVL	Kirchhoff's Voltage Law
LV	Low-Voltage
MMC	Modular Multi-Level Converter
MODWT	Maximal Overlap Discrete Wavelet Transform
MV	Medium Voltage
NSG	Non-Synchronous Generation
OCRs	Overcurrent Relays
PCC	Point of Common Coupling
PLL	Phase-Locked Loop
PMU	Phasor Measurement Unit

PQ	Active and Reactive Power
PS	Plug Setting
PV	Photovoltaic
QUAD	Quadrilateral
ROCOF	Rate of the Change of Frequency
ROCOV	Rate of the Change of Voltage
RTDS	Real-Time Digital Simulator
SCs	Synchronous Condensers
SCR	Short Circuit Ratio
SF	Scaling Factor
SGs	Synchronous Generators
SNR	Signal to Noise Ratio
SRF-PLL	Synchronous Reference Frame Phase Locked Loop
SSC	Summation of Squared Three-Phase Current
STFT	Short-Time Fourier Transform
THD	Total Harmonic Distortion
TKEO	Teager-Kaiser energy operator
TMS	Time Multiplier Setting
TWE	Transient Wavelet Energy
USA	United States of America

VF	Voltage and Frequency Control
VSC	Voltage Source Converter
VT	Voltage Transformer
WT	Wavelet Transform

Symbols:

v_a, v_b, v_c	Three Phase Voltages
i_a, i_b, i_c	Three Phase Currents
v^+, v^-, v^0	Positive, Negative and Zero Sequence Voltages
i^+, i^-, i_0	Positive, Negative and Zero Sequence Currents
$v_\perp^+, v_\perp^-$	Orthogonal Positive and Negative Sequence Voltages
v_d^+, v_q^+	Positive Sequence Voltages in dq Frame
i_d^+, i_q^+	Positive Sequence Currents in dq Frame
v_d^-, v_q^-	Negative Sequence Voltages in dq Frame
i_d^-, i_q^-	Negative Sequence Currents in dq Frame
P, Q	Active and Reactive Power
P_r, Q_r	Active and Reactive Power References
$\bar{P}, \bar{Q}$	Average Active and Reactive Power from Converter
P_C, P_S	AC Part of Active Power from Converter
Q_C, Q_S	AC Part of Reactive Power from Converter

v_d, v_q	Voltages in dq Frame
i_d, i_q	Currents in dq Frame
i_{dr}, i_{qr}	Current References in dq Frame
i_{dr}^+, i_{qr}^+	Positive Sequence Current References in dq Frame
i_{dr}^-, i_{qr}^-	Negative Sequence Current References in dq Frame
θ_{PLL}	Angle from PLL
θ_{GFM}	Angle of Grid-Forming Converter
θ_{MHO}	Operating Angle between Vectors of $S1$ and $S2$ of MHO Characteristics
C_f, L_f	Capacitor and Inductor Filter
Z_g	Grid Internal Impedance
Z_{AG}	Measured Impedance of AG Impedance Measuring Element
Z_{BG}	Measured Impedance of BG Impedance Measuring Element
Z_{CG}	Measured Impedance of CG Impedance Measuring Element
Z_{AB}	Measured Impedance of AB Impedance Measuring Element
Z_{BC}	Measured Impedance of BC Impedance Measuring Element
Z_{CA}	Measured Impedance of CA Impedance Measuring Element
v_{LL}	System Line to Line Voltage
FL_{Grid}	Fault Level of Connected AC Grid
s_{con}	Capacity of Converter Based Resource

SCR_{Grid}	Short Circuit Ratio of Connected AC Grid
v_{base}	Voltage Base
i_{base}	Current Base
s_{base}	Apparent Power Base
$i^{+}_{dr,nor}, i^{+}_{qr,nor}$	Normal Positive Sequence Current References in dq Frame
$i^{+}_{dr,lim}, i^{+}_{qr,lim}$	Limited Positive Sequence Current References in dq Frame
$i^{-}_{dr,lim}, i^{-}_{qr,lim}$	Limited Negative Sequence Current References in dq Frame
K_0	Residual Compensation Factor
Z_L	Impedance of the Protected Line
Z_R	Reach setting of relay
S_1, S_2	Operating Vectors of MHO-based Distance Relay
ρ	Polarising Factor of memory-polarised MHO Characteristic
ω_s	System Angular Frequency
V_{cross}	Cross-Polarised Voltage
V_{mem}	Memory Polarised Voltage
ΔI_{thr}	Current Threshold of Superimposed Quantities-Based Faulted Phase Selector
$\Delta i_{ab}, \Delta i_{bc}, \Delta i_{ca}$	Superimposed Phase to Phase Currents
β^{21}_{zone}	Angle of Individual Segment of the Negative and Positive Sequence Faulted Phase Selection Plane

β_{zone}^{20}	Angle of Individual Segment of the Negative and Zero Sequence Faulted Phase Selection Plane
δ^{21}	Angle Difference of Superimposed Negative and Positive Sequence Currents
δ^{20}	Angle Difference of Superimposed Negative and Zero Sequence Currents
α	Rotational Factor
t_{incep}	Fault Inception Time
t_{zone}	Intentional Zone Delay of Distance Relay
t_{trip}	Tripping Time of Distance Relay
t_{op}	Operating Time of Distance Relay
FL_{SG1}, FL_{SG2}	Fault Levels of SG1 and SG2
m	Percentage Indicating the Fault Position
Z_L	Total Impedance of Protected Line
R_F	Fault Resistance
$\Delta\psi$	Angle Difference of Current Infeed from Both Ends of Protected Line
p	Phases A, B, C
Z_E	Impedance Measurement Error of Distance Relay
Z_{DR1}	Impedance Measured by Distance Relay 1
Z_{DR2}	Impedance Measured by Distance Relay 2

$Z_{CBR}^{+}, Z_{CBR}^{-}, Z_{CBR}^{0}$	Sequence Source Impedance of Converter-Based Resources
$Z_{tr}^{+}, Z_{tr}^{-}, Z_{tr}^{0}$	Sequence Impedance of Isolation Transformer between Converter-Based Resources and Grid
$Z_{G}^{+}, Z_{G}^{-}, Z_{G}^{0}$	Sequence Source Impedance of Connected AC Grid
$Z_{L}^{+}, Z_{L}^{-}, Z_{L}^{0}$	Sequence Impedances of Transmission Line
$v_{DR1}^{+}, v_{DR1}^{-}, v_{DR1}^{0}$	Sequence Voltages Measured by Distance Relay 1
$v_{DR2}^{+}, v_{DR2}^{-}, v_{DR2}^{0}$	Sequence Voltages Measured by Distance Relay 2
$v_{F}^{+}, v_{F}^{-}, v_{F}^{0}$	Sequence Voltages at Fault Position
$i_{CBR}^{+}, i_{CBR}^{-}, i_{CBR}^{0}$	Sequence Currents Generated by Converter-Based Resources
$i_{G}^{+}, i_{G}^{-}, i_{G}^{0}$	Sequence Currents Generated by Connected AC Grid
$i_{F}^{+}, i_{F}^{-}, i_{F}^{0}$	Sequence Currents at Fault Position
i_{tr}^{0}	Zero Sequence Current Flowing Through Isolation Transformer
v_{pre}	Pre-fault voltage at the fault point
Δv	Superimposed voltage at the fault point
D_l	Level - l Detail Coefficients in the DWT Algorithm
A_l	Level - l Approximation Coefficients in the DWT Algorithm
W_j	j^{th} Wavelet Coefficients at Level 1 in the MODWT Algorithm
E_j	j^{th} Individual Wavelet Energy
TWE_j	j^{th} Transient Wavelet Energy

Δi_{CT_n}	Superimposed Current Measured by CT_n
$\Delta i_{CT_n}^{p}$	Superimposed Phase Currents Measured by CT_n
W_{j,CT_n}^{p}	j^{th} Three-Phase Wavelet Coefficients of CT_n
E_{j,CT_n}^{p}	j^{th} Individual Wavelet Energy of CT_n
TWE_{j,CT_n}^{p}	j^{th} Three-Phase Individual Wavelet Energy of CT_n
$TWE_{j,CT_n}^{p_{max}}$	j^{th} Maximum-Phase Transient Wavelet Energy of CT_n
$TWE_{j,Bus}^{max}$	j^{th} Maximum Transient Wavelet Energy at a Certain Busbar
TWE_{thr}	Transient Wavelet Energy Threshold
I_{thr_pe}	Current Threshold Represented by Peak Value
TWE_{j,CT_n}^{Peak}	Peak Value of Maximum-Phase Transient Wavelet Energy of CT_n
SNR_{dB}	Signal to Noise Ratio Represented by dB

Chapter 1

1 Introduction

1.1 Research Background

Electricity plays a critical role in modern society and the healthy development of the global economy. As the International Energy Agency estimates, the global electricity demand will continuously grow by 2.1 % per year by 2040 [1]. To satisfy the increased power demand and reduce carbon emission, significant amounts of renewable resources such as solar and wind, which are typically interfaced by power-electronic converters, are interconnected to the existing power system and this increasing trend will remain in the next few decades. Meanwhile, to transfer the bulk energy and interconnect the networks in different areas and countries, an increasing number of converter-based HVDC links are developed worldwide. In this section, three representative countries/organizations, i.e., the UK, EU and USA, are selected to illustrate this rising trend of the CBRs, which is also the background of the research conducted in this thesis.

1.1.1 UK

Driven by the ambitious objective of achieving net-zero operation of the whole system in 2050, a rapid increase in renewable-based generation can be observed in Great Britain's (GB) power system over the next ten years, especially in Scotland as it has abundant wind resources [2]. The detailed growth of renewables is presented in Figure 1-1, where the energy generated by the wind, solar, nuclear and bioenergy with carbon capture and storage (BECCS) will provide over 90 % of the total electricity output in 2050 [3]. On the other hand, more HVDC links are going to be constructed to facilitate bulk energy transmission among different areas and interconnect the GB power network to the networks operated by other European countries. As shown in Figure 1-2, the number of HVDC links will increase from 7 in 2019 to 34 after the

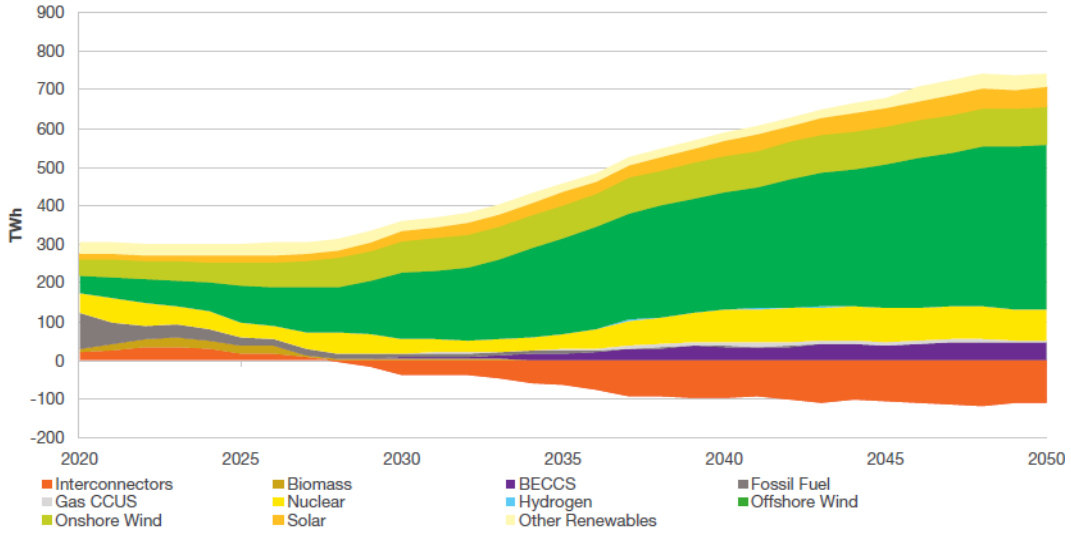

Figure 1-1. Electricity output by technology (excluding non-networked offshore wind generation) [3]

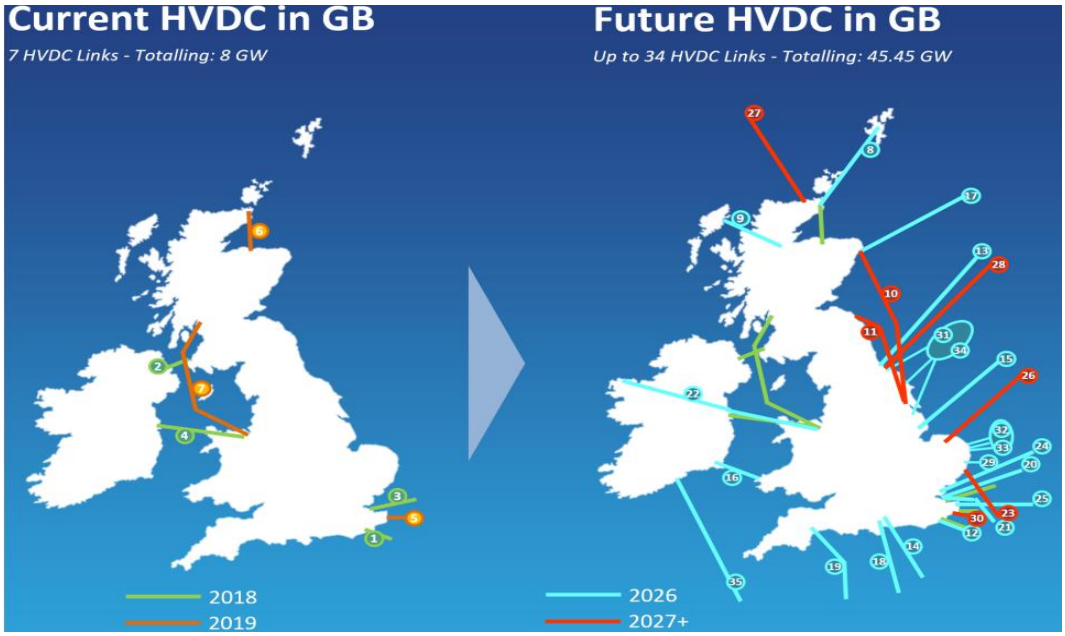

Figure 1-2. HVDC links planned to be constructed in the GB system [4]

year 2027, which results in the total transmission capacity of the HVDC links increasing from 8 GW to 45.45 GW [4]. Those increased renewables and HVDC links will significantly change system fault responses. Thus, it is necessary to investigate the change's impacts on the existing protection system and develop reliable solutions to address raised protection issues.

1.1.2 EU

Based on the long-term strategy of the European Union (EU), the EU will achieve

the climate-neutral by 2050, where an economy with net-zero greenhouse gas emissions can be realised [5]. The detailed plan for electricity generation and shares of different generation techniques of the EU between 2000 and 2050 are presented in Figure 1-3 [6]. By this figure, the share of solar energy will rise from 4% in 2015 to 18% by 2050, and the share of wind generation, including onshore and offshore, will increase from 9% to 40% by 2050. Additionally, the EU also plans to develop supergrids to interconnect the power networks in different countries and transmit the power from the resource-rich area to the areas with the major electricity demands [7]. Compared to conventional wide-area transmission, the supergrids are developed mainly based on HVDC technologies [8].

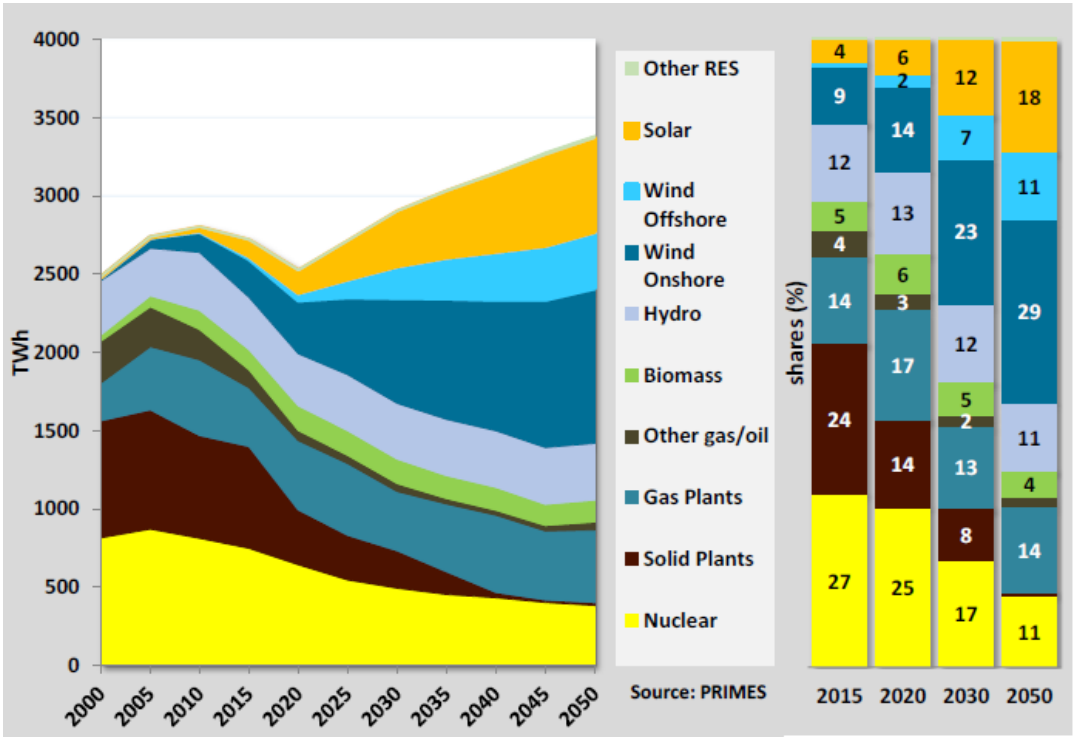

Figure 1-3. Electricity generation by plant type in the EU [6]

1.1.3 USA

As the largest economy in the world, the USA also designs ambitious plans to accommodate more renewables-based energy to the power system to replace fossil fuels, e.g., coal. Based on the data in Figure 1-4 [9], which is provided by the U.S. Energy Information Administration, the share of U.S. power generation contributed by renewables will rise from 21% in 2021 to 44% in 2050, and the share of the natural

gas in this transitioning process will remain relatively constant at 35% from 2021 to 2050 due to the sustained low natural gas prices in the US energy market [9]. The map of the global HVDC project distribution is presented in Figure 1-5 [10]. Based on this figure, more HVDC links are constructed in China, Europe and the UK compared to the cases in the U.S. because of the lack of interconnection among regions and political and bureaucratic constraints such as the right of way and environmental approvals [11]. However, this status will change in the next few decades due to the requirement for long-distance energy transmission and more renewables in the market [12].

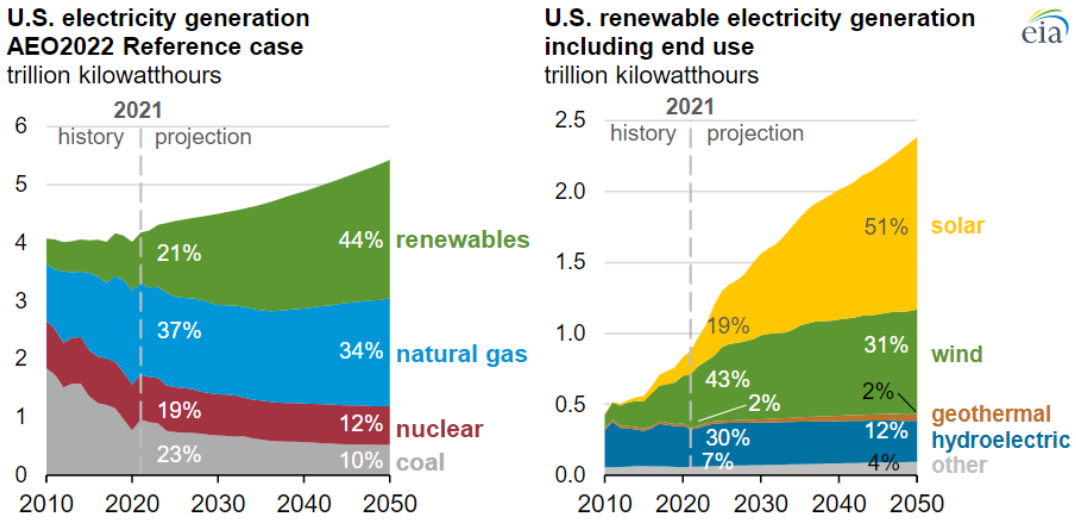

Figure 1-4. US renewable development plan between 2010 to 2050 [9]

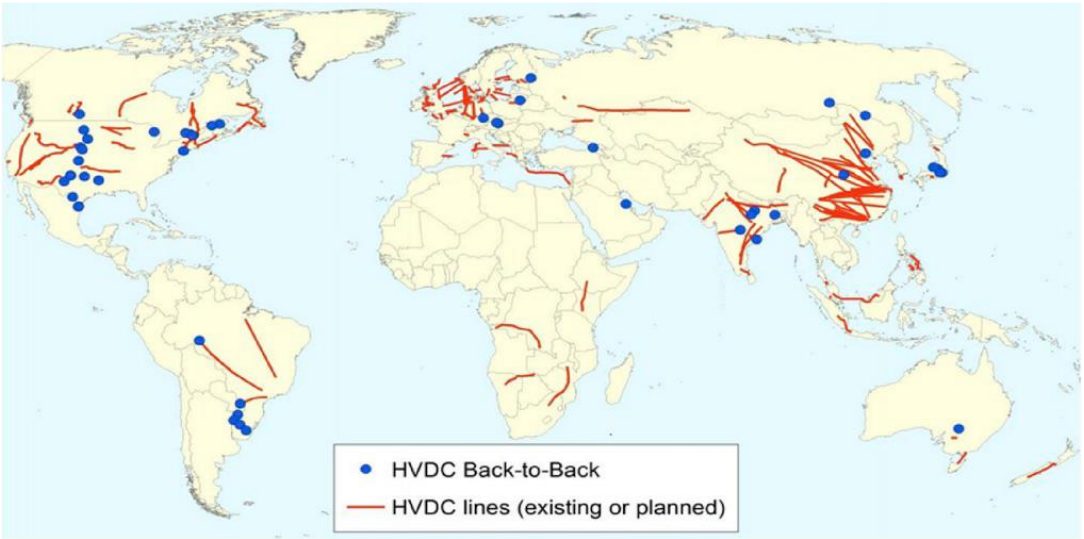

Figure 1-5. Maps of HVDC project distribution [10]

1.2 Protection Challenges and Research Objectives

As proposed in Section 1.1, the global power system is expected to see a significant increase in the penetration of non-synchronous CBRs, e.g., HVDC systems, renewable power generation, and battery storage systems, in the coming decades to achieve the ambitious decarbonization target. Compared to conventional SGs, which exhibit a natural and predictable response during faults with high short-term thermal capability, the dynamic fault behaviour of CBRs is governed by their embedded controllers and dependent on associated grid code requirements [13]. Additionally, owing to the low short-term thermal capability of power electronic devices, the short circuit current contributed by the CBRs is typically no more than 1.5 pu of its rated current [14], which is significantly lower than conventional SGs. Those characteristics pose severe challenges to the reliable operation of protection systems.

As one of the main protection schemes used in the transmission system, distance protection, operating based on the detected faulted loop impedance, plays an essential role in safeguarding the operation of the power system. As reported in [15], an additional impedance will be introduced to the measured impedance of the distance relay owing to the combined effect of the phase angle difference between the local and remote-end infeed and the fault resistance. In a conventional transmission system dominated by SGs, that phase angle difference is typically slight (e.g., in the range of a few degrees). Therefore, the observed under-reach and over-reach issues in SG-dominated networks are insignificant [13]. However, this assumption does not hold in a converter-dominated network as the converters' fault responses are determined by embedded controllers, where the phase difference may experience a significant increase and pose the risks of maloperation to distance protection [16]. Relevant research on the reach issues above is reported in [17] - [20]. The phase selection issues of distance protection are discussed in [21] - [23], where the performance of the sequence component-based phase selector is evaluated. The sequence component-based phase selection algorithm compares angle relations between the negative and positive sequence currents and the negative and zero sequence currents. It was found that the connection of CBRs can lead to incorrect angle relations among the sequence components, thus resulting in incorrect identification of fault types. The different controllers' impacts on distance protection performance are evaluated in [24]. This

paper reports that the converter with a constant reactive power controller could introduce numerical instability problems to the impedance measuring element of the distance relay in phase-to-phase faults.

Except for distance protection issues in the transmission system, the substantial amounts of IIDGs also introduce severe challenges to the protection of distribution systems. The microgrid, which appears in the distribution network, is used as an example to demonstrate the protection challenges of the distribution system. In microgrids and distribution systems, overcurrent relays (OCRs) are implemented as the primary protection [25]. In microgrids, false trips can be raised by the bidirectional power flow owing to the interconnection of distributed generators (DGs) [26]. Those additional DGs also change the fault current distribution on feeders, which leads to the issues of protection blinding and sympathetic tripping [27]. Unlike conventional distribution systems, microgrids can operate in grid-connected and islanded modes depending on the operating conditions of the main grid. The dual-mode capability of microgrids changes fault levels dynamically between two operating modes, particularly for microgrids dominated by IIDGs. The variation of fault levels results in severe challenges to the coordination of overcurrent relays [28] and the fault detection with a high level of discrimination in islanded microgrids [29].

To address the above protection challenges, the research objectives of this thesis are defined as follows:

- The first objective is to develop a systematic HIL test methodology to evaluate the HVDC system's impacts on distance protection performance and analyse sources behind the compromised performance.
- The second objective is to develop a reliable distance measuring algorithm to address the under/over-reach issues of conventional impedance-based distance measurement.
- The third objective is to design a protection scheme to protect microgrids dominated by IIDGs in both grid-connected and islanded modes, whose protection performance is not sensitive to the fault level variation and applied control strategies of IIDGs.

1.3 Principal Contributions

This thesis has four major contributions.

- Development of a flexible controller for CBRs, which can emulate different operating modes of converters and satisfy requirements of the fast fault current injection proposed by the GB Grid Code. Compared to existing research in technical literature, the proposed controller has a simplified structure and is easily implemented in simulation and on programmable hardware. Therefore, it provides a powerful and flexible tool for future research to evaluate the converter's impacts on protection performance.
- Development of a methodology for systematically assessing the impact of HVDC systems on distance protection performance. The proposed methodology was implemented in a realistic HIL laboratory environment. Hardware tests were performed on two commercially available relays. The root causes of the found protection issues were determined and analysed, i.e., under-reach/over-reach, faulted phase selection and impedance measurement. This work was peer-reviewed and published in [30].
- A new sequence components-based distance measuring algorithm is developed to address the under/over-reach issues of the conventional impedance-based distance measuring elements. The proposed measuring approach is not sensitive to the variation of system fault level, protected line length, fault resistance, fault type or fault location.
- A new transient wavelet energy-based protection scheme was developed to protect LV microgrids. As the proposed scheme does not use the fundamental frequency voltages nor the currents supplied by the generators in the network, its performance is not sensitive to the changes in the types of generators and controllers of CBRs. The protective algorithm can detect faults and locate the faulted feeders within a few milliseconds, which is much faster than any conventional protection method. Compared to the travelling wave-based protection (a popular high-frequency components-based protection), the proposed scheme only uses a 10 kHz sampling frequency and effectively isolates close-up faults. This work was peer-reviewed and published in [31].

1.4 Structure of the Thesis

The structure of this thesis is presented below.

Chapter 2 demonstrates the modelling of converters in the following studies, where two typical control structures, including the single and dual sequence current controllers, are implemented. A flexible controller is developed for the converter using dual sequence current control structure to realise three different operating modes and inject reactive currents during faults. The short-circuit responses of developed converter models are evaluated using RTDS-based case studies.

Chapter 3 assesses distance protection challenges caused by the connection of HVDC systems through implementing systematic HIL experimental tests, where a total number of 480 cases, covering different fault conditions, different HVDC control strategies, varied system strengths and different levels of synchronous compensation, are included, along with detailed studies with selected representative cases to understand the sources behind the observed distance protection issues. Additionally, the solutions in the literature to improve distance protection performance are also reviewed in this chapter.

Chapter 4 reviews the protection challenges of inverter-dominated microgrids. The solutions of microgrid protection are reviewed, along with the analysis of the benefits and limitations of different methods to facilitate understanding.

Chapter 5 proposes a sequence component-based distance measuring algorithm. The fundamentals of the symmetrical analysis are reviewed at the beginning of this chapter. The detailed derivation of the developed fault distance measuring element is presented. The performance of this scheme is evaluated under a wide range of system and fault scenarios, including different fault types, resistances, locations, system fault levels and protected line length.

Chapter 6 demonstrates a transient wavelet energy-based scheme to protect LV microgrids with substantial inverter-interfaced resources. The Maximal Overlap Discrete Wavelet Transform (MODWT) is implemented in this protection algorithm to decompose the wavelet coefficients, which is used to calculate the transient wavelet energy employed in the developed protection algorithm. The energy relation of the Current Transformers (CTs) at the individual busbar is derived and implemented to coordinate the relays in microgrids. The performance of this algorithm is evaluated by

a 400 V CIGRE benchmark microgrid developed in MATLAB/SIMULINK.

Chapter 7 summarises the work presented in this thesis and provides direction for future research.

1.5 List of Publications

The following publications have been completed during this PhD:

Journal Articles:

- **D. Liu**, A. Dyśko, Q. Hong, D. Tzelepis and C. D. Booth, "Transient Wavelet Energy-Based Protection Scheme for Inverter-Dominated Microgrid," in *IEEE Transactions on Smart Grid*, vol. 13, no. 4, pp. 2533-2546, July 2022.
- **D. Liu**, Q. Hong, A. Dyśko, D. Tzelepis, G. Yang, C. D. Booth, I. Cowan and B. Ponnalagan, "Evaluation of HVDC system's impact and quantification of synchronous compensation for distance protection", in *IET Renewable Power Generation*, vol. 16, no. 9, pp. 1925-1940, 2022.
- M. Khan, Q. Hong, **D. Liu**, A. E. Alvarez, A. Dyśko, C. Booth and D. Rostom, "Experimental assessment and validation of inertial behaviour of virtual synchronous machines", in *IET Renewable Power Generation*, vol. 16, no. 9, pp. 1897-1907, 2022.

Conference Papers:

- **D. Liu**, Q. Hong, M. A. Uddin Khan, A. Dyśko, A. Egea-Alvarez and C. D. Booth, " Evaluation of Grid-Forming Converter's impact on distance protection performance," *The 16th International Conference on Developments in Power System Protection*, 2022, pp.1-6.
- K. Kawal, Q. Hong, S. Paladhi, **D. Liu**, P. N. Papadopoulos, S. Blair, and C. D. Booth, " Vulnerability assessment of line current differential protection in converter-dominated power systems," *The 16th International Conference on Developments in Power System Protection*, 2022, pp.1-6.
- **D. Liu**, Q. Hong, A. Dyśko, A. Egea-Alvarez, L. Xu, C. D. Booth, I. Cowan and B. Ponnalagan, " A flexible real time network model for evaluating HVDC systems' impact on AC protection performance," *The 9th Renewable Power Generation Conference*, 2021, pp. 216-221.

- **D. Liu**, Q. Hong, A. Dyśko, D. Tzelepis, C. D. Booth, I. Cowan and B. Ponnalagan, "Hardware-in-the-Loop Tests and Analysis of HVDC System's Impact on Distance Protection Performance," *The 17th International Conference on AC and DC Power Transmission (ACDC 2021)*, 2021, pp. 96-101.
- **D. Liu**, Q. Hong, A. Dyśko, D. Tzelepis, G. Yang, C. D. Booth, I. Cowan and B. Ponnalagan, "Impact of system strength and HVDC control strategies on distance protection performance," *The 9th Renewable Power Generation Conference (RPG Dublin Online 2021)*, 2021, pp. 100-105.
- W. Yan, Q. Hong, **D. Liu** and A. Dyśko, "Feasibility studies on black start capability of distributed energy resources," *The 10th Renewable Power Generation Conference (RPG 2021)*, 2021, pp. 869-875.
- M. A. Uddin Khan, Q. Hong, **D. Liu**, A. Egea-Alvarez, A. Dyśko, C. D. Booth, and D. Rostom, "Comparative evaluation of dynamic performance of virtual synchronous machine and synchronous machines," *The 9th International Conference on Renewable Power Generation (RPG Dublin Online 2021)*, 2021.
- **D. Liu**, D. Tzelepis, A. Dyśko, and C. D. Booth, "A novel protection scheme for inverter-dominated microgrid," *The 15th International Conference on Developments in Power System Protection*, 2020.
- **D. Liu**, D. Tzelepis and A. Dyśko, "Protection of Microgrids with High Amounts of Renewables: Challenges and Solutions," *2019 54th International Universities Power Engineering Conference (UPEC)*, 2019, pp. 1-6.

1.6 Chapter References

[1] 'World Energy Outlook', International Energy Agency, 2019.

[2] 'Electricity Ten Years Statement', National Grid ESO, November 2021.

[3] 'Future Energy Scenarios', National Grid ESO, July 2021.

[4] 'Multi - Terminal Test Environment (MTTE) for HVDC Systems – Future Business Model', National HVDC Centre, February 2021.

[5] "Press corner", *European Commission - European Commission*, 2022. [Online]. Available: https://ec.europa.eu/commission/presscorner/detail/en/IP_20_2096. [Accessed: 30- Mar- 2022].

[6] 'EU Reference Scenario 2020', Directorate-General for Energy, Directorate-

General for Climate Action and Directorate-General for Mobility and Transport of the European Commission, July 2021.

[7] 'Innovation landscape brief: Supergrids', International Renewable Energy Agency (IERNA), Abu Dhabi, 2019.

[8] M. B. Blarke and B. M. Jenkins, "SuperGrid or SmartGrid: Competing strategies for large-scale integration of intermittent renewables?," *Energy Policy*, vol. 58, pp. 381–390, Jul. 2013.

[9] 'Annual Energy Outlook 2022 (AEO 2022)', U.S. Energy Information Administration, March 2022.

[10] M. Ardelean and P. Minnebo, *A China-EU Electricity Transmission Link: Assessment of Potential Connecting Countries and Routes*. Ispra, Italy: Joint Research Center (JRC), 2017.

[11] S. Khalid, M. Sheppard, C. Burg, S. Saeed and S. Khalid, "The Role of HVDC in the U.S. Energy Transition | Power Technology Research", Powertechresearch.com, 2022. [Online]. Available: https://powertechresearch.com/the-role-of-hvdc-in-the-u-s-energy-transition/.

[12] A. Bloom et al., "The Value of Increased HVDC Capacity Between Eastern and Western U.S. Grids: The Interconnections Seam Study," in *IEEE Transactions on Power Systems*, vol. 37, no. 3, pp. 1760-1769, May 2022.

[13] A. Hooshyar, M. A. Azzouz and E. F. El-Saadany, "Distance Protection of Lines Emanating From Full-Scale Converter-Interfaced Renewable Energy Power Plants—Part I: Problem Statement," in *IEEE Transactions on Power Delivery*, vol. 30, no. 4, pp. 1770-1780, Aug. 2015.

[14] B. Brearley and R. Prabu, "A review on issues and approaches for microgrid protection", *Renewable and Sustainable Energy Reviews*, vol. 67, pp. 988-997, 2017.

[15] Y. Fang, K. Jia, Z. Yang, Y. Li and T. Bi, "Impact of Inverter-Interfaced Renewable Energy Generators on Distance Protection and an Improved Scheme," in *IEEE Transactions on Industrial Electronics*, vol. 66, no. 9, pp. 7078-7088, Sept. 2019.

[16] A. Hooshyar, M. A. Azzouz and E. F. El-Saadany, "Distance Protection of Lines Emanating From Full-Scale Converter-Interfaced Renewable Energy Power

Plants—Part II: Solution Description and Evaluation," in *IEEE Transactions on Power Delivery*, vol. 30, no. 4, pp. 1781-1791, Aug. 2015.

[17] A. Banaiemoqadam, A. Hooshyar and M. A. Azzouz, "A Control-Based Solution for Distance Protection of Lines Connected to Converter-Interfaced Sources During Asymmetrical Faults," in *IEEE Transactions on Power Delivery*, vol. 35, no. 3, pp. 1455-1466, June 2020.

[18] S. Paladhi and A. K. Pradhan, "Adaptive Distance Protection for Lines Connecting Converter-Interfaced Renewable Plants," in *IEEE Journal of Emerging and Selected Topics in Power Electronics*, vol. 9, no. 6, pp. 7088-7098, Dec. 2021.

[19] R. Li et al., "Impact of low (zero) carbon power systems on power system protection: a new evaluation approach based on a flexible modelling and hardware testing platform", in *IET Renewable Power Generation*, vol. 14, no. 5, pp. 906-913, 2020.

[20] M. Alam, H. Leite, J. Liang and A. da Silva Carvalho, "Effects of VSC based HVDC system on distance protection of transmission lines", in *International Journal of Electrical Power & Energy Systems*, vol. 92, pp. 245-260, 2017.

[21] M. Azzouz and A. Hooshyar, "Dual Current Control of Inverter-Interfaced Renewable Energy Sources for Precise Phase Selection", in *IEEE Transactions on Smart Grid*, vol. 10, no. 5, pp. 5092-5102, 2019.

[22] A. Haddadi, M. Zhao, I. Kocar, U. Karaagac, K. W. Chan and E. Farantatos, "Impact of Inverter-Based Resources on Negative Sequence Quantities-Based Protection Elements," in *IEEE Transactions on Power Delivery*, vol. 36, no. 1, pp. 289-298, Feb. 2021.

[23] K. Xu, Z. Zhang, Q. Lai and X. Yin, "Fault phase selection method applied to tie line of renewable energy power stations", *IET Generation, Transmission & Distribution*, vol. 14, no. 13, pp. 2549-2557, 2020.

[24] J. Jia, G. Yang, A. H. Nielsen and P. Rønne-Hansen, "Impact of VSC Control Strategies and Incorporation of Synchronous Condensers on Distance Protection Under Unbalanced Faults," in *IEEE Transactions on Industrial Electronics*, vol. 66, no. 2, pp. 1108-1118, Feb. 2019.

[25] M. Khederzadeh, "Preservation of overcurrent relays coordination in microgrids by application of static series compensators," *11th IET International Conference*

on Developments in Power Systems Protection (DPSP 2012), 2012, pp. 1-5.

[26] A. Jalilian, M. T. Hagh and S. M. Hashemi, "An Innovative Directional Relaying Scheme Based on Postfault Current," in *IEEE Transactions on Power Delivery*, vol. 29, no. 6, pp. 2640-2647, Dec. 2014.

[27] V. A. Papaspiliotopoulos, G. N. Korres, V. A. Kleftakis and N. D. Hatziargyriou, "Hardware-In-the-Loop Design and Optimal Setting of Adaptive Protection Schemes for Distribution Systems With Distributed Generation," in *IEEE Transactions on Power Delivery*, vol. 32, no. 1, pp. 393-400, Feb. 2017.

[28] H. M. Sharaf, H. H. Zeineldin and E. El-Saadany, "Protection Coordination for Microgrids With Grid-Connected and Islanded Capabilities Using Communication Assisted Dual Setting Directional Overcurrent Relays," in *IEEE Transactions on Smart Grid*, vol. 9, no. 1, pp. 143-151, Jan. 2018.

[29] H. J. Laaksonen, "Protection Principles for Future Microgrids," in *IEEE Transactions on Power Electronics*, vol. 25, no. 12, pp. 2910-2918, Dec. 2010.

[30] D. Liu, Q. Hong, A. Dyśko, D. Tzelepis, G. Yang, C. D. Booth, I. Cowan and B. Ponnalagan, "Evaluation of HVDC system's impact and quantification of synchronous compensation for distance protection", in *IET Renewable Power Generation*, vol. 16, no. 9, pp. 1925-1940, 2022.

[31] D. Liu, A. Dyśko, Q. Hong, D. Tzelepis and C. D. Booth, "Transient Wavelet Energy-Based Protection Scheme for Inverter-Dominated Microgrid," in *IEEE Transactions on Smart Grid*, vol. 13, no. 4, pp. 2533-2546, July 2022.

Chapter 2

2 Converter-Based Generator Modelling and Short-Circuit Analysis

2.1 Introduction

As indicated in Chapter 1, the short-circuit response of a CBR is dependent on the implemented control strategy, which can potentially affect the performance of the protection devices in the power system. Therefore, the converter short-circuit response is evaluated in this section first before moving into the protection parts.

The converter control can be implemented in several different reference frames, including the synchronous reference frame (dq frame), the stationary reference frame ($\alpha\beta$ frame) and the neutral reference frame (abc frame). In this thesis, all converters are designed in the synchronous reference frame (dq frame), which is widely adopted for converter control. In Section 2.2, the instantaneous power theory is reviewed, which is the fundamentals of the controller design. In Section 2.3, modelling of the converter with conventional active and reactive power controller is proposed, where it only has the positive sequence inner current control loop. Additionally, the short-circuit response of the designed converter with a conventional controller is evaluated by applying all types of faults. In Section 2.4, the modelling of the converter with a dual-sequence current controller is discussed, where a flexible control strategy is implemented to realise different control strategies, i.e., the balanced current control to inject positive sequence currents, the constant active power control and the constant reactive power control to suppress the AC ripples on the generated active power and reactive power and inject reactive currents during faults. To evaluate the short-circuit response of a converter with the dual-sequence current controller, case studies are conducted in Section 2.4. The summary of this chapter is discussed in Section 2.5.

2.2 Instantaneous Power Theory

In the normal state, the transmission system can be considered as a three-phase balanced network, where the voltage only has the positive sequence components. However, when asymmetrical faults occur, the negative sequence components will be superimposed to the positive-sequence voltage and current [1]. In this condition, the voltages and currents at the measuring point are described in $(2-1)$ and $(2-2)$ respectively, where the superscripts "+" and "-" stand for the positive and negative sequence components of the measured voltages and currents.

$$v = v^{+} + v^{-} \tag{2-1}$$

$$i = i^{+} + i^{-} \tag{2-2}$$

According to the instantaneous power theory [2], the instantaneous active and reactive power (i.e., P and Q) from the converter are shown as $(2-3)$ and $(2-4)$.

$$P = v \cdot i \tag{2-3}$$

$$Q = v_{\perp} \cdot i \tag{2-4}$$

where $v_{\perp}$ is the orthogonal version of grid voltage v. Substituting the v and i in $(2-1)$ and $(2-2)$ into $(2-3)$ and $(2-4)$, the $(2-5)$ and $(2-6)$ are derived.

$$P = \overbrace{v^{+}i^{+} + v^{-}i^{-}}^{\text{constant power}} + \overbrace{v^{+}i^{-} + v^{-}i^{+}}^{\text{oscillating power}} \tag{2-5}$$

$$Q = \overbrace{v_{\perp}^{+}i^{+} + v_{\perp}^{-}i^{-}}^{\text{constant power}} + \overbrace{v_{\perp}^{+}i^{-} + v_{\perp}^{-}i^{+}}^{\text{oscillating power}} \tag{2-6}$$

According to equations $(2-5)$ and $(2-6)$, it can be seen that both active power and reactive power consist of two parts, i.e., the constant and oscillating power. The oscillating power parts are raised by the interaction between the positive and negative sequence voltages and currents, which is analysed in Section 2.3.2 in detail.

As the converter control is developed in the dq frame, the $(2-5)$ and $(2-6)$, which are in the abc frame, are transformed into the dq frame by applying the Park Transform, which yields $(2-7)$ to $(2-12)$ [3].

$$\bar{P} = \frac{3}{2}\left(v_d^+ i_d^+ + v_q^+ i_q^+ + v_d^- i_d^- + v_q^- i_q^-\right) \quad (2-7)$$

$$P_C = \frac{3}{2}\left(v_d^- i_d^+ + v_q^- i_q^+ + v_d^+ i_d^- + v_q^+ i_q^-\right) \quad (2-8)$$

$$P_S = \frac{3}{2}\left(v_q^- i_d^+ - v_d^- i_q^+ - v_q^+ i_d^- + v_d^+ i_q^-\right) \quad (2-9)$$

$$\bar{Q} = \frac{3}{2}\left(v_q^+ i_d^+ - v_d^+ i_q^+ + v_q^- i_d^- - v_d^- i_q^-\right) \quad (2-10)$$

$$Q_C = \frac{3}{2}\left(v_q^- i_d^+ - v_d^- i_q^+ + v_q^+ i_d^- - v_d^+ i_q^-\right) \quad (2-11)$$

$$Q_S = \frac{3}{2}\left(-v_d^- i_d^+ - v_q^- i_q^+ + v_d^+ i_d^- + v_q^+ i_q^-\right) \quad (2-12)$$

Where v_d^+, v_q^+, i_d^+ and i_q^+ are the positive sequence voltages and currents in the d and q axes; v_d^-, v_q^-, i_d^- and i_q^- are the negative sequence voltages and currents in the d and q axes; $\bar{P}$ and $\bar{Q}$ are the average real and reactive power, which are the power references given by the user; P_C, Q_C and P_s, Q_s are the cosine and sine terms of active power and reactive power. The $(2-7)$ to $(2-12)$ can be further expressed in the form of a matrix as presented in $(2-13)$.

$$\begin{bmatrix} \bar{P} \\ P_C \\ P_S \\ \bar{Q} \\ Q_C \\ Q_S \end{bmatrix} = \frac{3}{2}\begin{bmatrix} +v_d^+ & +v_q^+ & +v_d^- & +v_q^- \\ +v_d^- & +v_q^- & +v_d^+ & +v_q^+ \\ +v_q^- & -v_d^- & -v_q^+ & +v_d^+ \\ +v_q^+ & -v_d^+ & +v_q^- & -v_d^- \\ +v_q^- & -v_d^- & +v_q^+ & -v_d^+ \\ -v_d^- & -v_q^- & +v_d^+ & +v_q^+ \end{bmatrix} \times \begin{bmatrix} i_d^+ \\ i_q^+ \\ i_d^- \\ i_q^- \end{bmatrix} \quad (2-13)$$

In $(2-13)$, values of i_d^+, i_q^+, i_d^- and i_q^- on the right-hand side can be controlled by academic researchers by setting the current references of the outer power controller. Therefore, these are controllable variables. However, the characteristics of the converter's output power are determined by six variables, including the $\bar{P}, P_C, P_S, \bar{Q}, Q_C, Q_S$, as shown in $(2-13)$, which means two power variables cannot be controlled. Typically, the control of the average active and reactive power should be considered first and the other two objectives could be decided based on the user's

preference. For the designed controller in Section 2.4, it realises three control strategies by setting three different control objectives, i.e., constant active power control by setting the P_C and P_S in $(2-8)$ and $(2-9)$ to zero, constant reactive power control by setting the Q_C and Q_S in $(2-11)$ and $(2-12)$ to zero and balanced current control by setting the i_d^- and i_q^- in $(2-13)$ to zero. The detailed derivation of the current references to realise three control modes is discussed in Section 2.4.

2.3 Modelling and Performance Evaluation of Converter with Conventional Active and Reactive Power Controller

2.3.1 Converter Modelling with Active and Reactive Power Controller

In this section, the converter model with a conventional controller is developed based on [4], whose structure is shown in Figure 2-1. As this type of controller is to regulate the active and reactive power to the grid, it is also called the active and reactive power control strategy. As presented in this figure, the three-phase voltages, v_{abc}, and currents, i_{abc}, measured at the delta side of the interface transformer are used as the inputs of this controller. The 'Synchronous Reference Frame Phase-Locked Loop (SRF-PLL)' [5] is used to synchronise the converter with the grid voltage and its structure is shown in Figure 2-2, where ω_s is the system angular frequency. Typically, the reference value for v_q is set as zero to estimate the system phase angle. In this case, the active power and reactive power delivered from the converter can be calculated by $(2-14)$ and $(2-15)$.

$$P = \frac{3}{2} v_d i_d \qquad (2-14)$$

$$Q = -\frac{3}{2} v_d i_q \qquad (2-15)$$

The calculated power is used as input for the outer power loop to generate the current references, i_{dr} and i_{qr}. The derived references will be further tracked by the inner current controller to generate a set of output voltage signals and these voltage signals are finally converted into pulses to control the operation of the converter. Additionally, owing to the safety requirement of the converter, the maximum phase

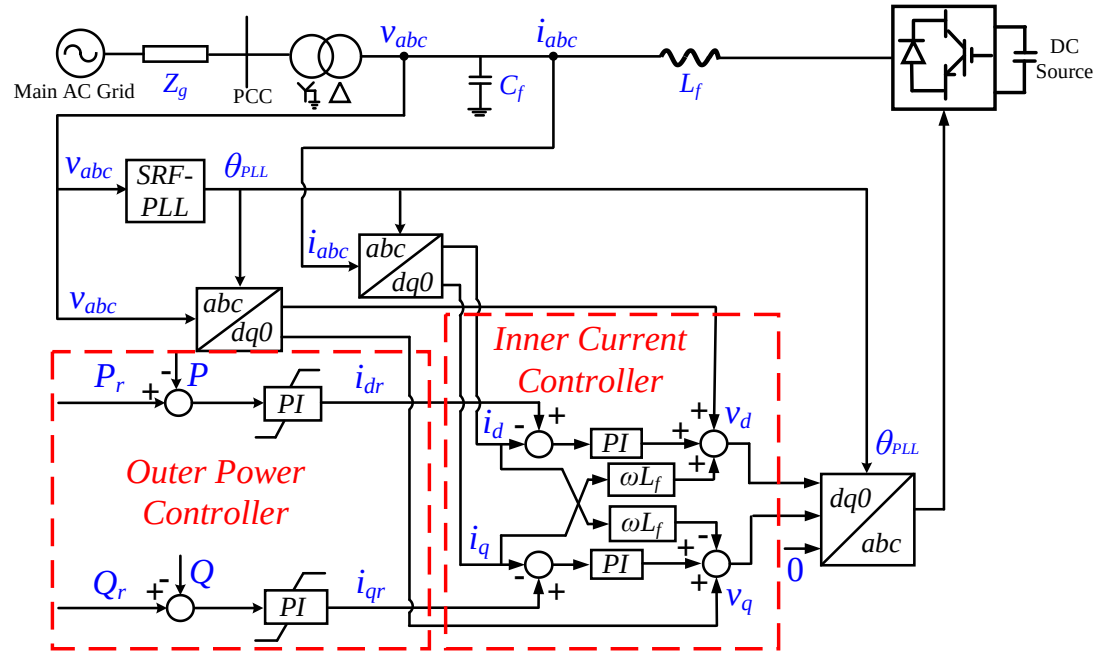

Figure 2-1. Converter with Conventional PQ Controller [4]

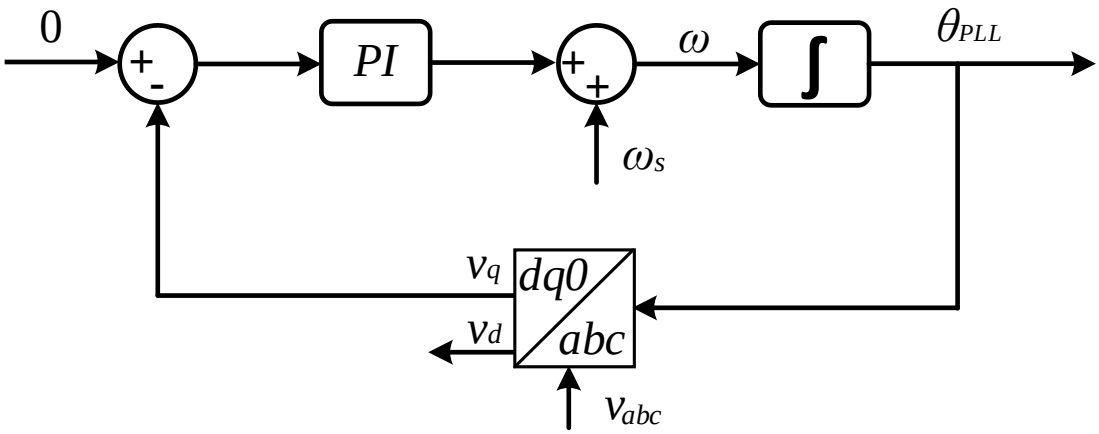

Figure 2-2. Structure of the SRF-PLL [5]

current should always be lower than the defined tolerable level [6]. In this case, a fault current limiter based on $(2-16)$ is developed, where i_{dr} and i_{qr} are the current references in dq frame and i_{max} is the maximum acceptable current of the converter.

$$i_{dr} = \sqrt{(i_{max})^2 - (i_{qr})^2} \qquad (2-16)$$

2.3.2 Short-Circuit Response of Converter with Active and Reactive Power Controller

The controller in Figure 2-1 has been implemented in RSCAD, a software specially designed for RTDS, to control the designed converter, whose short-circuit responses under various types of faults are evaluated in this section.

The test network is shown in Figure 2-3. In this network, the capacity of the studied converter is 839 MVA. Conventionally, a network with a Short Circuit Ratio (SCR) lower than 3 is considered as a weak system [7]. The boundary value of SCR of the strong and weak system, i.e., $SCR = 3$, is applied in this test to evaluate the performance of the converter model with a conventional controller. By applying the equations $(2-17)$ and $(2-18)$, the corresponding impedance of Z_g with $SCR = 3$ is $30.05\angle 84.8^{\circ}\ \Omega$. In equations of $(2-17)$ and $(2-18)$, the SCR_{Grid} and FL_{Grid} are the SCR value and fault level of the connected AC network; s_{con} is the capacity of the investigated converter; v_{LL} is the system line-to-line voltage and $|Z_g|$ is the magnitude of the equivalent impedance of the AC network.

$$SCR_{Grid} = \frac{FL_{Grid}}{s_{con}} \tag{2-17}$$

$$|Z_g| = \frac{v_{LL}^2}{FL_{Grid}} \tag{2-18}$$

The results in this test are measured at the delta side of the interfacing transformer and the results are presented as per unit values referring to the bases in $(2-19)$ to $(2-21)$. In those equations, s_{base}, v_{base}, i_{base} are the bases of the power, voltage and current. As the converter should limit its instantaneous outputs to being lower than its maximum tolerable currents, i.e., $i_{max} = 1.2$ pu in $(2-16)$, the bases in $(2-20)$ and $(2-21)$ are represented by peak values.

$$s_{base} = 839\ MVA \tag{2-19}$$

$$v_{base} = \frac{360\sqrt{2}}{\sqrt{3}} = 293.94\ kV \tag{2-20}$$

$$i_{base} = \frac{2}{3} \times \frac{s_{base}}{v_{base}} = 1.90\ kA \tag{2-21}$$

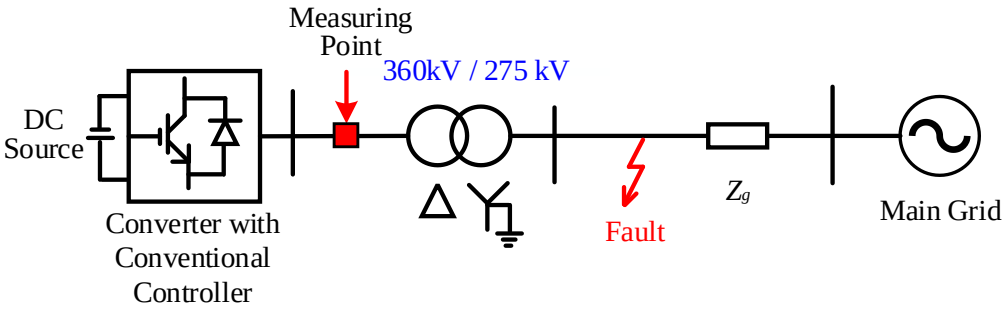

Figure 2-3. Network to evaluate the performance of converter with a conventional controller

The short-circuit response of the converter is presented in Figure 2-4, where three bolted faults are applied at the grid side, and all variables are measured at the converter side of the interfacing transformer. From Figure 2-4, the converter with conventional active and reactive controller suffers from overcurrent issues, i.e., some phase currents being greater than 1.2 pu, under asymmetrical faults, such as phase-A-to-ground fault (AG) and phase-A-to-phase-B fault (AB), while it is capable of limiting the current properly in balanced faults. The thing that needs to be highlighted is that the mentioned overcurrent issue above refers to the overcurrents in the steady state of faults rather than the initial overshoots, as presented in Figure 2-4 (c), and the reasons behind the overcurrents in the steady state and the initial overshoots are not same. The initial overshoots in balanced faults are raised by the significant phase adjustment of the PLL due to the sudden drop of three-phase terminal voltages [8]. While the steady-state overcurrents are caused by the interaction between the positive and negative sequence voltages and currents in asymmetrical faults, as explained below.

The designed converter is synchronised by the SRF-PLL in Figure 2-2, which tracks the angles of the positive sequence voltage of the connected AC system. In the normal operating state, the transmission network is a balanced system with only positive sequence voltage and current. The voltage and current behave as constant variables after the Park Transform owing to the rotating synchronisation between the dq frame and the grid. However, when asymmetrical faults occur, negative sequence components are introduced to the system voltages and currents, which rotate at the same angular velocity but in the opposite direction of the positive sequence components in the synchronous reference frame. In this case, 2^{nd} harmonic ripples will appear in the transformed voltage and current. Such undesired oscillation could

degrade the tracking performance of the PI controller, which further causes the current limiting issues observed in the results. Although this issue can be relieved by increasing the bandwidth of PI control, it can result in instability issues of the converter [9]. Therefore, it is necessary to decouple the positive and negative-sequence voltage and current and introduce another inner current control loop to regulate the negative-sequence current independently. This controller with another negative-sequence control algorithm is called the 'dual-sequence current controller', which is discussed in Section 2.4.

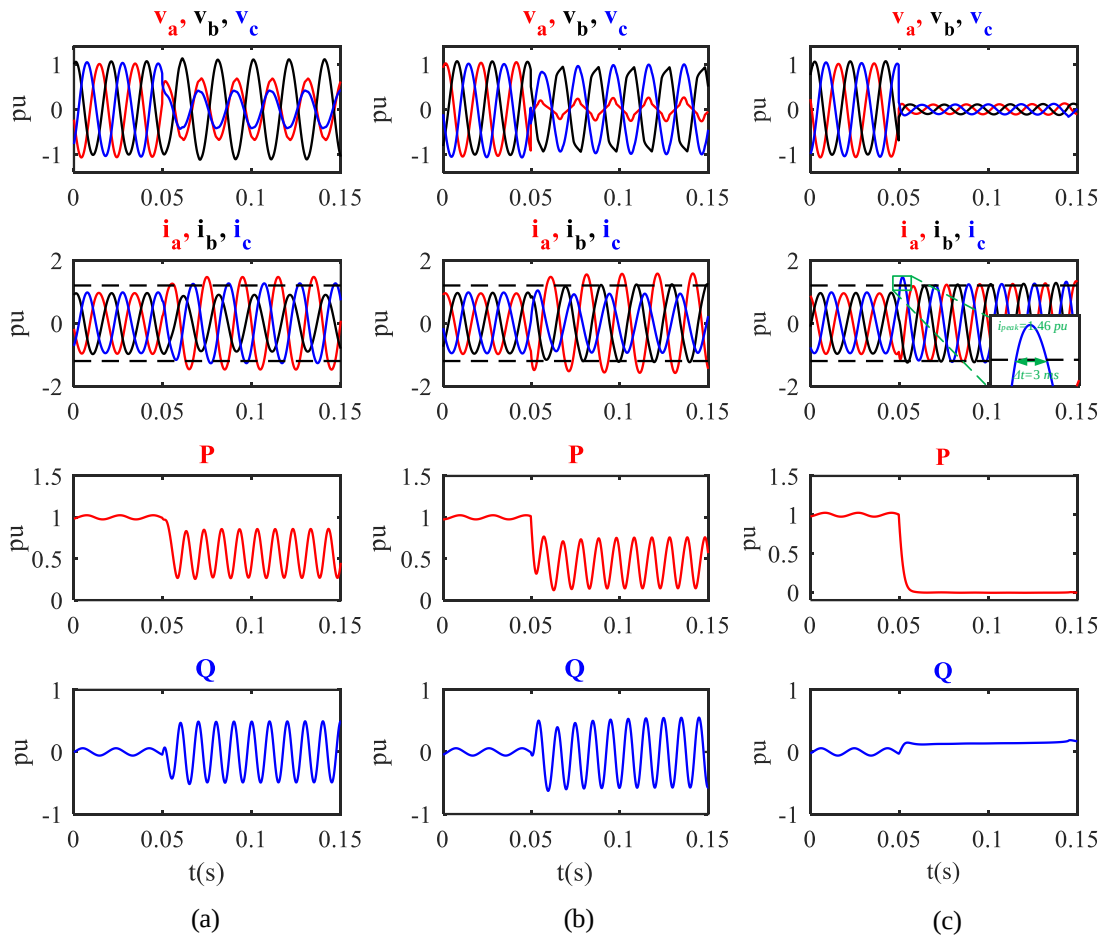

Figure 2-4. Short-circuit response of the converter with conventional PQ controller in the event of, (a) AG fault, (b) AB fault, (c) ABCG fault

2.4 Modelling and Short–Circuit Response of Converter with Dual-Sequence Current Control Strategy

2.4.1 Overview of the Dual-Sequence Current Controller

As proposed in Section 2.3.2, the presence of negative sequence components during asymmetrical faults could introduce overcurrent issues to the converter with a conventional PQ controller. To address this issue, a new control scheme was proposed at the end of the 1990s by adding a negative sequence control loop to decouple the interaction between the positive and negative sequence components [10]. Additionally, different control objectives can be achieved with this dual-sequence strategy, which improves the flexibility of the converter control. Among these control objectives, the balanced current, constant active power and constant reactive power controllers are the most typically used. The balanced current control strategy aims to mitigate the negative sequence components of the output currents. In this control strategy, the references of the negative sequence currents are set to zero. Therefore, it is relatively easier to be designed. As proposed in [11], in the case of asymmetrical faults, the unbalanced voltage will cause the AC ripples on the active power, which will further induce the oscillation on the DC side voltage of the converter system. To address this issue, the constant active power controller is proposed by mitigating the oscillation on the active power of the converter. The last control strategy is the constant reactive power control, which is used to suppress the AC ripples on the reactive power. This strategy can deliver a high quality of reactive power in the case of asymmetrical fault and decrease the voltage unbalance at the Point of Common Coupling (PCC) in the transmission network with the inductive characteristic [12].

The structure of the converter with a dual-sequence current control is shown in Figure 2-5 [10]. In this figure, the converter is synchronised by the SRF-PLL in Figure 2-2. Assume the phase angle of the positive sequence voltage is θ_{PLL}, the angle of the negative sequence voltage will be $-\theta_{PLL}$ due to the opposite rotational direction between the positive and negative sequence components in the dq frame. The derived angles are used in the following Park Transform. The positive and negative sequence components are separated by the notch filter, where the cut-off frequency equals two times the fundamental frequency. The behaviour of the converter during faults is

mainly determined by the current references generated from the outer power controller. The designed flexible outer power loop could realise the following control objectives:

1) Emulate different control strategies in asymmetrical faults, e.g., constant reactive power control to suppress the ripples on the output reactive power, balanced current control to generate symmetrical fault currents and constant active power control to suppress the ripples on the output active power.
2) Inject certain amounts of the positive sequence reactive current during faults based on the injection curve defined in the GB Grid Code [13].
3) Limit the phase current to 1.2 pu to avoid the overcurrent issues of converters.

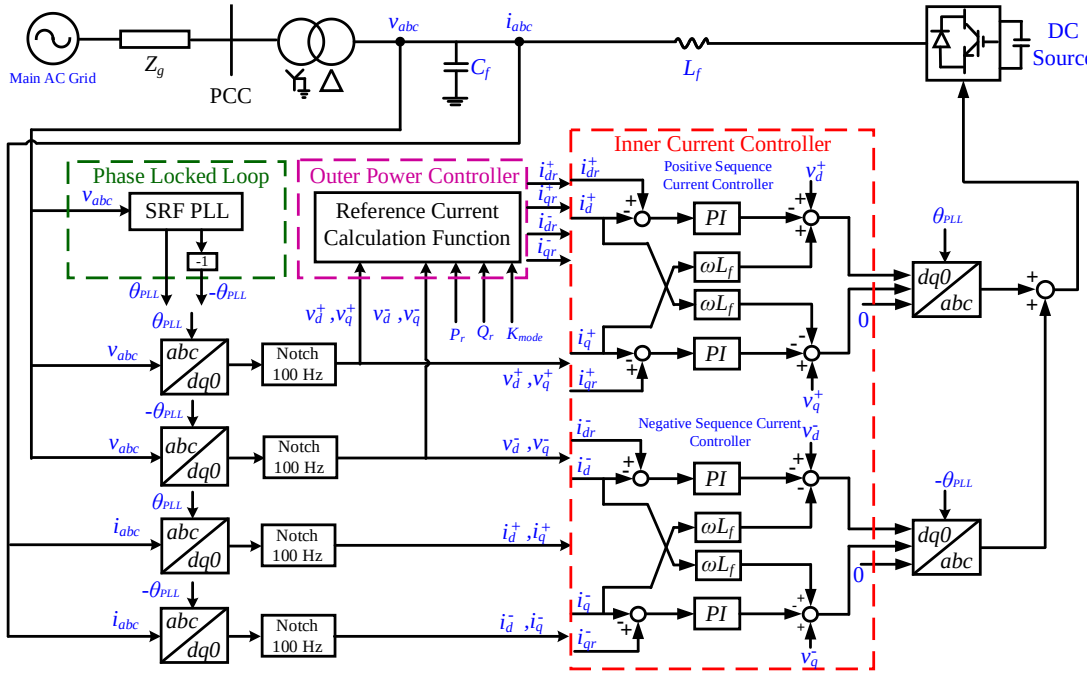

Figure 2-5. Structure of converter with dual-sequence current controller [10]

The generated current references are further tracked in the inner current controller, where the positive and negative sequence currents are controlled separately. Therefore, it is also called the 'dual-sequence current controller' [14].

2.4.2 Design of the Converter's Outer Power Controller

2.4.2.1 Capability of the Fast Fault Current Injection

The GB Grid Code requires the Type B, Type C and Type D Power Park Module and HVDC equipment to inject the positive-sequence reactive current during faults to

support the reduced faulted phase voltage. The definition of Type A, B, C, and D Power Park Module is presented in Table 2-1 [13]. As in the following case studies, the voltage level of the studied transmission network is 275 kV and the capacity of the designed converter interfaced HVDC system is 839 MVA, the fast fault current injection (FFCI) capability should be considered in the process of converter design.

In the following studies, the amount of the injected reactive current is based on the solid black line presented in Figure 2-6 [13]. The function of the positive sequence voltage, v^+, and the injected positive sequence reactive current, i_q^+, is shown by $(2-22)$, where the positive sequence voltage, v^+, is estimated by $(2-23)$. In $(2-23)$, the v_d^+ and v_q^+ are the positive sequence voltage in d and q axes.

Table 2-1: Definition of Type A, B, C and D Power Park Modules [13]

Type Name	Definition
Type A	A Power-Generating Module (including an Electricity Storage Module) with a Grid Entry Point or User System Entry Point below 110 kV and a Maximum Capacity of 0.8 kW or greater but less than 1 MW.
Type B	A Power-Generating Module (including an Electricity Storage Module) with a Grid Entry Point or User System Entry Point below 110 kV and a Maximum Capacity of 1MW or greater but less than 10 MW.
Type C	A Power-Generating Module (including an Electricity Storage Module) with a Grid Entry Point or User System Entry Point below 110 kV and a Maximum Capacity of 10 MW or greater but less than 50 MW.
Type D	A Power-generating Module: (including an Electricity Storage Module) • with a Grid Entry Point or User System Entry Point at, or greater than, 110 kV. • Or with a Grid Entry Point or User System Entry Point below 110 kV and with a Maximum Capacity of 50MW or greater.

$$i_q^+(pu) = -3.28v^+ + 2.64, 0 \le i_q^+ \le 1 \qquad (2-22)$$

$$v^+ = \sqrt{{v_d^+}^2 + {v_q^+}^2} \qquad (2-23)$$

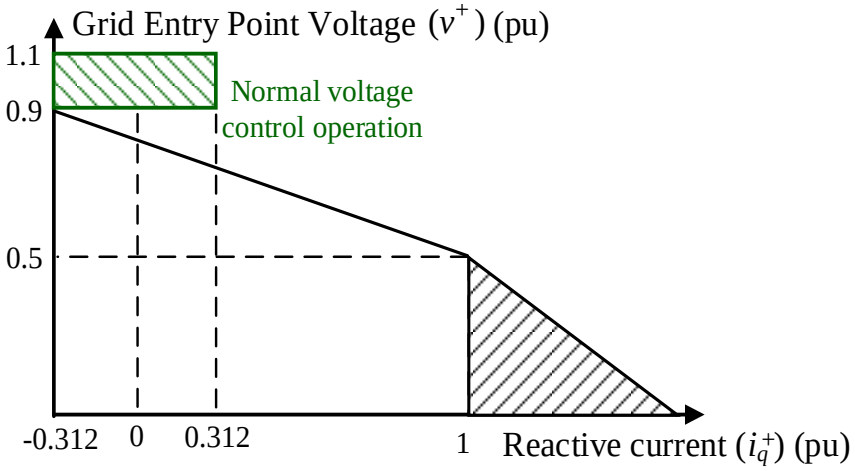

Figure 2-6. Reactive Current Injection Requirement defined in the Grid Code [13]

Based on the Grid Code, the maximum level of the injected reactive current should be no large than 1 pu unless the special requirement is suggested by the developer. Therefore, the injected reactive current of the developed converter model is restricted to 1 pu.

Although the current GB grid code does not require injecting the negative sequence currents during asymmetrical faults, the lack of negative sequence currents can lead to overvoltage issues of the healthy phases [15] and the maloperation of protection devices [16]. Therefore, the injection of negative sequence currents during faults has been approved in the latest IEEE standard (i.e., *IEEE Std 2800* [17]). Additionally, significant amounts of renewables and HVDC systems are going to be connected and constructed in the GB system, which could accelerate the revision of the GB grid code to allow the negative sequence current injection in the following years. To facilitate investigating the impacts of the negative sequence current injection on distance relays, two additional control strategies, including the constant active power controller and the constant reactive power controller, are proposed in Section 2.4.2.3 and Section 2.4.2.4 by injecting some levels of negative sequence currents.

2.4.2.2 Balanced Current Control Strategy

With the balanced current control strategy, the values of negative sequence current references, i_{dr}^- and i_{qr}^- are chosen as zero so that the output current can only have the positive sequence components [18][19]. Meanwhile, owing to the requirement of the FFCI capability, the reference of positive-sequence reactive current, i_{qr}^+, is calculated

by $(2-22)$ and the reference of positive-sequence active current, i_{dr}^{+}, is determined by $(2-24)$, where the i_{max} is the maximum magnitude of the fault current.

$$i_{dr}^{+} = \sqrt{(i_{max})^2 - \left(i_{qr}^{+}\right)^2} \qquad (2-24)$$

After substituting $i_{dr}^{-} = i_{qr}^{-} = 0$ to $(2-13)$, the values of the AC components P_C, P_S, Q_C, Q_S, with the balanced current controller can be estimated by $(2-25)$.

$$\begin{bmatrix} P_C \\ P_S \\ Q_C \\ Q_S \end{bmatrix} = \frac{3}{2}\begin{bmatrix} +v_d^- & +v_q^- & +v_d^+ & +v_q^+ \\ +v_q^- & -v_d^- & -v_q^+ & +v_d^+ \\ +v_q^- & -v_d^- & +v_q^+ & -v_d^+ \\ -v_d^- & -v_q^- & +v_d^+ & +v_q^+ \end{bmatrix} \times \begin{bmatrix} i_d^+ \\ i_q^+ \\ 0 \\ 0 \end{bmatrix} \qquad (2-25)$$

From $(2-25)$ and based on the analysis in Section 2.3.2, when the HVDC takes the balanced current control (e.g., i_{dr}^{+}, $i_{qr}^{+} \neq 0$ and i_{dr}^{-}, $i_{qr}^{-} = 0$), the values of the AC components P_C, P_S, Q_C, Q_S, will not be zero in asymmetrical faults due to the interaction of the positive sequence current and the negative sequence voltage, so there will be AC ripples in both active and reactive power from the converter system, which could introduce undesirable impact, e.g. DC side voltage oscillation [11], to the converter.

2.4.2.3 Constant Active Power Control Strategy

According to Section 2.4.2.2, it is known that there could be AC ripples on the active power with the balanced current controller in the case of asymmetrical faults. Such undesired ripples on the active power could potentially cause the oscillation of the DC side voltage of the converter. In the worst case, it may lead to the false tripping of the converter. To address this issue, a constant active power controller was first proposed in [11] to mitigate the ripples of the delivered active power and the DC side voltage during faults. However, this paper does not consider the FFCI capability. To inject certain amounts of reactive currents during faults, the references of the positive sequence currents calculated by $(2-22)$ and $(2-24)$ still need to be implemented and the references of the injected negative sequence current are calculated by $(2-26)$ and $(2-27)$, which can be derived by setting the P_C and P_S in $(2-8)$ and $(2-9)$ as zero.

$$i_{dr}^{-} = -\left(\frac{v_d^- v_d^+ - v_q^- v_q^+}{{v_d^+}^2 + {v_q^+}^2}\right) i_{dr}^{+} - \left(\frac{v_q^- v_d^+ + v_d^- v_q^+}{{v_d^+}^2 + {v_q^+}^2}\right) i_{qr}^{+} \qquad (2-26)$$

$$i_{qr}^{-} = -\left(\frac{v_d^- v_q^+ + v_q^- v_d^+}{{v_d^+}^2 + {v_q^+}^2}\right) i_{dr}^{+} - \left(\frac{v_q^- v_q^+ - v_d^- v_d^+}{{v_d^+}^2 + {v_q^+}^2}\right) i_{qr}^{+} \qquad (2-27)$$

In constant active power control, the reactive power delivered from the converter during faults could be depicted by $(2-28)$, which is derived by substituting the current references in $(2-26)$ and $(2-27)$ to $(2-11)$ and $(2-12)$. From equation of $(2-28)$, the 2nd harmonic ripples are still exhibited on the reactive power when the converter takes the constant active power controller in the case of asymmetrical faults.

$$\begin{bmatrix} Q_C \\ Q_S \end{bmatrix} = \frac{3}{2}\begin{bmatrix} 2v_q^- & -2v_d^- \\ -2v_d^- & -2v_q^- \end{bmatrix} \times \begin{bmatrix} i_d^+ \\ i_q^+ \end{bmatrix} \qquad (2-28)$$

2.4.2.4 Constant Reactive Power Control Strategy

To suppress the AC ripples on the reactive power during faults, the constant reactive power control is proposed by setting the values of Q_C and Q_S in $(2-11)$ and $(2-12)$ as zero [20]. Similarly, the values of the positive sequence current references are calculated by $(2-22)$ and $(2-24)$ to assist the FFCI capability of the converter. In this case, the corresponding current references are presented in $(2-29)$ and $(2-30)$, which can be derived by setting the Q_C and Q_S in $(2-11)$ and $(2-12)$ as zero. The features of the AC ripples on the active power with constant reactive power controller are illustrated by $(2-31)$, which is derived by substituting the current references in $(2-29)$ and $(2-30)$ to $(2-8)$ and $(2-9)$.

$$i_{dr}^{-} = \left(\frac{v_d^- v_d^+ - v_q^- v_q^+}{{v_d^+}^2 + {v_q^+}^2}\right) i_{dr}^{+} + \left(\frac{v_d^- v_q^+ + v_d^+ v_q^-}{{v_d^+}^2 + {v_q^+}^2}\right) i_{qr}^{+} \qquad (2-29)$$

$$i_{qr}^{-} = \left(\frac{v_d^- v_q^+ + v_d^+ v_q^-}{{v_d^+}^2 + {v_q^+}^2}\right) i_{dr}^{+} + \left(\frac{v_q^- v_q^+ - v_d^- v_d^+}{{v_d^+}^2 + {v_q^+}^2}\right) i_{qr}^{+} \qquad (2-30)$$

$$\begin{bmatrix} P_C \\ P_S \end{bmatrix} = \frac{3}{2}\begin{bmatrix} 2v_d^- & 2v_q^- \\ 2v_q^- & -2v_d^- \end{bmatrix} \times \begin{bmatrix} i_d^+ \\ i_q^+ \end{bmatrix} \qquad (2-31)$$

2.4.2.5 Flexible Control Strategy

In the previous sections, three typical control strategies of the converter have been discussed. It would be desirable to implement these three strategies using a single control structure, where the three control objectives can be flexibly realised by adjusting the settings of the controller. Therefore, a 'flexible controller' has been implemented by introducing a new variable K_{mode}. The current references of this type of controller are presented in $(2-32)$ to $(2-35)$, where the constant active power, balanced current and constant reactive power strategies can be achieved by setting the value of K_{mode} to -1, 0 and 1 respectively. Similar control strategies, which can achieve the aforementioned three control strategies, are reported in [12][21]. However, for the work in [12], the FFCI capability has not been considered during the design of the controller, therefore, it cannot deliver the reactive currents to the grid during faults. Another flexible controller proposed in [21] solves this gap by introducing the reactive current injection algorithm. However, compared to the controller proposed in this thesis, the fault current limiting strategy in [21] is too complicated.

In addition to the three control modes as discussed above, the value of K_{mode} can be ranged from -1 to 1, hence, different levels of the negative sequence current can be injected into the grid by varying the value of K_{mode} (via a slider in the model) for emulating different fault characteristics to test the protection performance.

$$i_{dr}^{+} = \sqrt{1.2^2 - \left(i_{qr}^{+}\right)^2} \qquad (2-32)$$

$$i_{qr}^{+} = -3.28v^{+} + 2.64, 0 \le i_{qr}^{+} \le 1 \qquad (2-33)$$

$$i_{dr}^{-} = K_{mode}\left(\frac{v_d^{+}v_d^{-} - v_q^{+}v_q^{-}}{{v_d^{+}}^2 + {v_q^{+}}^2}\right)i_{dr}^{+} + K_{mode}\left(\frac{v_d^{+}v_q^{-} + v_d^{-}v_q^{+}}{{v_d^{+}}^2 + {v_q^{+}}^2}\right)i_{qr}^{+} \qquad (2-34)$$

$$i_{qr}^{-} = K_{mode}\left(\frac{v_d^{+}v_q^{-} + v_d^{-}v_q^{+}}{{v_d^{+}}^2 + {v_q^{+}}^2}\right)i_{dr}^{+} + K_{mode}\left(\frac{v_q^{+}v_q^{-} - v_d^{+}v_d^{-}}{{v_d^{+}}^2 + {v_q^{+}}^2}\right)i_{qr}^{+} \qquad (2-35)$$

2.4.2.6 Fault Current Limiting Strategy

For a power electronic interfaced converter, one crucial issue that needs to be considered is to avoid overcurrents during the fault period. In the developed model, a

fault current limiter has been designed to ensure the maximum phase current of the converter is within the defined safety level in all types of faults, and meanwhile, it could realise the aforementioned different control strategies.

The flowchart of the developed fault current limiter is shown in Figure 2-7. There are two stages in this fault current limiter, i.e., stage I for fault detection and stage II for current suppression. In stage I, the positive sequence voltage calculated by $(2-23)$ is transformed to per unit value and compared to the defined voltage threshold. If the value of v^+ (pu) is above the threshold, the converter will take the current references in the normal state, $i_{d,nor}^+$ and $i_{q,nor}^+$, which are calculated by $(2-36)$. The references, $i_{d,nor}^+$ and $i_{q,nor}^+$, in $(2-36)$ can be derived by substituting $i_d^- = i_q^- = 0$ to $(2-7)$ and $(2-10)$.

$$\begin{bmatrix} i_{dr,nor}^+ \\ i_{qr,nor}^+ \end{bmatrix} = \frac{2}{3} \begin{bmatrix} \dfrac{v_d^+}{{v_d^+}^2 + {v_q^+}^2} & \dfrac{v_q^+}{{v_d^+}^2 + {v_q^+}^2} \\ \dfrac{v_q^+}{{v_d^+}^2 + {v_q^+}^2} & \dfrac{-v_d^+}{{v_d^+}^2 + {v_q^+}^2} \end{bmatrix} \begin{bmatrix} P_r \\ Q_r \end{bmatrix} \qquad (2-36)$$

If the value of v^+ (pu) is lower than the threshold (0.9 pu used in this scheme), the converter will consider there is a fault in the grid and it will move to stage II to suppress the fault current from the converter. The selection of 0.9 pu is based on the CC.6.1.4 regulation in the GB grid code [13], which defines the voltage variation of a 275-kV transmission system in normal conditions should be no more than $\pm 10\%$. In stage II, the initial current references from $(2-32)$ to $(2-35)$ are scaled down by dividing the value of the scaling factor, i.e., SF, as stated from $(2-38)$ to $(2-41)$. In those equations, the scaling factor, SF, is calculated by $(2-37)$, where the i_{dr}^+, i_{qr}^+, i_{dr}^-, i_{qr}^- are the initial positive and negative sequence current references from $(2-32)$ to $(2-35)$ and i_{max} is the maximum tolerable current of the designed converter. The numerator in $(2-37)$ calculates the maximum phase current of converters and its value changes with system and fault conditions, which leads to a changeable SF in $(2-37)$. For example, a larger SF is calculated in bolted faults due to a high magnitude of fault currents, while a smaller SF is adopted in high-resistance faults. After applying this current limiting strategy, the fault current of the converter can be maintained to be lower than the defined maximum current level effectively.

$$SF = \frac{\sqrt{{i_{dr}^{+}}^2 + {i_{qr}^{+}}^2} + \sqrt{{i_{dr}^{-}}^2 + {i_{qr}^{-}}^2}}{i_{max}} \qquad (2-37)$$

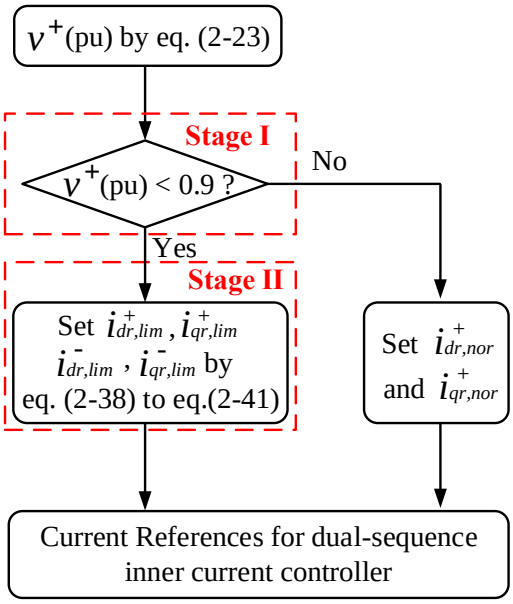

Figure 2-7. Flowchart of the designed fault current limiting strategy

$$i_{dr,lim}^{+} = \frac{i_{dr}^{+}}{SF} \qquad (2-38)$$

$$i_{qr,lim}^{+} = \frac{i_{qr}^{+}}{SF} \qquad (2-39)$$

$$i_{dr,lim}^{-} = \frac{i_{dr}^{-}}{SF} \qquad (2-40)$$

$$i_{qr,lim}^{-} = \frac{i_{qr}^{-}}{SF} \qquad (2-41)$$

2.4.3 Short-Circuit Response of Converter with Dual-Sequence Current Control Strategy

In this section, simulation results are presented to demonstrate the performance of the converter with the flexible controller in Section 2.4.2.5 and Section 2.4.2.6. The network in Figure 2-8 is used to test the short-circuit response of the developed converter model under AG, AB and ABCG faults. To make results more comparable

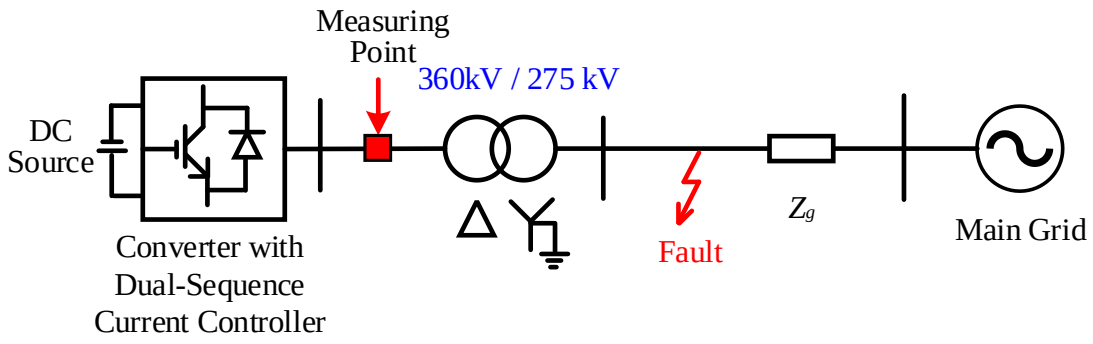

Figure 2-8. Network to evaluate the performance of the converter with the proposed dual-sequence current controller

to the short-circuit response in Section 2.3.2, the equivalent impedance, Z_g, uses the same impendence as the test of converter with conventional PQ controller.

The results in AG and AB faults are shown in Figure 2-9 and Figure 2-10, where all variables are presented as per unit values referring to the bases in equations of $(2-42)$ to $(2-44)$. The bases in $(2-43)$ and $(2-44)$ are represented using peak values, where s_{base}, v_{base}, i_{base} are the bases of the power, voltage and current respectively.

$$s_{base} = 839MVA \qquad (2-42)$$

$$v_{base} = \frac{360\sqrt{2}}{\sqrt{3}} = 293.94kV \qquad (2-43)$$

$$i_{base} = \frac{2}{3} \times \frac{s_{base}}{v_{base}} = 1.90kA \qquad (2-44)$$

The maximum current from the converter is restricted to 1.2 pu, which has been highlighted in figures. In Figure 2-9 and Figure 2-10, the value of K_{mode} moves from 1 to -1 through 0.5, 0 and -0.5. Based on the results, when K_{mode} equals 1, the controller will attempt to eliminate the ripples on the reactive power, while the ripples on the active power will have the largest magnitude. Then, with the decrease in the values of K_{mode}, the ripples' magnitude of the reactive power rises and the opposite trend is displayed on the active power. When K_{mode} equals -1, the ripples on the active power are suppressed but the ripples on the reactive power reach the maximum magnitude. From the results, it is clear that for all operating modes, the currents can

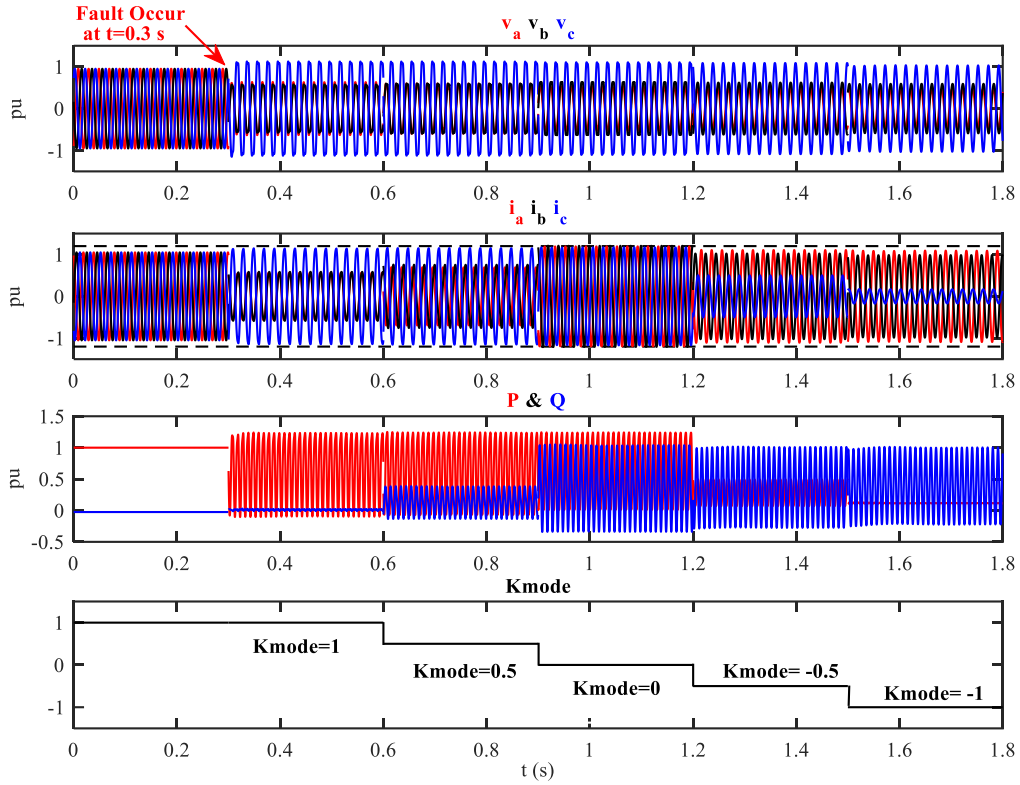

Figure 2-9. Short circuit response of dual-sequence controller-based converter under AG fault

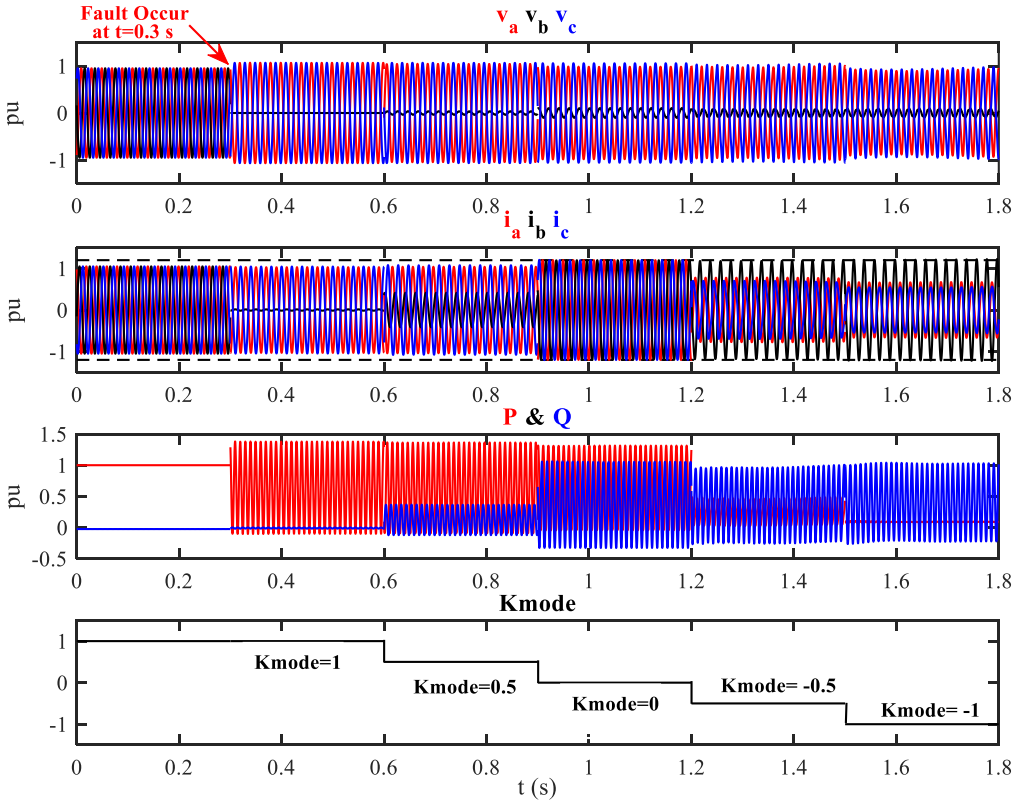

Figure 2-10. Short circuit response of dual-sequence controller-based converter under AB fault

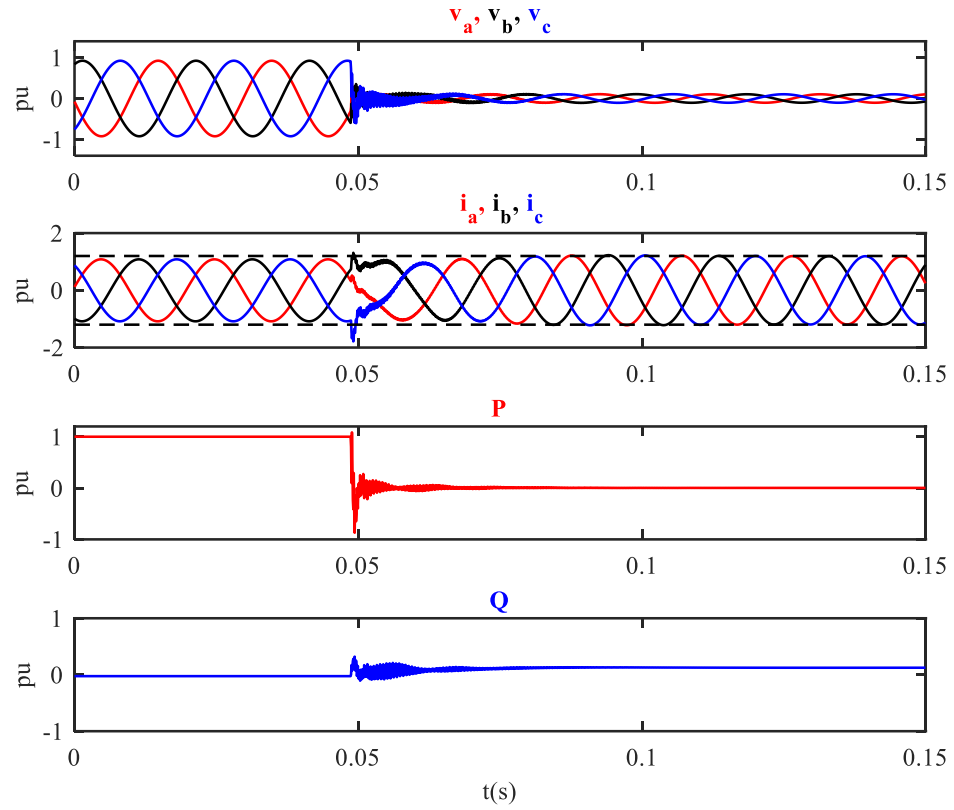

Figure 2-11. Short circuit response of dual-sequence controller-based converter under ABCG fault

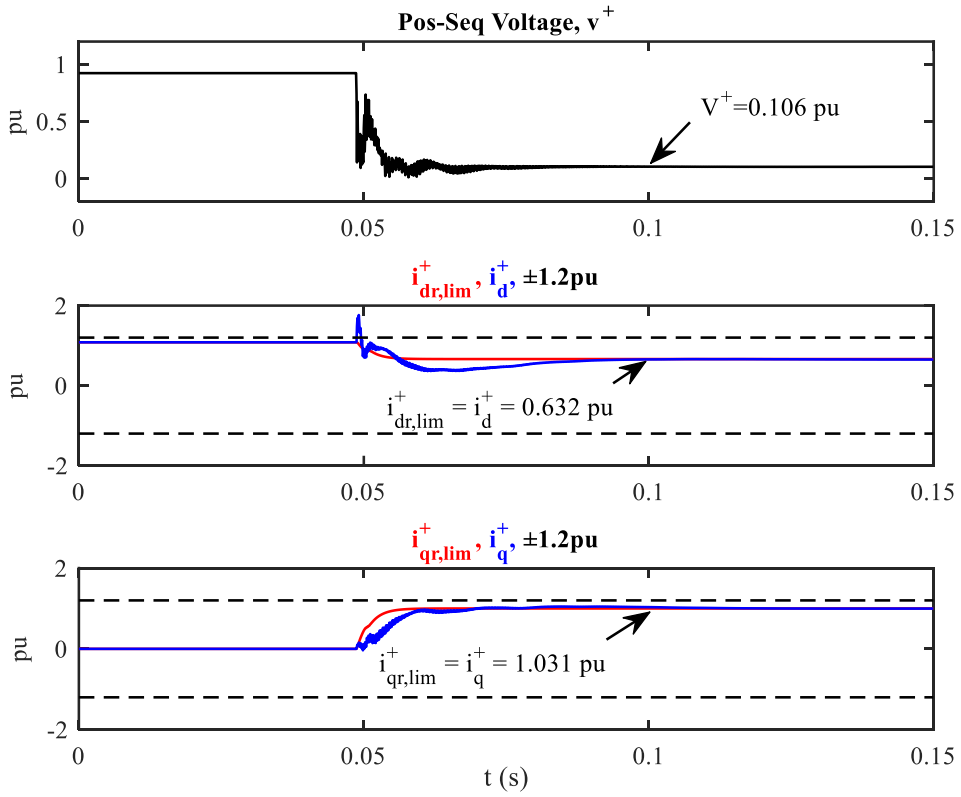

Figure 2-12. Results of positive sequence voltages and currents under ABCG fault

always be limited to 1.2 pu. Additionally, the injected negative sequence currents can be controlled by the values of K_{mode}. When K_{mode} equals 0, the output currents only have the positive sequence components. The simulation results demonstrate that the performance of the converter aligns with the design specification as discussed in Sections 2.4.2.5 and 2.4.2.6.

Since there is no negative sequence voltage in a balanced fault scenario, the negative sequence current references in $(2-34)$ and $(2-35)$ are always zero. In this condition, the converter can only operate in the balanced current mode and purely inject the positive sequence currents into the grid. The simulation results of an ABCG fault are shown in Figure 2-11, where all three phase currents are restricted to 1.2 pu. Owing to the absence of the negative sequence voltages and currents, the ripples on the active and reactive power do disappear as explained by $(2-8)$, $(2-9)$, $(2-11)$ and $(2-12)$. Additionally, in the balanced fault condition, the active and reactive power generated by the converter is approaching zero, which is resulted by a significant three-phase voltage drop in the grid side (i.e., close to zero). But this does not mean the converter does not supply the reactive currents to the grid in the fault period, which can be convinced by the results in Figure 2-12. In this figure, the reactive current of 1.031 pu (close to the accurate value of 1 pu) and active current of 0.632 pu (close to the accurate value of $\sqrt{1.2^2-1.031^2}=0.614$ pu) are contributed during faults, which aligns with the values calculated by $(2-32)$ and $(2-33)$. Therefore, the developed dual-sequence current controller has a satisfying performance in balanced faults.

2.5 Chapter Summary

This chapter proposes the development of converters with conventional PQ and dual-sequence current controllers, along with analysing their short-circuit responses. For the conventional PQ control strategy, where it only has a single inner current loop, the overcurrent issues appear in the steady state of asymmetrical faults due to the superimposed negative sequence voltages and currents during faults. Those negative sequence voltages and currents further result in the 100 Hz oscillation on the voltages and currents in the dq frame, which compromise the tracking capability of PI controllers and lead to the limiting issues of fault currents.

To improve control flexibility and address the overcurrent issue for the converter with a single inner current loop, a controller with a dual-seqeunce current control structure and a flexible control strategy is developed in this chapter, which could emulate different operating modes (i.e., modes of constant active and reactive power and balanced current), inject reactive currents and limit fault current magnitude during faults. From the results, the designed flexible controller can satisfy all expected control objectives and meet the requirements of the GB Grid Code. Therefore, it provides a valuable converter model for future research to investigate the converter's impacts on protection performance.

2.6 Chapter References

[1] J. Jia, "Assessment of Short Circuit Power and Protection Systems for Future Low Inertia Power Systems," Ph.D dissertation, Department of Electrical Engineering, Technical University of Denmark, Lyngby, Denmark, 2018.

[2] H. Akagi, E. H. Watanabe and M. Aredes, Instantaneous Power Theory and Applications to Power Conditioning, NJ, Piscataway: IEEE Press, 2007.

[3] P. Rioual, H. Pouliquen and J.Louis, "Regulation of a PWM rectifier in the unbalanced network state using a generalized model," in *IEEE Transactions on Power Electronics*, vol. 11, no. 3, pp. 495-502, May 1996.

[4] J. Rocabert, A. Luna, F. Blaabjerg and P. Rodríguez, "Control of Power Converters in AC Microgrids," in *IEEE Transactions on Power Electronics*, vol. 27, no. 11, pp. 4734-4749, Nov. 2012.

[5] V. Kaura and V. Blasko, "Operation of a phase locked loop system under distorted utility conditions," in *IEEE Transactions on Industry Applications*, vol. 33, no. 1, pp. 58-63, Jan.-Feb. 1997.

[6] E. Afshari et al., "Control Strategy for Three-Phase Grid-Connected PV Inverters Enabling Current Limitation Under Unbalanced Faults," in *IEEE Transactions on Industrial Electronics*, vol. 64, no. 11, pp. 8908-8918, Nov. 2017.

[7] S. Huang, J. Schmall, J. Conto, J. Adams, Y. Zhang and C. Carter, "Voltage control challenges on weak grids with high penetration of wind generation: ERCOT experience," *2012 IEEE Power and Energy Society General Meeting*, 2012, pp. 1-7.

[8] Y. Pan, W. Ren, S. Ray, R. Walling and M. Reichard, "Impact of inverter interfaced distributed generation on overcurrent protection in distribution systems," *2011 IEEE Power Engineering and Automation Conference*, Wuhan, China, 2011, pp. 371-376.

[9] Jundi Jia, Guangya Yang and A. H. Nielsen, "Investigation of grid-connected voltage source converter performance under unbalanced faults," *2016 IEEE PES Asia-Pacific Power and Energy Engineering Conference (APPEEC)*, 2016, pp. 609-613.

[10] R. Teodorescu, M. Liserre and P. Rodriguez, Grid Converters for Photovoltaic and Wind Power Systems, 2011.

[11] H. Song and K. Nam, "Dual current control scheme for PWM converter under unbalanced input voltage conditions," in *IEEE Transactions on Industrial Electronics*, vol. 46, no. 5, pp. 953-959, Oct. 1999.

[12] R. Kabiri, D. G. Holmes and B. P. McGrath, "Control of Active and Reactive Power Ripple to Mitigate Unbalanced Grid Voltages," in *IEEE Transactions on Industry Applications*, vol. 52, no. 2, pp. 1660-1668, March-April 2016.

[13] 'The Grid Code Issue 6 Revision 11', National Grid, February 2022.

[14] J. Jia, G.Yang and A. H. Nielsen. Fault Analysis Method Considering Dual-Sequence Current Control of VSCs under Unbalanced Faults. *Energies* 2018, *11*, 1660.

[15] N. Baeckeland and M. Kleemann, "Influence of reactive current settings of converters on distance protection," *2020 3rd International Colloquium on Intelligent Grid Metrology (SMAGRIMET)*, Cavtat, Croatia, 2020, pp. 79-84.

[16] A. Haddadi, M. Zhao, I. Kocar, U. Karaagac, K. W. Chan and E. Farantatos, "Impact of Inverter-Based Resources on Negative Sequence Quantities-Based Protection Elements," in *IEEE Transactions on Power Delivery*, vol. 36, no. 1, pp. 289-298, Feb. 2021.

[17] "IEEE Standard for Interconnection and Interoperability of Inverter-Based Resources (IBRs) Interconnecting with Associated Transmission Electric Power Systems," in *IEEE Std 2800-2022*, vol., no., pp.1-180, 22 April 2022.

[18] D. Guo, "Modelling of MMC-HVDC System for EMT Study," Ph.D dissertation, Department of Electronic and Electrical Engineering, University of Strathclyde,

Glasgow, UK, 2020.

[19] H. Aji, M. Ndreko, M. Popov and M. Meijden, "Investigation on different negative sequence current control options for MMC-HVDC during single line to ground AC faults," *2016 IEEE PES Innovative Smart Grid Technologies Conference Europe (ISGT-Europe)*, Ljubljana, 2016, pp. 1-6.

[20] P. Rodriguez, G. Medeiros, A. Luna, M. C. Cavalcanti and R. Teodorescu, "Safe current injection strategies for a STATCOM under asymmetrical grid faults," *2010 IEEE Energy Conversion Congress and Exposition*, Atlanta, GA, 2010, pp. 3929-3935.

[21] J. Jia, G. Yang and A. H. Nielsen, "A Review on Grid-Connected Converter Control for Short-Circuit Power Provision Under Grid Unbalanced Faults," in *IEEE Transactions on Power Delivery*, vol. 33, no. 2, pp. 649-661, April 2018.

Chapter 3

3 Performance Assessment of Transmission System Distance Protection, Main Issues and Existing Solutions

3.1 Introduction

In most countries, including the GB transmission network, distance and differential protection schemes are typically used as the main protection. As reported in [1], differential protection is more reliable and less impacted by the dynamic behaviour of converters owing to its inherently discriminative and sensitive advantages. Compared to differential protection, protection engineers are more concerned with distance protection because of its compromised performance in the network with CBRs. In this chapter, distance protection is systematically evaluated to provide evidence of the protection challenges of the transmission system with the connection of CBRs.

In a transmission system with only SGs, the angle difference of currents from both ends of the protected line is typically small. Therefore, the observed under/over-reach issues are insignificant [2]. However, this angle difference experiences a significant increase after the interconnection of the HVDC system (or other general CBRs) as the fault responses of converters are determined by their embedded controllers, which further poses the risks of maloperation to distance relays. Except for the reach issue, the distance relay also suffers from the faulted phase selection issue raised by the abnormal increase of phase-to-phase superimposed currents and incorrect angle relations of sequence components. Some other problems, such as the issues of

erroneous impedance measurement and oscillating impedance locus, can also occur in distance protection after the connection of CBRs [3].

In this chapter, a HIL-based methodology is developed for a systematic assessment of the impact of the HVDC system on distance protection. The detailed reasons behind the protection issues are analysed and solutions in the literature are reviewed. The structure of this chapter is presented as follows. The fundamentals of distance protection are proposed in Section 3.2. The results of HIL tests and analysis are presented in Section 3.3 and Section 3.4. The review of protection solutions is presented in Section 3.5. The summary is discussed in Section 3.6.

3.2 Fundamentals of Distance Protection

In this section, the fundamentals of distance protection are introduced. The focus is placed on elements most relevant to converter integration's impacts, including the impedance measuring functions, protection characteristics and faulted phase selection algorithm.

3.2.1 Impedance Measuring Elements

When a fault occurs in the transmission network, the distance relay located at the busbar will measure the impedance between the relay and fault position based on the local voltages and currents. The relay will detect a fault if the measured impedance is within the protective zone. Therefore, the accurate impedance measurement is essential for the correct operation of distance relays. Typically, distance relay has two impedance measuring groups, including the phase-to-earth group (including AG, BG and CG elements) and the phase-to-phase group (including AB, BC and CA elements), and the expressions of all measuring elements are presented in Table 3-1 [4].

In Table 3-1, the $Z_{AG}, Z_{BG}, Z_{CG}, Z_{AB}, Z_{BC}$ and Z_{CA} are the measured impedance of the corresponding impedance measuring elements; v_a , v_b and v_c are the input voltages of phase a, b and c; i_a , i_b and i_c are the input currents of phase a, b and c; i_0 is the measured zero-sequence current and K_0 is the residual compensation factor, which is calculated by $(3-1)$, where Z_0 and Z_1 are the zero sequence and positive sequence impedance of the protected line respectively.

$$K_0 = \frac{Z_0 - Z_1}{3Z_1} \qquad (3-1)$$

Table 3-1. Expressions of all impedance measuring elements of distance protection [4]

Measuring Groups	Impedance Elements	Expressions
Phase-to-earth fault	AG	$Z_{AG} = \frac{v_a}{i_a + 3K_0 i_0}$
	BG	$Z_{BG} = \frac{v_b}{i_b + 3K_0 i_0}$
	CG	$Z_{CG} = \frac{v_c}{i_c + 3K_0 i_0}$
Phase-to-phase fault	AB/ABG	$Z_{AB} = \frac{v_a - v_b}{i_a - i_b}$
	BC/BCG	$Z_{BC} = \frac{v_b - v_c}{i_b - i_c}$
	CA/CAG	$Z_{CA} = \frac{v_c - v_a}{i_c - i_a}$

3.2.2 Protection Characteristics

The MHO and QUAD characteristics are the most widely implemented in distance protection. Therefore, the fundamentals of those two characteristics are discussed in Section 3.2.2.1 and Section 3.2.2.2.

3.2.2.1 MHO-Based Protection Characteristics

As proposed in Section 3.2.1, the tripping decision of a distance relay is determined by a set of tripping conditions. One of the critical tripping conditions for the MHO characteristic is realised by introducing comparators. For MHO-based distance protection, there are two typical comparators, including the magnitude comparator and the phase comparator. Given that the magnitude comparator is superseded by the phase comparator in modern relays, only the phase comparator is introduced in this section.

The protective zone of the MHO characteristic is shown in Figure 3-1, where V is the faulted phase loop voltage; I is the fault current and Z_R is reach setting. The relay will consider a fault to be within the protected zone if the value of the angle θ_{MHO} is larger than 90°. The expressions of the tripping condition are illustrated by $(3-2)$ to $(3-4)$. This method is proposed as 'self-polarisation' because it uses the directly measured voltage signal to decide whether θ is great than 90°.

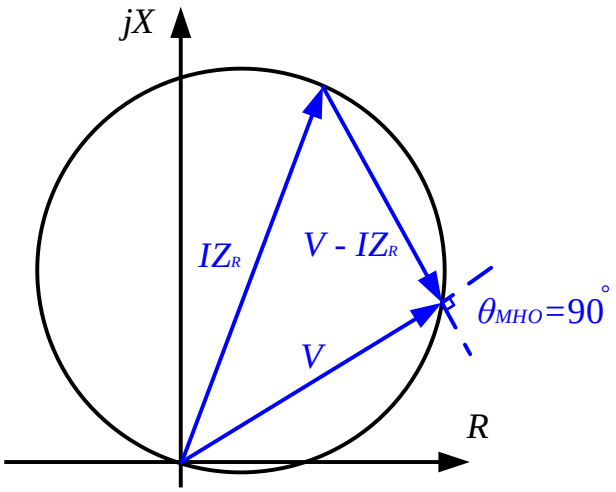

Figure 3-1. Protective zone of self-polarised MHO relay

$$S_1 = V \qquad (3-2)$$

$$S_2 = V - IZ_R \qquad (3-3)$$

$$ang\left(\frac{S_1}{S_2}\right) > 90^{\circ} \qquad (3-4)$$

As reported in [5], the MHO characteristic with self-polarisation may suffer from reliability issues in the case of the close-up faults, where the measured voltage of the faulted phases can decrease to almost zero. To address this problem, two voltage-polarised methods called 'cross-polarisation' and 'memory polarisation' are introduced. For the cross-polarisation, the voltage on the healthy phases will be employed to assist the polarisation of the vector S_1. In this case, the new developed vectors of the comparator are presented by $(3-5)$ and $(3-6)$, where the ρ is the polarising factor and V_{cross} is the cross-polarised voltage. The representation of V_{cross} is summarised in Table 3-2 [6], where α is the rotational factor, $\alpha = e^{j120^{\circ}}$ and $\alpha^2 = e^{j240^{\circ}}$. However, in some cases, the polarised voltage will not be available, e.g., in balanced faults. To address this issue, the memory-polarised MHO is developed.

$$S_1 = V + \rho V_{cross} \qquad (3-5)$$

$$S_2 = V - IZ_R \qquad (3-6)$$

Table 3-2. Representation of the cross-polarised voltage

Measuring Groups	Impedance Loop	Cross-Polarised Signal
Phase-to-earth fault	AG	$0.5(\alpha v_b + \alpha^2 v_c)$
	BG	$0.5(\alpha v_c + \alpha^2 v_a)$
	CG	$0.5(\alpha v_a + \alpha^2 v_b)$
Phase-to-phase fault	AB	$\sqrt{3}v_c \angle -90^\circ$
	BC	$\sqrt{3}v_a \angle -90^\circ$
	CA	$\sqrt{3}v_b \angle -90^\circ$

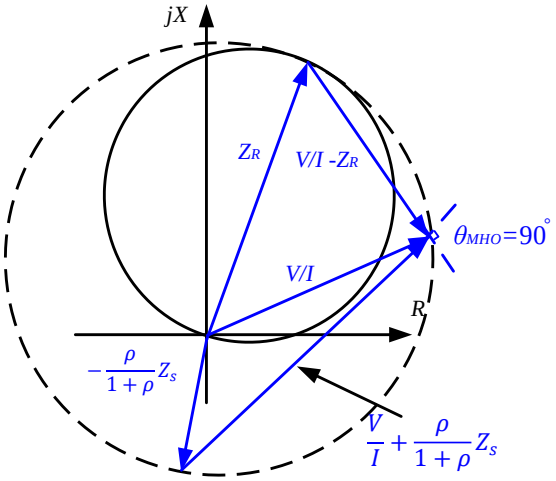

Figure 3-2. Protective zone of memory-polarised MHO relay [6]

The vectors used in the memory-polarised MHO are depicted as $(3-7)$ and $(3-8)$, where ρ is the polarising factor and V_{mem} is the memory-polarised voltage (typically several cycles before the fault).

$$S_1 = V + \rho V_{mem} \qquad (3-7)$$

$$S_2 = V - IZ_R \qquad (3-8)$$

The protective zone for forward faults after memory polarisation is shown in Figure 3-2, where Z_s stands for the equivalent source impedance behind the relay point. From Figure 3-2, it is clear the memory-polarised voltage will cause the expansion of the protective zone and this expansion will increase as the rise of polarising factor, ρ.

In the memory-polarised MHO, the distance relay will consider the fault is within the protection zone if the absolute value of the angle θ_{MHO} is larger than 90°. Apart from the use of the pre-fault phase voltage, the positive sequence voltage during faults is used as well to polarise the voltage in some physical relays. In that case, the vector S_1 will equal to the measured positive sequence voltage during faults.

3.2.2.2 Quadrilateral (QUAD) Based Protection Characteristics

Compared to the MHO characteristic, the QUAD relay can provide an increased resistance coverage, thus better performing in high resistive faults [7]. An example of the protective zone of the QUAD relay is presented in Figure 3-3 [6], where the measured impedance will be compared with the characteristic's boundary to determine whether the fault is within the protection zone.

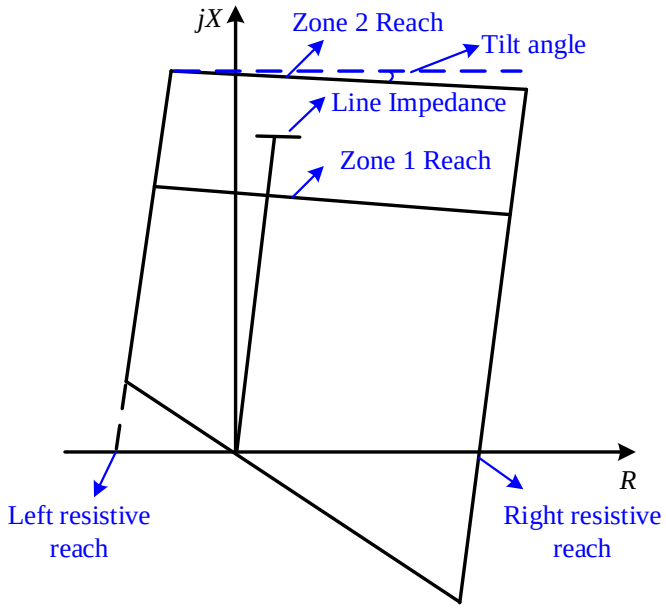

Figure 3-3. Protective zone of QUAD relay [6]

3.2.3 Faulted Phase Selection Algorithm

3.2.3.1 Overview of the Faulted Phase Selection

The faulted phase selection is implemented to identify the fault types and facilitate the single-phase tripping capability [8]. The reliable faulted phase selection can enhance the security of the distance protection since the unnecessary trips can be blocked if the results from the phase selection elements do not agree with the results from the other elements, e.g., the impedance measuring element of distance relays [9].

The phase selection algorithm using fundamental phasors can be categorised into four groups, including the overcurrent-based phase selection, voltage-based phase selection, superimposed quantities-based phase selection (also called 'delta quantities-based phase selection') and sequence components-based phase selection [10].

The overcurrent-based phase selection algorithm compares the magnitudes of three-phase currents, where the phase with the highest current increase is identified as the faulted phase. This selection algorithm is simple and easy to be implemented, while it is not sensitive to detect high impedance faults and is not reliable in the network dominated by the CBRs, where the magnitudes of fault currents are limited and the fault characteristic is highly dependent on the implemented converter control strategy. In the voltage-based phase selector, the faulted phase is identified as the phase with the highest voltage drop. Similar to the overcurrent-based approach, the voltage-based phase selector is not capable of detecting high-impedance faults and its performance is affected by the dynamic behaviour of CBRs. Compared to the phase selectors using the superimposed quantities and sequence components, the phase selection algorithms using the magnitudes of voltage and current are rarely implemented in modern numeric relays. Therefore, the following sections will mainly focus on the fundamentals of the phase selectors using the superimposed quantities and sequence components.

3.2.3.2 Superimposed Quantities-Based Faulted Phase Selection

In superimposed quantities-based faulted phase selector, the fault type is identified by the magnitude relations between the phase-to-phase superimposed quantities in $(3-9)$ to $(3-11)$ [10].

$$\Delta i_x = i_x - i_{x,pre-fault} \tag{3-9}$$

$$\Delta i_y = i_y - i_{y,pre-fault} \tag{3-10}$$

$$\Delta i_{xy} = \Delta i_x - \Delta i_y \tag{3-11}$$

Where x and y represent any pair of phases a, b and c; i_x and i_y refer to the measured three-phase currents in real time; $i_{x,pre-fault}$ and $i_{y,pre-fault}$ are the pre-fault three-phase currents, which are measured several cycles before the faults; Δi_x, Δi_y and Δi_{xy} represent the superimposed phase and phase-to-phase quantities.

Table 3-3. Principles of the superimposed quantities-based faulted phase selection [6]

Fault Type	**Relations of Δi_{ab}, Δi_{bc} and Δi_{ca}**
AG	$\Delta i_{ab} > \Delta I_{thr}$ & $\Delta i_{ca} > \Delta I_{thr}$ & $\Delta i_{bc} < \Delta I_{thr}$
BG	$\Delta i_{ab} > \Delta I_{thr}$ & $\Delta i_{bc} > \Delta I_{thr}$ & $\Delta i_{ca} < \Delta I_{thr}$
CG	$\Delta i_{bc} > \Delta I_{thr}$ & $\Delta i_{ca} > \Delta I_{thr}$ & $\Delta i_{ab} < \Delta I_{thr}$
AB/ABG	$\Delta i_{ab} > \Delta I_{thr}$ & $\Delta i_{bc} < \Delta I_{thr}$ & $\Delta i_{ca} < \Delta I_{thr}$
BC/BCG	$\Delta i_{bc} > \Delta I_{thr}$ & $\Delta i_{ab} < \Delta I_{thr}$ & $\Delta i_{ca} < \Delta I_{thr}$
CA/CAG	$\Delta i_{ca} > \Delta I_{thr}$ & $\Delta i_{ab} < \Delta I_{thr}$ & $\Delta i_{bc} < \Delta I_{thr}$
ABC/ABCG	$\Delta i_{ab} > \Delta I_{thr}$ & $\Delta i_{bc} > \Delta I_{thr}$ & $\Delta i_{ca} > \Delta I_{thr}$

The principle of the superimposed quantities-based faulted phase selector is presented in Table 3-3 [6][11], where the ΔI_{thr} is the current threshold used in the superimposed quantities-based faulted phase selector. From Table 3-3, in single-phase-to-ground faults, two superimposed phase-to-phase currents are greater than the defined threshold and the faulted phase is the common phase of those two superimposed phase-to-phase currents. In phase-to-phase or phase-to-phase-to-ground faults, only one superimposed phase-to-phase current is higher than the threshold, which indicates the faulted phases. In three-phase faults, all three superimposed currents are greater than the threshold.

3.2.3.3 Sequence Components-Based Faulted Phase Selection

Except for the superimposed quantities-based phase selector, the sequence components-based phase selector is also widely implemented in distance relays. The fundamentals of the sequence components-based phase selector are explained in Figure 3-4 [12] - [14], where the angle relations of the negative to positive sequence components and the negative to zero sequence components are used to identify the fault types.

As presented in Figure 3-4, multiple symmetrical zones are included in phase selection planes, i.e., six symmetrical zones in the negative-to-positive sequence plane and three symmetrical zones in the negative-to-zero sequence plane. The width of an

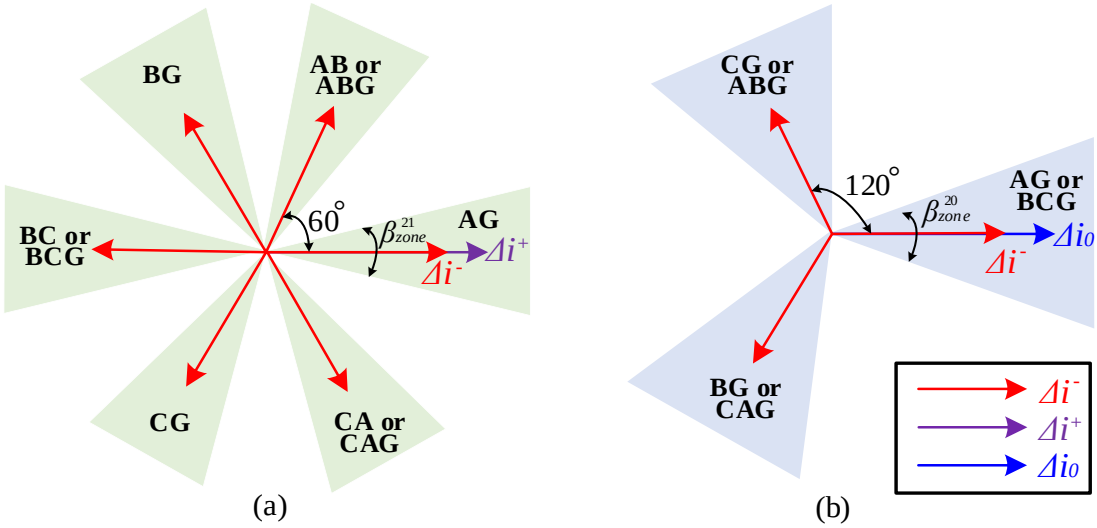

Figure 3-4. Sequence components-based phase selection plane, (a) relations of the negative sequence current and the positive sequence current, (b) relations of the negative sequence current and the zero sequence current

individual zone in the same plane keeps the same, which is defined as β_{zone}^{21} and β_{zone}^{20} as presented in Figure 3-4 (a) and Figure 3-4 (b). The values of β_{zone}^{21} and β_{zone}^{20} are normally set to half of the angle difference between two consecutive fault type angles, i.e., $\beta_{zone}^{21} = 0.5 \times 60^{\circ} = 30^{\circ}$ and $\beta_{zone}^{20} = 0.5 \times 120^{\circ} = 60^{\circ}$ [12].

The variables, Δi^{-}, Δi^{+} and Δi_0, in Figure 3-4 refer to the superimposed negative, positive and zero sequence currents, which are calculated by $(3-12)$ to $(3-17)$, where the symbol Δ represents the superimposed quantities and α is the rotational factor, i.e., $\alpha = e^{j120^{\circ}}$ and $\alpha^2 = e^{j240^{\circ}}$. The operating vectors, δ^{21} and δ^{20}, in two sequence planes are defined by $(3-18)$ and $(3-19)$. After combining angle values calculated from $(3-18)$ and $(3-19)$ to the planes in Figure 3-4 (a) and Figure 3-4 (b), the relay can identify the faulted phases. The angle relations presented in Figure 3-4 are also valid for the system voltage, which can be used to cope with the weak infeed conditions in [13] and enhance the protection dependability in [14]. Either plane in Figure 3-4 can be implemented individually in distance relays to realise the function of faulted phase selection, but they can also be implemented together to increase protection security.

$$\Delta i_a = i_a - i_{a,pre-fault} \qquad (3-12)$$

$$\Delta i_b = i_b - i_{b,pre-fault} \qquad (3-13)$$

$$\Delta i_c = i_c - i_{c,pre-fault} \quad (3-14)$$

$$\Delta i^- = \frac{1}{3}(\Delta i_a + \alpha^2 \Delta i_b + \alpha \Delta i_c) \quad (3-15)$$

$$\Delta i^+ = \frac{1}{3}(\Delta i_a + \alpha \Delta i_b + \alpha^2 \Delta i_c) \quad (3-16)$$

$$\Delta i_0 = \frac{1}{3}(\Delta i_a + \Delta i_b + \Delta i_c) \quad (3-17)$$

$$\delta^{21} = \angle \Delta i^- - \angle \Delta i^+ \quad (3-18)$$

$$\delta^{20} = \angle \Delta i^- - \angle \Delta i_0 \quad (3-19)$$

3.3 Systematic HIL Tests of Distance Relays

In this section, high-level systematic tests for two commercial distance relays are implemented to evaluate the impact of the HVDC system (or CBRs in general) on distance protection, where a total number of 480 cases, under different fault conditions, HVDC control modes, system strengths and varied levels of synchronous compensation, is investigated.

3.3.1 Overview of the Studied Network and HIL Setup

The network model in [15], which is specifically designed for evaluating distance protection performance with high penetration of CBRs, is used in this study, as presented in Figure 3-5. In the developed network model, the SG1 and SG2 are voltage sources, representing the equivalent "lumped" synchronous generation sources at the busbars, where the protected line is connected; Load 1 represents the equivalent loads connecting at the busbar B; the MMC-HVDC represents the Modular Multi-level Converter (MMC)-based HVDC system, where a flexible controller discussed in Section 2.4.2, is developed to emulate different control strategies of the HVDC system, e.g., constant reactive power control to suppress the ripples on the reactive power, balanced current control to mitigate the negative sequence output current and constant active power control to suppress the ripples on the active power; the SC represents the synchronous condenser installed at the HVDC site with an AVR controller based on the IEEE type 1 excitation system [16]; the NSG represents the converter-interfaced non-synchronous generation at the remote end of the protected line, which includes

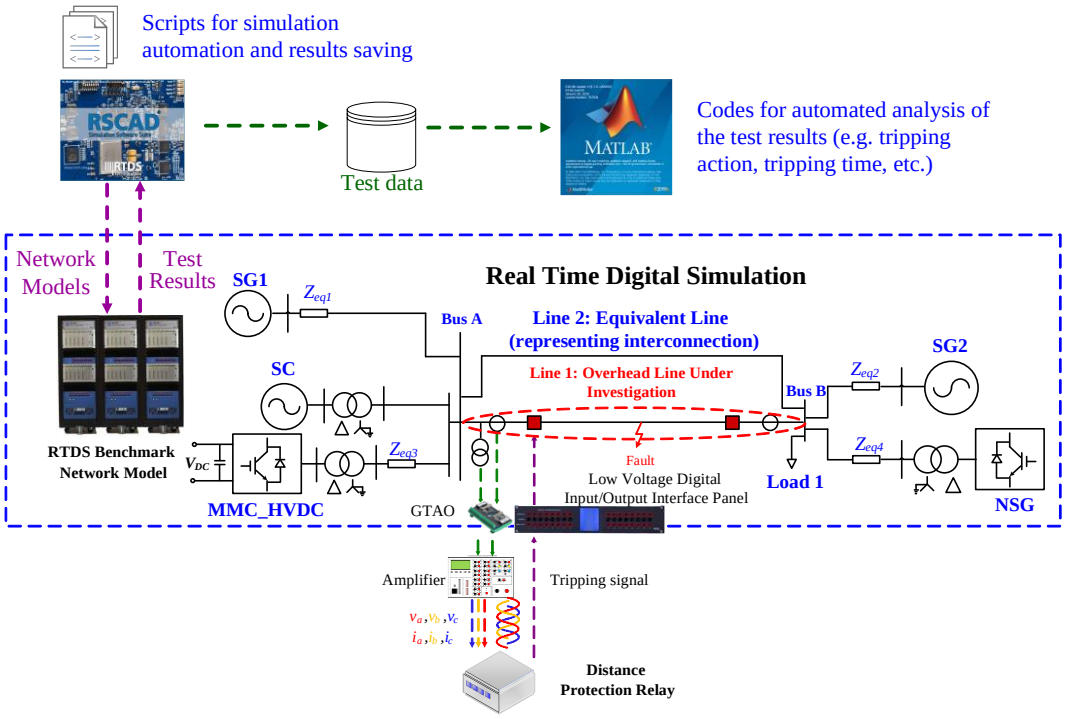

Figure 3-5. Studied network and HIL setup used for the systematic tests

wind, PV and other converter-based generators in both distribution and transmission levels, and it is modelled using a two-level detailed power electronic converter with the control strategy in Section 2.3.1; the Z_{eq1} and Z_{eq2} represent the equivalent impedances of SG1 and SG2, which directly determine the fault levels at Bus A and B, which determines the fault contributions from SG1 and SG2; Z_{eq3} is the impedance between the HVDC converter and the connected Bus A, while Z_{eq4} represents the equivalent impedance of NSG unit with the grid, which can be manually adjustable by the users to ensure the operating stability of the NSG unit; Line 1 and Line 2 are to represent the protected line under investigation and the connected parallel line between Bus A and B. The parameters of the studied system are displayed in Table 3-4.

Compared to the pure simulation-based studies, a significant advantage of RTDS is that the signals and measurements in RTDS are in real-time, which can interface with the external protective relays via I/O cards to emulate realistic system and fault conditions accurately [17]. The relays in tests include two commercial distance relays widely used in the existing power system. Therefore, the conducted RTDS-based HIL tests can ensure the tested results are close to the performance of relays installed in the real power system. In this test, the secondary side three-phase voltage and current at

Bus A will be measured by the voltage and current transformer (VT and CT) models in RSCAD, a software specially designed for RTDS, and the voltage and current will be further scaled down so that they fall into ± 10 V, which is the output voltage range of the GTAO card. The output signals from the GTAO card are amplified to the same voltage and current levels as the outputs of the VT and CT using an analogue amplifier. The amplified voltages and currents are then injected into the physical relay, which will make a tripping decision based on the input voltages and currents. If the relay trips, the tripping signal will be transmitted back to the RTDS through the digital input/output interface, i.e., the GTFPI card, where the tripping signal will be monitored and recorded, along with other critical data, e.g., voltage and current waveforms. To facilitate the tests of a large number of cases, the simulation and data collection process are automated by a set of scripts. Furthermore, the MTALAB codes have also been developed to automatically analyse the recorded testing results, which are capable of importing the data, interpreting the tripping action, calculating the tripping time, and indicating whether the performance has met specified tripping requirements.

Table 3-4. Parameters of the Studied Network

Elements	**Description**	**Value**
System Voltage	Power system voltage	275 kV
MMC-HVDC	Rated power	839 MVA
	Transformer voltage	275 kV / 360 kV
	Rated DC-side voltage	640 kV
Protected Line	Total line length	12.1 km
	Positive and zero sequence resistance per km	r_1=0.0378 Ω/km, r_0=0.159 Ω/km.
	Positive and zero sequence inductance per km	l_1=1.324 mH/km, l_0=3.202 mH/km.
	Positive and zero sequence capacitance per km	C_1=8.964 nF/km, C_0=6.48 nF/km.

Table 3-5. Settings with MHO characteristics of both relays

Parameter Name	**Relay Settings**
Protection characteristic	Memory-polarised MHO
Polarising factor	Relay 1: $\rho = 1$ (Pre-fault voltage used); Relay 2: Positive-sequence voltage used
Reach setting	Zone 1: 80%; Zone 2: 120%
Residual compensation factor	$K_0 = 0.48\angle -6.4^\circ$
Delay setting	Zone1: 0 ms; Zone 2: 400 ms

Table 3-6. Settings with QUAD characteristics of both relays

Parameter Name	**Relay Settings**
Protection characteristic	QUAD based
Reach setting	Zone 1: 80%; Zone 2: 120%
Residual compensation factor	$K_0 = 0.48\angle -6.4^\circ$
Delay setting	Zone1: 0 ms; Zone 2: 400 ms
Right resistive reach	6.72 Ω
Left resistive reach	1.68 Ω
Directional angle	60°
Tilt angle	-3°

3.3.2 Settings of Physical Relays

Settings of two commercial relays, i.e., Relay 1 and Relay 2, are presented in Table 3-5 and Table 3-6. For the MHO characteristic in Table 3-5, the memory-polarised technique proposed in Section 3.2.2.1 is implemented, where Relay 1 uses the phase voltage two cycles before faults, while Relay 2 uses the positive-sequence voltage during faults to realise the voltage polarisation. The reach of Zone 1 and Zone 2 covers 80 % and 120 % of the total length of the protected line and the time delays of Zone 1

and Zone 2 are set to 0 ms and 400 ms. The residual compensation factor, K_0, is calculated by $(3-1)$. The settings of zone reach and time delays used in the QUAD characteristic are the same as the values for the MHO characteristic and the other parameters, such as right/left resistive reach, directional angle and tilt angle, are set based on a typical setting practice in the UK.

Table 3-7. Cases of the systematic tests

Parameter	Definition	Test Settings
FL_{BusA} & FL_{BusB}	Fault levels at Bus A and Bus B	0 MVA & 3000 MVA/ 1836 MVA & 1372 MVA
SC	SC capacity	0 MVA/ 300 MVA
HVDC	HVDC control modes	CP/ BI/ CQ
Fault	Fault resistance	2 Ω
	Fault types	AG/ AB
	Fault positions	20 %/ 70 %/ 75 %/ 80 %/ 85 %
Distance Relay	Relay characteristics	MHO/ QUAD
NSG	Power generated by NSG	839 MVA ($pf = 0.93$)
Load 1	Power consumed by Load 1	300 MVA ($pf = 0.9$)

3.3.3 Cases of the Systematic HIL Tests

In systematic tests, Relay 1 and Relay 2 are investigated by the cases in Table 3-7, where the fault currents from the HVDC and NSG are limited to 1.2 pu. In this table, the impact of various factors, e.g., fault level of the connected AC system, synchronous compensation, HVDC operating mode, different fault scenarios and protection characteristics, are all considered. Unlike the current magnitude-based protection such as the overcurrent protection, which has a better performance in the netwrok with a high local system fault level, the distance protection performance is dependent on the relative relation of local and remote-end fault levels as analysed in Section 3.4.2.2. In tests, two groups of fault levels (i.e., 0 MVA at Bus A and 3000 MVA at Bus B, and

1836 MVA at Bus A and 1372 MVA at Bus B) are selected in systematic tests to represent an extreme condition, where no fault infeed is contributed from SG1, and a real system operating condition, where the realistic fault level in the Spittal and Thurso South substations in Scotland are adopted. Balanced faults are not tested in this part as the HVDC system will always inject balanced currents regardless of the control modes used, so cases with balanced faults will be considered separately in Section 3.4. The total number of the studied cases is 480, but more cases and scenarios can be tested using the developed HIL platform by revising the studied cases in RTDS scripts.

Compared to the research in [2][18], where the performance of distance protection is evaluated using software-based simulation and the number of investigated cases is limited, the tests in this section are conducted via a realistic HIL approach and comprehensive cases are included in tests to evaluate commercial relays' performance in a wide range of system and fault conditions. Additionally, the following actions are conducted before the formal injection to ensure the credibility and reliability of the systematic HIL test result in Section 3.3.4, which include:

- The RTDS network model is configured using realistic network data (i.e., fault level data at the Spittal and Thurso South substations and realistic data of the line between the Spittal and Thurso South substations).
- The outputs from the amplifier are checked before injection to ensure the secondary-side voltages and currents from the VT and VT models in RTDS are the same as the injected voltages and currents of physical relays.
- The tested relays are widely used in the UK commercial market.
- The distance relays are set based on a typical setting practice in the UK and the settings are validated by relay manufacturers before injection.

The results and analysis in this chapter can provide valuable insights and references to scholars to understand the challenges of the distance relays in the transmission network with CBRs and facilitate the development of novel solutions to improve the relay's performance.

3.3.4 Results of the Systematic HIL Tests

3.3.4.1 Results Description

In this systematic test, the relay's tripping actions are categorized into four groups,

i.e., ‘Healthy Trip’, ‘Delayed Trip’, ‘Trip in False Zone’, and ‘Not Trip’, based on the operating time calculated by $(3-20)$.

$$t_{op} = t_{trip} - t_{incep} - t_{zone} \quad (3-20)$$

where t_{op} is the calculated relay operating time; t_{trip} is the tripping time of the relay; t_{incep} is the fault inception time and t_{zone} is the configured intentional zone delay, i.e., 0 ms for Zone 1 and 400 ms for Zone 2.

The detailed criteria for classifying the relay's performance into these four tripping groups are presented below.

1) Healthy Trip: relay trips in the correct zone with an operating delay less than 90 ms.
2) Delayed Trip: relay trips in the correct zone but with an operating delay longer than 90 ms.
3) Trip in False Zone: relay trips in a false zone (e.g., trip in Zone 2 for the Zone 1 fault).
4) Not Trip: relay does not trip for faults in the protective zone.

The selection of the tripping time of 90 ms is based on the grid code, which requires short-circuit faults in the 275 kV transmission networks should be isolated no more than 140 ms [19], which includes the relay tripping time, the circuit breaker (CB) operating time and other potential delays. Assuming a CB operating time is approximately 50 ms [20], the relay operating time is defined as 90 ms. However, in practice, some other delays will be introduced in the fault isolation process and the operating time of CB may be larger than 50 ms, so the required time of 90 ms is intentionally set at the high end, thus when the operating time is longer than this value, it will indeed indicate compromised performance that is not acceptable for transmission system protection.

3.3.4.2 Overview of Distance Protection Performance

A high-level view of the two relays’ performance in tests is provided in Figure 3-6 and Figure 3-7. These figures include test results from all cases with different fault conditions, HVDC control modes, fault levels, etc. Therefore, it provides a high-level comparison of the two relays’ performance and an initial indicator for the scale of the

potential compromised protection performance. It can be seen from the figures that both relays manage to provide desirable performance for around 50% of the tested cases. Additionally, the two relays have different performances for the tested cases, where Relay 2 has a slightly higher number of desirable operation cases. Notably, both relays suffer from the 'Not Trip' and 'Delayed Trip', which are particularly alarming as they indicate both relays could fail to meet protection requirements in some scenarios. In conventional networks dominated by SGs, distance protection is expected to be highly dependable and secure. From the above test results, in future scenarios involving the integration of HVDC systems and more renewable-based generation, the protection system performance is indeed concerning as it could be compromised significantly.

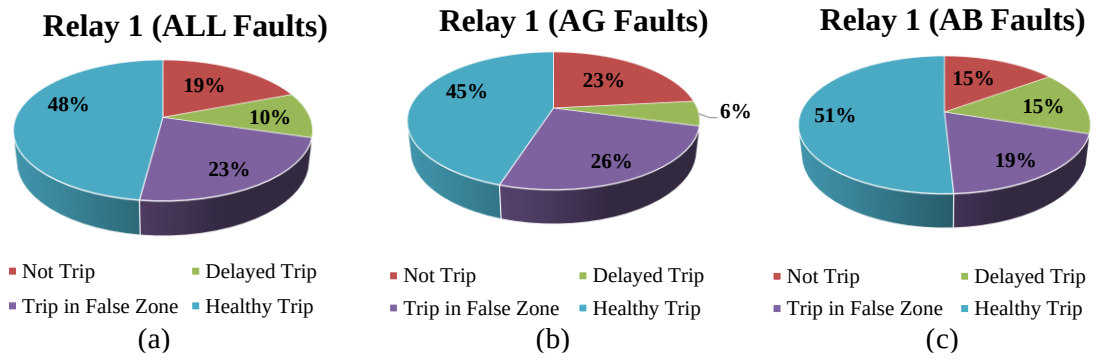

Figure 3-6. Overall performance of Relay 1 with, (a) AG and AB faults, (b) AG faults, (c) AB faults

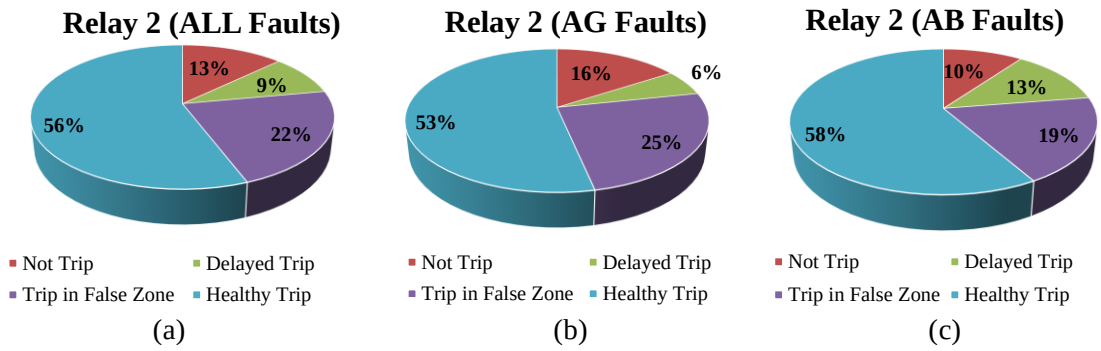

Figure 3-7. Overall performance of Relay 2 with, (a) AG and AB faults, (b) AG faults, (c) AB faults

3.3.4.3 Impact of Local and Remote-end Fault Level

The results indicating the impact of the local and remote-end fault levels are shown in Figure 3-8 and Figure 3-9. It can be seen that the performance of both relays has degraded significantly when the FL_{SG1} decreases to 0 MVA and the FL_{SG2} rises to

3000 MVA, compared to the cases with FL_{SG1}=1832 MVA and FL_{SG2}=1372 MVA (the present system fault level data from actual substations in Scotland). This problematic scenario is caused by the increased angle difference and current magnitude ratio between the remote and local-end infeed, which will be analysed later in Section 3.4.2.2.

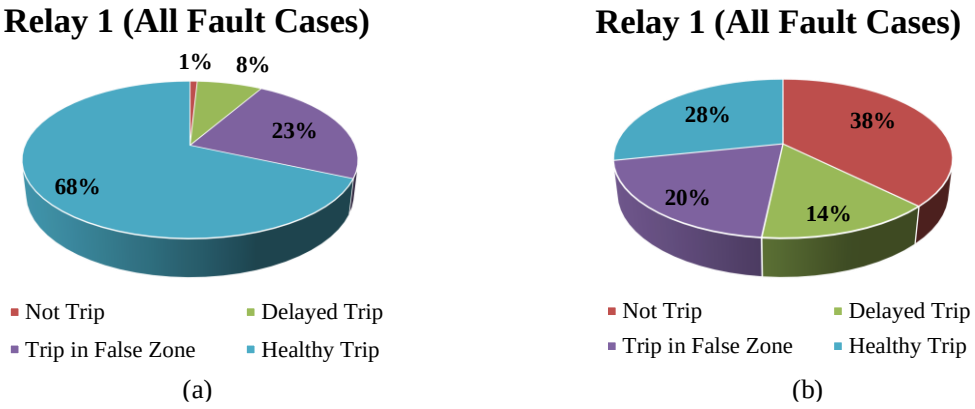

Figure 3-8. Performance of Relay 1 with, (a) FL_{SG1}= 1832 MVA; FL_{SG2}= 1372 MVA; (b) FL_{SG1}= 0 MVA; FL_{SG2}=3000 MVA

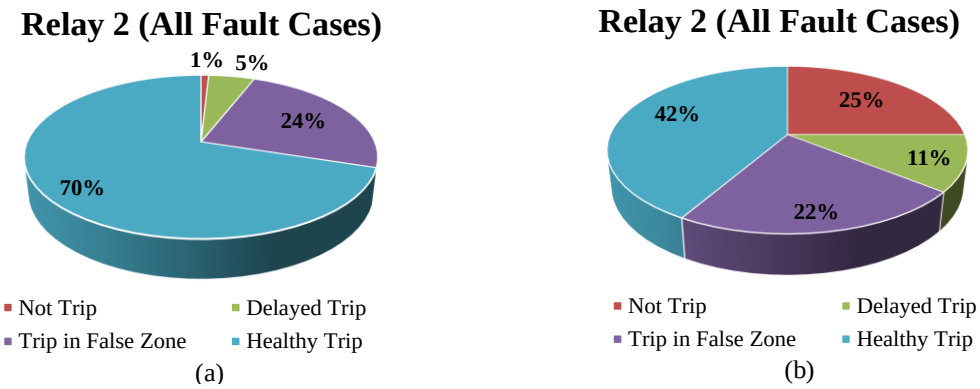

Figure 3-9. Performance of Relay 2 with, (a) FL_{SG1}= 1832 MVA; FL_{SG2}= 1372 MVA; (b) FL_{SG1}= 0 MVA; FL_{SG2}=3000 MVA

3.3.4.4 Impact of Converter Control Strategy

In this section, three typically used control strategies during faults, including the balanced current control, constant active power control and constant reactive power control, are applied to the developed HVDC model. Figure 3-10 and Figure 3-11 present a summary of the results to evaluate the HVDC control strategies' impacts on distance protection. From the results, while both distance relays have compromised performance in some cases with all HVDC control modes, there is a clear difference

in the overall performance when different modes are used. It appears that the most problematic control mode is the constant reactive power control, where the severe faulted phase selection and impedance measurement issues are observed from investigated relays, which are explained later in Section 3.4.2.1 and Section 3.4.2.3. Additionally, as discussed in Section 3.4.2.1, the connection of the HVDC system with a balanced current controller can result in the phase selection failure of Relay 1 with the superimposed phase-to-phase current-based selection algorithm, while Relay 2 can avoid that failed tripping issue but an undesired delay will be introduced to the phase selection. Therefore, the failed tripping risk of Relay 1 is higher than Relay 2, while the delayed tripping risk of Relay 1 is lower than Relay 2 when balanced current controllers are adopted by the HVDC system.

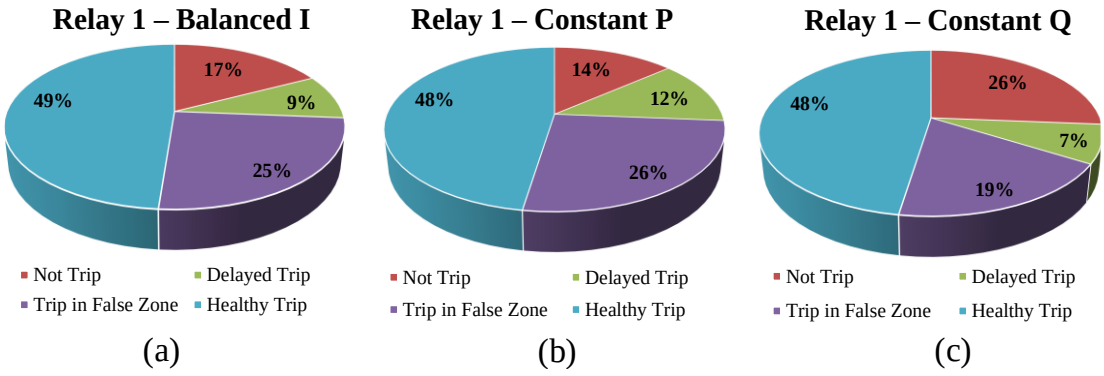

Figure 3-10. Performance of Relay 1 with, (a) Balanced current control; (b) Constant active power control; (c) Constant reactive power control

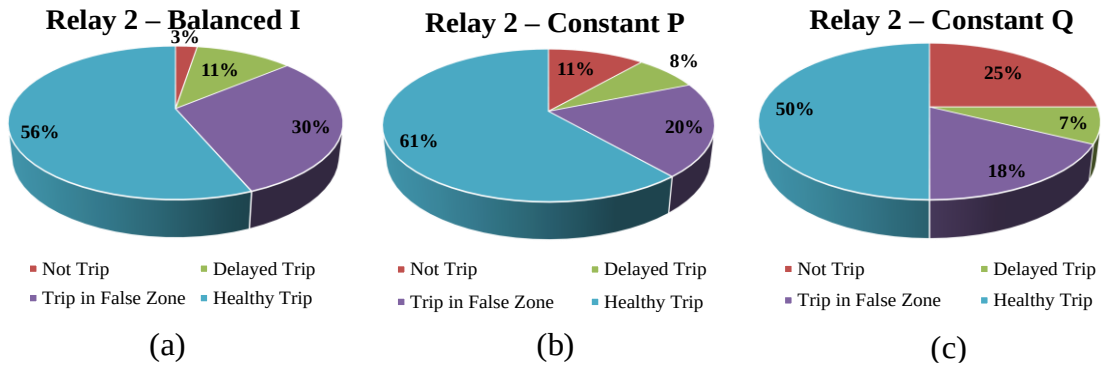

Figure 3-11. Performance of Relay 2 with, (a) Balanced current control; (b) Constant active power control; (c) Constant reactive power control

3.3.4.5 Impact of Distance Protection Characteristic

In this part, both MHO and QUAD characteristics with the settings in Table 3-5 and Table 3-6 are applied to both relays to investigate the impacts of the protection characteristics. The test results are shown in Figure 3-12 and Figure 3-13. For Relay 1, the MHO and QUAD characteristics have similar performance, while for Relay 2, the QUAD characteristic appears to perform better overall performance (from the perceptive of the percentage of the healthy trip and not trip cases).

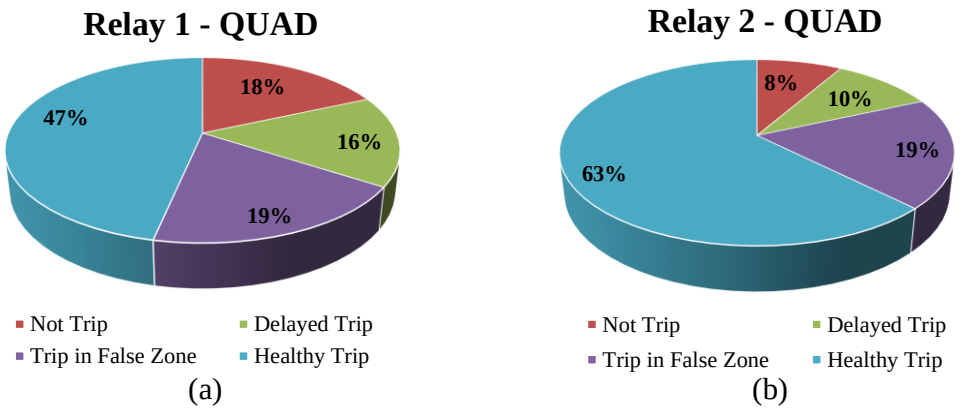

Figure 3-12. Performance of relays with QUAD characteristics, (a) Relay 1, (b) Relay 2

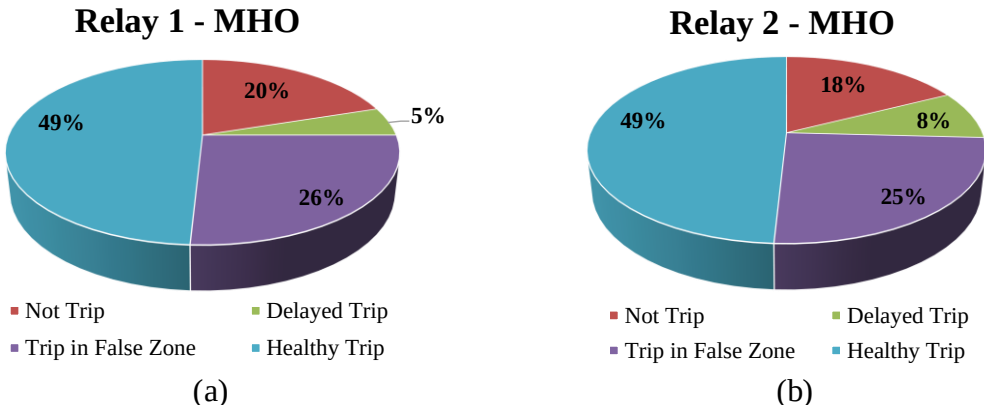

Figure 3-13. Performance of relays with MHO characteristics, (a) Relay 1, (b) Relay 2

3.4 Detailed HIL Tests of Distance Relays

3.4.1 Cases of the Detailed HIL Tests

In Section 3.3, high-level insight into the performance of distance protection in tests conducted under various system conditions is discussed. As the objective of this section is to investigate the HVDC system's impact on distance protection, the NSG,

SC and Load 1 in Figure 3-5 are not included in the following analysis. The reduced network used in detail tests is presented in Figure 3-14, where m is the fraction of the line length representing the distance between distance relay and fault location. The controller of the HVDC system is proposed in Section 2.4.

The cases in Table 3-8 are specially designed to investigate the reasons behind the identified protection issues, where NA means no HVDC was connected in the studied system; CP, BI and CQ refer to the constant active power controller, balanced current controller and constant reactive power controller and the faults are all applied at the 15% of the line, i.e., $m = 15$ % in Figure 3-14. For the designed cases in Table 3-8. Case 1 and Case 2 are reference cases where the network only comprises the voltage sources SG1 and SG2. Case 3 to case 5 and Case 6 to Case 8 are used to investigate the impact of HVDC control modes on the distance protection performance in AG and AB faults. Case 9 is implemented to investigate the distance protection performance in the balanced fault.

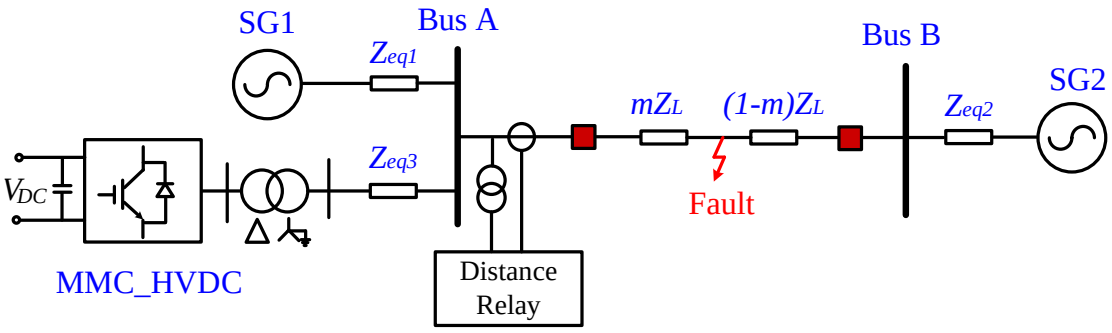

Figure 3-14. The studied network used for the detailed tests

3.4.2 Results of the Detailed HIL Tests

The HIL test results of the cases in Table 3-8 are presented in Table 3-9 and Table 3-10, where the cases with problematic tripping actions, i.e., Not Trip, Delay Trip and Trip in False Zone, are highlighted in red. Compared to the results in Table 3-9 and Table 3-10, more problematic cases are observed in the relays with the QUAD characteristic. Additionally, the sources behind protection issues are similar for the relays with QUAD and MHO characteristics in most cases, so the analysis of relays with the QUAD characteristic will be presented in the following discussion.

Table 3-8. Cases of the detailed tests

Cases	FL_{SG1}	FL_{SG2}	HVDC Control	Fault Condition
1	839 MVA	3000 MVA	NA	AG, 15 %, 2 Ω
2	839 MVA	3000 MVA	NA	AB, 15 %, 2 Ω
3	0 MVA	3000 MVA	CP	AG, 15 %, 2 Ω
4	0 MVA	3000 MVA	BI	AG, 15 %, 2 Ω
5	0 MVA	3000 MVA	CQ	AG, 15 %, 2 Ω
6	0 MVA	3000 MVA	CP	AB, 15 %, 2 Ω
7	0 MVA	3000 MVA	BI	AB, 15 %, 2 Ω
8	0 MVA	3000 MVA	CQ	AB, 15 %, 2 Ω
9	0 MVA	3000 MVA	BI	ABCG, 15 %, 2 Ω

Table 3-9. HIL Results of the relays with QUAD characteristic

Cases	Relay Trips?		Relay Operating Time	
	Relay 1	Relay 2	Relay 1	Relay 2
1	Yes	Yes	50 ms	59 ms
2	Yes	Yes	29 ms	60 ms
3	Yes	Yes	68 ms	40 ms
4	No	Yes	-	100 ms
5	No	No	-	-
6	Yes	Yes	87 ms	61 ms
7	No	Yes	-	43 ms
8	No	No	-	-
9	Yes	Yes	468 ms	50 ms

Table 3-10. HIL Results of the relays with MHO characteristic

Cases	Relay Trips?		Relay Operating Time	
	Relay 1	Relay 2	Relay 1	Relay 2
1	Yes	Yes	38 ms	59 ms
2	Yes	Yes	26 ms	59 ms
3	Yes	Yes	74 ms	40 ms
4	No	Yes	-	104 ms
5	Yes	No	63 ms	-
6	Yes	Yes	53 ms	63 ms
7	Yes	Yes	74 ms	51 ms
8	No	No	-	-
9	Yes	Yes	48 ms	55 ms

3.4.2.1 Cases 4 and 5: Issues of Faulted Phase Selection

From the results in Table 3-9, Relay 1 fails to trip in Case 4 and Case 5 when the HVDC system uses the balanced current and constant reactive power controller. Relay 2 experiences a severe tripping delay of 100 ms in Case 4 and fails to trip in Case 5. In this test, Relay 1 selects the faulted phases based on the magnitudes of the superimposed phase-to-phase currents, i.e., Δi_{ab}, Δi_{bc} and Δi_{ca}, while Relay 2 uses the angle relations of sequence components, i.e., the angle relations of the negative and positive sequence currents and voltages and the angle relations of the negative and zero sequence currents and voltages. The fundamentals of both techniques are proposed in Section 3.2.3.2 and Section 3.2.3.3.

To figure out the sources behind the problematic cases, the impedance locus, input currents and the RMS values of the phase-to-phase superimposed currents measured by Relay 1 for Case 4 and Case 5 are presented in Figure 3-15 and Figure 3-16 respectively. For Relay 1, any superimposed currents greater than 80% of the largest superimposed current will be considered to contain the faulted phase. For example, in the event of the investigated AG faults, the relay is capable of detecting the fault type

when the values of Δi_{ab} and Δi_{ca} are both greater than the threshold while the values of Δi_{bc} is lower than the threshold. However, by observing the RMS values of the superimposed phase-to-phase currents in Figure 3-15, it is clear that all values of the Δi_{ab}, Δi_{bc} and Δi_{ca} are larger than the current threshold, ΔI_{thr}, which results in the relay incorrectly identifying the fault as a balanced fault. Additionally, it can be confirmed that similar phase selection issues are also experienced by Relay 1 when the HVDC uses the constant reactive power controller as shown in Figure 3-16, where the relay detects the fault as the phase-A-to-phase-C-to-ground (ACG) fault since only the value of Δi_{ca} is greater than the calculated threshold and other two phase-to-phase superimposed currents are both lower than the threshold. For the above reasons, the outputs of the phase selection algorithm of the distance relay will be inconsistent with the faulted phase detected by the impedance measuring elements, which causes the blocking of Relay 1 tripping action (although the impedance locus is presented in the protective zone in Case 4 and Case 5).

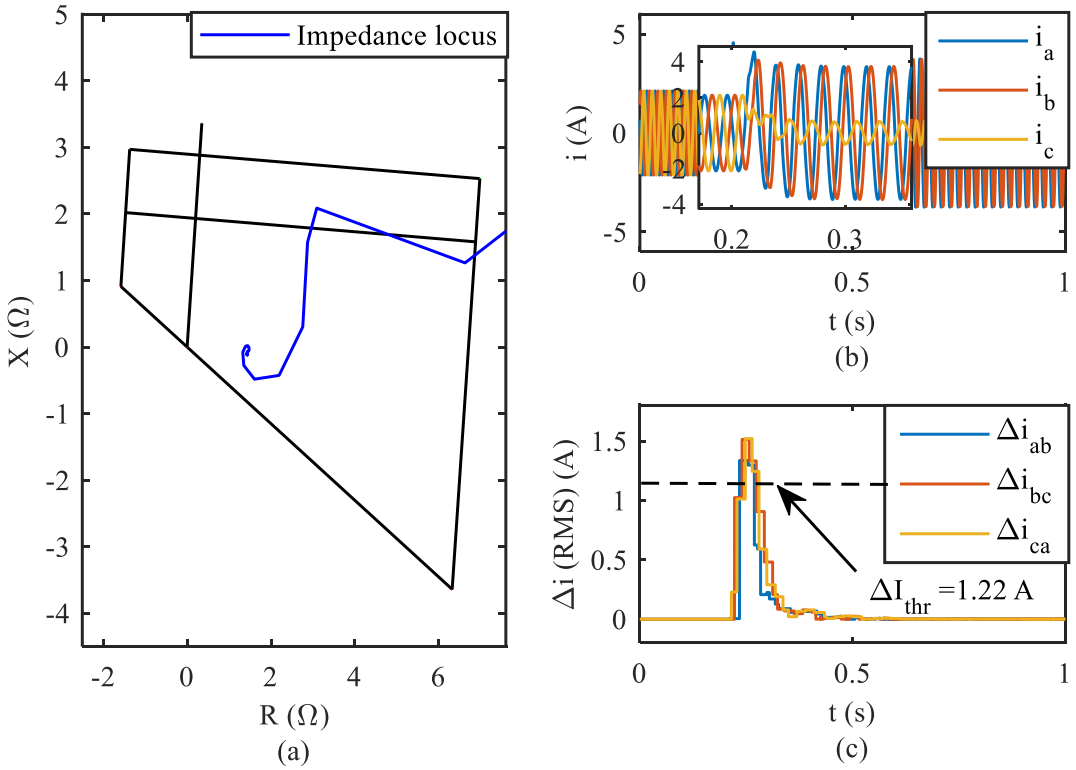

Figure 3-15. Test results of Case 4, (a) impedance locus, (b) relay input currents, (c) phase-to-phase superimposed currents

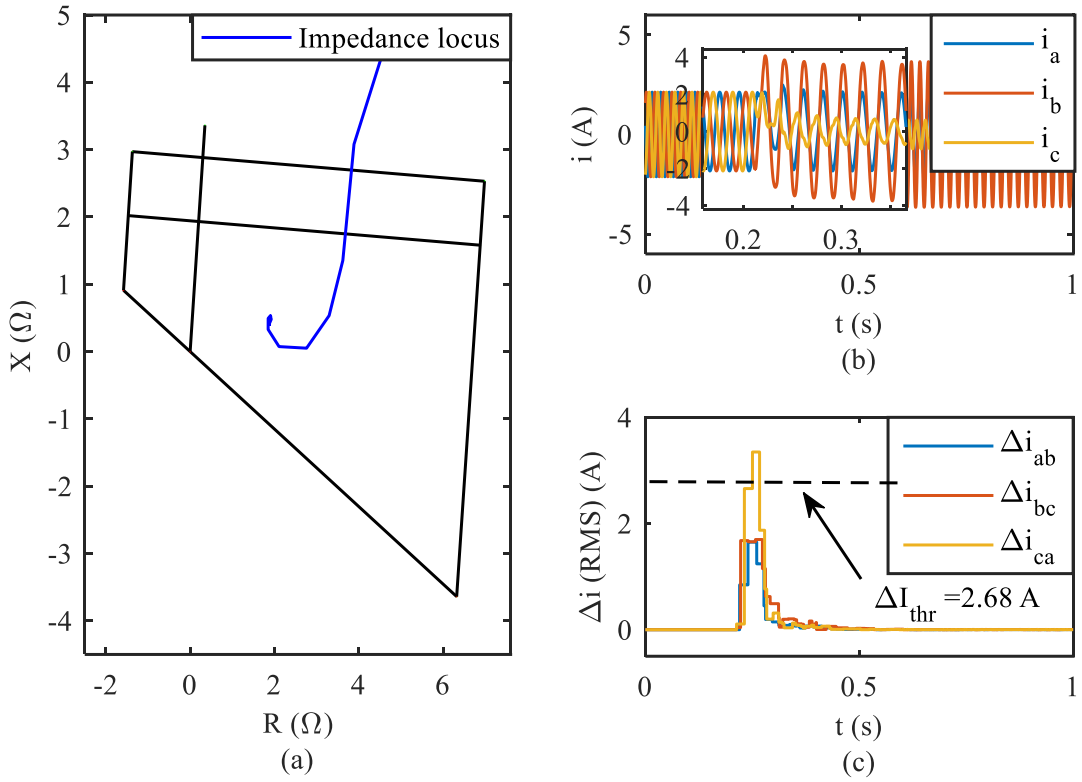

Figure 3-16. Test results of Case 5, (a) Impedance locus, (b) relay input currents, (c) phase-to-phase superimposed currents

Table 3-11. Angle relations of sequence currents and voltages in Case 4 and Case 5

Angles	**Case 4**	**Case 5**
i^-/i^+	117.2°	-167.5°
i^-/i_0	176.7°	-98.5°
v^-/v^+	9.2°	12.42°
v^-/v_0	6.4°	26.92°

The sequence components-based phase selection plane shown in Figure 3-4 is used in Relay 2 to identify the faulted phases, where the values of β_{zone}^{21} and β_{zone}^{20} are set to 30° and 60° respectively. For instance, in the event of AG faults, the angles of i^-/i^+ and i^-/i^0 should be in the zones of -15° to 15° and -30° to 30° respectively. To increase the dependability and avoid the maloperation in some specific operating conditions, e.g., weak-infeed conditions, the phase selection logics in Figure 3-4 are also applied to analyse sequence components of the system voltages if the current-

based phase selection cannot recognise the type of faults. The simulated angles of the i^-/i^+, i^-/i^0, v^-/v^+ and v^-/v_0 in Case 4 and Case 5 are presented in Table 3-11. From the results in Table 3-11 of Case 4, the angle of i^-/i^+ and i^-/i_0 are in the zones of 'BG' and 'out of the zone' respectively, therefore, the relay fails to detect AG faults by the relations of the sequence contents of the measured currents. In such conditions, the relay will use voltage phasors, which can successfully recognise the AG faults. However, an undesired delay, i.e., 100 ms (refer to Table 3-9), will be introduced in this case. The above analysis can also be applied to explain the results of Case 5, where the angles of i^-/i^+ and i^-/i_0 are in the incorrect zones but the v^-/v^+ and v^-/v_0 are in the AG zones. Given the internal functional blocks and signals of the physical relay are inaccessible, the simulated angles in Table 3-11 are calculated from an analysing tool developed in the RSCAD software based on the relay manual. Therefore, there could be some errors between the actual angle values used in the physical relays and the corresponding simulated angles. Additionally, the angle of v^-/v_0 of Case 5 in Table 3-11 reaches to 26.92°, which is close to the upper boundary of the AG Zone, i.e., 30°. Therefore, it is considered that this is the potential cause that leads to the failed tripping issue of Relay 2. Similar faulted phase selection issues of distance relays are also reported in [12][21][22].

3.4.2.2 Case 7: Issues of Over-reach

In Case 7, Relay 1 does not trip during the AB fault when the HVDC employs the balanced current control strategy, where the fault level of SG1 is set to 0 MVA. Therefore, the impedance measured by distance relay during faults can be illustrated by $(3-21)$, which is derived by applying Kirchhoff's Voltage Law (KVL) from the fault position to the relay location in Figure 3-14.

$$Z_R = mZ_L + \left(1 + \overbrace{\left(\frac{i_{SG2}}{i_{HVDC}}\right)}^{A\angle\Delta\psi}\right)R_F \qquad (3-21)$$

where Z_R is the impedance measured by the distance relay; mZ_L is the line impedance between the relay and fault position; i_{SG2} and i_{HVDC} are the current infeed from SG2 and HVDC system and R_F is the fault resistance. To facilitate the following

analysis, the amplitude and angle of the part of $\frac{i_{SG2}}{i_{HVDC}}$ are marked as A and $\Delta\psi$.

As reported in [23], the fault infeed from the HVDC system with a balanced current controller could be illustrated by $(3-22)$, where p refers to phase a, b and x ; i_d^+ and i_q^+ are the injected positive sequence current in the dq axes; ω is the system angular frequency; θ_{vd}^+ is the angle of the positive sequence voltage after the inception of fault in the d axe; θ_p is the phase angle, i.e., 0°, -120°, and 120° for phases a, b and c respectively.

$$i_p(t) = \sqrt{{i_d^+}^2 + {i_q^+}^2}\, sin\left(\omega t + arctan\left(\frac{i_q^+}{i_d^+}\right) + \theta_{vd}^+ + \theta_p\right) \qquad (3-22)$$

From $(3-22)$, the angle of fault current injected by the HVDC system can vary between 0° to 360° and this angle is related to the ratio of the injected reactive and active currents. This causes the angle difference of current infeed from both ends of the protected line, marked as $\Delta\psi$ in $(3-21)$, also varies between 0° to 360°. When the value of $\Delta\psi$ ranges from 0° to 180°, the measured reactance in the distance relay will increase and become larger than the actual reactance as presented in Figure 3-17 (b), which will introduce the under-reach issue to the protection. When the angle of $\Delta\psi$ ranges from $180^\circ$to 360°, Z_E will be capacitive, so it could lead to over-reach issues as shown in Figure 3-17 (c). Additionally, the severity of aforementioned under and over-reach issues are dependent on the amplitude and angle of $\Delta\psi$.

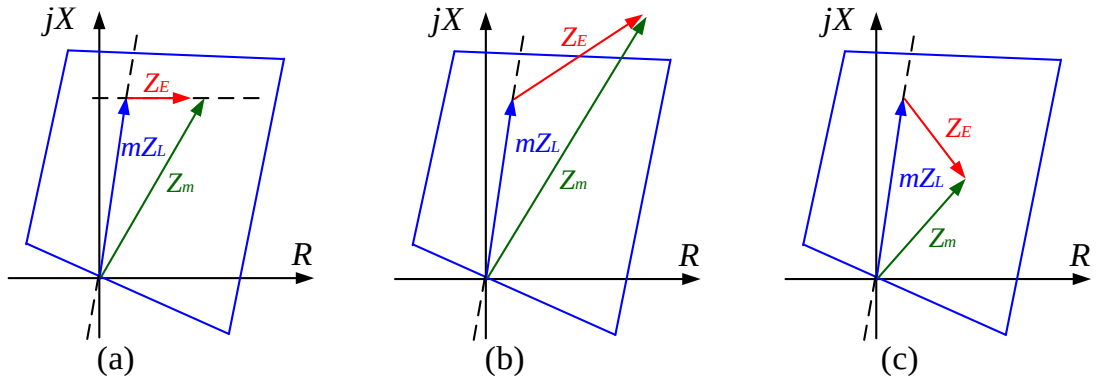

Figure 3-17. Measured impedance of distance relay with (a) $\Delta\psi = 0^\circ$, (b) $\Delta\psi \in (0^\circ, 180^\circ)$, (c) $\Delta\psi \in (180^\circ, 360^\circ)$

The impedance locus and angle values of $\Delta\psi$ are plotted in Figure 3-18. According to Figure 3-18 (b), the angle difference of the current infeed contributed from two ends of the protected line, $\Delta\psi$, is $-82.63°$ in the fault scenario of Case 7, which results the over-reach issues of distance protection. Additionally, owing to the limited current contribution of the HVDC system, those observed over-reach issues become more apparent, which results in the impedance locus appearing at the reverse side of the protective zone. Therefore, the fault cannot be detected by distance relay and further leads to the failed trip issues. However, Relay 2 successfully trips for the fault in Case 7. Presently, it is unclear the reason for the tripping behaviour of Relay 2 owing to the lack of information about the detailed internal implementation of Relay 2, which will be part of future research with support from the relay manufacturer. More literature on the under/over-reach issues of distance protection can be found in [18][24].

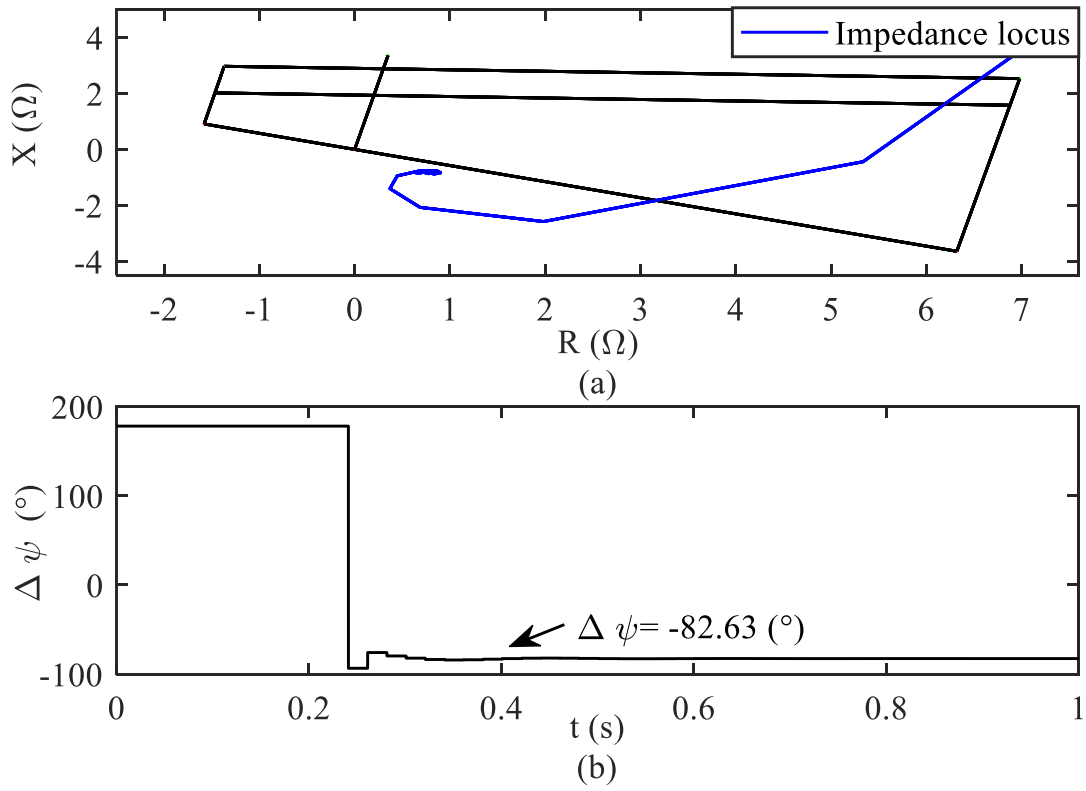

Figure 3-18. Test results of Case 7, (a) Impedance locus, (b) angle difference of the current infeed from both ends of the protected line

3.4.2.3 Case 8: Issues of Impedance Measurement

In Case 8, both relays fail to trip during the AB fault when the HVDC employs the

constant reactive power control strategy, where the fault level of SG1 is set to 0 MVA. The impedance locus, relay input voltages and currents are presented in Figure 3-19. According to the locus in Figure 3-19 (a), the measured impedance does not enter the protective zone and increases to a large value during faults. This scenario can be explained by Figure 3-19 (c), where the phase a and phase b currents are almost identical and their magnitudes are close. As proposed in Table 3-1, the impedance of AB fault is calculated by $(3-23)$, where the denominator value in $(3-23)$ will close to zero, which leads to a significant increase in the impedance measured by the distance relay. More information on the issue in Case 8 is proposed in [26].

$$Z_{AB} = \frac{v_a - v_b}{i_a - i_b} \qquad (3-23)$$

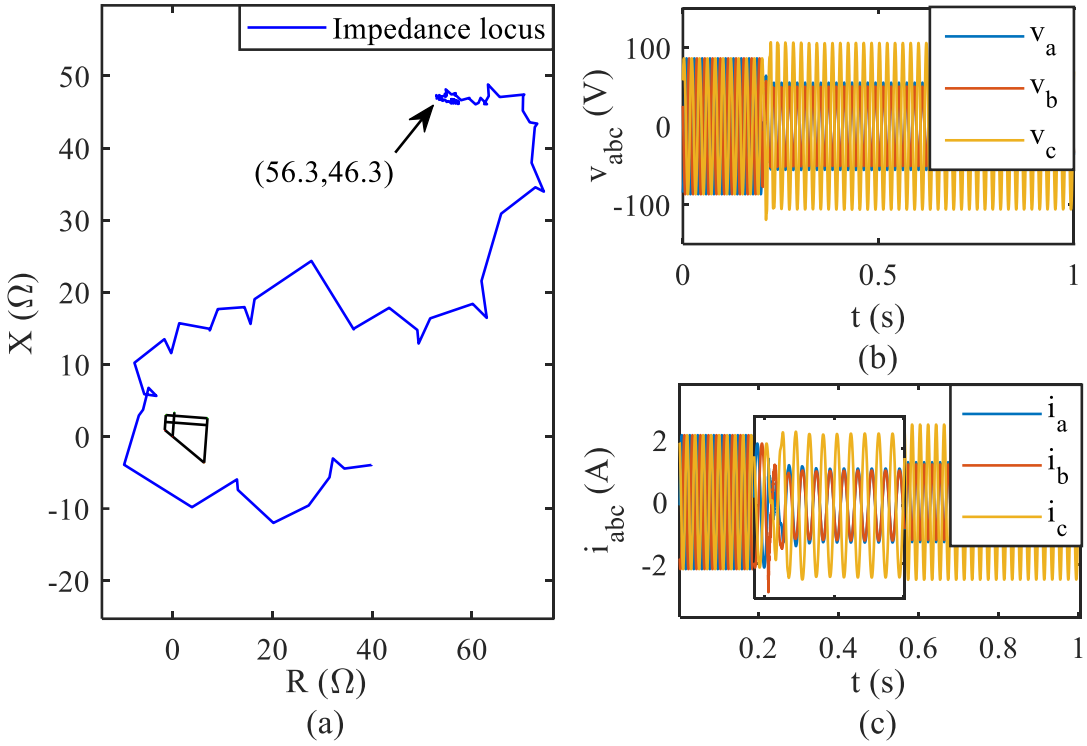

Figure 3-19. Test results of Case 8, (a) Impedance locus, (b) relay input voltages, (c) relay input currents

3.4.2.4 Case 9: Issues of Oscillating Impedance Locus

In Case 9, the ABCG fault is applied in the power network. Based on the results in Table 3-9, Relay 1 suffers from the zone discrimination issue, i.e., it trips in Zone 2 for the fault at 15 % of the line. The impedance locus and angle values of $\Delta\psi$ are presented in Figure 3-20.

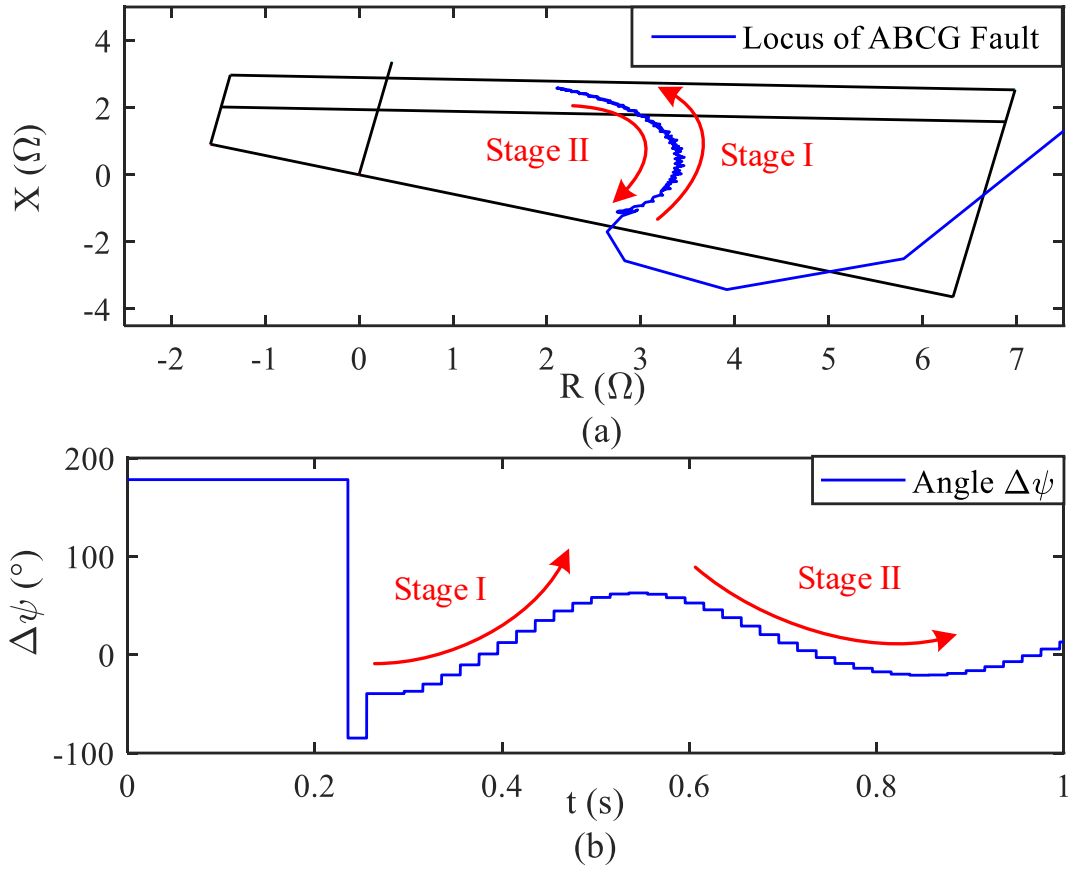

Figure 3-20. Test results of case 9, (a) Impedance locus, (b) angle difference of the current infeed from both ends of the protected line

Given that the three-phase voltage of the main network will drop to almost zero in the case of ABCG faults, the Phase-Locked Loop (PLL) of the HVDC system cannot track system voltage effectively [27], which causes the oscillation of injected positive sequence currents in dq axes. From $(3-22)$, the changes of i_q^+/i_d^+ will vary the angles of the three-phase currents contributed from the HVDC system, thus changing the angle difference of the current infeed from both ends of the protected line as illustrated by $(3-21)$, i.e., the angle values of $\Delta\psi$ increases in the Stage I and decreases in the Stage II after the inception of the faults. As stated in Section 3.4.2.2, the varying $\Delta\psi$ will further introduce the increase (positive $\Delta\psi$) or the decrease (negative $\Delta\psi$) of the measured impedance of distance relay as shown in Figure 3-20 (a), which results in the zone discrimination issues of the relay.

3.5 Review of Protection Solutions of Transmission System

As analysed in Section 3.3 and Section 3.4, the performance of distance protection is compromised significantly after the interconnection of HVDC systems or any other CBRs owing to the issues of under/over-reach, faulted phase selection, problematic impedance measurement and oscillating impedance locus. To increase the protection reliability, many solutions have been proposed in the literature. Based on the implementation principles, those solutions can be further grouped as enhanced distance protection, control-assisted protection, travelling wave-based protection, and intelligent techniques-based protection.

3.5.1 Enhanced Distance Protection Scheme

To address the under/over-reach issues presented in Section 3.4.2.2, the enhanced distance protection schemes are proposed in [25], [28] - [30]. In [28], the author proposes an adaptive distance protection strategy, where an adaptive coefficient is introduced to adjust the operating zone of the developed distance relay adaptively based on the fault conditions. The calculation of the proposed adaptive coefficient depends on the angle of fault supplementary impedance, i.e., φ_Z in Figure 3-21, which is estimated using the measured negative sequence current at the relaying point and the current at the fault point. A similar work is proposed in [29], where an adaptive coefficient estimated using the angular difference between the measured currents and the currents at the fault point is adopted to control the protective zone.

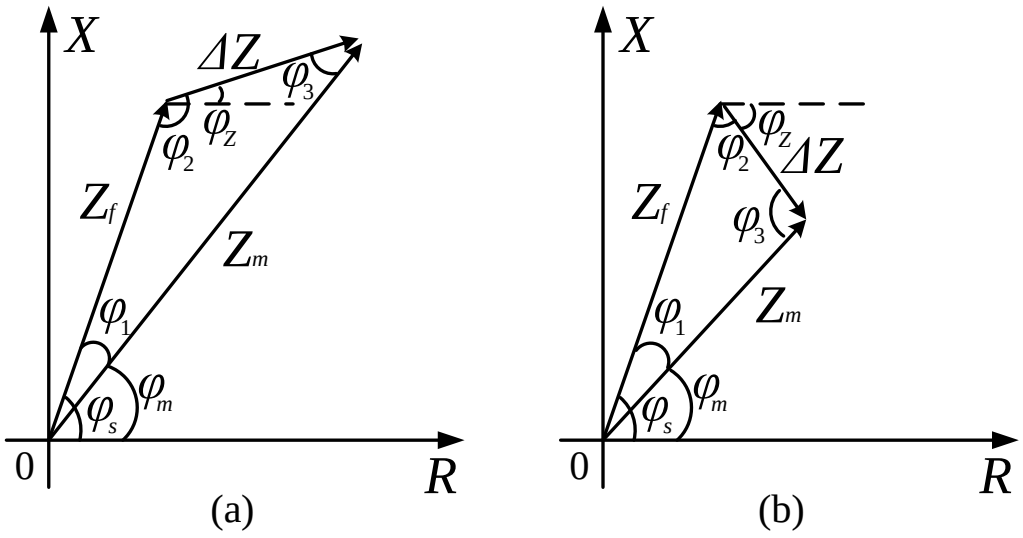

Figure 3-21. Impedance complex plane, (a) ΔZ is resistive-inductive, (b) ΔZ is resistive-capacitive [28]

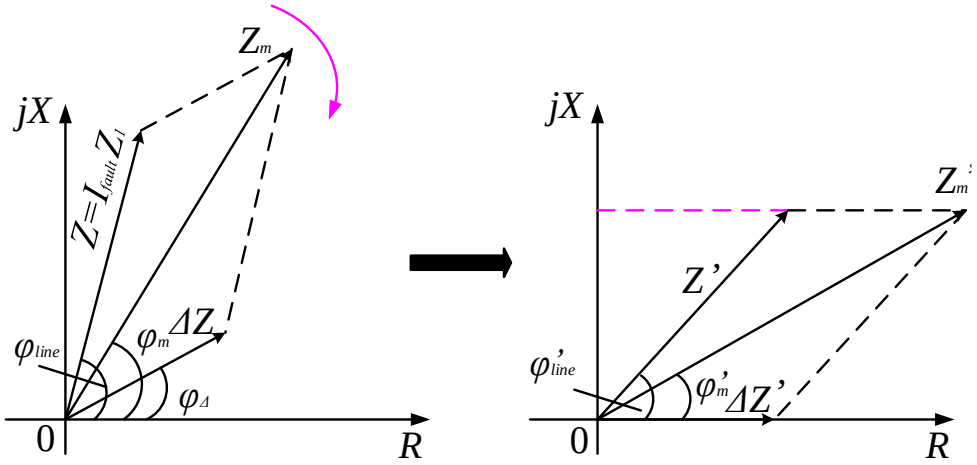

(a)

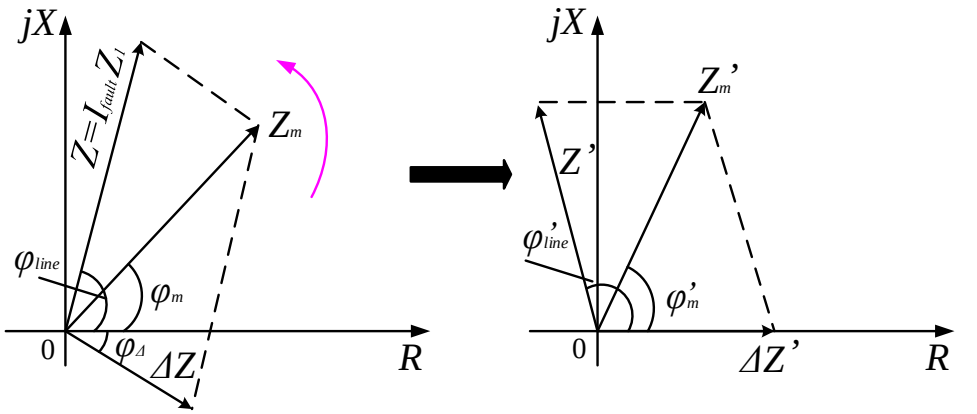

(b)

Figure 3-22. Impedance rotating in the complex plane, (a) ΔZ is resistive-inductive, (b) ΔZ is resistive-capacitive [30]

The authors in [30] suggest rotating the ΔZ to align to the real axes as presented in Figure 3-22 to address the reach issues caused by the supplementary impedance ΔZ. After rotation, the imaginary parts of the rotated fault line impedance, i.e., Z' in Figure 3-22, and the rotated measured impedance, i.e., Z'_m in Figure 3-22, are same, which provides a useful geometrical relation to estimate the actual fault locations and correct the operation of distance relays. After the mathematical derivation, the fault line impedance, i.e., Z in Figure 3-22, can be calculated by $(3-24)$, where the value of φ_Δ is estimated by the superimposed sequence network analysis.

$$Z = \frac{|Z_m||sin(\varphi_m - \varphi_\Delta)|}{|sin(\varphi_{line} - \varphi_\Delta)|} \cdot (cos\,\varphi_{line} + j\,sin\,\varphi_{line}) \qquad (3-24)$$

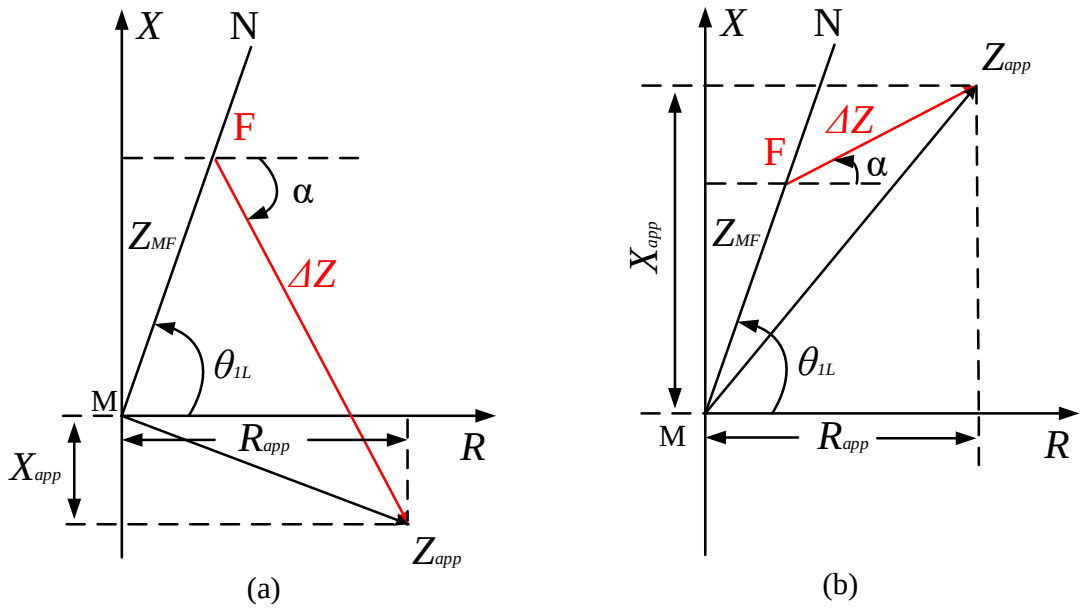

Figure 3-23. Impedance complex plane, (a) ΔZ is resistive-capacitive, (b) ΔZ is resistive-inductive [25]

Although the distance protection schemes in [28]-[30] can mitigate the under/over-reach issues in the network purely comprising SGs, those schemes are not suitable for the protection of the network with CBRs since the assumptions used in those papers do not exist in the network penetrated by CBRs whose fault responses are determined by the embedded controller rather than the natural short-circuit responses as the SGs [31]. For example, the [28] assumes the angle of the negative sequence current at the relay point equals the negative sequence current at the fault point and the [29] and [30] assume the angles of power sources and protected line are the same. To address the technical limitation of the works in [28]-[30], another distance protection algorithm is proposed in [25], where the impacts of the CBRs are considered. In [25], the author proposes an adaptive solution to estimate the fault line impedance. Firstly, it uses geometrical relations in the complex impedance plane in Figure 3-23 to represent the fault line impedance, Z_{MF}, as the function of the gradient of error impedance α. Then this paper analyses the values of α in different types of faults using the developed pure-fault network models. According to the simulation results, the proposed scheme is unaffected by fault types, fault locations, fault resistance, converter control strategies and power swing. However, the proposed distance protection cannot be used to protect the weak transmission network as it assumes there exists a strong AC grid at the remote end of the CBRs.

3.5.2 Control Assisted Protection Scheme

The control-assisted protection schemes are reported in [12][32][33], which improve the protection performance by generating the desired fault signatures by tuning the converter control algorithm. The work in [12] presents a solution to address the issues of the sequence components-based faulted phase selection algorithm discussed in Section 3.4.2.1. There are three stages in this method. In the first stage, the fault type is identified using the sequence information of the system voltage. Then, the converter will calculate the references of the negative sequence currents to ensure the sequence current relations presented in Figure 3-4. In Stage 3, the generated current references in Stage 2 are tracked by the dual-sequence current controller in Figure 2-5. Compared to the current sequence components, the voltage sequence components are more reliable in most scenarios to identify faulted phases. However, as presented in Section 3.4.2.1, the voltage sequence components-based phase selector could also fail to distinguish fault types in some conditions such as the AG fault with the constant reactive power controller. This failed detection of the voltage-based selector will result in the incorrect current injection of CBRs and further leads to the failed operation of the scheme proposed in [12]. As analysed in Section 3.4.2.2, the non-zero values of the angular difference between the local and remote-end infeed will result in the under/over-reach issues of distance protection in resistive faults, where the R_F in $(3-21)$ is not zero. Additionally, as presented in $(3-22)$, the angles of three-phase currents generated from CBRs can be governed by tuning the ratio of the injected reactive and active currents, i.e., i_q^+ and i_d^+, during faults. Following this idea, the author proposes a control algorithm in [32] to keep the angle of converter currents being same as the current angle of the remote-end infeed by tuning the injection ratio of i_q^+ and i_d^+. However, to control the current references accurately, this scheme requires the communication link to transmit the angle information of the remote-end infeed in real-time. Therefore, it needs a relatively high investment. Additionally, the injected reactive and active currents in this scheme could violate the injection curve defined in the Grid Code because of the particular concern from the protection perspective. Compared to the solutions in [12][32], where only one specific protection issue is investigated, the research in [33] addresses both issues of the under/over-reach and faulted phase selection by emulating the fault behaviour of SGs. However, in this

work, due to the limited current capability of CBRs, the proposed control strategy cannot totally address the protection issues of distance relays.

3.5.3 Travelling Wave Protection Scheme

When a fault occurs in the transmission line, an electromagnetic pulse called the 'travelling wave' is generated at the fault position and propagates along the transmission line with a velocity close to the speed of light [34]. The protection schemes operating by such fault-generated high-frequency travelling waves are called travelling wave-based protection. In recent years, many scholars have shown great interest in travelling wave-based protection because of its benefits of being not sensitive to the changes in generator types and converter control strategies and the fast operation speed, i.e., operating within a few milliseconds [35]. Based on the protection principles, the travelling wave protection schemes can be further grouped as the travelling wave polarity comparison-based protection, travelling wave amplitude comparison-based protection, travelling wave distance protection and the travelling wave differential protection [36].

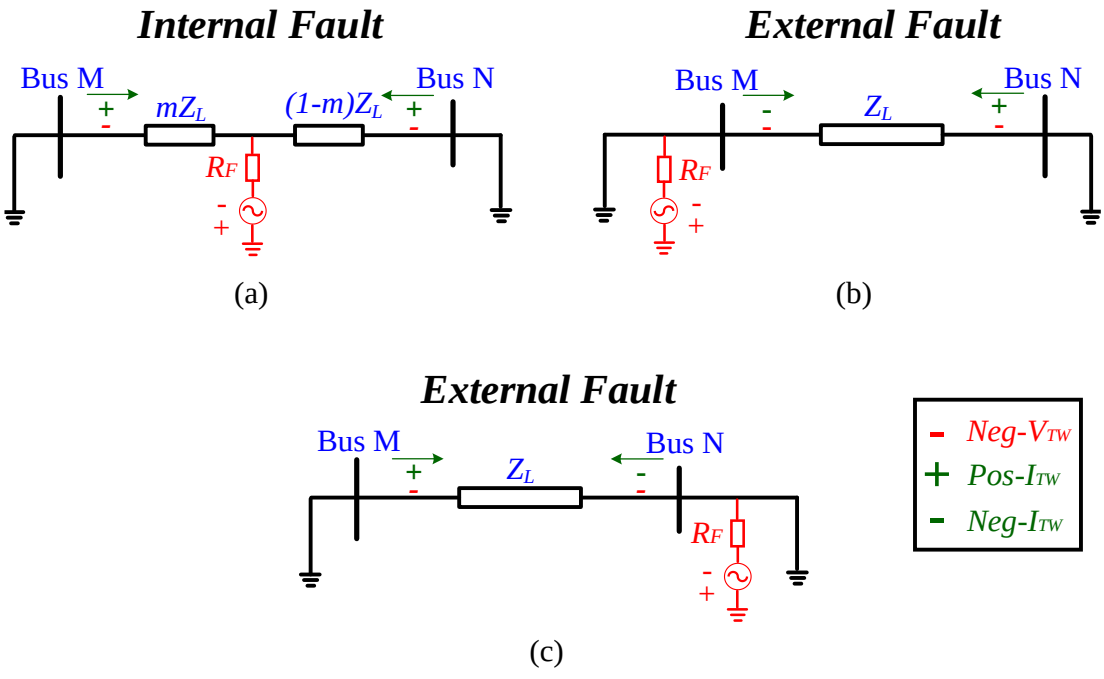

Figure 3-24. Polarities of voltage and current travelling waves, (a) internal fault, (b) external fault on Bus M side, (c) external fault on Bus N side

Table 3-12. Operating principles of travelling wave polarity comparison-based protection scheme

Implemented Travelling Wave	**Relay Does Operate (Internal Faults)**	**Relay Does Not Operate (External Faults)**
Pure Current Travelling Wave	Polarities of the current travelling wave at Bus M and Bus N are the same	Polarities of the current travelling wave at both Bus M and Bus N are opposite
Both Voltage and Current Travelling Wave	Polarities of voltage and current travelling waves at both Bus M and Bus N are opposite	Polarities of voltage and current travelling waves at either side of Bus M and Bus N are the same

The fundamentals of travelling wave polarity comparison-based protection are demonstrated in Figure 3-24 [37], where the superimposed voltage sources induced by faults are highlighted, along with polarities of initial voltage and current travelling waves measured at Bus M and Bus N in different fault scenarios. In those figures, the $Neg - V_{TW}$, $Pos - I_{TW}$ and $Neg - I_{TW}$ refer to the voltage travelling wave with negative polarity, current travelling wave with positive polarity and current travelling wave with negative polarity, where the positive direction of the measured travelling waves is towards the inner side of the protected line.

Based on the relations of the voltage and current travelling wave polarities presented in Figure 3-24, the operating principles of the polarity comparison-based protection scheme are summarised in Table 3-12. The protection schemes using polarities of current travelling waves are reported in [38][39], where relays at both ends of the protected line will operate if the polarities of initial current travelling waves are the same. Otherwise, the relays will maintain stable. The protection scheme using polarities of the initial voltage and current travelling waves is proposed in [40][41], where relays will operate when the polarities of voltage and current travelling waves measured at Bus M and Bus N are opposite.

The travelling wave protection using amplitude comparison is proposed in [42] [43], which is realised by comparing the amplitude of the positive and negative direction travelling waves measured at the relay point. As reported in [42], within a short duration after a forward fault, e.g., the fault f_1 in Figure 3-25, the amplitude of

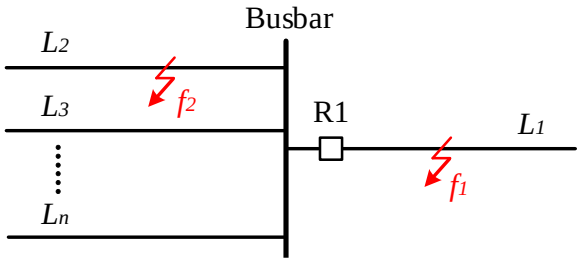

Figure 3-25. Configuration of a typical busbar

the positive direction travelling wave propagating from the busbar to the line is less than the amplitude of the negative travelling wave, while for the backward fault, e.g., the fault f_2 in Figure 3-25, the amplitude of the positive direction travelling wave is significantly greater than the amplitude of the negative travelling wave. Based on this principle, the author proposes a protection algorithm by comparing the ratio of two developed variables, i.e., S_1 and S_2 in $(3-25)$ and $(3-26)$, where t_0 is the fault inception time, τ is two times of the minimum travelling wave line propagation time among all lines connected to the same busbar, $u^+(t)$ is the detected positive direction travelling waves and $u^-(t)$ is the detected negative direction travelling waves. The forward fault is detected when the value of S_1/S_2 is less than the defined threshold, otherwise, the backward fault is identified. A similar work of [42] is presented in [43], where the fault direction is identified by comparing the ratio of the integration of travelling waves propagating toward the positive and negative directions to the defined threshold.

$$S_1 = \int_{t_0}^{t_0+\tau} |u^+(t)|dt \qquad (3-25)$$

$$S_2 = \int_{t_0}^{t_0+\tau} |u^-(t)|dt \qquad (3-26)$$

The travelling wave distance protection algorithm, where only local measurement is required, is implemented to calculate the fault distance by $(3-27)$. This equation is derived by analysing the Lattice diagram presented in Figure 3-26, where τ_1 and τ_2

$$l_1 = \frac{(\tau_2 - \tau_1)v}{2} \qquad (3-27)$$

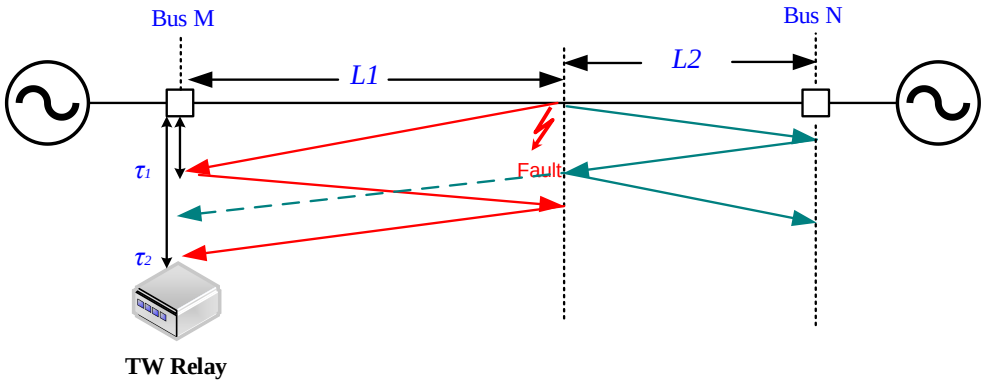

Figure 3-26. Lattice diagram of travelling wave

are the arrival time of the initial and reflected travelling waves from the fault point and v is the velocity of the travelling wave. The works of travelling wave distance protection are reported in [44]-[46]. Compared to the aforementioned travelling wave protection schemes, the distance protection-based travelling wave solution cannot identify the direction of the fault, although it can operate only depending on the local measurement and does not need communication assistance. Furthermore, in some fault scenarios such as the scenario presented in Figure 3-26, where the fault occurs beyond the midpoint of the line, it is difficult to distinguish the reflected travelling wave from the remote busbar and fault point, which might result in the mal-operation of the protection scheme.

The idea of the travelling wave differential protection scheme is explained in [48]. As presented in Figure 3-26, when an internal fault occurs in the transmission line, the polarities of the initial current travelling wave measured at Bus M and Bus N are the same, while for the external faults, their polarities are opposite. Inspired by this phenomenon, the algorithm of travelling wave differential protection is established, where the operating and restrain vectors used in the differential scheme are shown in $(3-28)$ and $(3-31)$. In equations of $(3-28)$ to $(3-31)$, the superscripts 'M'

$$i_{op(t)} = i^{M}_{TW(t\pm\Delta T)} + i^{N}_{TW(t)} \qquad (3-28)$$

$$i^{M}_{TW(t)} = \left| i^{M}_{TW(t-TWLPT)} - i^{N}_{TW(t)} \right| \qquad (3-29)$$

$$i^{N}_{TW(t)} = \left| i^{N}_{TW(t-TWLPT)} - i^{M}_{TW(t)} \right| \qquad (3-30)$$

$$i_{res} = max\left(i^{M}_{TW(t)}, i^{N}_{TW(t)}\right) \qquad (3-31)$$

and 'N' refers to the busbar M and N at both ends of the protected line; the subscripts 'op' and 'res' refer to the calculated operating and restrain current travelling wave vectors; ΔT is the arrival time difference of the initial travelling waves measured at busbar M and N and $TWLPT$ refers to the travelling wave line propagation time, which is calculated by the entire length of the protected line over the propagation velocity of the travelling wave. In external faults, owing to the opposite polarities of $i^{M}_{TW(t\pm\Delta T)}$ and $i^{N}_{TW(t)}$, the magnitude of the operating vector, $i_{op(t)}$, will close to zero, while for the restrain vector, i_{res}, its magnitude will increase to a significant value. Therefore, the travelling wave differential protection will remain stable. A similar analysis can be applied to the internal fault scenario, where the magnitude of $i_{op(t)}$ increases while the value of i_{res} decreases, and thus, the relay will operate. In [49], the author proposes a protection algorithm by comparing the magnitudes of V^{M}_{op} and V^{N}_{op} in $(3-32)$ and $(3-33)$ to V_{res} in $(3-34)$. In those equations, the subscripts 'mea' and 'com' refer to the measured travelling wave without compensation and the compensated travelling wave; the 'B' and 'F' are the backward and forward travelling waves; K_k, Z_c and i_{thr}

$$V^{M}_{op} = |B^{M}_{mea} - B_{com}| \qquad (3-32)$$

$$V^{N}_{op} = |F^{N}_{mea} - F_{com}| \qquad (3-33)$$

$$V_{res} = K_k|Z_c i_{thr}| \qquad (3-34)$$

are the reliable coefficient ranging from 0.3 to 0.6, the line surge impedance and the threshold current. In this scheme, the relays are restrained if the value of V_{res} is greater than both values of V^{M}_{op} and V^{N}_{op}, otherwise, the proposed scheme will operate to isolate the fault. More examples of travelling wave differential protection schemes are reported in [50][51], where the current energy ratio defined in $(3-35)$ are used to distinguish the internal and external faults to enhance the sensitivity of the developed scheme. If the value of ER_{mk} is greater than the value of the defined internal fault criterion, then the relay will operate. Otherwise, it will keep stable.

$$ER_{mk} = \frac{2\|i_{mrk}(t) - i_{nrk}(t-\tau)\|^2_2}{\|i_{mrk}(t)\|^2_2 + \|i_{nrk}(t-\tau)\|^2_2} \qquad (3-35)$$

3.5.4 Intelligent Techniques-based Protection Scheme

Benefitting from the significant achievements of computer science and signal processing techniques, the schemes designed by intelligent tools, such as neural networks [52] - [56], decision trees [57] - [60], fuzzy logic [61][62], and support vector machine [63] - [65], have been investigated to protect the transmission network. To increase the efficiency and accuracy of the protection algorithm, advanced signal processing tools, e.g., Fourier Transform, Wavelet Transform, S-Transform, Hilbert-Huang Transform and Empirical Mode Decomposition, etc., are conventionally adopted to extract the fault signatures. Then, those extracted fault features are further implemented to train the developed intelligent models [66] to detect and distinguish types of faults. The intelligent techniques-based protection scheme typically requires substantial amounts of fault data to train the developed model and has a relatively higher requirement on the implemented hardware platform. So far, intelligent techniques-based protection schemes are mainly used for fault detection and faulted phase selection, which is rarely applied to locate the fault in the transmission network.

3.6 Chapter Summary

In this chapter, the challenges of distance protection in the transmission system with CBRs, i.e., the HVDC system, are illustrated by conducting systematic and detailed HIL studies for two commercially available relays. From the results of the systematic study with a total of 480 cases, it observes that distance protection suffers from a large number of protection issues, including failed trips, delayed trips, and zone discrimination issues when the conventional voltage sources are replaced by the converter-based HVDC system. Furthermore, by implementing the detailed analysis of the selected cases, the reasons behind those found issues are revealed, including under/over-reach, faulted phase selection, impedance measurement and oscillating impedance locus. The solutions in the literature are reviewed in this chapter, which includes enhanced distance protection, control-assisted protection, travelling wave-based protection and intelligent techniques-based protection. To facilitate the understanding of those methods, the key advantages and limitations of those algorithms are compared and summarised below.

- *Enhanced distance protection:* it typically uses local information so the

communication channels are not required, which reduces the costs and increases the protection reliability. However, those solutions only work for the transmission systems with assumed operating conditions.

- *Control-assisted protection:* it addresses the protection issues by generating expected fault signatures by changing the converter control. Therefore, it does not require the modification of the existing protection logic of distance relays. However, the control-assisted protection algorithm could violate the other injection requirements due to the particular concern from the protection perspective.
- *Travelling Wave-based protection:* the benefits of travelling wave protection are apparent in the future power network with substantial amounts of CBRs since its performance is unaffected by the converter control, generator type and fault level variation. However, the travelling wave approaches need a significant sampling frequency to capture the initial wavefronts, especially for the protection of short lines. In some schemes, such as polarity-based and differential schemes, a fast and reliable communication link between two ends of the protected line is required, which increases the protection investment. The travelling wave protection is challenging to distinguish the initial and reflected wavefronts in the close-up faults because of the frequent wave reflections between the fault point and neighbouring terminals [40]. Additionally, for faults with a low fault inception angle (FIA), the travelling wave relay could be failed because of the reduced magnitudes of travelling waves.
- *Intelligent techniques-based protection:* unlike conventional distance protection, which relies on a limited number of fault features, intelligent techniques-based protection extracts significant amounts of fault signatures by implementing advanced signal processing tools. Therefore, intelligent techniques-based protection has higher accuracy in detecting and distinguishing faults. However, substantial amounts of fault data are typically required in this method to train the developed intelligent model and it has a high requirement on the implemented hardware platform.

3.7 Chapter References

[1] S. Valsan and K. Swarup, "Wavelet transform based digital protection for transmission lines", in *International Journal of Electrical Power & Energy Systems*, vol. 31, no. 7-8, pp. 379-388, 2009.

[2] A. Hooshyar, M. A. Azzouz and E. F. El-Saadany, "Distance Protection of Lines Emanating From Full-Scale Converter-Interfaced Renewable Energy Power Plants—Part I: Problem Statement," in *IEEE Transactions on Power Delivery*, vol. 30, no. 4, pp. 1770-1780, Aug. 2015.

[3] D. Liu, Q. Hong, A. Dyśko, D. Tzelepis, G. Yang, C. D. Booth, I. Cowan and B. Ponnalagan, "Evaluation of HVDC system's impact and quantification of synchronous compensation for distance protection", in *IET Renewable Power Generation*, vol. 16, no. 9, pp. 1925-1940, 2022.

[4] B. Kasztenny and D. Finney, "Fundamentals of Distance Protection," *2008 61st Annual Conference for Protective Relay Engineers*, 2008, pp. 1-34.

[5] D. D. Fentie, "Understanding the dynamic mho distance characteristic," *2016 69th Annual Conference for Protective Relay Engineers (CPRE)*, 2016, pp. 1-15.

[6] Technical Manual: MiCOM, P40 Agile P443 ver92, GE, June 2021.

[7] M. J. Domzalski, K. P. Nickerson and P. R. Rosen, "Application of mho and quadrilateral distance characteristics in power systems [relay protection]," *2001 Seventh International Conference on Developments in Power System Protection (IEE)*, 2001, pp. 555-558.

[8] O. A. S. Youssef, "New algorithm to phase selection based on wavelet transforms," in *IEEE Transactions on Power Delivery*, vol. 17, no. 4, pp. 908-914, Oct. 2002.

[9] C. Venkatesh and I. Voloh, "Impact of renewable generation resources on the distance protection and solutions," *2021 Western Protective Relay Conference*, 2021, pp. 1-20.

[10] C. Venkatesh and I. Voloh, "Cross Country Faults - Protection Challenges and Improvements," *2021 74th Conference for Protective Relay Engineers (CPRE)*, 2021, pp. 1-15.

[11] P. Horton and S. Swain, "Using superimposed principles (Delta) in protection techniques in an increasingly challenging power network," *2017 70th Annual*

Conference for Protective Relay Engineers (CPRE), 2017, pp. 1-12.

[12] M. A. Azzouz and A. Hooshyar, "Dual Current Control of Inverter-Interfaced Renewable Energy Sources for Precise Phase Selection," in *IEEE Transactions on Smart Grid*, vol. 10, no. 5, pp. 5092-5102, Sept. 2019.

[13] B. Kasztenny, B. Campbell B, and J. Mazereeuw J, "Phase selection for single-pole tripping: Weak infeed condition and cross-country faults," *Proc. 27th Annual Western Protective Relay Conf.*, Spokane, WA, Oct. 24–26, 2000.

[14] D60 Line Distance Protection System, GE, November 2020.

[15] D. Liu, Q. Hong, A. Dyśko, *et al.*: 'A flexible real time network model for evaluating HVDC Systems' impact on AC Protection Performance', *The 9th Renewable Power Generation Conference (RPG Dublin 2021)*, 2021, pp. 1-6.

[16] IEEE Recommended Practice for Excitation System Models for Power System Stability Studies," in *IEEE Std 421.5-2016 (Revision of IEEE Std 421.5-2005)*, vol., no., pp.1-207, 26 Aug. 2016.

[17] J. Li, R. Xiong, H. Mu, B. Cornélusse, P. Vanderbemden, D. Ernst, and W. Yuan, "Design and real-time test of a hybrid energy storage system in the microgrid with the benefit of improving the battery lifetime," *Applied Energy*, vol. 218, pp. 470–478, 2018.

[18] M. Alam, H. Leite, J. Liang and A. da Silva Carvalho, "Effects of VSC based HVDC system on distance protection of transmission lines", in *International Journal of Electrical Power & Energy Systems*, vol. 92, pp. 245-260, 2017.

[19] 'The Grid Code Issue 6 Revision 11', National Grid, February 2022.

[20] J Duncan Glover, T. J. Overbye, and M. S. Sarma, Power system analysis & design. Boston, Ma: Cengage Learning, 2017.

[21] A. Haddadi, M. Zhao, I. Kocar, U. Karaagac, K. W. Chan and E. Farantatos, "Impact of Inverter-Based Resources on Negative Sequence Quantities-Based Protection Elements," in *IEEE Transactions on Power Delivery*, vol. 36, no. 1, pp. 289-298, Feb. 2021.

[22] K. Xu, Z. Zhang, Q. Lai and X. Yin, "Fault phase selection method applied to tie line of renewable energy power stations", in *IET Generation, Transmission & Distribution*, vol. 14, no. 13, pp. 2549-2557, 2020.

[23] Y. Fang, K. Jia, Z. Yang, Y. Li and T. Bi, "Impact of Inverter-Interfaced

Renewable Energy Generators on Distance Protection and an Improved Scheme," in *IEEE Transactions on Industrial Electronics*, vol. 66, no. 9, pp. 7078-7088, Sept. 2019.

[24] A. Banaiemoqadam, A. Hooshyar and M. A. Azzouz, "A Control-Based Solution for Distance Protection of Lines Connected to Converter-Interfaced Sources During Asymmetrical Faults," in *IEEE Transactions on Power Delivery*, vol. 35, no. 3, pp. 1455-1466, June 2020.

[25] S. Paladhi and A. K. Pradhan, "Adaptive Distance Protection for Lines Connecting Converter-Interfaced Renewable Plants," in *IEEE Journal of Emerging and Selected Topics in Power Electronics*, vol. 9, no. 6, pp. 7088-7098, Dec. 2021.

[26] J. Jia, G. Yang, A. H. Nielsen and P. Rønne-Hansen, "Impact of VSC Control Strategies and Incorporation of Synchronous Condensers on Distance Protection Under Unbalanced Faults," in *IEEE Transactions on Industrial Electronics*, vol. 66, no. 2, pp. 1108-1118, Feb. 2019.

[27] Ö. Göksu, R. Teodorescu, C. L. Bak, F. Iov and P. C. Kjær, "Instability of Wind Turbine Converters During Current Injection to Low Voltage Grid Faults and PLL Frequency Based Stability Solution," in *IEEE Transactions on Power Systems*, vol. 29, no. 4, pp. 1683-1691, July 2014.

[28] J. Ma, X. Xiang, P. Li, Z. Deng and J. Thorp, "Adaptive distance protection scheme with quadrilateral characteristic for extremely high-voltage/ultra-high-voltage transmission line", in *IET Generation, Transmission & Distribution*, vol. 11, no. 7, pp. 1624-1633, 2017.

[29] J. Ma, W. Ma, Y. Qiu and J. S. Thorp, "An Adaptive Distance Protection Scheme Based on the Voltage Drop Equation," in *IEEE Transactions on Power Delivery*, vol. 30, no. 4, pp. 1931-1940, Aug. 2015.

[30] Y. Liang, Z. Lu, W. Li, W. Zha and Y. Huo, "A Novel Fault Impedance Calculation Method for Distance Protection Against Fault Resistance," in *IEEE Transactions on Power Delivery*, vol. 35, no. 1, pp. 396-407, Feb. 2020.

[31] R. Li et al., "Impact of low (zero) carbon power systems on power system protection: a new evaluation approach based on a flexible modelling and hardware testing platform", *IET Renewable Power Generation*, vol. 14, no. 5, pp.

906-913, 2020.

[32] A. Banaiemoqadam, A. Hooshyar and M. A. Azzouz, "A Control-Based Solution for Distance Protection of Lines Connected to Converter-Interfaced Sources During Asymmetrical Faults," in *IEEE Transactions on Power Delivery*, vol. 35, no. 3, pp. 1455-1466, June 2020.

[33] A. Banaiemoqadam, A. Hooshyar and M. A. Azzouz, "A Comprehensive Dual Current Control Scheme for Inverter-Based Resources to Enable Correct Operation of Protective Relays," in *IEEE Transactions on Power Delivery*, vol. 36, no. 5, pp. 2715-2729, Oct. 2021.

[34] M. Aftab, S. Hussain, I. Ali and T. Ustun, "Dynamic protection of power systems with high penetration of renewables: A review of the traveling wave based fault location techniques", in *International Journal of Electrical Power and Energy Systems*, vol. 114, p. 105410, 2020.

[35] A. O. Ibe and B. J. Cory, "A Travelling Wave-Based Fault Locator for Two- and Three-Terminal Networks," in *IEEE Transactions on Power Delivery*, vol. 1, no. 2, pp. 283-288, April 1986.

[36] D. Wang, H. Gao, G. Zou and S. Luo, "Ultra-high-speed travelling wave directional protection based on electronic transformers", in *IET Generation, Transmission & Distribution*, vol. 11, no. 8, pp. 2065-2074, 2017.

[37] Wang, H. Gao, S. Luo and G. Zou, "Ultra-High-Speed Travelling Wave Protection of Transmission Line Using Polarity Comparison Principle Based on Empirical Mode Decomposition", in *Mathematical Problems in Engineering*, vol. 2015, pp. 1-9, 2015.

[38] F. Namdari and M. Salehi, "High-Speed Protection Scheme Based on Initial Current Traveling Wave for Transmission Lines Employing Mathematical Morphology," in *IEEE Transactions on Power Delivery*, vol. 32, no. 1, pp. 246-253, Feb. 2017.

[39] X. Li, A. Dyśko and G. M. Burt, "Traveling Wave-Based Protection Scheme for Inverter-Dominated Microgrid Using Mathematical Morphology," in *IEEE Transactions on Smart Grid*, vol. 5, no. 5, pp. 2211-2218, Sept. 2014.

[40] X. Dong et al., "Implementation and Application of Practical Traveling-Wave-Based Directional Protection in UHV Transmission Lines," in *IEEE Transactions*

on Power Delivery, vol. 31, no. 1, pp. 294-302, Feb. 2016.

[41] Wei Chen, O. P. Malik, Xianggen Yin, Deshu Chen and Zhe Zhang, "Study of wavelet-based ultra high speed directional transmission line protection," in *IEEE Transactions on Power Delivery*, vol. 18, no. 4, pp. 1134-1139, Oct. 2003.

[42] G. Zou and H. Gao, "A Traveling-Wave-Based Amplitude Integral Busbar Protection Technique," in *IEEE Transactions on Power Delivery*, vol. 27, no. 2, pp. 602-609, April 2012.

[43] H. Gao, D. Li, G. Zou and Z. Pan, "A Novel Travelling Waves Based Ultra-High Speed Ratio Directional Protection," *2008 IET 9th International Conference on Developments in Power System Protection (DPSP 2008)*, 2008, pp. 568-572.

[44] P. A. Crossley and P. G. McLaren, "Distance Protection Based on Travelling Waves," in *IEEE Transactions on Power Apparatus and Systems*, vol. PAS-102, no. 9, pp. 2971-2983, Sept. 1983.

[45] Chen Shi long, Shu Hong Chun, Wang Yong zhi and Zeng Fang, "Distance protection scheme with travelling wave for UHVDC transmission line based on wavelet transform," *2008 Third International Conference on Electric Utility Deregulation and Restructuring and Power Technologies*, 2008, pp. 2162-2165.

[46] S. Sawai and A. Pradhan, "Travelling-wave-based protection of transmission line using single-end data", in *IET Generation, Transmission & Distribution*, vol. 13, no. 20, pp. 4659-4666, 2019.

[47] A. Johns, "New ultra-high-speed directional comparison technique for the protection of e.h.v. transmission lines", in *IEE Proceedings C Generation, Transmission and Distribution*, vol. 127, no. 4, p. 228, 1980.

[48] SEL-T401L Ultra-High-Speed Line Relay – Instruction Manual, Schweitzer Engineering Laboratories (SEL), March 2022.

[49] H. Ha, Z. Zhang, Y. Tan, Z. Bo and B. Chen, "Novel Transient Differential Protection Based on Distributed Parameters For EHV Transmission Lines," *2008 IET 9th International Conference on Developments in Power System Protection (DPSP 2008)*, 2008, pp. 186-191.

[50] L. Tang, X. Dong, S. Shi and B. Wang, "Travelling wave differential protection based on equivalent travelling wave," *13th International Conference on Development in Power System Protection 2016 (DPSP)*, 2016, pp. 1-6.

[51] L. Tang, X. Dong, S. Luo, S. Shi and B. Wang, "A New Differential Protection of Transmission Line Based on Equivalent Travelling Wave," in *IEEE Transactions on Power Delivery*, vol. 32, no. 3, pp. 1359-1369, June 2017.

[52] N. Zhang and M. Kezunovic, "Transmission Line Boundary Protection Using Wavelet Transform and Neural Network," in *IEEE Transactions on Power Delivery*, vol. 22, no. 2, pp. 859-869, April 2007.

[53] P. Bhowmik, P. Purkait and K. Bhattacharya, "A novel wavelet transform aided neural network based transmission line fault analysis method", in *International Journal of Electrical Power & Energy Systems*, vol. 31, no. 5, pp. 213-219, 2009.

[54] C. Bhende, S. Mishra and B. Panigrahi, "Detection and classification of power quality disturbances using S-transform and modular neural network", in *Electric Power Systems Research*, vol. 78, no. 1, pp. 122-128, 2008.

[55] K. M. Silva, B. A. Souza and N. S. D. Brito, "Fault detection and classification in transmission lines based on wavelet transform and ANN," in *IEEE Transactions on Power Delivery*, vol. 21, no. 4, pp. 2058-2063, Oct. 2006.

[56] M. Gil and A. Abdoos, "Intelligent busbar protection scheme based on combination of support vector machine and S-transform", in *IET Generation, Transmission & Distribution*, vol. 11, no. 8, pp. 2056-2064, 2017.

[57] A. Jamehbozorg and S. M. Shahrtash, "A Decision Tree-Based Method for Fault Classification in Double-Circuit Transmission Lines," in *IEEE Transactions on Power Delivery*, vol. 25, no. 4, pp. 2184-2189, Oct. 2010.

[58] A. Jamehbozorg and S. M. Shahrtash, "A Decision-Tree-Based Method for Fault Classification in Single-Circuit Transmission Lines," in *IEEE Transactions on Power Delivery*, vol. 25, no. 4, pp. 2190-2196, Oct. 2010.

[59] M. Meena, O. P. Mahela, M. Kumar and N. Kumar, "Detection and Classification of Power Quality Disturbances Using Stockwell Transform and Rule Based Decision Tree," *2018 International Conference on Smart Electric Drives and Power System (ICSEDPS)*, 2018, pp. 227-232.

[60] J. Upendar, C. Gupta and G. Singh, "Statistical decision-tree based fault classification scheme for protection of power transmission lines", in *International Journal of Electrical Power & Energy Systems*, vol. 36, no. 1, pp. 1-12, 2012.

[61] R. Mahanty and P. Gupta, "A fuzzy logic based fault classification approach using

current samples only", in *Electric Power Systems Research*, vol. 77, no. 5-6, pp. 501-507, 2007.

[62] O. A. S. Youssef, "Combined fuzzy-logic wavelet-based fault classification technique for power system relaying," in *IEEE Transactions on Power Delivery*, vol. 19, no. 2, pp. 582-589, April 2004.

[63] P. K. Dash, S. R. Samantaray and G. Panda, "Fault Classification and Section Identification of an Advanced Series-Compensated Transmission Line Using Support Vector Machine," in *IEEE Transactions on Power Delivery*, vol. 22, no. 1, pp. 67-73, Jan. 2007.

[64] X. G. Magagula, Y. Hamam, J. A. Jordaan and A. A. Yusuff, "Fault detection and classification method using DWT and SVM in a power distribution network," *2017 IEEE PES PowerAfrica*, 2017, pp. 1-6.

[65] M. Gil and A. Abdoos, "Intelligent busbar protection scheme based on combination of support vector machine and S-transform", in *IET Generation, Transmission & Distribution*, vol. 11, no. 8, pp. 2056-2064, 2017.

[66] R. Godse and S. Bhat, "Mathematical Morphology-Based Feature-Extraction Technique for Detection and Classification of Faults on Power Transmission Line," in *IEEE Access*, vol. 8, pp. 38459-38471, 2020.

Chapter 4

4 Review of Protection Challenges and Solutions in Inverter-Dominated Microgrids

4.1 Introduction

While the previous chapter focused on protection-related issues in high-voltage (HV) transmission systems, this chapter takes a closer look at distribution networks, particularly microgrids.

A microgrid is a small-scale network including generators, energy storage devices and loads, which plays an essential role in developing the smart grid. For the successful implementation of microgrids, one of the main concerns is reliable power system protection. In a conventional distribution network, the flow of fault currents is unidirectional, which is from the upstream substation to the downstream fault point. However, significant amounts of distributed energy resources (DERs) exist in microgrids, which evolve the microgrids into active systems with bidirectional power flow and change the fault current distribution of the network. This results in the issues of under-reach, over-reach and sympathetic tripping of overcurrent relays. Additionally, the fault level of a microgrid can change dynamically in different operating modes. In the grid-connected mode, the fault level of the microgrid is typically high, owing to the infeed from the main grid. However, in islanded mode, the fault level can reduce significantly since the fault infeed is only contributed by the local distributed generators (DGs) with small capacity. The reduction and variation of fault level will be particularly significant if the microgrid is dominated by IIDGs. For this reason, the faults in islanded microgrids are challenging to detect with a high level

of discrimination and a long delay (or even failed trips) can be introduced to the traditional overcurrent relays in microgrids, which are designed with a single setting group and operate based on high-magnitude fault currents.

This chapter reviews the challenges of microgrid protection and protection solutions in the literature. The chapter is organised as follows. The overview of the microgrid is presented in Section 4.2. The protection challenges of microgrids are reviewed in Section 4.3. The existing solutions in the technical literature for microgrid protection are reviewed in Section 4.4, and the chapter summary is included in Section 4.5.

4.2 Overview of Microgrid

In the future, more and more small-scale sources, such as photovoltaic (PV) modules, wind turbines, fuel cells, etc., are expected to be integrated into the distribution system to fulfil the increased power demands [1]. Those microsources are represented as the 'DERs' or the 'DGs' in the literature. The connected DERs in the distribution network can reduce carbon emissions and energy losses during power transmission and avoid the high investment of extending the conventional power system. On the other hand, their connection also improves the energy efficiency, power quality and efficiency of peak-valley management [2]. However, substantial amounts of DERs introduce significant challenges to the effective control of the power system since they behave as uncontrollable sources, which leads to the network operators paying considerable efforts to manage those DERs [3].

To address the management problem of DERs, the literature of [4] suggests viewing the generation and loads as a subsystem connected to the utility grid by a single point, i.e., the Point of Common Coupling (PCC). This type of subsystem is the 'microgrid'. The microgrids are typically constructed in low voltage (LV) networks, i.e., $V \leq 1\ kV$, and medium voltage (MV) networks, i.e., usually $1\ kV < V \leq 69\ kV$, operating as a single electrical supplier or consumer in distribution networks [2]. Compared to the conventional power system, the microgrid can operate in grid-connected and islanded modes by controlling the switch at PCC [5]. In grid-connected mode, the microgrid can deliver or absorb power from the connected system depending on the operating conditions of the main grid. In islanded mode, it is able to support all

local loads and maintain the voltage and frequency of an islanded system, thus reducing the risks of the power outage and improving the system's reliability [6]. Therefore, the microgrid can be used as a reliable backup source for critical infrastructures such as hospitals, airports and military bases and supply power to remote areas [7]. The features of microgrids are summarised below.

- Dual-mode operation: the microgrid can operate in grid-connected and islanded modes according to the operator's demands and main network conditions.
- Short-length feeders: the microgrids are typically in LV and MV networks. Therefore, the length of feeders in microgrids is relatively short. For example, the maximum length of feeders in the MV microgrid in [8] and the LV microgrid in [9] are 4.7 km and 105 m respectively.
- Continuously changed operating conditions: the power flow of microgrids constantly changes because of the uncertain nature of renewables and changeable loading conditions.
- Various fault responses: in microgrids, the IIDGs are commonplace, whose fault behaviour depends on their embedded controllers [10]. Therefore, the fault responses of microgrids dominated by IIDGs could have different fault characteristics, which depend on the associated grid code and control strategies adopted by IIDGs.
- Available communication infrastructure: in modern microgrids, two-way communication infrastructures are available [11].

4.3 Protection Challenges in Microgrids

4.3.1 Under/Over-Reach Issues

In a conventional radial distribution system, the flow of fault currents is unidirectional from the upstream large-capacity synchronous machine to the downstream fault point [12], which results in the upstream fault level always being higher than the fault level of the downstream busbar. Additionally, since the SG is the main infeed source of faults in the conventional distribution network, the margin of fault level between the neighbouring busbar is significant for the proper coordination of overcurrent relays.

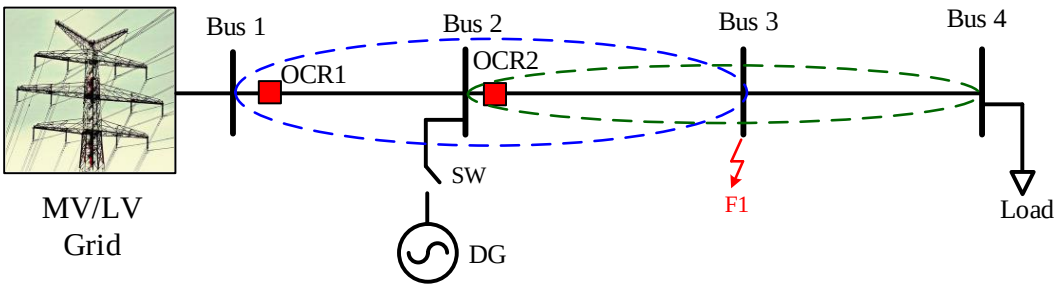

Figure 4-1. Network to analyse the under/over-reach issues of overcurrent protection

For example, in Figure 4-1, where the switch connected to Bus 2 is initially open, the overcurrent relay 1, i.e., OCR1, should play a role as the primary protection for the faults between Bus 1 and Bus 2, and it should provide reliable backup protection for the faults between Bus 2 and Bus 3 at the same time. This principle should also be adopted by the overcurrent relay 2, i.e., OCR2, where it is implemented as the primary protection for faults between Bus 2 and Bus 3 and the backup protection for faults between Bus 3 and Bus 4. In this condition, the expected protection reaches of OCR1 and OCR2 are demonstrated by the blue dash and green dash lines in Figure 4-1. The fault, F_1, in Figure 4-1 is used to illustrate the issues of under-reach and over-reach. The following analysis is based on the study in [13].

Based on the superimposition theorem, the faulted network can be regarded as the sum of the pre-fault and superimposed networks [14]. Considering the current increases raised by faults are typically much higher than pre-loading currents, the impacts of loading currents are neglected in the following analysis. The superimposed network of the fault F_1 in Figure 4-1 is shown in Figure 4-2, where Z_{sys} is the upstream grid equivalent impedance of Bus 1; Z_{L12}, Z_{L23}, Z_{L34} are the line impedance between neighbouring busbars; Z_{Load} is the load equivalent impedance and Z_{DG} is the DG equivalent impedance. In the network of Figure 4-2, the only active source is superimposed voltage source applied at the fault position, whose magnitude equals the pre-fault voltage at the fault point, while the voltage polarity of the superimposed voltage source is opposite to the pre-fault voltage [15]. The superimposed currents measured by OCR1 and OCR2 are highlighted as Δi_{OCR1} and Δi_{OCR2}. The magnitudes of Δi_{OCR1} and Δi_{OCR2} without the connection of DG is calculated by $(4-1)$ and the Δi_{OCR2} with DG is presented in $(4-2)$. By comparing values of $\Delta i_{OCR2}^{no\ DG}$ and $\Delta i_{OCR2}^{with\ DG}$ in $(4-1)$ and $(4-2)$, it was found that the connection of DG will increase

the fault current measured by OCR2, which results in the over-reach issues of OCR2. After implementing the current division principle, the superimposed currents measured by OCR1 with DG can be estimated by $(4-3)$. By comparing the $\Delta i_{OCR1}^{with\ DG}$ in $(4-3)$ to the result in $(4-1)$, the connection of DG decreases the fault current measured by OCR1, and thus, it causes the under-reach issue of the OCR1, also known as 'protection blinding'.

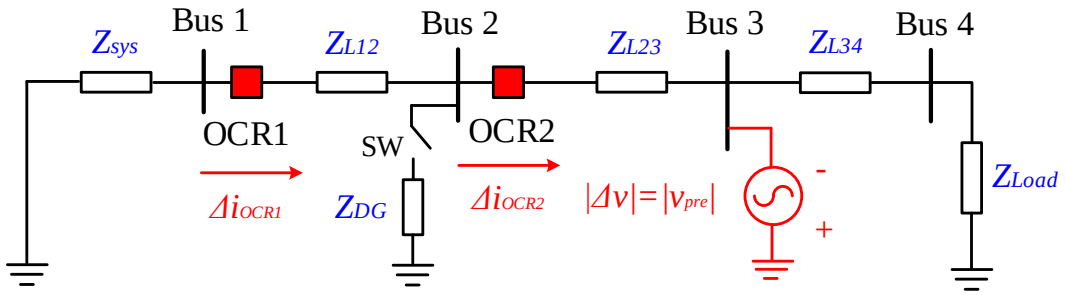

Figure 4-2. Superimposed network for the fault at Bus 3

$$\Delta i_{OCR1}^{no\ DG} = \Delta i_{OCR2}^{no\ DG} = \frac{\Delta v}{Z_{sys} + Z_{L12} + Z_{L23}} \qquad (4-1)$$

$$\Delta i_{OCR2}^{with\ DG} = \frac{\Delta v}{\frac{(Z_{sys} + Z_{L12}) \times Z_{DG}}{Z_{sys} + Z_{L12} + Z_{DG}} + Z_{L23}} \qquad (4-2)$$

$$\Delta i_{OCR1}^{with\ DG} = \frac{\Delta v}{(Z_{sys} + Z_{L12}) + Z_{L23} \times \left(1 + \frac{Z_{sys} + Z_{L12}}{Z_{DG}}\right)} \qquad (4-3)$$

4.3.2 Sympathetic Tripping

The issues of sympathetic tripping (or called 'false tripping') are reported in [13], [16][17], which are illustrated by Figure 4-3. For the fault F_1 in Figure 4-3, the relay OCR1 is potentially to trip when the fault infeed from the DG, i.e., i_f^{DG} in Figure 4-3, is greater than the current threshold of OCR1, which causes the power outage of the healthy line such as the Line 1 in Figure 4-3. This undesired tripping is the 'sympathetic tripping' in the literature, which can be solved by equipping the directional unit to the overcurrent relays.

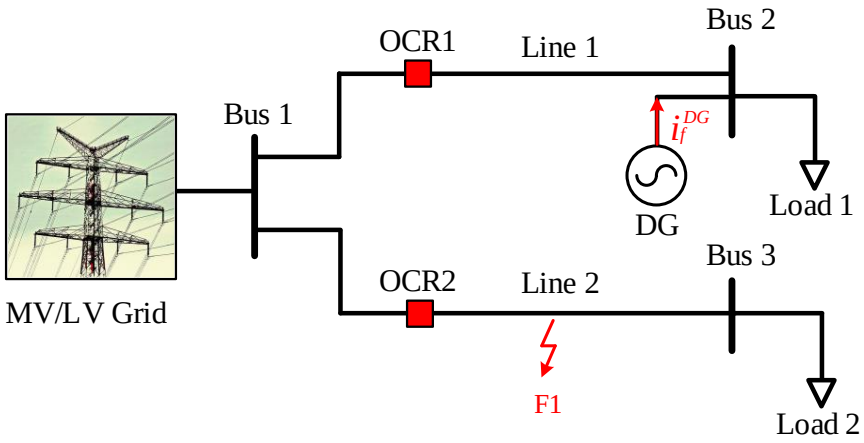

Figure 4-3. Network to analyse the sympathetic tripping issues of overcurrent protection [13]

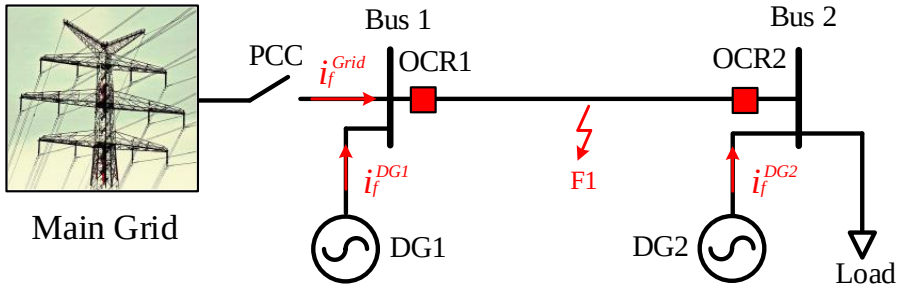

Figure 4-4. Network to illustrate the issues raised by fault level variation of the grid-connected and islanded microgrid

4.3.3 Varied Fault Levels between Dual-Mode Microgrids

As proposed in Section 4.2, the microgrid can operate in either grid-connected or islanded mode based on system operator demands and main system conditions, which results in a significant variation of the system fault level between the two operating modes. The protection issues raised by the varied fault level are reported in [18] – [20], which are explained by a simple network in Figure 4-4. In Figure 4-4, the i_f^{Grid}, i_f^{DG1}, and i_f^{DG2} refer to the fault infeed contributed from the main grid, DG1 and DG2 respectively. The switch at PCC will close in grid-connected mode and it will open in islanded mode. As the main source of varied fault levels is the fault infeed from the utility grid, it assumes that the OCR2 could always detect and successfully trip the fault, F_1, in both grid-connected and islanded microgrids. For this reason, the following analysis is only for OCR1.

For OCR1, it adopts the standard Inverse Definite Minimum Time (IDMT) curve as presented in Figure 4-5, where i_{f1} and i_{f2} are the fault current measured by OCR1

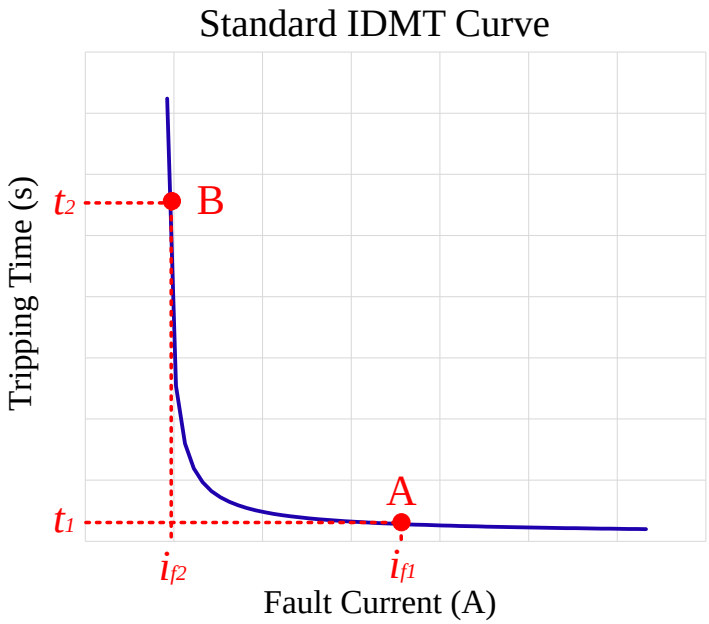

Figure 4-5. Protection curve of standard IDMT

$$t = TMS \times \frac{0.14}{I_r^{0.02} - 1} \qquad (4-4)$$

in grid-connected and islanded microgrids; t_1 and t_2 are the tripping time of OCR1 with the fault currents of i_{f1} and i_{f2}. The equation of employed IDMT characteristics is proposed in $(4-4)$, which is designed based on the standard of IEC 60255 [21]. In this equation, the TMS is the Time Multiplier Setting and I_r is the Plug Setting Multiplier, which is calculated by the ratio of the measured fault current and the pickup current of the relay. As illustrated in Figure 4-5, as the reduction of fault currents in islanded microgrids, the issues of delayed tripping appear on OCR1, i.e., t_1 moving to t_2. In the worst condition, the OCR1 even fails to detect faults if the magnitude of i_f^{DG1} is less than the pickup current setting of the relay, which is highly potential to appear in microgrids dominated by IIDGs.

4.4 Protection Solutions for Microgrid

In this section, microgrid protection solutions are reviewed comprehensively, which include adaptive protection, differential protection, active method-based protection, intelligent techniques-based protection, travelling wave protection and other types of protection.

4.4.1 Adaptive Protection

To cope with protection issues raised by the varied fault levels between the grid-connected and islanded modes, adaptive protection algorithms are proposed in [13], [22] - [27], where relays' settings are amended adaptively to cater for the prevailing system conditions. According to the operating principles, there are three typical approaches to realise adaptive protection.

In the first approach, the load flow and short-circuit analysis are implemented initially by considering all possible network configurations and operating status of DGs, i.e., on/off, in the microgrid. Then, the analysed results are stored in an event table and used to calculate relay settings and the calculated settings are saved in an action table. Finally, those pre-calculated settings are selected and updated to the relays in the microgrid based on the real-time microgrid conditions. Examples of adapting this strategy are presented in [22][23]. However, considering the intermittent natures of renewables and the changeable features of microgrids, it is difficult to cover all possible fault scenarios in microgrids. For this reason, some scholars propose the second adaptive protection approach by estimating the relay settings in real time, such as [13], [24][25]. In [13], settings of the TMS and PS of DOCRs are formulated as a non-linear optimisation problem, where the objective function is to minimise the total operating time of the primary and backup relays and some constraints, such as the setting range of pickup current, TMS and time margin between the primary and backup protection, are considered in the setting process. The solvers of Ipopt and Baron are employed in this paper to get the solutions of the established non-linear equation. The work in [24] adopts a similar approach as [13], but it simplifies the setting process to a linear problem by pre-determining the pickup current settings of relays. Another three-layer real-time adaptive protection is proposed in [25], whose architecture is shown in Figure 4-6. In this algorithm, the execution layer is responsible for monitoring and collecting the prevailing system conditions. The collected information, including voltages, currents and conditions of CBs, is transmitted to the upper coordination layer, where the new relay settings are calculated to coordinate the relays in microgrids. Additionally, a management layer is designed at the top of this protection algorithm to coordinate the protection and active network management systems. Unlike approaches above, where centralized protection strategies are adopted,

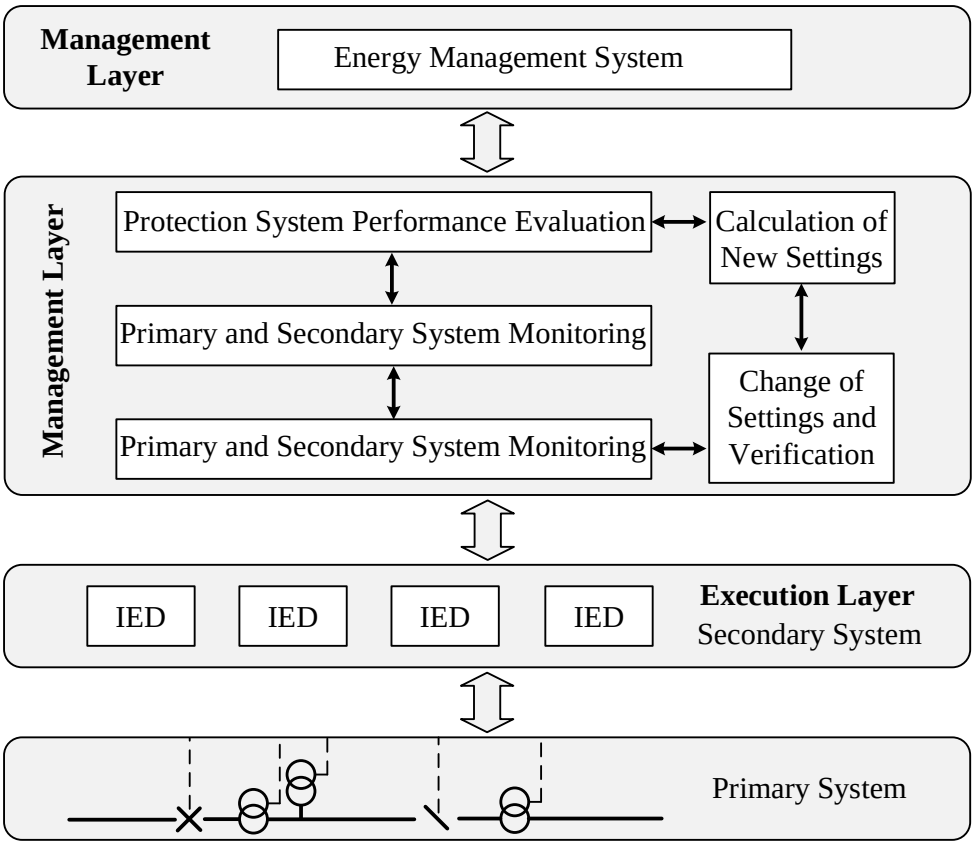

Figure 4-6. Multi-layer adaptive protection algorithm [25]

the distributed architecture using multi-agent techniques is proposed in [26][27], which can avoid the potential protection failure caused by the collapse of the protection centre. As illustrated in [26], the agent is a computer system that is capable of operating solely to achieve its objectives, which can be grouped into different societies based on their functions. The data between agents and agent societies can be shared via the communication channels between them. Therefore, this method does not require a control centre to monitor the whole power system and process the collected data centrally as did in the first and second adaptive protection approaches, thus avoiding protection failure caused by the breakdown of the control centre.

4.4.2 Differential Protection

Differential protection is another commonly used method for microgrid protection. The basic operating fundamentals and parameter setting procedure of differential protection are explained in [28]. As proposed in this paper, current differential protection is less sensitive to fault level variation, bi-directional power flow, DG status and changes in system configurations. Differential protection was implemented as the

primary protection scheme in [29] to protect the microgrid. In this protection system, all relays are digital and equipped with communication capability, which can sample current waveforms at 16 samples per cycle or more. Those relays are installed at both ends of the protected feeders to sample the currents synchronously. If the current difference captured by terminal relays are greater than the defined threshold, relays will trip to isolate faults. According to the results, the proposed differential system can protect the microgrid effectively, while it requires a relatively higher investment in practice as it needs accurate synchronous measurement and high-bandwidth communication channels. The differential schemes relying on the spectral energy of currents are discussed in [30] - [35], where the advanced signal processing, e.g., S Transform in [30] - [32], Hilbert-Huang Transform [33], Ensemble Empirical Mode Decomposition [34], a combination of Variational Mode Decomposition and Hilbert Transform [35], are implemented to process the measured currents and calculate the spectral energy contents. If the differential energy, defined as the energy difference of the currents measured at two ends of the protected feeder, is greater than the threshold, the relays at two terminals will be tripped to isolate the faults. Compared to the conventional time-domain current-based differential system, the spectral energy approach has a higher tolerance of synchronising errors and is more sensitive to high-impedance faults (HIFs).

4.4.3 Active Protection Methods

The active method is realised by controlling IIDGs to inject off-normal frequency components during faults to facilitate fault detection and relay coordination. Several active protection methods are proposed in the literature [36] – [40]. In [36], the off-normal frequency currents, e.g., 70 Hz, are injected by one of the IIDGs during faults and relays in the network are coordinated using a differential protection strategy. For internal faults, a significant magnitude difference will exist on the injected off-normal frequency components detected by relays at two ends of the protected feeder, while the magnitude difference will be slight for the external faults. In [37], the injected harmonic components are used to coordinate relays in the microgrid using IDMT characteristics. The network diagram in Figure 4-7 is to demonstrate the principle of this algorithm, where all DGs are capable of injecting different harmonic components

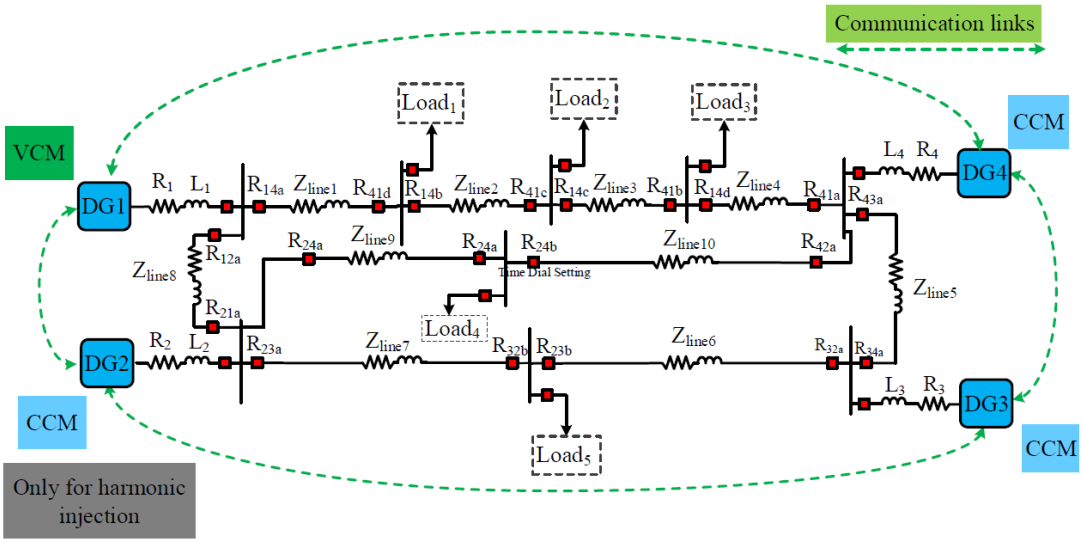

Figure 4-7. Microgrid diagram in [37]

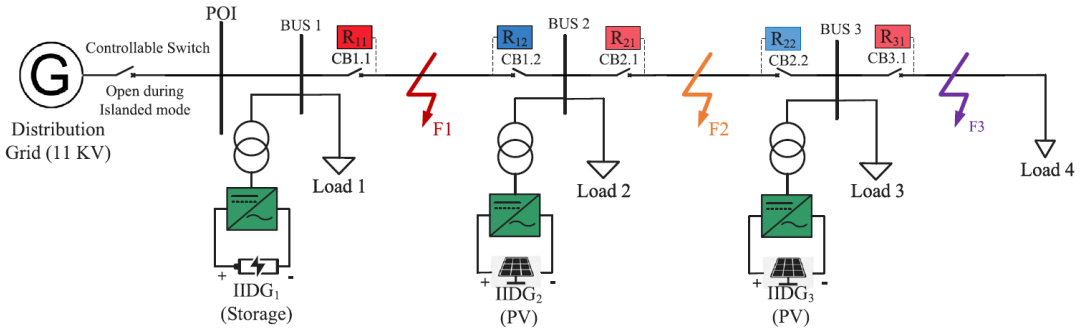

Figure 4-8. Microgrid diagram in [38]

and the communication links are developed between DGs in the microgrid. This protection algorithm has four steps. In step 1, the DG with a minimum terminal voltage was selected to inject specific harmonic currents. In step 2, the relays on the forward side of the injecting DG will trip after certain delays calculated by the IDMT characteristic. In step 3, the CBs will open based on the received tripping signal from step 2. The above three steps are repeated in step 4 to open the breaker on another side of the protected feeder. In [38], the defined time characteristic is implemented to coordinate the relays in the microgrid. The principle of this protection algorithm is explained using the network in Figure 4-8, where the $IIDG_1$, $IIDG_2$ and $IIDG_3$ can inject the 2^{nd}, 3^{rd} and 4^{th} harmonic currents during faults. The settings of all relays are presented in Table 4-1. For example, for the fault F2 in Figure 4-8, the R_{21} will detect the 2^{nd} and 3^{rd} harmonic currents injected by $IIDG_1$, $IIDG_2$, and the R_{22} will detect the

Table 4-1. Relay settings of the proposed scheme in [38]

Relay Group	Relays	Operating Times (s)	Identified Harmonics
Forward Relay Group	R_{11}	0.3	2^{nd}
	R_{21}	0.2	2^{nd} or 3^{rd}
	R_{31}	0.1	2^{nd} or 3^{rd} or 4^{th}
Backward Relay Group	R_{12}	0.1	3^{rd} or 4^{th}
	R_{22}	0.2	4^{th}

4^{th} harmonic currents injected by $IIDG_3$. Based on the relay settings, the R_{21} and R_{22} will trip breakers CB 2.1 and CB 2.2 after 0.2 s delays. The R_{31} and R_{12} cannot detect faults and the R_{11} will trip after 0.3s delays, which is longer than the delays of R_{21}. Unlike the schemes above, where the injected off-normal frequency currents are employed to localise the faulted feeder and coordinate the relays in the microgrid. The algorithm in [39] injects the fifth harmonic currents for fault detection using the criteria proposed in $(4-5)$. In this equation, i_5 and i_1 are the magnitudes of the 5^{th}-order harmonic currents and the fundamental frequency currents and α is the detection threshold. Considering the impacts of the non-linear load, another restraining factor in $(4-6)$ is proposed to avoid the false operation of relays.

$$C_o = \frac{i_5}{i_1} \geq \alpha \qquad (4-5)$$

$$C_r = \frac{i_3 + i_7 + i_9 + i_{11} + i_{13} + i_{15}}{i_1} \leq \beta \qquad (4-6)$$

The main advantage of active protection methods is that they operate based on intentionally designed fault signatures rather than high-magnitude fault currents. Therefore, it is not affected by the reduced system fault level in islanded microgrids [40]. However, this approach modifies the control strategies of IIDGs to cater for the protection requirements, which could distort the inverter's performance from other perspectives and be challenging to realise for inverters from different vendors.

4.4.4 Intelligent Techniques-Based Protection

The intelligent techniques-based approaches are implemented in [41] – [46] to protect microgrids, which detect, classify and isolate faults by training the developed intelligent models. For example, the currents after wavelet analysis and the sequence voltages and currents are used in [41] to train the developed decision tree to detect and classify the faults in microgrids using the structure presented in Figure 4-9. Similar approaches as [41] are implemented in [42] to [45] to protect microgrids by training different intelligent tools, which include the models of the deep neural network in [42], the data mining in [43], the artificial neural network in [44] and the convolutional neural network in [45]. Except for fault detection and classification, the paper [46] uses intelligent techniques to train the protective relays in microgrids, where the differential features of two-end measurements, such as the differential rate of change of frequency and the differential rate of change of voltage, are extracted as inputs of the data mining model to isolate the faulted feeder. However, the performance of intelligent techniques-based protection algorithms significantly depends on the accuracy of the input fault signatures, and it requires substantial amounts of fault data in the training process.

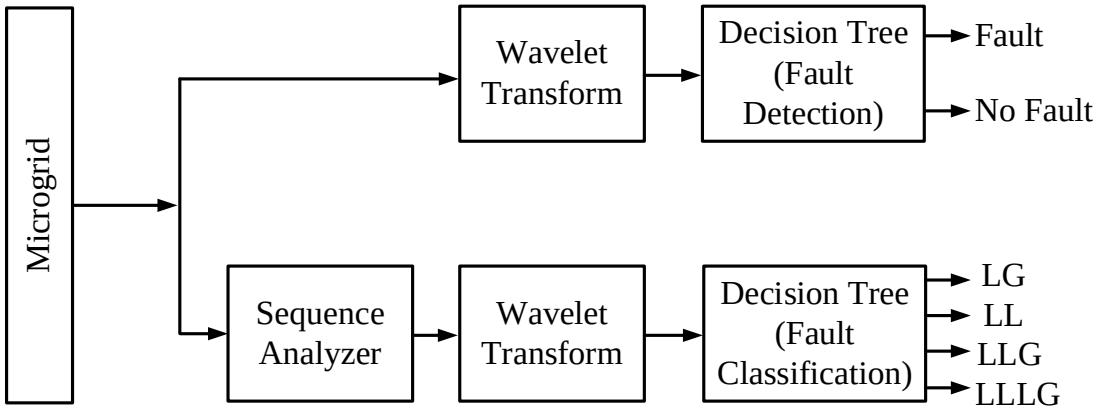

Figure 4-9. Schematic of the protection scheme in [41]

4.4.5 Travelling Wave Protection

As discussed in Section 3.5.3, the travelling wave approach has been widely implemented to protect the high-voltage transmission line owing to its benefits of fast operating speed and independence of generation type and converter control. However, given the features of microgrids, e.g., short feeder length and complicated network

structure, travelling wave protection is rarely to be implemented in distribution systems, especially for LV microgrids. As proposed in [12], the feeders in MV and LV microgrids appear the resistive-dominated feature, which significantly damps the magnitudes of the reflected wavefronts. Therefore, the travelling wave algorithm relying on the reflected wavefront, such as the travelling wave distance protection, is not suggested for microgrid protection.

Microgrid protection using the travelling wave polarity is reported in [47] – [50], where only the information of initial wavefronts is employed. The authors in [47] and [48] propose a protection scheme purely using the polarities of initial current travelling waves. In this algorithm, the mathematical morphology method is applied to extract the polarities of initial travelling waves, where the internal fault is identified when the polarities of initial wavefronts measured by the relays at two terminals of the protected line are the same. The work in [49] distinguishes the faulted feeder and healthy feeder using the relations of the initial current travelling waves at the same busbar as illustrated in $(4-7)$, where n is the number of branches connected to the busbar and

$$\sum_{k=1}^{n} TW_i^k = 0 \qquad (4-7)$$

TW_i^k is the instant current travelling wave through the number k branch. Considering the polarity of faulted feeder is opposite to the healthy feeders connected to the same busbar, the magnitude of the initial current travelling wave of the faulted feeder should equal the sum of current travelling waves in sound feeders at the same busbar. By comparing the travelling wave magnitude, the faulted feeder can be selected. Both initial wavefronts of voltage and current are implemented in [50] to identify the faulted feeder, where the faulted feeder is recognised when the polarities of initial voltage and current travelling waves are opposite. Otherwise, the feeder is healthy.

All solutions above have strict requirements on the sampling frequency of relays to capture the initial wavefront of travelling waves, which makes the implementation of those schemes extremely challenging, especially in the LV microgrids with short feeders. To address this problem and fully use the advantages of high-frequency components-based protection, e.g., less impacted by the fault level variation, generation type and converter control, a transient wavelet energy-based scheme is

proposed in Chapter 6 to protect the microgrids dominated by IIDGs.

4.4.6 Other Types of Protection

Given the limited magnitude of fault current in the islanded microgrid, the authors in [51] developed a voltage-based algorithm to detect and classify faults. In this scheme, the measured voltages at DG terminals are transformed into dq frame by the Park Transform and the error in q axes calculated in $(4-8)$ is employed for fault detection and fault classification. In $(4-8)$, the v_{qref} is the reference voltage and v_q is the measured voltage in q axes. In normal conditions, the value of v_q equals to the reference voltage, which leads to the value of the $v_{error-q}$ approaching zero in normal

$$v_{error-q} = v_{qref} - v_q \qquad (4-8)$$

conditions. In three-phase faults, the values of v_q will reduce and behave as DC constants, which increase the magnitudes of $v_{error-q}$. In asymmetrical faults, the AC ripples with two times the fundamental frequency are superimposed to V_q due to the fault-induced negative sequence voltage. Additionally, it was found that in single-phase-to-ground faults, the values of $v_{error-q}$ oscillate from zero to its maximum value, while in phase-to-phase faults, the $v_{error-q}$ oscillate from a value greater than zero to its maximum value. Based on the fault signatures above, the faults in microgrids can be detected and classified. However, the threshold selection of the proposed scheme is hard and it does not consider the unbalanced nature of LV microgrids. Compared to healthy phases, the faulted-phase voltage contains a high value of Total Harmonic Distortions (THDs), whose magnitude increases with the decrease of the fault distance. According to this principle, a THDs-based method is proposed in [52] to protect the inverter-dominated microgrids. This method requires reliable communication, whose performance depends on the adopted current limiting strategies of IIDGs [53].

In [53][54], fault detection and classification algorithms are developed by analysing the time-domain current waveforms. The transient monitoring function proposed in [55] is implemented to analyse the local current waveforms. In normal conditions, the outputs of the developed transient monitoring function will close to zero. When faults occur in microgrids, a significant increase can be observed from the

function outputs. If the outputs are higher than the defined threshold, the faults can be detected. The author in [54] detects faults using the 'summation of squared three-phase current (SSC)' in $(4-9)$. After processing the SSC by the Teager-Kaiser energy operator (TKEO), the fault detection criterion (FDC) used in this work is developed in $(4-10)$, where $SSC(n)$, $SSC(n-1)$ and $SSC(n-2)$ are the current sample, the sample with one-step delay and the sample with two-step delay respectively. When a fault occurs in the microgrid, the magnitude of FDC in $(4-10)$ will increase to indicate the fault occurrence. This time domain-based protection typically has a fast operating speed as it can directly use the waveform information. However, the performance of this method is impacted by the current limiting strategies of IIDGs and the threshold selection is difficult.

$$SSC = i_A^2(t) + i_B^2(t) + i_C^2(t) \qquad (4-9)$$

$$FDC = |SSC^2(n-1) - SSC(n-2)SSC(n)| \qquad (4-10)$$

4.5 Chapter Summary

In this chapter, the challenges and solutions of microgrid protection are reviewed. Compared to the conventional distribution system, the power flow in microgrids is bidirectional and the fault level of microgrids changes dynamically in grid-connected and islanded modes. Those features cause under/over-reach issues, sympathetic trips, long-delay trips and failed trips of conventional overcurrent relays. To address those issues, some solutions, such as adaptive protection, differential protection, active method-based protection, intelligent techniques-based protection, travelling wave-based protection and other protection methods, are proposed in the literature. The key advantages and limitations of those solutions are summarised below to facilitate the understanding and selection of those methods.

- *Adaptive protection:* in adaptive protection, the settings of protection devices change adaptively according to the prevailing system condition to address the varied fault levels of microgrids. However, real-time monitoring and reliable communication are required in adaptive protection. Therefore, it needs high investments.

- *Differential protection:* differential protection operates based on the current difference measured at both ends of the protected line, which is less sensitive to fault level variation and bidirectional power flow. However, synchronised measurement and high-bandwidth communication channels are needed in differential protection schemes, which increases the protection cost.
- *Active method-based protection:* the active methods protect microgrids by injecting the off-normal frequency components during faults. The main advantage of this method is that the IIDGs could create fault signatures intentionally according to the protection requirements. However, the specially designed control algorithm of IIDGs could violate the other control objectives, such as the capability of the fast fault current injection.
- *Intelligent techniques-based protection:* in intelligent techniques-based protection, the faults are detected and classified by training the developed intelligent models, e.g., data mining, neural network, etc. This approach needs substantial training data and has high requirements on the implemented hardware platform.
- *Travelling wave protection:* Compared to other protection schemes, travelling wave protection is rarely implemented to protect microgrids due to the high sampling frequency of relays. However, it provides a promising solution as its performance is unaffected by the fault level variation, generation type and inverter control. To fully use the benefits of travelling wave-based protection, which has a fast operating speed and is unaffected by the generator types and control strategies of converter/inverter-based resources, and avoid the limitation of the high sampling frequency, a transient wavelet energy-based protection scheme is proposed in Chapter 6 to protect the microgrids dominated by IIDGs.

4.6 Chapter References

[1] V. K. Garg and S. Sharma, "Overview on Microgrid System," *2018 Fifth International Conference on Parallel, Distributed and Grid Computing (PDGC)*, 2018, pp. 694-699.

[2] N. Hatziargyriou, H. Asano, R. Iravani and C. Marnay, "Microgrids," in *IEEE*

Power and Energy Magazine, vol. 5, no. 4, pp. 78-94, July-Aug. 2007.

[3] X. Zhou, T. Guo and Y. Ma, "An overview on microgrid technology," *2015 IEEE International Conference on Mechatronics and Automation (ICMA)*, 2015, pp. 76-81.

[4] R. H. Lasseter and P. Paigi, "Microgrid: a conceptual solution," *2004 IEEE 35th Annual Power Electronics Specialists Conference (IEEE Cat. No.04CH37551)*, 2004, pp. 4285-4290 Vol.6.

[5] F. Katiraei, R. Iravani, N. Hatziargyriou and A. Dimeas, "Microgrids management," in *IEEE Power and Energy Magazine*, vol. 6, no. 3, pp. 54-65, May-June 2008.

[6] B. Kroposki, T. Basso and R. DeBlasio, "Microgrid standards and technologies," *2008 IEEE Power and Energy Society General Meeting - Conversion and Delivery of Electrical Energy in the 21st Century*, 2008, pp. 1-4.

[7] E. Hossain, E. Kabalci, R. Bayindir and R. Perez, "Microgrid testbeds around the world: State of art", in *Energy Conversion and Management*, vol. 86, pp. 132-153, 2014.

[8] X. Li, A. Dyśko and G. M. Burt, "Traveling Wave-Based Protection Scheme for Inverter-Dominated Microgrid Using Mathematical Morphology," in *IEEE Transactions on Smart Grid*, vol. 5, no. 5, pp. 2211-2218, Sept. 2014.

[9] S. Papathanassiou, H. Nikos, and S. Kai, “A benchmark low voltage microgrid network,” *Proc. CIGRE Symp. power Syst. with dispersed Gener.*, 2005, pp. 1–8.

[10] A. Hooshyar, M. A. Azzouz and E. F. El-Saadany, "Distance Protection of Lines Emanating From Full-Scale Converter-Interfaced Renewable Energy Power Plants—Part I: Problem Statement," in *IEEE Transactions on Power Delivery*, vol. 30, no. 4, pp. 1770-1780, Aug. 2015.

[11] S. Tan, Y. Wu, P. Xie, J. M. Guerrero, J. C. Vasquez and A. Abusorrah, "New Challenges in the Design of Microgrid Systems: Communication Networks, Cyberattacks, and Resilience," in *IEEE Electrification Magazine*, vol. 8, no. 4, pp. 98-106, Dec. 2020.

[12] X. Li, "Enhanced Control and Protection for Inverter Dominated Microgrids," Ph.D dissertation, Department of Electronic and Electrical Engineering, University of Strathclyde, Glasgow, UK, 2014.

[13] V. A. Papaspiliotopoulos, G. N. Korres, V. A. Kleftakis and N. D. Hatziargyriou, "Hardware-In-the-Loop Design and Optimal Setting of Adaptive Protection Schemes for Distribution Systems With Distributed Generation," in *IEEE Transactions on Power Delivery*, vol. 32, no. 1, pp. 393-400, Feb. 2017.

[14] M. Vitins, "A Fundamental Concept for High Speed Relaying," in *IEEE Transactions on Power Apparatus and Systems*, vol. PAS-100, no. 1, pp. 163-173, Jan. 1981.

[15] G. Benmouy and J. Roberts, "Superimposed quantities: Their true nature and application in relays, Schweitzer Engineering Laboratories," Inc. Pullman, WA USA, SEL USA, vol. 199, 1999.

[16] B. Patnaik, M. Mishra, R. Bansal and R. Jena, "AC microgrid protection – A review: Current and future prospective", in *Applied Energy*, vol. 271, p. 115210, 2020.

[17] V. Telukunta, J. Pradhan, A. Agrawal, M. Singh and S. G. Srivani, "Protection challenges under bulk penetration of renewable energy resources in power systems: A review," in *CSEE Journal of Power and Energy Systems*, vol. 3, no. 4, pp. 365-379, Dec. 2017.

[18] R. Haron, A. Mohamed, H. Shareef and H. Zayandehroodi, "Analysis and solutions of overcurrent protection issues in a microgrid," *2012 IEEE International Conference on Power and Energy (PECon)*, 2012, pp. 644-649.

[19] A. Dagar, P. Gupta and V. Niranjan, "Microgrid protection: A comprehensive review", in *Renewable and Sustainable Energy Reviews*, vol. 149, p. 111401, 2021.

[20] G. Buigues, A. Dysko, V. Valverde, I. Zamora, and E. Fernandez, "Microgrid protection: Technical challenges and existing techniques," *Proc. Int. Conf. Renew. Energies Power Quality*, Bilbao, Spain, Mar. 2013, pp. 222–227.

[21] Network Protection and Automation Guide Protective Relays, Measurements and Control, Alstom Grid, Saint-Ouen, France, 2011.

[22] S. M. Brahma and A. A. Girgis, "Development of adaptive protection scheme for distribution systems with high penetration of distributed generation," in *IEEE Transactions on Power Delivery*, vol. 19, no. 1, pp. 56-63, Jan. 2004.

[23] P. Mahat, Z. Chen, B. Bak-Jensen and C. L. Bak, "A Simple Adaptive

Overcurrent Protection of Distribution Systems With Distributed Generation," in *IEEE Transactions on Smart Grid*, vol. 2, no. 3, pp. 428-437, Sept. 2011.

[24] A. Abdelaziz, H. Talaat, A. Nosseir and A. Hajjar, "An adaptive protection scheme for optimal coordination of overcurrent relays", in *Electric Power Systems Research*, vol. 61, no. 1, pp. 1-9, 2002.

[25] F. Coffele, C. Booth and A. Dyśko, "An Adaptive Overcurrent Protection Scheme for Distribution Networks," in *IEEE Transactions on Power Delivery*, vol. 30, no. 2, pp. 561-568, April 2015.

[26] H. Wan, K. K. Li and K. P. Wong, "An Adaptive Multiagent Approach to Protection Relay Coordination With Distributed Generators in Industrial Power Distribution System," in *IEEE Transactions on Industry Applications*, vol. 46, no. 5, pp. 2118-2124, Sept.-Oct. 2010.

[27] M. Ataei and M. Gitizadeh, "A distributed adaptive protection scheme based on multi-agent system for distribution networks in the presence of distributed generations", in *IET Generation, Transmission & Distribution*, vol. 16, no. 8, pp. 1521-1540, 2021.

[28] M. Dewadasa, A. Ghosh and G. Ledwich, "Protection of microgrids using differential relays," *AUPEC 2011*, 2011, pp. 1-6.

[29] E. Sortomme, S. S. Venkata and J. Mitra, "Microgrid Protection Using Communication-Assisted Digital Relays," in *IEEE Transactions on Power Delivery*, vol. 25, no. 4, pp. 2789-2796, Oct. 2010.

[30] S. R. Samantaray, G. Joos and I. Kamwa, "Differential energy based microgrid protection against fault conditions," *2012 IEEE PES Innovative Smart Grid Technologies (ISGT)*, 2012, pp. 1-7.

[31] S. Kar and S. Samantaray, "Time-frequency transform-based differential scheme for microgrid protection", in *IET Generation, Transmission & Distribution*, vol. 8, no. 2, pp. 310-320, 2014.

[32] A. Langarizadeh and S. Hasheminejad, "A new differential algorithm based on S-transform for the micro-grid protection", in *Electric Power Systems Research*, vol. 202, p. 107590, 2022.

[33] A. Gururani, S. Mohanty and J. Mohanta, "Microgrid protection using Hilbert–Huang transform based-differential scheme", in *IET Generation, Transmission &*

Distribution, vol. 10, no. 15, pp. 3707-3716, 2016.

[34] A. Anand and S. Affijulla, "Ensemble empirical mode decomposition-based differential protection scheme for islanded and grid-tied AC microgrid", in *IET Generation, Transmission & Distribution*, vol. 14, no. 26, pp. 6674-6681, 2020.

[35] B. Chaitanya, A. Yadav and M. Pazoki, "An improved differential protection scheme for micro-grid using time-frequency transform", in *International Journal of Electrical Power & Energy Systems*, vol. 111, pp. 132-143, 2019.

[36] A. Soleimanisardoo, H. Kazemi Karegar and H. H. Zeineldin, "Differential Frequency Protection Scheme Based on Off-Nominal Frequency Injections for Inverter-Based Islanded Microgrids," in *IEEE Transactions on Smart Grid*, vol. 10, no. 2, pp. 2107-2114, March 2019.

[37] S. Beheshtaein, R. Cuzner, M. Savaghebi and J. M. Guerrero, "A New Harmonic-based Protection structure for Meshed Microgrids," *2018 IEEE Power & Energy Society General Meeting (PESGM)*, 2018, pp. 1-6.

[38] M. Khan, Q. Hong, A. Egea-Àlvarez, A. Dyśko and C. Booth, "A communication-free active unit protection scheme for inverter dominated islanded microgrids", in *International Journal of Electrical Power & Energy Systems*, vol. 142, p. 108125, 2022.

[39] Z. Chen, X. Pei, M. Yang, L. Peng and P. Shi, "A Novel Protection Scheme for Inverter-Interfaced Microgrid (IIM) Operated in Islanded Mode," in *IEEE Transactions on Power Electronics*, vol. 33, no. 9, pp. 7684-7697, Sept. 2018.

[40] Z. Chen, X. Pei and L. Peng, "Harmonic Components based Protection Strategy for Inverter-Interfaced AC Microgrid," *2016 IEEE Energy Conversion Congress and Exposition (ECCE)*, 2016, pp. 1-6.

[41] D. P. Mishra, S. R. Samantaray and G. Joos, "A Combined Wavelet and Data-Mining Based Intelligent Protection Scheme for Microgrid," in *IEEE Transactions on Smart Grid*, vol. 7, no. 5, pp. 2295-2304, Sept. 2016.

[42] J. J. Q. Yu, Y. Hou, A. Y. S. Lam and V. O. K. Li, "Intelligent Fault Detection Scheme for Microgrids With Wavelet-Based Deep Neural Networks," in *IEEE Transactions on Smart Grid*, vol. 10, no. 2, pp. 1694-1703, March 2019.

[43] S. Baloch and M. S. Muhammad, "An Intelligent Data Mining-Based Fault Detection and Classification Strategy for Microgrid," in *IEEE Access*, vol. 9, pp.

22470-22479, 2021.

[44] Y. Hong and M. T. A. M. Cabatac, "Fault Detection, Classification, and Location by Static Switch in Microgrids Using Wavelet Transform and Taguchi-Based Artificial Neural Network," in *IEEE Systems Journal*, vol. 14, no. 2, pp. 2725-2735, June 2020.

[45] S. Bukhari, C. Kim, K. Mehmood, R. Haider and M. Saeed Uz Zaman, "Convolutional Neural Network-Based Intelligent Protection Strategy for Microgrids", in *IET Generation, Transmission & Distribution*, vol. 14, no. 7, pp. 1177-1185, 2020.

[46] S. Kar, S. R. Samantaray and M. D. Zadeh, "Data-Mining Model Based Intelligent Differential Microgrid Protection Scheme," in *IEEE Systems Journal*, vol. 11, no. 2, pp. 1161-1169, June 2017.

[47] X. Li, A. Dyśko and G. Burt, "Enhanced protection for inverter dominated microgrid using transient fault information," *11th IET International Conference on Developments in Power Systems Protection (DPSP 2012)*, 2012, pp. 1-5.

[48] X. Li, A. Dyśko and G. M. Burt, "Traveling Wave-Based Protection Scheme for Inverter-Dominated Microgrid Using Mathematical Morphology," in *IEEE Transactions on Smart Grid*, vol. 5, no. 5, pp. 2211-2218, Sept. 2014.

[49] S. Shi, B. Jiang, X. Dong and Z. Bo, "Protection of microgrid," *10th IET International Conference on Developments in Power System Protection (DPSP 2010)*, 2010, pp. 1-4.

[50] X. Dong, J. Wang, S. Shi, B. Wang, B. Dominik and M. Redefern, "Traveling Wave based Single-Phase-to-Ground Protection Method for Power Distribution System," in *CSEE Journal of Power and Energy Systems*, vol. 1, no. 2, pp. 75-82, June 2015.

[51] H. Al-Nasseri, M. A. Redfern and F. Li, "A Voltage based Protection for Micro-grids Containing Power Electronic Converters," *2006 IEEE Power Engineering Society General Meeting*, 2006, pp. 1-7.

[52] H. Al-Nasseri and M. A. Redfern, "Harmonics Content based Protection Scheme for Micro-grids Dominated by Solid State Converters," *2008 12th International Middle-East Power System Conference*, 2008, pp. 50-56.

[53] I. Sadeghkhani, M. E. Hamedani Golshan, A. Mehrizi-Sani, J. M. Guerrero and

A. Ketabi, "Transient Monitoring Function–Based Fault Detection for Inverter-Interfaced Microgrids," in *IEEE Transactions on Smart Grid*, vol. 9, no. 3, pp. 2097-2107, May 2018.

[54] M. A. Jarrahi, H. Samet and T. Ghanbari, "Novel Change Detection and Fault Classification Scheme for AC Microgrids," in *IEEE Systems Journal*, vol. 14, no. 3, pp. 3987-3998, Sept. 2020.

[55] A. G. Phadke and J. S. Thorp, *Computer Relaying for Power Systems*. Chichester, U.K.: Wiley, 2009.

Chapter 5

5 Novel Sequence Components - based Distance Protection for Transmission Line Connected to Converter - Based Resources

5.1 Introduction

As demonstrated in Chapter 3, the distance relay at the converter side can become unreliable owing to the issues of inaccurate impedance measurement, failed faulted phase selection and unstable impedance measurement, which significantly compromises the distance protection performance. So far, most of the existing research neglects the performance of the distance relay at the remote end of the protected line since they constantly assume the remote-end AC network is a strong power system (i.e., SCR≫3). However, this assumption is unlikely to hold in the future due to the increased penetration of CBRs and long-distance power transmission. Therefore, protection issues of distance relay at the grid side will be the main focus of this chapter.

Following the GB grid code, only the positive sequence components are required to be injected during faults from the CBRs, which is useful to conduct the sequence analysis since the negative sequence network at the converter side behaves as an open circuit. In this chapter, a novel sequence component-based distance protection logic is proposed, where an accurate fault distance measuring element is developed for the relay at the grid side. Compared to the conventional impedance-based distance measurement algorithm, the proposed method can protect the asymmetrical faults with varied types, fault resistances, fault locations, fault levels and lengths of the protected

line. The proposed scheme can be embedded into the hardware platform of modern distance relays without needing to change the existing hardware arrangement. Therefore, it provides an economical solution.

This chapter is structured as follows. The fundamentals of symmetrical components analysis are presented in Section 5.2. The development of the proposed sequence components-based distance protection is proposed in Section 5.3. The case studies used to evaluate the performance of the proposed scheme are presented in Section 5.4, and the chapter summary is proposed in Section 5.5.

5.2 Fundamentals of Symmetrical Components-Based Analysis

5.2.1 Sequence Components

The idea of symmetrical analysis was proposed by Fortescue in 1918, where the author suggested that any set of unbalanced phasors can be represented as the superimposition of a set of balanced phasors [1]. This idea was further extended by electrical engineers to investigate the unbalanced operation of the power system and asymmetrical faults [2], which is named 'symmetrical analysis'.

In the method of symmetrical analysis, a three-phase system can be represented as the linear combination of three balanced components, namely positive, negative and zero sequence components [3]. The diagrams of those sequence components are presented in Figure 5-1 [4], where the positive and negative sequence components rotate in the direction of ABC and ACB and the zero sequence components are in phase. The equations to connect the components in the phasor domain and sequence domain are presented in $(5-1)$ and $(5-2)$, where i_a, i_b and i_c are the three-phase

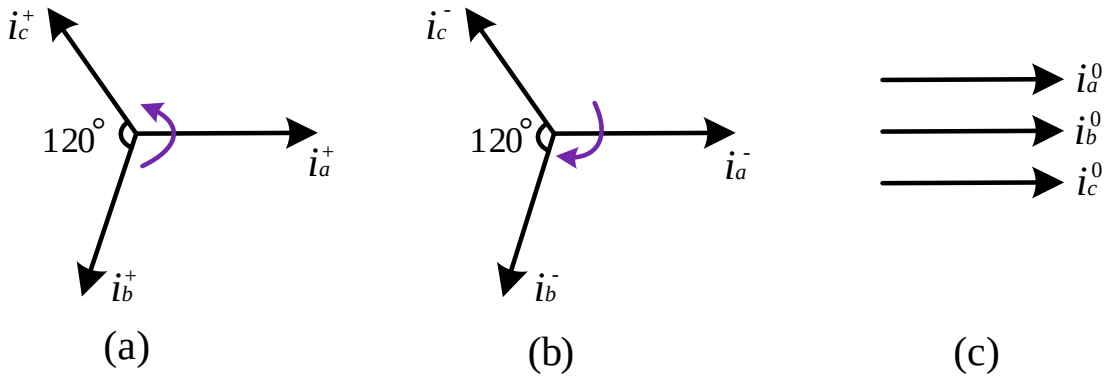

Figure 5-1. Diagrams of, (a) positive, (b) negative, and (c) zero sequence components [4]

currents; i_0, i^+ and i^- are the zero, positive and negative sequence currents; α and α^2 are the rotating vectors by 120° and 240° anticlockwise. The relations in $(5-1)$ and $(5-2)$ are also available for the system voltages as presented in $(5-3)$ and $(5-4)$.

$$\begin{bmatrix} i_a \\ i_b \\ i_c \end{bmatrix} = \begin{bmatrix} 1 & 1 & 1 \\ 1 & \alpha^2 & \alpha \\ 1 & \alpha & \alpha^2 \end{bmatrix} \begin{bmatrix} i_0 \\ i^+ \\ i^- \end{bmatrix} \quad (5-1)$$

$$\begin{bmatrix} i_0 \\ i^+ \\ i^- \end{bmatrix} = \frac{1}{3} \begin{bmatrix} 1 & 1 & 1 \\ 1 & \alpha & \alpha^2 \\ 1 & \alpha^2 & \alpha \end{bmatrix} \begin{bmatrix} i_a \\ i_b \\ i_c \end{bmatrix} \quad (5-2)$$

$$\begin{bmatrix} v_a \\ v_b \\ v_c \end{bmatrix} = \begin{bmatrix} 1 & 1 & 1 \\ 1 & \alpha^2 & \alpha \\ 1 & \alpha & \alpha^2 \end{bmatrix} \begin{bmatrix} v_0 \\ v^+ \\ v^- \end{bmatrix} \quad (5-3)$$

$$\begin{bmatrix} v_0 \\ v^+ \\ v^- \end{bmatrix} = \frac{1}{3} \begin{bmatrix} 1 & 1 & 1 \\ 1 & \alpha & \alpha^2 \\ 1 & \alpha^2 & \alpha \end{bmatrix} \begin{bmatrix} v_a \\ v_b \\ v_c \end{bmatrix} \quad (5-4)$$

In those equations, the phase-a phasor was selected as the base [4], while the different converting matrixes can be derived using the bases of phase b or phase c [3]. The selection of bases depends on the analysed type of faults. For example, the base of phase a is used to investigate the AG, BC and BCG faults. The base of phase b is used to study the BG, CA and CAG faults and the base of phase c is applied for the CG, AB and ABG faults. The proposed method in Section 5.3 can also be extended to phase b and phase c bases.

5.2.2 Sequence Networks During Faults

As reported in Section 5.2.1, the three-phase vectors in the phase domain can be represented by the positive, negative and zero sequence components, which provides a powerful tool to simplify the analysis of unbalanced faults. Each sequence component has its sequence network, namely positive, negative and zero sequence networks, which exist independently when the system is in balanced condition [4]. Those independent sequence networks are connected during faults based on their inherent relations [5]. Such relations can be derived using the boundary conditions in the phase domain as illustrated in [6].

The boundary conditions of AG faults (single-phase-to-ground faults) in the phase

domain are presented in $(5-5)$ and $(5-6)$, where R_F is the fault resistance. After substituting $(5-5)$ to $(5-2)$, the matrix of $(5-7)$ is obtained. Based on $(5-7)$, the relations of the positive, negative and zero sequence currents in AG faults can be illustrated by $(5-8)$. The relation between the sequence voltages and currents is presented in $(5-9)$, which is derived by substituting the expressions of v_a, i.e., $v_a = v_0 + v^+ + v^-$, and i_a, i.e., $i_a = 3i_0 = 3i^+ = 3i^-$, to the boundary condition in $(5-6)$. According to $(5-8)$ and $(5-9)$, it was found that the positive, negative and zero sequence networks are connected in series in AG faults as presented in Figure 5-2 (a), where 'N1', 'N2' and 'N0' represent the positive, negative and zero sequence networks respectively.

$$i_b = i_c = 0 \tag{5-5}$$

$$v_a = i_a R_F \tag{5-6}$$

$$\begin{bmatrix} i_0 \\ i^+ \\ i^- \end{bmatrix} = \frac{1}{3}\begin{bmatrix} 1 & 1 & 1 \\ 1 & \alpha & \alpha^2 \\ 1 & \alpha^2 & \alpha \end{bmatrix}\begin{bmatrix} i_a \\ 0 \\ 0 \end{bmatrix} \tag{5-7}$$

$$i_0 = i^+ = i^- = \frac{1}{3} i_a \tag{5-8}$$

$$v_0 + v^+ + v^- = i^+(3R_F) = i^-(3R_F) = i_0(3R_F) \tag{5-9}$$

The boundary conditions of BC faults (phase-to-phase faults) in the phase domain are presented in $(5-10)$ to $(5-12)$. After substituting the conditions in $(5-10)$ and $(5-11)$ to $(5-2)$, the matrix of $(5-13)$ can be derived. From $(5-13)$, the relations of sequence currents in BC fault are presented in $(5-14)$ and $(5-15)$. The relation between the sequence voltages and currents is presented in $(5-16)$, which is derived by substituting the expressions of v_b, i.e., $v_0 + \alpha^2 v^+ + \alpha v^-$, v_c, i.e., $v_0 + \alpha v^+ + \alpha^2 v^-$ and i_b, i.e., $i_0 + \alpha^2 i^+ + \alpha i^-$, to the boundary condition in $(5-12)$. Given the fact that the zero sequence network is disconnected in BC faults, i.e., $i_0 = 0$, the magnitude of zero sequence voltage, i.e., v_0, is zero. Based on $(5-15)$ and$(5-16)$, it was found that the BC faults only comprise the positive and negative sequence networks and those two networks are connected in parallel as presented in Figure 5-2 (b).

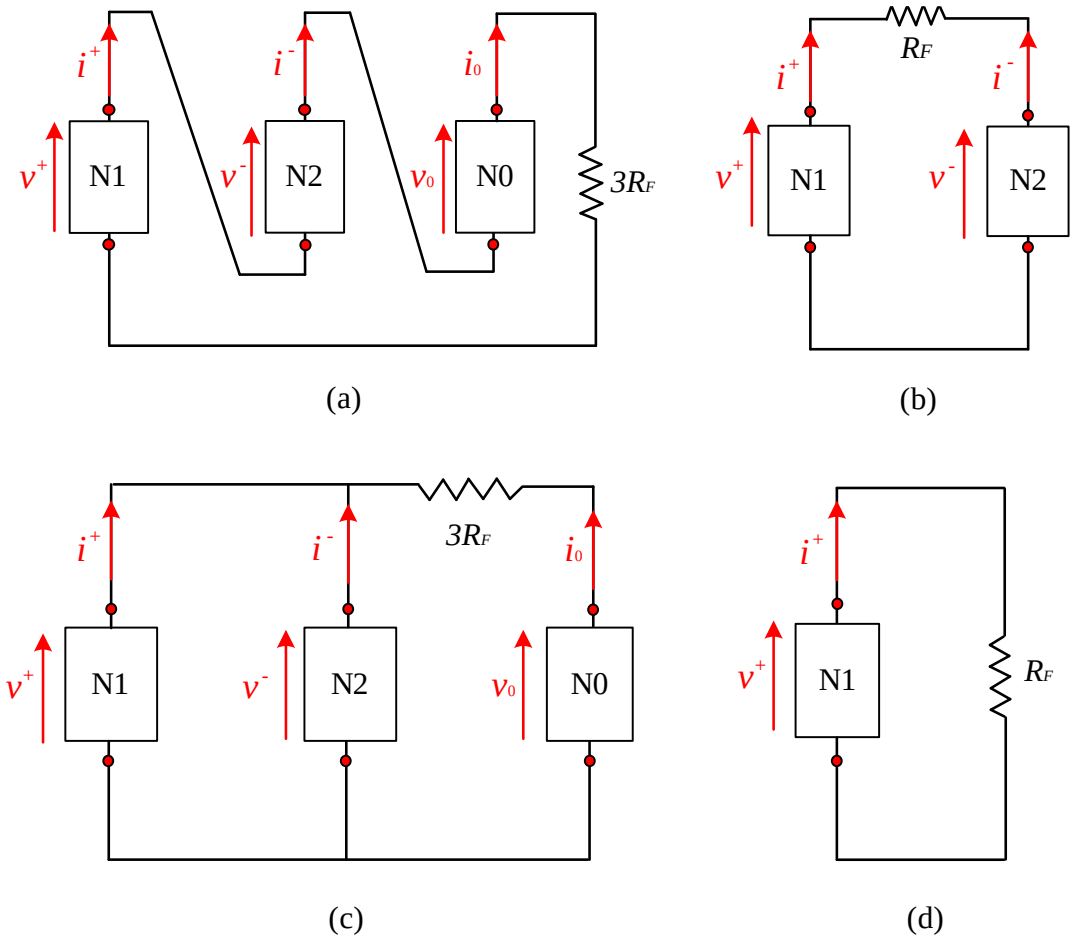

Figure 5-2. Sequence network connections of, (a) AG faults (single-phase-to-ground faults), (b) BC faults (phase-to-phase faults), (c) BCG faults (phase-to-phase-to-ground faults), (d) ABC/ABCG faults (balanced faults) [3]

$$i_a = 0 \qquad (5-10)$$

$$i_b = -i_c \qquad (5-11)$$

$$v_b - v_c = i_b R_F \qquad (5-12)$$

$$\begin{bmatrix} i_0 \\ i^+ \\ i^- \end{bmatrix} = \frac{1}{3}\begin{bmatrix} 1 & 1 & 1 \\ 1 & \alpha & \alpha^2 \\ 1 & \alpha^2 & \alpha \end{bmatrix}\begin{bmatrix} 0 \\ i_b \\ -i_b \end{bmatrix} \qquad (5-13)$$

$$i_0 = 0 \qquad (5-14)$$

$$i^+ = -i^- \qquad (5-15)$$

$$v^+ - v^- = i^+ R_F \qquad (5-16)$$

The boundary conditions of BCG faults (phase-to-phase-to-ground faults) in the phase domain are presented in $(5-17)$ and $(5-18)$. After substituting the boundary condition in $(5-17)$ to $(5-1)$, the relation between sequence currents is presented in $(5-19)$. As the phase b voltage equals the phase c voltage in BCG fault as presented in $(5-18)$, the equation of $(5-20)$ can be obtained. That condition in $(5-18)$, i.e., $v_b = (i_b + i_c)R_F$, can be applied together with the results in $(5-19)$ and $(5-20)$ to get the voltage relations between the zero and positive sequence networks as displayed in $(5-21)$. According to $(5-19)$ to $(5-21)$, it was found that the positive, negative and zero sequence networks all exist and are connected in parallel in BCG faults as presented in Figure 5-2 (c).

$$i_a = 0 \tag{5-17}$$

$$v_b = v_c = (i_b + i_c)R_F \tag{5-18}$$

$$i^+ + i^- + i_0 = 0 \tag{5-19}$$

$$v^+ = v^- \tag{5-20}$$

$$v_0 - v^+ = 3i_0R_F \tag{5-21}$$

Since the fault currents and voltages keep balanced in ABC and ABCG faults (i.e., with the same magnitude and 120° phase shift between the neighbouring phases), only the positive sequence components will exist in the balanced fault conditions as presented in Figure 5-2 (d).

5.3 Proposed Sequence Components-Based Distance Measuring Element

5.3.1 Issues of Distance Relays at Grid Side

A typical transmission line connected to the CBR is presented in Figure 5-3, where the converter is interfaced with the transmission system by a star/delta-connected transformer. In this study, the control strategy of the converter is designed according to the requirements presented in the GB grid code, i.e., only supply the positive sequence current and inject the reactive current based on the equation of $(2-22)$.

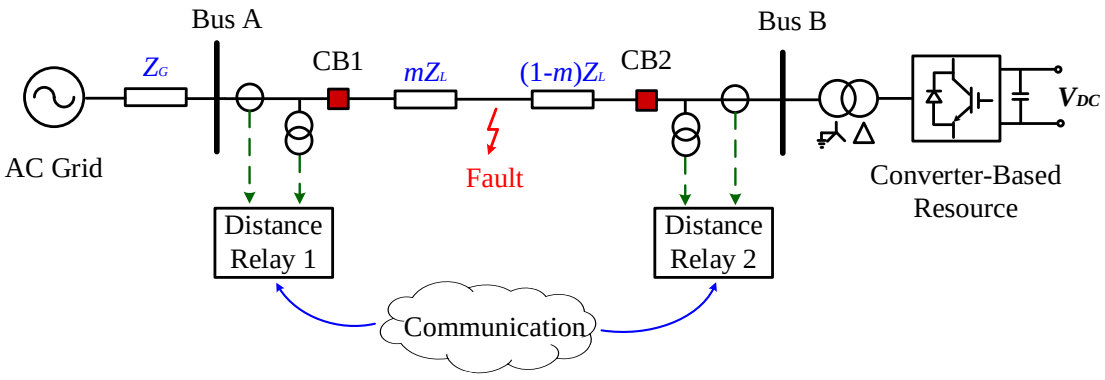

Figure 5-3. Transmission network with a line connected to converter-based resource

Based on the best knowledge of the author, the current research focuses on evaluating and improving the performance of distance relay at the converter side [7] - [15], where the connected AC system on the remote end of CBRs is typically assumed to be a strong power system with $SCR \gg 3$. By implementing the KVL from the fault point to the locations of Distance Relay 1 (DR1) and Distance Relay 2 (DR2) in Figure 5-3, the impedance measured by two distance relays can be described by $(5-22)$ and $(5-23)$, where Z_{DR1} and Z_{DR2} are the impedances measured by the DR1 and DR2 respectively; m is the fraction of the line length representing the distance between Busbar A and fault location; Z_L is the total line impedance; i_{Grid} and i_{CBR} are the fault

$$Z_{DR1} = mZ_L + \left(1 + \frac{i_{CBR}}{i_{Grid}}\right) R_F \qquad (5-22)$$

$$Z_{DR2} = (1-m)Z_L + \left(1 + \frac{i_{Grid}}{i_{CBR}}\right) R_F \qquad (5-23)$$

infeeds from the grid and converter sides, and R_F is the fault resistance. From $(5-23)$, when the magnitude of i_{Grid} is significantly higher than the current infeed from CBRs, i.e., i_{CBR}, the error of reactance measurement raised by the combined effect of $\frac{i_{CBR}}{i_{Grid}}$ and R_F is negligible, which results in the distance relay at the grid side being significantly unaffected by the under/over-reach issues. However, with the increased penetration of non-synchronous generation, the fault level of the connected AC system can be significantly reduced, which leads to potentially severe under/over-reach issues for the relay at the grid side.

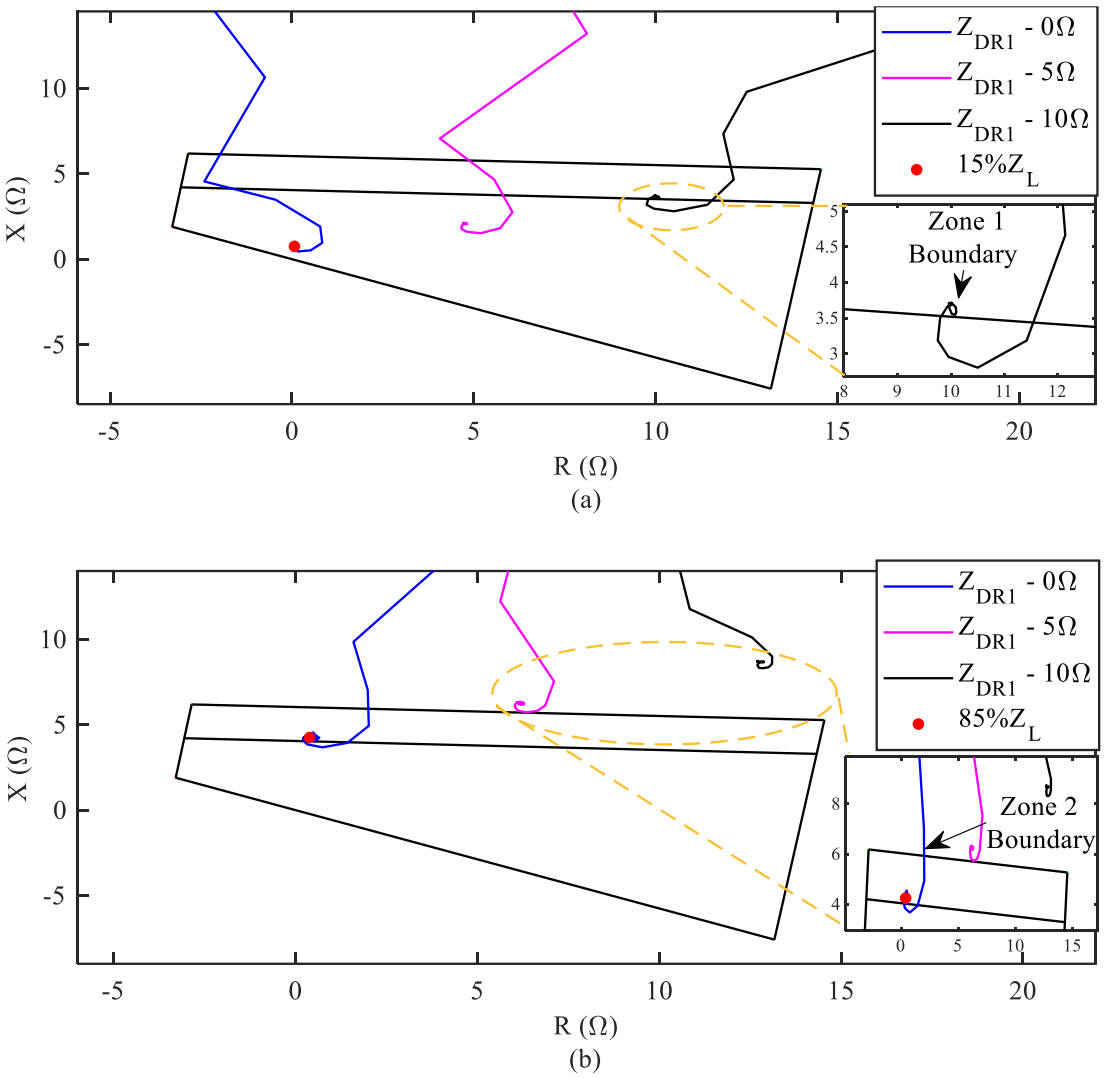

Figure 5-4. Impedance locus of DR1for AG faults at, (a) 15 % of the line, (b) 85 % of the line

To illustrate the above analysis, where the DR1 has a high potential to fail, several simulation case studies are conducted in this section using the RTDS to evaluate the relay performance in the presence of a weak system (SCR=2.5), where the single-phase-to-ground faults (most frequent in nature) are applied in the network in Figure 5-3; the parameters of the protected line are presented in Table 3-4 and the protection settings of DR1 and DR2 are presented in Table 3-6. The faults are applied at 15% and 85% of the line. Since the resistive reach setting for the distance relay is 14 Ω (primary value), the fault resistances of 0 Ω, 5 Ω and 10 Ω are selected to ensure the protection issues are mainly raised by the connection of CBR rather than the high fault resistance.

The simulation results are presented in Figure 5-4, where the '$Z_{DR1} - 0\ \Omega$', '$Z_{DR1} - 5\ \Omega$' and '$Z_{DR1} - 10\ \Omega$' are the measured impedance locus of DR1 in the

faults with 0 Ω, 5 Ω and 10 Ω resistance and the 15%Z_L and 85%Z_L are the accurate impedance of DR1 for the faults at 15% and 85% of the protected line, which equals 0.07+ j0.75 Ω and 0.39+j4.25 Ω respectively. The impedance locus in Figure 5-4 refers to the primary-side values of distance relays. According to the simulation results, for faults at 15% of the protected line, the DR1 can detect the fault distance accurately when bolted fault occurs, where the measured impedance equals the accurate impedance based on the calculation. However, when the fault resistance increases to 5 Ω, the locus of DR1 will suffer from the over-reach issue and it will be out of Zone 1 when the fault resistance increases to 10 Ω. For the results of faults at 85% of the line, the DR1 cannot detect faults with 5 Ω and 10 Ω resistance since the measured impedance locus is out of its protective zone, which leads to the protection failure of DR1.

In distance protection, the relay tripping time depends on which zone is activated during the fault. For the fault in Zone 1 (typically set to 80 % of the total length of the protected line), the relay will trip instantaneously once the fault is detected, while an intentional delay, e.g., 400 ms, is implemented to the fault detected in Zone 2 to coordinate with the other relays in the transmission system. To avoid the delay of Zone 2 protection, the inter-tripping algorithm is conventionally implemented in a real application to accelerate the isolation of internal faults [16]. One of the commonly inter-tripping schemes is called the 'permissive tripping scheme' [6], where the relay detecting the fault in Zone 1 will send an inter-tripping signal to the remote-end relay and both relays will trip when the relay receiving the inter-trip signal also detects the fault in its Zone 2 range. According to the simulation results, the 'permissive tripping scheme' has a long tripping delay for a 10 Ω resistive fault at 15% of the line and it will fail to trip for a fault at 85% with 5 Ω and 10 Ω resistance. To address the aforementioned reach issues of the distance relay at the grid side and the potential failure of the inter-tripping algorithm, a new sequence components-based distance measuring element is presented in Section 5.3.2 for the distance relay at the grid side and its performance is evaluated in Section 5.4.

5.3.2 Sequence Component–Based Impedance Measuring Element

According to the conclusions in Section 5.2.2, the sequence networks for the transmission system in Figure 5-3 in different types of asymmetrical faults are

presented in Figure 5-5 to Figure 5-7 [5][10], where Z_{CBR}^{+}, Z_{CBR}^{-}, Z_{CBR}^{0} are the positive, negative and zero sequence internal impedances of converter; Z_{tr}^{+}, Z_{tr}^{-}, Z_{tr}^{0} are the positive, negative and zero sequence impedances of the transformer; Z_{L}^{+}, Z_{L}^{-}, Z_{L}^{0} are the positive, negative and zero sequence impedances of the protected line; Z_{G}^{+}, Z_{G}^{-}, Z_{G}^{0} are the positive, negative and zero sequence impedances of the connected AC grid; v_{DR1}^{+}, v_{DR1}^{-}, v_{DR1}^{0} are the positive, negative and zero sequence voltages of the three phase voltages measured by DR1; v_{DR2}^{+}, v_{DR2}^{-}, v_{DR2}^{0} are the positive, negative and zero sequence voltages of the three phase voltages measured by DR2; v_{F}^{+}, v_{F}^{-}, v_{F}^{0} are the positive, negative and zero sequence voltages at the fault points; v_{G}^{+} is the positive sequence grid voltage equalling the nominal phase voltage; i_{CBR}^{+}, i_{CBR}^{-} are the positive and negative sequence currents generated by CBRs; i_{tr}^{0} is the zero sequence current flowing through the star side of the isolating transformer between CBRs and connected transmission line; i_{F}^{+}, i_{F}^{-}, i_{F}^{0} are the positive, negative and zero sequence currents at the fault point; i_{G}^{+}, i_{G}^{-}, i_{G}^{0} are the positive, negative and zero sequence currents at the grid side; m is the percentage value of the fault position and R_F is the fault resistance.

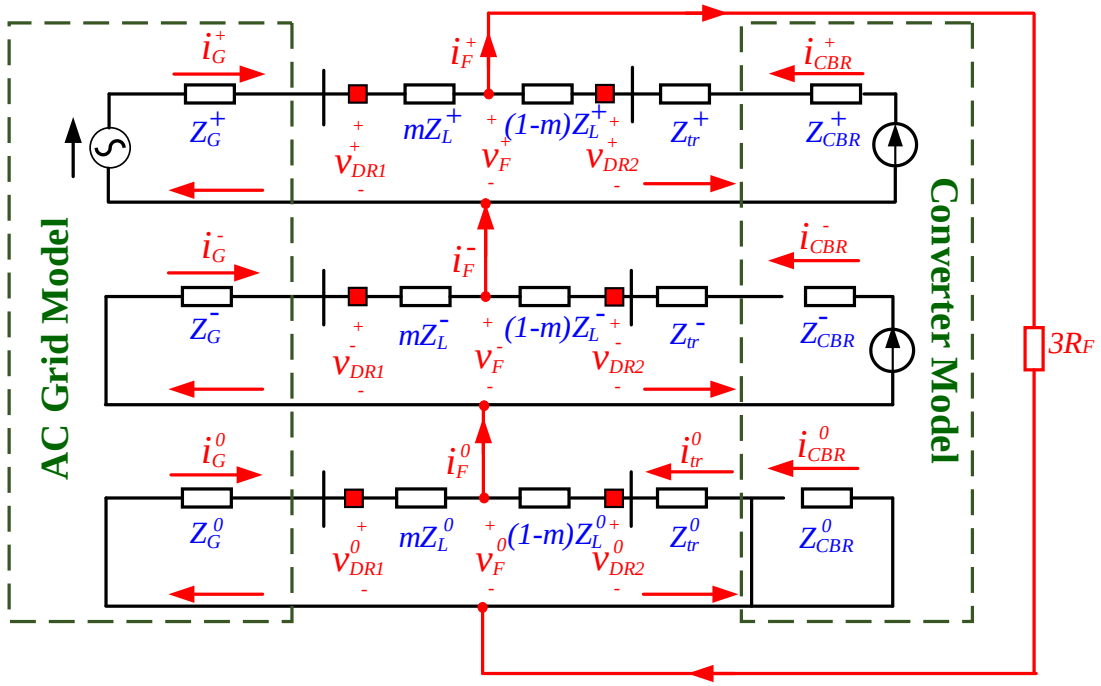

Figure 5-5. Sequence network diagram in AG fault of the transmission network in Figure 5-3

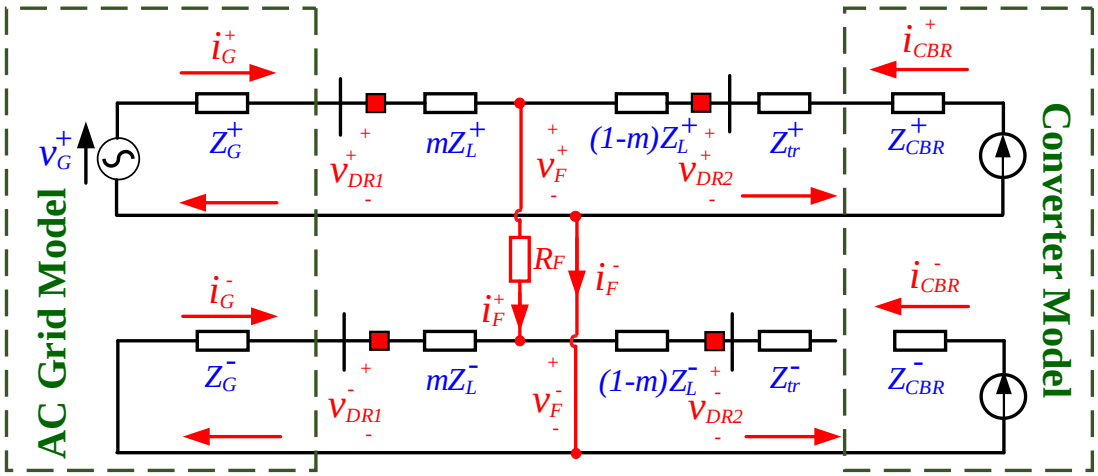

Figure 5-6. Sequence network diagram in BC fault of the transmission network in Figure 5-3

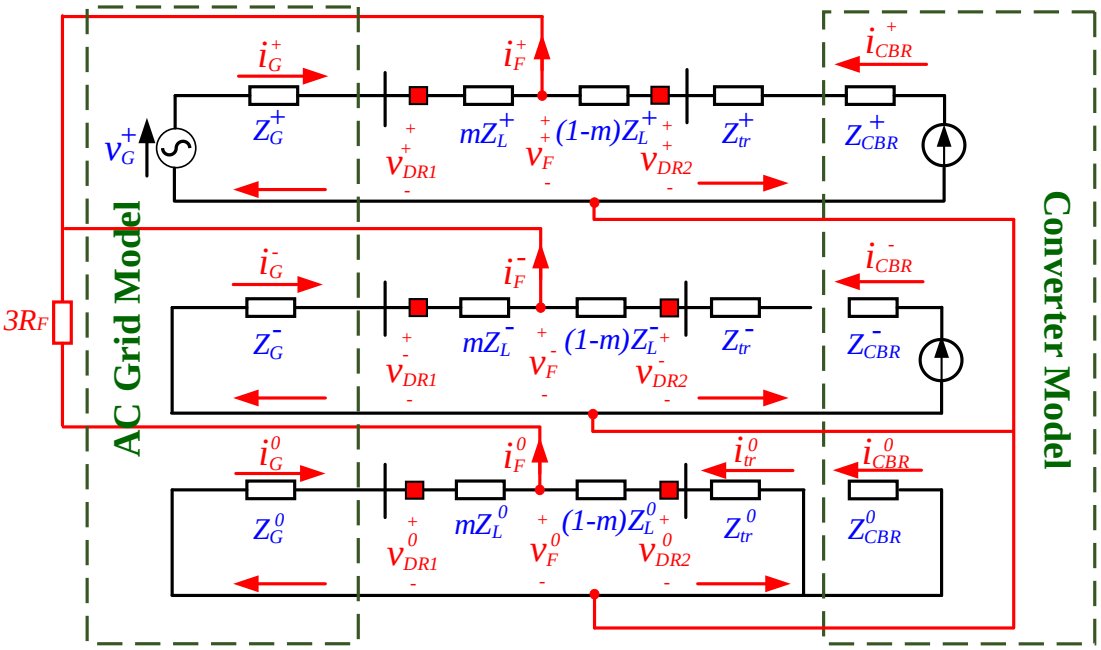

Figure 5-7. Sequence network diagram in BCG fault of the transmission network in Figure 5-3

Given the fact that the designed GFL does not inject the negative sequence current during faults [17] and the zero sequence current cannot flow through the delta side of the isolation transformer, the negative and zero sequence networks (delta side) will behave as the open circuits during faults as presented in the figures. Those sequence networks in Figure 5-5 to Figure 5-7 are used to further develop the new distance measuring elements proposed in Section 5.3.2.1 to 5.3.2.3.

5.3.2.1 Impedance Measurement in AG Fault

The sequence network of AG fault is presented in Figure 5-5, where the positive, negative and zero sequence networks are connected in serial at the fault point. From $(5-8)$, the sequence fault currents in AG fault, i.e., i_F^+, i_F^- and i_F^0, should satisfy the current relations in $(5-24)$.

$$i_F^+ = i_F^- = i_F^0 \qquad (5-24)$$

As the negative sequence current from CBR's side is zero, the total negative sequence fault current, i_F^-, should be the same as the negative sequence current contributed by the AC grid as presented in $(5-25)$. Although the zero sequence current cannot flow through the delta side of the isolating transformer (behaving as an open circuit), the star side of the transformer provides a smooth path of the zero sequence current from the fault point. Therefore, the total zero sequence current at the fault position should equal the sum of the currents from both sides of the CBR and AC grid as presented in $(5-26)$. By combining the current relations in $(5-24)$ to $(5-26)$, the zero sequence current from the CBR side can be calculated by $(5-27)$.

$$i_F^- = i_G^- \qquad (5-25)$$

$$i_F^0 = i_{tr}^0 + i_G^0 \qquad (5-26)$$

$$i_{tr}^0 = i_G^- - i_G^0 \qquad (5-27)$$

By applying the KVL from the fault point to both positions of DR1 and earthing point of the star side of the isolation transformer in the zero sequence network, the $(5-28)$ and $(5-29)$ can be obtained. By combining the equations of $(5-27)$, $(5-28)$ and $(5-29)$, the fault location of DR1 can be calculated by $(5-30)$.

$$v_F^0 = v_{DR1}^0 - i_G^0 m Z_L^0 \qquad (5-28)$$

$$v_F^0 = -i_{tr}^0 (Z_{tr}^0 + (1-m) Z_L^0) \qquad (5-29)$$

$$m = \frac{v_{DR1}^0 + (i_G^- - i_G^0)(Z_L^0 + Z_{tr}^0)}{i_G^- Z_L^0} \qquad (5-30)$$

In $(5-30)$, the i_G^0, v_{DR1}^0, i_G^- can be measured locally by DR1 and the Z_{tr}^0 and Z_L^0

are the parameters of the isolation transformer and protected line, which are the known variables. Based on test results in Section 5.4, the proposed equation can locate the faults accurately with an error smaller than 2.11% for the fault resistance up to 100 Ω, therefore, the derived equation also has a good performance in high resistive faults. An absolute operation is applied to ensure the distance measured in the non-fault condition is positive. The final impedance measuring equation in AG faults is presented in $(5-31)$.

$$|m| = \left| \frac{v_{DR1}^0 + (i_G^- - i_G^0)(Z_L^0 + Z_{tr}^0)}{i_G^- Z_L^0} \right| \qquad (5-31)$$

5.3.2.2 Impedance Measurement in BC Fault

The sequence network of the BC fault is presented in Figure 5-6, where the positive and negative sequence networks are connected in parallel at the fault point. By applying the KVL in the analysed circuit highlighted in Figure 5-8, the $(5-32)$ can be obtained. As illustrated in $(5-15)$, the magnitudes of the positive sequence and negative sequence fault currents in BC faults are the same but with the opposite polarity. Additionally, since the negative sequence currents are all contributed from the grid side, the negative sequence fault current is the same as the negative sequence current from the grid side. Therefore, the relationship in $(5-33)$ is derived. The equation of $(5-34)$ can be obtained by substituting the $(5-33)$ to $(5-32)$, where the v_F^+ can be calculated by applying the KVL from the fault points to the position of DR1 in the positive sequence network as presented in $(5-35)$.

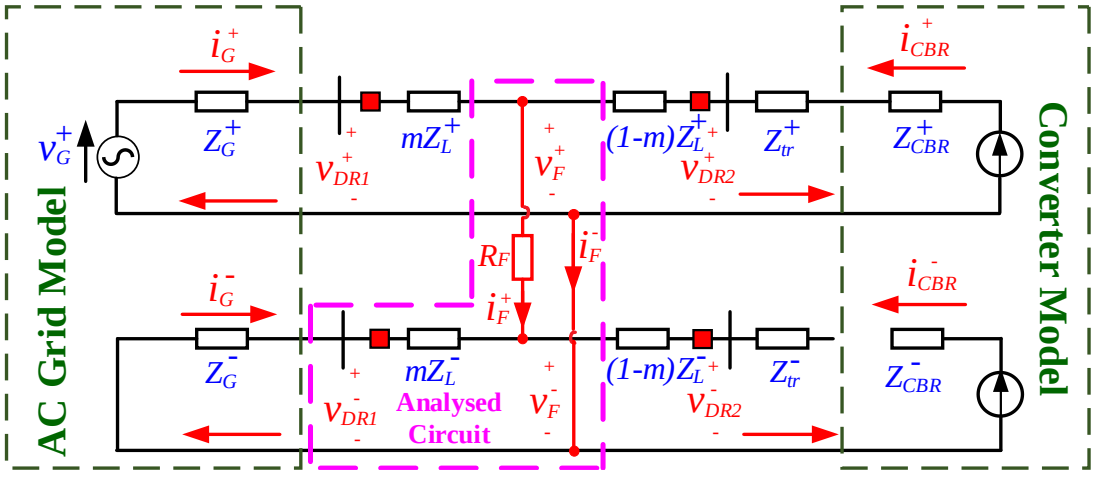

Figure 5-8. Analysed circuit to derive the equation of $(5-32)$

$$v_F^+ = v_{DR1}^- + i_F^+ R_F - i_G^- m Z_L^- \quad (5-32)$$

$$i_F^+ = -i_F^- = -i_G^- \quad (5-33)$$

$$v_F^+ = v_{DR1}^- - i_G^- R_F - i_G^- m Z_L^- \quad (5-34)$$

$$v_F^+ = v_{DR1}^+ - i_G^+ m Z_L^+ \quad (5-35)$$

By combining the equations of $(5-32)$ and $(5-35)$, the fault location detected by the DR1 can be calculated by $(5-36)$, where it contains two unknown variables, i.e., m and R_F. As the relative distance to fault m is a real number, the angle of the numerator and denominator can be assumed to be the same.

$$m = \frac{v_{DR1}^- - v_{DR1}^+ - i_G^- R_F}{i_G^- Z_L^- - i_G^+ Z_L^+} \quad (5-36)$$

To simplify the following derivation, the expressions $(v_{DR1}^- - v_{DR1}^+ - i_G^- R_F)$ and $(i_G^- Z_L^- - i_G^+ Z_L^+)$ in $(5-36)$ are represented as $K_1 \angle \theta_1$ and $K_2 \angle \theta_2$, and the expressions $(v_{DR1}^- - v_{DR1}^+)$ and $(i_G^- R_F)$ are represented by $K_3 \angle \theta_3$ and $K_4 \angle \theta_4$, therefore, the $(5-36)$ can be rewritten as $(5-37)$.

$$m = \frac{v_{DR1}^- - v_{DR1}^+ - i_G^- R_F}{i_G^- Z_L^- - i_G^+ Z_L^+} = \frac{K_1 \angle \theta_1}{K_2 \angle \theta_2} = \frac{K_3 \angle \theta_3 - K_4 \angle \theta_4}{K_2 \angle \theta_2} \quad (5-37)$$

From $(5-37)$, the θ_1 can be expressed by K_3, θ_3, K_4, θ_4 as shown in $(5-38)$.

$$\theta_1 = tan^{-1}\left(\frac{K_3\, sin(\theta_3) - K_4\, sin(\theta_4)}{K_3\, cos(\theta_3) - K_4\, cos(\theta_4)}\right) \quad (5-38)$$

Additionally, the value of θ_1 should keep the same to θ_2 so that the m in $(5-37)$ can be a real number. In that condition, the $(5-38)$ can be expressed as $(5-39)$, where the only unknown variable K_4 (which depends on fault resistance, R_F). According to $(5-39)$, the variable of K_4 can be calculated by $(5-40)$. Therefore, the fault resistance, R_F, can be calculated by $(5-41)$.

$$\theta_2 = tan^{-1}\left(\frac{K_3\, sin(\theta_3) - K_4\, sin(\theta_4)}{K_3\, cos(\theta_3) - K_4\, cos(\theta_4)}\right) \quad (5-39)$$

$$K_4 = \frac{K_3\, cos(\theta_3)\, tan(\theta_2) - K_3\, sin(\theta_3)}{(cos(\theta_4)\, tan(\theta_2) - sin(\theta_4))} \qquad (5-40)$$

$$R_F = \frac{K_4}{|i_G^-|} = \frac{K_3\, cos(\theta_3)\, tan(\theta_2) - K_3\, sin(\theta_3)}{|i_G^-|(cos(\theta_4)\, tan(\theta_2) - sin(\theta_4))} \qquad (5-41)$$

After substituting the expression of R_F in $(5-41)$ to $(5-36)$, the fault distance can be calculated by $(5-42)$.

$$m = \left| \frac{v_{DR1}^- - v_{DR1}^+ - i_G^- \left(\frac{K_3\, cos(\theta_3)\, tan(\theta_2) - K_3\, sin(\theta_3)}{|i_G^-|(cos(\theta_4)\, tan(\theta_2) - sin(\theta_4))} \right)}{i_G^- Z_L^- - i_G^+ Z_L^+} \right| \qquad (5-42)$$

5.3.2.3 Impedance Measurement in BCG Fault

The sequence network of BCG fault is presented in Figure 5-7, where the positive, negative and zero sequence networks are connected in parallel. By applying the KVL from the fault points to the DR1 position in both positive and negative sequence networks, the equations of $(5-43)$ and $(5-44)$ can be derived. From $(5-20)$, the positive and negative sequence fault voltages in BCG are the same as presented in $(5-45)$. After combining the equations of $(5-43)$ to $(5-45)$, the distance to fault for a BCG fault can be calculated by $(5-46)$, where the positive sequence line impedance is assumed to be same to the negative sequence line impedance.

$$v_F^+ = v_{DR1}^+ - i_G^+ m Z_L^+ \qquad (5-43)$$

$$v_F^- = v_{DR1}^- - i_G^- m Z_L^- \qquad (5-44)$$

$$v_F^+ = v_F^- \qquad (5-45)$$

$$m = \left| \frac{v_{DR1}^+ - v_{DR1}^-}{(i_G^+ - i_G^-) Z_L^+} \right| \qquad (5-46)$$

5.3.3 Settings of DR1

As reported in [11], the impedance of the isolation transformer, Z_{tr}, is approximately several tens of ohm, i.e., $|Z_{tr}|$ in our case is 11.34 Ω, which is much higher than the total impedance of the protected line, i.e., $|Z_L|$=5.05 Ω. Therefore, for the fault occurring behind the transformer, the measured impedance of the new

developed algorithm will be at least the sum of $|Z_{tr}|$ and $|Z_L|$ and thus significantly higher than the total line impedance. Considering the measurement errors, the zone reach setting of 1.2 (i.e., 20% safety margin) is used to set the Zone 1 reach of DR1, which covers the total length of the protected line. With those settings, all faults on the protected line will be tripped by the Zone 1 protection of DR1. The reach setting of the proposed scheme for DR1 only uses a real number rather than an impedance characteristic. Therefore, the relay setting process is greatly simplified.

Additionally, to improve the protection security in non-fault transient disturbances, a counting logic can be implemented on the DR1 relay, which is activated when the value of 'm' is lower than the setting (i.e., 1.2 in this case). It counts the number of points entering the protected zone continuously after being activated. If the counter reaches the pre-defined threshold, the DR1 will trip. The implemented counter threshold is selected to 4, which considers both security of the protection algorithm and the delay raised by the counting process. The counter will reset automatically if the calculated distance becomes greater than the relay setting before reaching 4, and thus, the tripping action of DR1 will be restrained. Given that modern digital relays such as [18][19] can use the data from PMU to realise the protection function, the voltage and current phasors measured by the PMU module provided as part of the RTDS library are used as inputs to the protection algorithm. Those modules have a reporting rate of 200 frames per second [20]. Therefore, the counter threshold of 4 introduces a stabilising delay of $4 \cdot \frac{1}{200} = 20$ ms, which is considered acceptable but can be further optimised to meet the best speed/security trade-off under specific network conditions.

5.4 Case Studies to Evaluate Protection Performance

5.4.1 Parameters of Investigated System and Relay Settings

The diagram of the investigated network is presented in Figure 5-3, and the system parameters are displayed in Table 3-4. The CBR injects positive sequence reactive currents during faults following the injection curve in $(2-22)$. In this test, the zone reach is set to 120% (considering a 20% measurement error of VT and CT) and the tripping delay of Zone 1 is set to 0 ms and all faults are applied at 0.2 s.

5.4.2 Impact of Fault Resistance

In this section, the fault scenarios in Table 5-1 are simulated to evaluate the impacts of the fault resistance, where the AG, BC and BCG faults are applied with the resistance of 0 Ω, 10 Ω, 20 Ω and 100 Ω to emulate the low and high resistive faults.

The fault location used in this section is set to 15%, i.e., m in Figure 5-3 equals 0.15, and the SCR of the connected system is set to 2.5 (corresponding to 2440 MVA fault level) to emulate a weak system, where the conventional distance relay could fail to detect faults based on the simulation results in Section 5.3.1. More discussion about the impacts of fault location and fault level is presented in Section 5.4.3 and Section 5.4.4.

Table 5-1. Cases used to evaluate the impacts of fault resistance

Case	**Line Length (kM)**	$\boldsymbol{FL_{Grid}}$ **(MVA)**	**Fault Type**	**Fault Location – m (%)**	**Fault Resistance (Ω)**
A1	12.1	2440	AG	15 %	0
A2	12.1	2440	AG	15 %	10
A3	12.1	2440	AG	15 %	20
A4	12.1	2440	AG	15 %	100
A5	12.1	2440	BC	15 %	0
A6	12.1	2440	BC	15 %	10
A7	12.1	2440	BC	15 %	20
A8	12.1	2440	BC	15 %	100
A9	12.1	2440	BCG	15 %	0
A10	12.1	2440	BCG	15 %	10
A11	12.1	2440	BCG	15 %	20
A12	12.1	2440	BCG	15 %	100

The results of Cases A4, A8 and A12 in Table 5-3 are presented in Figure 5-9, where the diagrams of the measured fault distance are plotted, along with the relay tripping signals. From the results, in the normal operating condition, the measured fault distance of DR1 will be significantly higher than the reach setting of DR1, i.e., 120% in Figure 5-9 (a), while once the faults occur in the protected transmission line, the measured distance will reduce to be lower than 1.2 quickly. Additionally, the oscillations were found at the initial stage of the faults owing to the oscillations from the phasor measurement and sequence component calculation. This oscillation vanishes after 20 ms to 40 ms of faults. Finally, the measured distance closes to the actual fault distance (15%), i.e., the measured distances of DR1 in Cases A4, A8 and A12 are 13.32 %, 13.45 % and 14.95 % respectively. According to Figure 5-9 (b), the DR1 can trip the faults in Cases A4, A8 and A12 within 27.6 ms, 59.2 ms and 54.4 ms. The detailed results of all investigated cases in Table 5-1 are presented in Table 5-2, where the measured fault distance (%) refers to the stable fault distance value after the initial oscillation, the distance measurement error (%) is the absolute difference between the measured fault distance (%) and the actual fault distance (%), and the tripping time is the time difference between the tripping signal and fault inception time.

From the results in Table 5-2, the proposed algorithm can always measure the fault distance accurately with the maximum error being 1.68 % (but only at high resistive fault with 100 Ω resistance), and the relay can clear the fault correctly in both low and

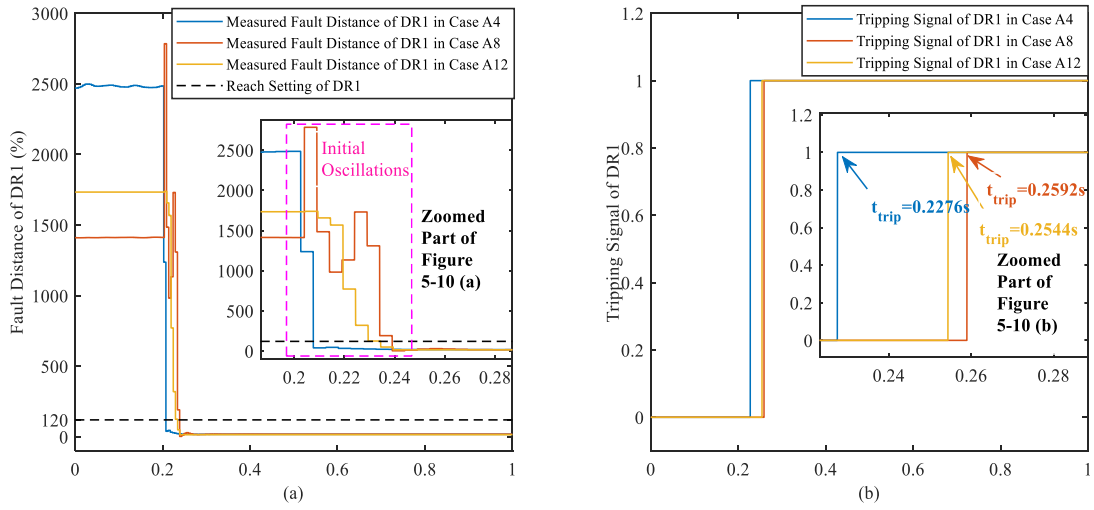

Figure 5-9. Simulation results of Case A4, A8 and A12, (a) measured fault distance (%) of DR1, (b) tripping signals of DR1

Table 5-2. Results of impacts of fault resistance

Case	Measured Fault Distance (%)	Distance Measurement Error (%)	Tripping Time (ms)
A1	14.49 %	0.51 %	26.5 ms
A2	14.41 %	0.59 %	25.4 ms
A3	14.27 %	0.73 %	23.3 ms
A4	13.32 %	1.68 %	27.6 ms
A5	14.93 %	0.07 %	53.8 ms
A6	14.27 %	0.73 %	52.9 ms
A7	15.53 %	0.51 %	54.1 ms
A8	13.45 %	1.55 %	59.2 ms
A9	14.92 %	0.08 %	53.8 ms
A10	14.93 %	0.07 %	55.4 ms
A11	14.92 %	0.08 %	56.6 ms
A12	14.95 %	0.05 %	54.4 ms

high resistive faults. The proposed method can accurately locate fault distance with a fault resistance up to 100 Ω. The average tripping time in the event of an AG, BC and BCG fault is 25.7 ms, 55.0 ms and 55.05 ms respectively. Given the operation of CBs is typically no more than 50 ms [21], the proposed scheme can isolate faults around 100 ms, which satisfies the fault clearance requirements for transmission system protection in the GB Grid Code (i.e., 140 ms).

5.4.3 Impacts of Fault Location

The cases used to evaluate the impact of fault location are defined in Table 5-3, where the faults are applied at 15%, 85% and two terminals of the protected line. Based on the results in Section 5.4.2, the conventional distance relay will have the protection issues such as delayed trips and failed trips if the fault resistance increases to 10 Ω. Therefore, 10 Ω resistance is selected for the cases in Table 5-3 to make the results

more comparable. The fault level of the connected AC system is 2440 MVA to emulate a weak AC system.

The simulation results of the cases in Table 5-3 are presented in Table 5-4. From the testing results, it was found that the proposed scheme can calculate fault distance accurately for faults at different locations. The maximum distance measurement error in AG, BC and BCG faults is 2.11%, 0.76 % and 0.2 %, which are neglectable compared to the conventional impedance-based distance protection algorithm. The DR1 can trip the faults with an average tripping time of 25.33 ms, 53.30 ms and 53.65 ms for AG, BC and BCG faults, which ensures the time requirement in the GB grid code.

Table 5-3. Cases used to evaluate the impacts of fault location

Case	**Line Length (kM)**	$\boldsymbol{FL_{Grid}}$ **(MVA)**	**Fault Type**	**Fault Location** $\boldsymbol{m}$ **(%)**	**Fault Resistance (Ω)**
B1	12.1	2440	AG	0 %	10
B2	12.1	2440	AG	15 %	10
B3	12.1	2440	AG	85 %	10
B4	12.1	2440	AG	100 %	10
B5	12.1	2440	BC	0 %	10
B6	12.1	2440	BC	15 %	10
B7	12.1	2440	BC	85 %	10
B8	12.1	2440	BC	100 %	10
B9	12.1	2440	BCG	0 %	10
B10	12.1	2440	BCG	15 %	10
B11	12.1	2440	BCG	85 %	10
B12	12.1	2440	BCG	100 %	10

Table 5-4. Results of impacts of fault locations

Case	Measured Fault Distance (%)	Distance Measurement Error (%)	Tripping Time (ms)
B1	0.36 %	0.36 %	25.6 ms
B2	14.41 %	0.59 %	25.4 ms
B3	83.23 %	1.77 %	23.7 ms
B4	97.89 %	2.11 %	26.6 ms
B5	0.14 %	0.14 %	56.2 ms
B6	14.27 %	0.73 %	52.9 ms
B7	84.24 %	0.76 %	53.0 ms
B8	99.60 %	0.40 %	51.1 ms
B9	0.12 %	0.12 %	53.9 ms
B10	14.93 %	0.07 %	55.4 ms
B11	84.95 %	0.05 %	53.7 ms
B12	99.80 %	0.20 %	51.6 ms

5.4.4 Impacts of Fault Level

The cases used to evaluate the impacts of fault level are presented in Table 5-5, where the different fault levels are applied to the connected AC system to emulate the different system scenarios, such as 2440 MVA representing a weak system with SCR of 2.5, 5831 MVA representing a strong system with SCR of 5 and 19128 MVA representing a very strong system with SCR of 10.

The testing results are presented in Table 5-6. From the results, the DR1 has a better performance in the system with a higher fault level (i.e., it has a minor measuring error and faster tripping speed as presented in the cases of C3, C6 and C9). However, this does not mean the performance of the proposed scheme is sensitive to the change in the system fault level. As convinced by the results in Table 5-6, this scheme has a satisfying performance in the weak system with an SCR of 2.5, where the maximum

Table 5-5. Cases used to evaluate the impacts of fault level

Case	Line Length (kM)	FL_{Grid} (MVA)	Fault Type	Fault Location m (%)	Fault Resistance (Ω)
C1	12.1	2440	AG	15 %	10
C2	12.1	5831	AG	15 %	10
C3	12.1	19128	AG	15 %	10
C4	12.1	2440	BC	15 %	10
C5	12.1	5831	BC	15 %	10
C6	12.1	19128	BC	15 %	10
C7	12.1	2440	BCG	15 %	10
C8	12.1	5831	BCG	15 %	10
C9	12.1	19128	BCG	15 %	10

Table 5-6. Results of impacts of fault level

Case	Measured Fault Distance (%)	Distance Measurement Error (%)	Tripping Time (ms)
C1	14.41 %	0.59 %	25.4 ms
C2	15.43 %	0.43 %	24.1 ms
C3	15.15 %	0.15 %	22.5 ms
C4	14.27 %	0.73 %	52.9 ms
C5	14.89 %	0.11 %	50.6 ms
C6	14.92 %	0.08 %	49.7 ms
C7	14.93 %	0.07 %	55.4 ms
C8	14.93 %	0.07 %	51.0 ms
C9	14.94 %	0.06 %	48.1 ms

measurment error is 0.73 % as presented in Case C4. This maximum error of 0.73 % is neglectable compared to the measuring error of the conventional algorithm in Section 5.3.1, where the distance relay failed to detect the faults. The average tripping time of DR1 in AG, BC and BCG faults are 24.0 ms, 50.07 ms and 51.50 ms. Therefore, it can satisfy the tripping time requirement, i.e., 140 ms, in the Grid Code.

5.4.5 Impacts of Line Length

The cases used to evaluate the impact of line length are presented in Table 5-7, where the transmission lines of 12.1 km (realistic line length between the Spittal and Thuro South substations in Scotland), 40 km and 70 km are implemented.

The faults are applied at 15% of the line and the 10 Ω fault resistance is applied. The maximum length in the investigated cases is set to 85 km, which is the maximum line length to guarantee the SCR equalling 2.5. In a weak system, the PLL of the grid-following converter is potentially to lose its synchronization with the main system due to the vulnerable terminal voltage [22]. Therefore, the minimum SCR is set to 2.5 in this section to avoid the instability issue. The calculation of 85 km is presented below.

Table 5-7. Cases used to evaluate the impacts of line length

Case	Line Length (kM)	FL_{Grid} (MVA)	Fault Type	Fault Location – m (%)	Fault Resistance (Ω)
D1	12.1	2440	AG	15 %	10
D2	40	3912	AG	15 %	10
D3	85	149887	AG	15 %	10
D4	12.1	2440	BC	15 %	10
D5	40	3912	BC	15 %	10
D6	85	149887	BC	15 %	10
D7	12.1	2440	BCG	15 %	10
D8	40	3912	BCG	15 %	10
D9	85	149887	BCG	15 %	10

Table 5-8. Results of impacts of line length

Case	Measured Fault Distance (%)	Distance Measurement Error (%)	Tripping Time (ms)
D1	14.41 %	0.59 %	25.4 ms
D2	14.84 %	0.16 %	23.8 ms
D3	14.90 %	0.1 %	22.5 ms
D4	14.27 %	0.73 %	52.9 ms
D5	14.57 %	0.43 %	52.0 ms
D6	14.61 %	0.39 %	47.9 ms
D7	14.93 %	0.07 %	55.4 ms
D8	14.93 %	0.07 %	51.4 ms
D9	14.94 %	0.06 %	46.6 ms

The SCR was identified in IEEE Std 1204 -1997 [23], which is defined as the ratio of the fault level of the AC power system to the nominal power infeed at the connection point to CBRs. Based on this concept, the total impedance, including both the internal impedance of the AC source and the impedance of the transmission line, can be calculated using $(5-47)$, where Z_T is the total impedance; v_{LL} is the line-to-line voltage of the power system; SCR is the short circuit ratio of the investigated power system and s_{CBR} is the capacity of the interfaced CBR.

$$Z_T = \frac{v_{LL}^2}{SCR \times s_{CBR}} \qquad (5-47)$$

After substituting v_{LL} of 275 kV, SCR of 2.5 and s_{CBR} of 839 MVA to $(5-47)$, the Z_T with SCR of 2.5 is 36.05 **Ω**, which corresponds to a line with 86.21 km. Finally, 85 km was selected as the maximum length in this study.

The results of investigated cases are shown in Table 5-8. From the results, the proposed scheme has a more accurate fault distance measurement and shorter tripping time with a longer length of the protected line under the same fault event. For example, for the results of D1 and D3, the error of distance measurement of DR1 reduces from

0.59 % to 0.1 % and the tripping time also decreases from 25.4 ms to 22.5 ms. In the tests, the maximum distance measuring error is 0.73 % (as presented in the results of Case D4). Therefore, it can be concluded that the proposed algorithm has an excellent performance in estimating the fault distance. The average tripping times of AG, BC and BCG fault cases are 23.90 ms, 50.93 ms and 51.13 ms, which can ensure the faults are isolated at less than 140 ms.

5.5 Chapter Summary

The connection of CBRs in the transmission system will lead to severe under/over-reach issues of distance protection owing to the combined effects of the infeed from both ends of the protected line and the fault resistance. This reach issue not only appears to the relay at the converter side but also compromises the relay performance at the grid side (especially in the weak system condition), which results in the delayed and failed operation of the distance relay.

The symmetrical analysis was conducted in this chapter to develop a new distance measuring element for the relay at the grid side to reflect the fault location accurately. The performance of the proposed algorithm is evaluated in a wide range of system operation conditions, including different fault parameters and the system with different fault levels and protected line lengths. Based on the simulation results, it was found that the developed method can calculate fault distance accurately in all scenarios above. For example, the maximum error in all investigated cases is 2.11%, which is much smaller compared to conventional distance protection. Additionally, the proposed method can be successfully isolated faults on the protected line with no more than 140 ms (assuming the CB operating time is 50 ms), which follows the tripping time requirement defined by the GB Grid Code. The proposed scheme can be embedded in the existing hardware platform of modern distance relays. Therefore, it also provides an economical solution for distance relays.

5.6 Chapter References

[1] C. L. Fortescue, "Method of Symmetrical Co-Ordinates Applied to the Solution of Polyphase Networks," in *Transactions of the American Institute of Electrical Engineers*, vol. XXXVII, no. 2, pp. 1027-1140, July 1918.

[2] C. I. Ciontea, "The Use of Symmetrical Components in Electrical Protection," *2019 72nd Conference for Protective Relay Engineers (CPRE)*, 2019, pp. 1-8.

[3] Amberg, A. Rangel (2015), Tutorial on Symmetrical Components, Schweitzer Engineering Laboratories, Available at: https://selinc.com/api/download/100688.

[4] A. Sudan, "Back to the basics — Event analysis using symmetrical components," *2018 71st Annual Conference for Protective Relay Engineers (CPRE)*, 2018, pp. 1-13.

[5] L. Shi, G. P. Adam, R. Li and L. Xu, "Control of Offshore MMC During Asymmetric Offshore AC Faults for Wind Power Transmission," in *IEEE Journal of Emerging and Selected Topics in Power Electronics*, vol. 8, no. 2, pp. 1074-1083, June 2020.

[6] Alstom Grid, Network Protection and Automation Guide – Protective Relays, Measurement & Control, Alstom Grid, 2011, [Online]. Available: https://www.gegridsolutions.com/multilin/publications/application_guide.htm.

[7] A. Hooshyar, M. A. Azzouz and E. F. El-Saadany, "Distance Protection of Lines Emanating From Full-Scale Converter-Interfaced Renewable Energy Power Plants—Part I: Problem Statement," in *IEEE Transactions on Power Delivery*, vol. 30, no. 4, pp. 1770-1780, Aug. 2015.

[8] A. Hooshyar, M. A. Azzouz and E. F. El-Saadany, "Distance Protection of Lines Emanating From Full-Scale Converter-Interfaced Renewable Energy Power Plants—Part II: Solution Description and Evaluation," in *IEEE Transactions on Power Delivery*, vol. 30, no. 4, pp. 1781-1791, Aug. 2015

[9] D. Liu, Q. Hong, A. Dyśko, D. Tzelepis, G. Yang, C. D. Booth, I. Cowan and B. Ponnalagan, "Evaluation of HVDC system's impact and quantification of synchronous compensation for distance protection", in *IET Renewable Power Generation*, vol. 16, no. 9, pp. 1925-1940, 2022.

[10] M. Alam, H. Leite, J. Liang and A. da Silva Carvalho, "Effects of VSC based HVDC system on distance protection of transmission lines", in *International Journal of Electrical Power & Energy Systems*, vol. 92, pp. 245-260, 2017.

[11] Y. Fang et al. , "Impact of Inverter-Interfaced Renewable Energy Generators on Distance Protection and an Improved Scheme," in *IEEE Transactions on Industrial Electronics*, vol. 66, no. 9, pp. 7078-7088, Sept. 2019.

[12] S. Tale, M. Mohan and K. P. Vittal, "Performance analysis of distance relay in an AC grid with VSC-HVDC connection," *2017 International Conference on Intelligent Computing, Instrumentation and Control Technologies (ICICICT)*, 2017, pp. 1363-1368.

[13] M. Alam, H. Leite, N. Silva and A. da Silva Carvalho, "Performance evaluation of distance protection of transmission lines connected with VSC-HVDC system using closed-loop test in RTDS", in *Electric Power Systems Research*, vol. 152, pp. 168-183, 2017.

[14] C. C. Teixeira and H. Leite, "The influence of a VSC based HVDC link on distance protection relay assessed by CAPE software," *2017 IEEE Manchester PowerTech*, 2017, pp. 1-4.

[15] S. Paladhi and A. K. Pradhan, "Adaptive Distance Protection for Lines Connecting Converter-Interfaced Renewable Plants," in *IEEE Journal of Emerging and Selected Topics in Power Electronics*, vol. 9, no. 6, pp. 7088-7098, Dec. 2021.

[16] B. R. Kumar, A. Mohapatra, R. Gokaraju and S. Chakrabarti, "Phase Angle-Based Sub-Cycle Algorithm for High-Speed Digital Relaying of Transmission Lines," in *IEEE Transactions on Power Delivery*, vol. 37, no. 4, pp. 3416-3419, Aug. 2022.

[17] 'The Grid Code Issue 6 Revision 11', National Grid, February 2022.

[18] D60 Line Distance Protection System, GE, November 2020.

[19] SEL-411L Advanced Line Differential Protection, Schweitzer Engineering Laboratories (SEL), November 2020.

[20] RTDS Technology Inc., "Real Time Digital Simulator Control Library Manual".

[21] J Duncan Glover, T. J. Overbye, and M. S. Sarma, Power system analysis & design. Boston, Ma: Cengage Learning, 2017.

[22] S. -H. Huang, J. Schmall, J. Conto, J. Adams, Y. Zhang and C. Carter, "Voltage control challenges on weak grids with high penetration of wind generation: ERCOT experience," *2012 IEEE Power and Energy Society General Meeting*, San Diego, CA, USA, 2012, pp. 1-7.

[23] A. IEEE, "IEEE Guide for Planning DC Links Terminating at AC Locations Having Low Short-Circuit Capacities," 1997.

Chapter 6

6 Transient Wavelet Energy-Based Protection Scheme for Inverter-Dominated Microgrid

6.1 Introduction

The microgrids can operate in both grid-connected and islanded modes, which results in a significant magnitude difference in the fault currents in microgrids. Additionally, because of the limited fault currents generated by the inverters, it would be difficult to detect and locate the faulted feeder in islanded microgrids. The solutions mostly suggested in the literature have been reviewed in Chapter 4, where their fundamentals, merits and limitations are discussed. Among those solutions, the methods using fault-generated high-frequency transients are more attractive since their performance is not sensitive to the variation of fault levels and converter controllers. Thus, it caters for the protection requirements in the future converter/inverter-dominated power system. However, it is challenging to implement travelling wave protection in microgrids with short-length feeders due to the high requirements on relay sampling frequency [1] and the frequent reflection of travelling waves [2]. Therefore, a transient energy-based protection scheme is proposed in this chapter to realise fast fault isolation and address the limitations of high sampling frequency.

This chapter is structured as follows. The overview of the wavelet transform is proposed in Section 6.2. The development of the transient wavelet energy-based protection scheme is proposed in Section 6.3. Case studies used to evaluate the performance of the developed scheme are discussed in Section 6.4. Finally, the chapter summary is presented in Section 6.5.

6.2 Overview of Wavelet Transform

In the modern engineering area, the tools of mathematical transformation are widely adopted to process the raw time-domain signal to reveal the hidden information. One of the common approaches is to transfer the signal into the frequency domain by the Fourier Transform (FT) in $(6-1)$ [3]. However, as reported in [4][5], the FT can only present the frequency information of the input signal, which cannot

$$FT(f) = \int_{-\infty}^{\infty} x(t) \cdot e^{-2j\pi ft}\, dt \qquad (6-1)$$

localize the appearing time of those frequency components. Therefore, the FT shows apparent advantages of analysing the stationary signal [6], where the frequency components of the input signal do not change with the time variation.

Given the fact that most signals in nature are non-stationary, where the frequency components of the input signal constantly change with the variation of time, a variant of FT called 'Short-Time Fourier Transform (STFT)' is proposed in $(6-2)$, where $x(t)$ is the time-domain signal; $s(t)$ is the introduced window function and t' refers to the window location.

$$STFT(t,f) = \int_{t1}^{t2} [x(t) \cdot s(t-t')] \cdot e^{-j2\pi ft}\, dt \qquad (6-2)$$

Compared to $(6-1)$, an additional sliding window is introduced to the conventional FT moving from the beginning to the end of the signal, where the adopted window length is short so that the split signal in the window can be assumed to be stationary [7]. However, this fixed window length cannot satisfy the demand for analysing the signals with different frequency components. For example, for the high-frequency signal, the narrow window length is preferred to realise a good time resolution, while for the low-frequency signal, a wide sampling window should be adopted to get a better frequency resolution. To further address the resolution problem of the STFT, the concept of the Wavelet Transform (WT) is proposed.

The Continuous Wavelet Transform (CWT) is presented in $(6-3)$ [8][9], where the $\Psi_{a,b}(t)$ is the function of the wavelet basis, which is derived by the mother wavelet

$$CWT(a,b) = \int_{-\infty}^{\infty} x(t) \cdot \Psi_{a,b}(t)\, dt \qquad (6-3)$$

$$\Psi_{a,b}(t) = \frac{1}{\sqrt{|a|}} \Psi\left(\frac{t-b}{a}\right) \qquad (6-4)$$

function $\Psi(t)$. In this equation, the variables of a and b are the scale and translation factors and $\frac{1}{\sqrt{|a|}}$ is for energy normalization across different scales. Unlike the FFT, where the sine and cosine functions are used as the basis, the wavelet basis function $\Psi_{a,b}(t)$ is not specified, which can be selected based on scholars' preferences [10]. In the real application, the value of a in $(6-4)$ starts from '1' and the wavelet basis with a equalling 1 will move along the signal from beginning to end to get all coefficients at the scale of 1. The above procedure will be repeated by increasing a continuously and it will stop when all desired values of a are covered in the computation process [10].

However, the continuous increase of a and b in $(6-3)$ results in a heavy computation burden. Therefore, the Discrete Wavelet Transform (DWT) is proposed to reduce the computation loads of CWT by discretizing the variables of a and b in $(6-3)$ [11]. The function of DWT is presented in $(6-5)$ and the discrete wavelet basis is shown in $(6-6)$ [12], where m, n are integers; $x(k)$ is the input signal; $\Psi\left(\frac{k-nb_0a_0^m}{a_0^m}\right)$ is the discrete wavelet basis. Practically, the values of a_0 and b_0 are set to 2 and 1 [13]. According to the research in [14], the DWT can be implemented by the pyramid algorithm presented in Figure 6-1, where $x(k)$ is the input signal; the H_0 and G_0 are the coefficients of the high pass and low pass filers; D_l and A_l are the detail

$$DWT(m,n) = \sum_k x(k)\, \Psi_{m,n}(k) \qquad (6-5)$$

$$\Psi_{m,n}(k) = \frac{1}{\sqrt{a_0^m}} \cdot \Psi\left(\frac{k-nb_0a_0^m}{a_0^m}\right) \qquad (6-6)$$

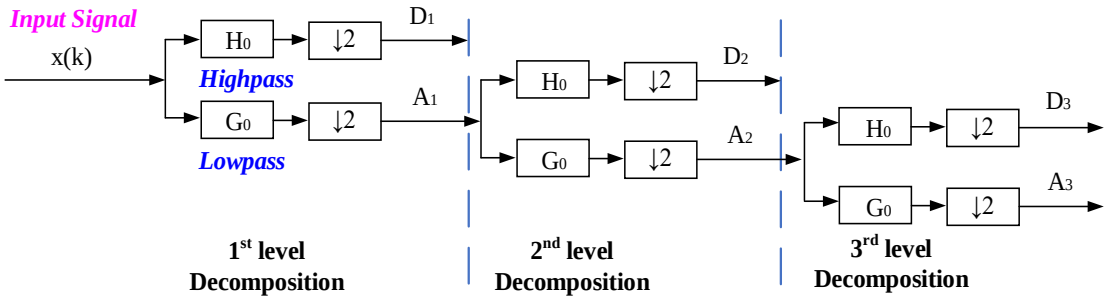

Figure 6-1. Example of three-level DWT decomposition tree [15]

Table 6-1. Frequency bands of decomposed DWT coefficients

	Level 1	**Level 2**	**Level 3**
$\boldsymbol{D_l}$	$\left({}^{f_{sig}}/_{2}, f_{sig}\right)$	$\left({}^{f_{sig}}/_{4}, {}^{f_{sig}}/_{2}\right)$	$\left({}^{f_{sig}}/_{8}, {}^{f_{sig}}/_{4}\right)$
$\boldsymbol{A_l}$	$\left(0, {}^{f_{sig}}/_{2}\right)$	$\left(0, {}^{f_{sig}}/_{4}\right)$	$\left(0, {}^{f_{sig}}/_{8}\right)$

and approximation coefficients at various levels, where l is the level of decomposition; the symbol of '↓2' refers to the down-sampling operation by 2. The frequency bands of coefficients at different decomposition levels are illustrated in Table 6-1, where the frequency of the input signal ranges between 0 Hz to f_{sig} Hz. The high-pass and low-pass filters in Figure 6-1 can be designed using the Finite Impulse Response (FIR) filters, and the decomposition process can be equivalent to convoluting the sampled inputs with the coefficients of the designed FIR filters [12]. The design of a wavelet filter can be achieved by the '*wfilters*' command in MATLAB [16]. In the DWT algorithm, the length of the input signal must be multiple of 2^l (l is the level of decomposition), and it losses the time invariance properties raised by the down-sampling steps [17][18]. To address the issues of the DWT, a variant of DWT, called MODWT [19], is developed by removing the down-sampling steps in the DWT and the filter coefficients used in the MODWT are scaled down by $\sqrt{2}$. Additionally, the MODWT has a faster computation speed than the DWT due to no need for down-sampling steps, which provides a valuable feature for real-time applications [20]. Therefore, the MODWT algorithm is used to develop the proposed transient-based protection algorithm.

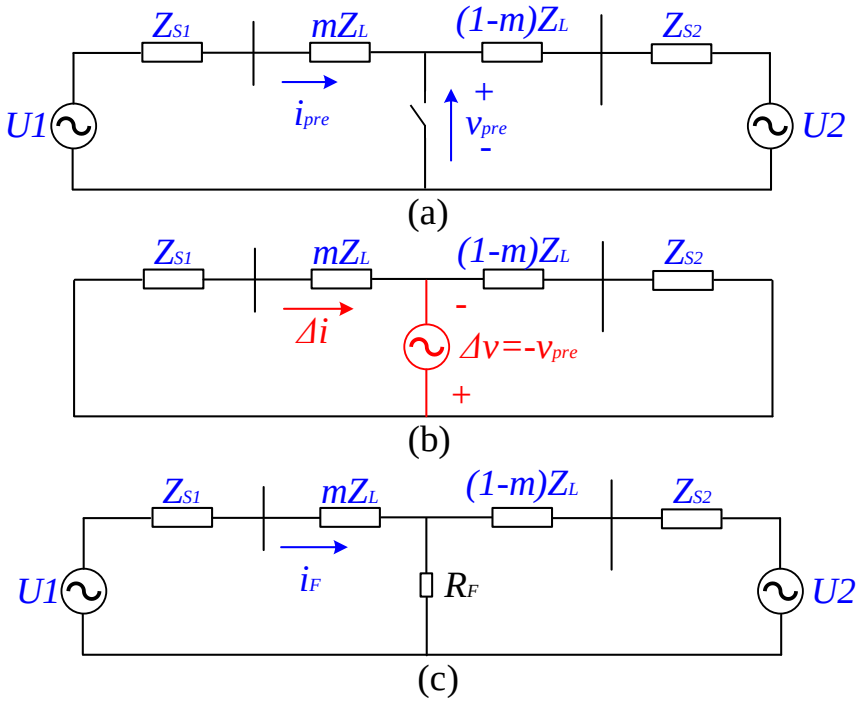

Figure 6-2. Diagram of, (a) pre-fault network, (b) superimposed network, (c) faulted network [21]

6.3 Development of the Transient-based Protection System

6.3.1 Fundamentals of Fault-Induced High-Frequency Transients

Before discussing the design of the protection scheme, the fundamentals of the implemented high-frequency transients are discussed in this section. According to Thevenin's and superposition theorem, the faulted network can be represented as the sum of the pre-fault network and the superimposed network as presented in Figure 6-2 [21], where the U_1 and U_2 stand for the pre-fault voltage sources in the network; v_{pre} is the pre-fault voltage at the fault point; Z_{S1} and Z_{S2} are the internal impedances of the voltage sources U_1 and U_2; Z_L is the line impedance; Δv is the superimposed voltage at the fault point and Δi is the current flowing in the superimposed network. In bolted faults, the magnitude of Δv equals to the magnitude of the pre-fault voltage at the fault position, while the voltage polarity of Δv is opposite to the pre-fault voltage [22]. As reported in [23], the term 'superimposed current' is a broad item which can be further categorised into different types according to the filtering operation to obtain specific features. In the proposed protection algorithm, the high-frequency components of the superimposed currents are extracted using the high-pass filter in the MODWT algorithm. Compared to the protection using superimposed components in

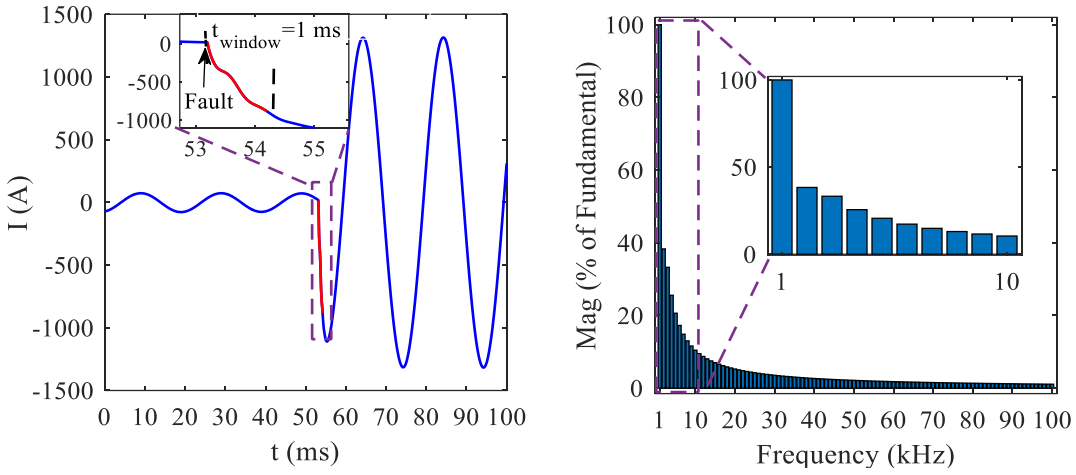

Figure 6-3. Fault current waveform and frequency spectrum of fault-induced high-frequency transients

the fundamental frequency, the performance of the proposed transient energy-based protection is not sensitive to the changes in inverter control strategies and system fault levels since it operates based on high-frequency signatures generated by faults rather than the generators. Therefore, it has a better performance in protecting microgrids dominated by IIDGs.

After fault inception, the travelling wave generated by the superimposed voltage source will be superimposed to the currents and voltages. In the initial stage of faults, the network behaves as a distributed parameter system [24], where the dynamic behaviour of travelling waves can be explained using a set of differential equations, i.e., the telegraph equation [25]. Those generated travelling waves are reflected by the singularity points in the networks such as busbars, transformers, etc. After multiple reflections of travelling waves, the network evolves into a transient-state lumped RLC network, where the analysed high-frequency transients appear [24]. In the travelling wave protection scheme, the exact arrival time of the wavefront is required to localise the faults as discussed in Section 3.5.3. Given the fast propagation speed of travelling waves and the short feeder length in microgrids, an extremely high sampling frequency (i.e., in the MHz range) is necessary to capture the accurate time information of arriving wavefronts [26]. In microgrids, the main objective is to identify the faulted feeder rather than localise the fault distance as did in the transmission system. Therefore, in the designed protection system, only the transient wavelet energy information, whose definition and calculation are proposed in Section 6.3.2, is implemented and the employed high-frequency transients of the superimposed

currents are available within a few milliseconds after fault inception [23][24]. Therefore, it significantly decreases sampling requirements compared to conventional travelling wave-based approaches.

One waveform of the transient fault current is presented in Figure 6-3, along with its frequency spectrum. The fundamental frequency of the Fast Fourier Transform (FFT) analysis is set to 1 kHz. Given the fast attenuation of high-frequency transients, the signal of 1 ms duration following the fault inception is analysed as presented in the zoomed-in figure. In Figure 6-3, the magnitude spectrum is represented as a percentage of the magnitude of the fundamental frequency, i.e., 1 kHz in this case. Based on the FFT results in Figure 6-3, the frequency spectrum of fault-induced high-frequency transients ranges widely and it is evident that frequencies below 10 kHz are considered sufficient to analyse the fault-induced transients. Such sampling frequency is feasible to be implemented on a conventional numerical relay [27].

6.3.2 Definition of Transient Wavelet Energy

The 'Daubechies 4' (db4) mother wavelet is implemented in the MODWT algorithm to design the high-pass and low-pass filters due to its satisfying performance in analysing the short and fast transient disturbances [28]. The wavelet coefficients (similar to the detail coefficients in the DWT) at the first decomposition level are used in the proposed scheme. The energy of the individual wavelet coefficient is calculated by $(6-7)$ [29], where the W_j is the j^{th} wavelet coefficient at level 1, which is the most recent coefficient. However, the energy of an individual wavelet coefficient in

$$E_j = W_j^2 \qquad (6-7)$$

$(6-7)$ can be sensitive to the system noise and non-fault disturbances such as load switching, motor start, etc. To mitigate the potential protection instability issue, a moving-average window is applied to smooth the short-term fluctuations of the energy. Therefore, the transient wavelet energy, TWE_j, after applying a moving average window, is defined as $(6-8)$, where M is the length of the moving-average window.

$$TWE_j = \frac{E_j + E_{j-1} + \cdots + E_{j-M+1}}{M} = \frac{1}{M}\sum_{i=j-M+1}^{j} E_i \qquad (6-8)$$

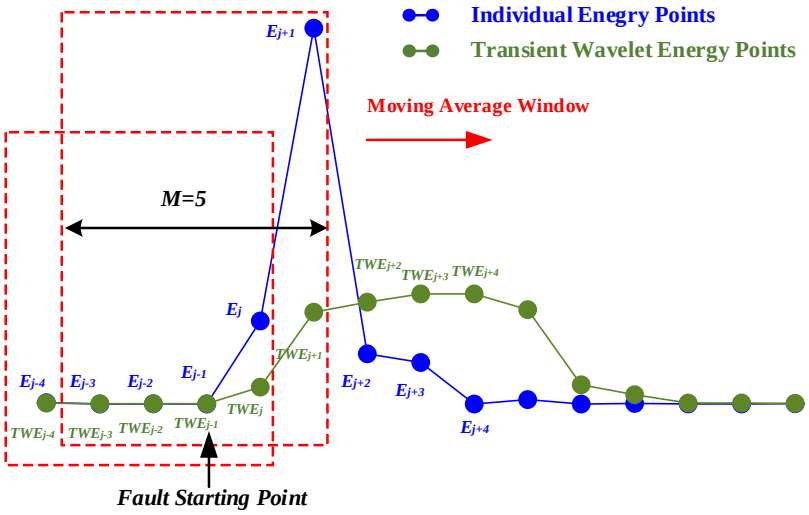

Figure 6-4. Moving average window of the energy of individual wavelet coefficient

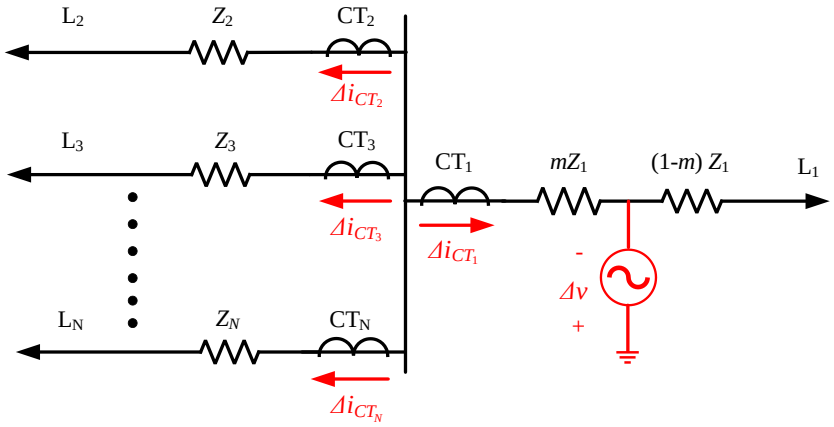

Figure 6-5. Superimposed circuit for the fault at a feeder connected to the busbar

This moving average process is illustrated in Figure 6-4. Higher sensitivity can be achieved for a shorter window length, but it can also raise the risks of maloperation caused by noise. Based on the simulation, it was found that the main energy is concentrated in the initial five samples after the fault inception, i.e., the E_j to E_{j+4} in Figure 6-4. Therefore, the length of the moving average window is set to 5, which provides a good trade-off between noise smoothing and speed of operation.

6.3.3 Relationship of Transient Wavelet Energy

To coordinate relays in the microgrid, the energy relations of the CTs at the same busbar need to be derived first. The superimposed circuit of a typical busbar in microgrids is presented in Figure 6-5, where L_1 to L_N stand for the feeders connected at the busbar, Z_1 to Z_N are the equivalent impedance of the feeders and CT_1 and CT_N

are the CTs installed at the terminals. In the case of the fault at L_1, the superimposed voltage source, Δv, is applied at the fault position and the superimposed currents, Δi_{CT_1} to Δi_{CT_N}, are introduced into the feeders. The assumed convention here is that the superimposed currents flowing away from the busbar have a positive value. It should be noted that the following derivation applies to the superimposed network only, and the conclusion is not necessarily true for the pre-fault or faulted network.

According to the research in [30], with the positive direction defined in Figure 6-5, the polarity of the superimposed current on the faulted feeder is opposite to the currents on the healthy feeder connected at the same busbar. According to the KCL, the input currents should equal the output currents at the same node. Therefore, the relations of the superimposed currents in Figure 6-5 can be described by $(6-9)$, where p refer to the phase a, b and c and k is the index of CTs connected to the same busbar.

$$\Delta i^p_{CT_1}(t) = -\sum_{k=2}^{N} \Delta i^p_{CT_k}(t) \qquad (6-9)$$

In this study, the MODWT algorithm is implemented by the FIR filter [31], where the wavelet coefficients are extracted by convoluting the sampled current with the coefficients of the designed high-pass filter [12][32]. Since the filter used in that scheme has fixed coefficients, the output wavelet coefficients will have the same relations as the input currents as indicated by $(6-10)$.

$$W^p_{j,CT_1} = -\sum_{k=2}^{N} W^p_{j,CT_k} \qquad (6-10)$$

From $(6-10)$, the coefficient magnitude of the CT closest to the fault equals the sum of the CTs on the other branches. According to the individual energy defined by $(6-7)$, the energy of the CT on the fault side should be greater than the energy of any of the other CTs at the same busbar, which is depicted as $(6-11)$.

$$E^p_{j,CT_1} > E^p_{j,CT_k}, k = 2, \dots, N \qquad (6-11)$$

After applying the moving average operation in $(6-8)$, the energy relation in $(6-12)$ can be derived.

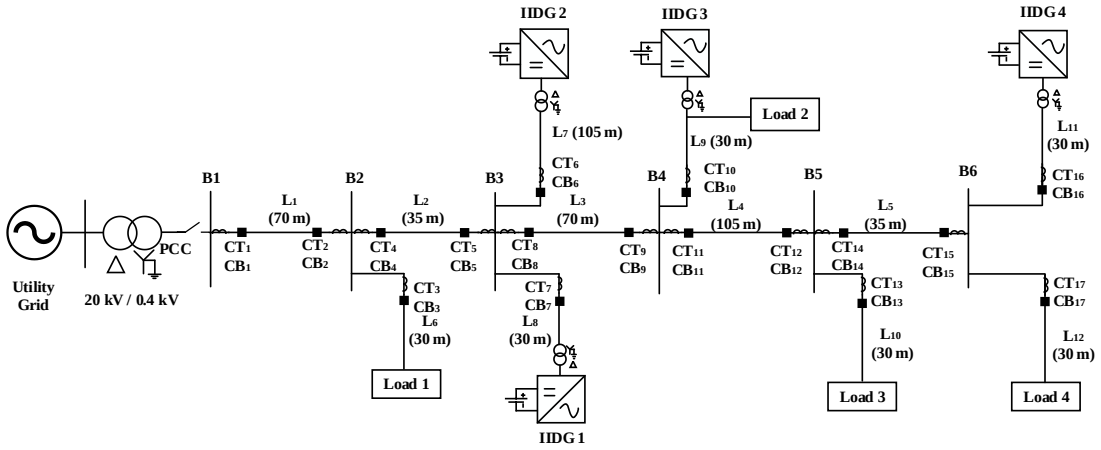

Figure 6-6. Diagram of CIGRE benchmark microgrid [33]

$$TWE_{j,CT_1}^{p} > TWE_{j,CT_k}^{p}, k = 2, \dots, N \qquad (6-12)$$

As presented in $(6-12)$, for the same phase currents, the energy of the CT on the fault side will be the largest, while to simplify the design and real-time implementation of the protection algorithm, the maximum phase TWE is selected. After simplification, the energy at the same busbar is described as $(6-13)$, where the $TWE_{j,CT_1}^{p_{max}}$ and $TWE_{j,CT_k}^{p_{max}}$ are the maximum-phase TWE of CT_1 and CT_k respectively. For example, in the event of an AG fault, the energy of phase a will be the largest. Therefore, the p_{max} in $(6-13)$ refers to the energy of phase a. As the proposed scheme needs to select the branch with the maximum energy among all feeders connected to the busbar, the CTs are assumed to be installed on every feeder in microgrids.

$$TWE_{j,CT_1}^{p_{max}} > TWE_{j,CT_k}^{p_{max}}, k = 2, \dots, N \qquad (6-13)$$

To convince the analysis above, an AG fault with 1 Ω resistance and 30° fault inception angle (FIA) is applied on L_5 in the developed CIGRE benchmark microgrid model [33] developed in MATLAB/SIMULINK (as presented in Figure 6-6). More information on this microgrid model can be found in Section 6.4.1. The simulation results of superimposed currents measured by CT_{15} to CT_{17} are presented in Figure 6-7, along with their wavelet coefficients and energy values.

According to the results in Figure 6-7 (a), the polarity of Δi_{CT15}^{a} is opposite to the polarities of Δi_{CT16}^{a} and Δi_{CT16}^{a} and the magnitude of Δi_{CT15}^{a} is the sum of Δi_{CT16}^{a} and Δi_{CT17}^{a} as revealed by $(6-9)$, where the sum of Δi_{CT15}^{a}, Δi_{CT16}^{a} and Δi_{CT17}^{a} are zero as

presented in the bottom diagram of Figure 6-7 (a). After processing those currents by the MODWT algorithm, it was found that the conclusion in $(6-10)$ can be reflected by the results in Figure 6-7 (b), where the polarity of $W^a_{j,CT15}$ is opposite to the polarities of $W^a_{j,CT16}$ and $W^a_{j,CT17}$ and the magnitude of $W^a_{j,CT15}$ equals to the sum of $W^a_{j,CT16}$ and $W^a_{j,CT17}$. The energy relations, including both individual and transient wavelet energies, are plotted in Figure 6-7 (c), where the energy of CT_{15}, including both the individual energy and the transient wavelet energy, is greater than the values of CT_{16} and CT_{17} as demonstrated in $(6-11)$ and $(6-12)$.

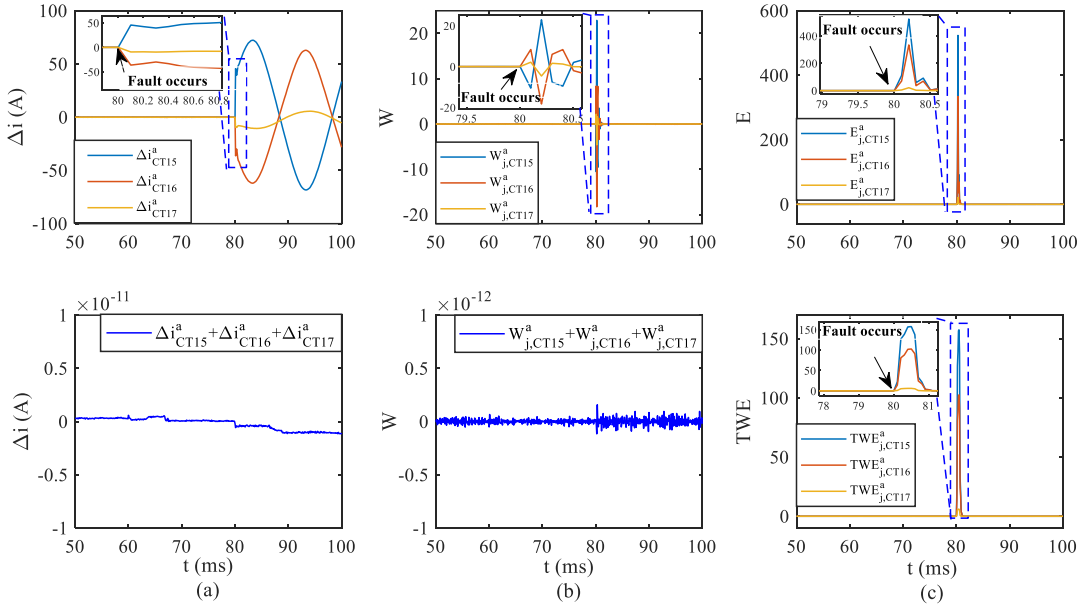

Figure 6-7. Simulation results of, (a) superimposed currents of CT_{15}, CT_{16}, CT_{17} and the sum of superimposed currents, (b) wavelet coefficients and the sum of wavelet coefficients, (c) individual and transient wavelet energies

6.3.4 Coordination of Relays in Microgrids

In Section 6.3.1, the energy relation of the CT connected at the individual busbar is derived, where the CT closest to the fault will have the largest energy values. This energy feature will be used in this section to design the new protection algorithm to coordinate the microgrid relays. There are two assumptions for the design of the protection algorithm. Firstly, for every busbar in the microgrid, one digital relay is installed to collect and analyse the three-phase currents from all CTs of the feeder connected to that busbar. Secondly, communication channels are available between the relays on the opposite ends of the protected lines. It should be stressed that although

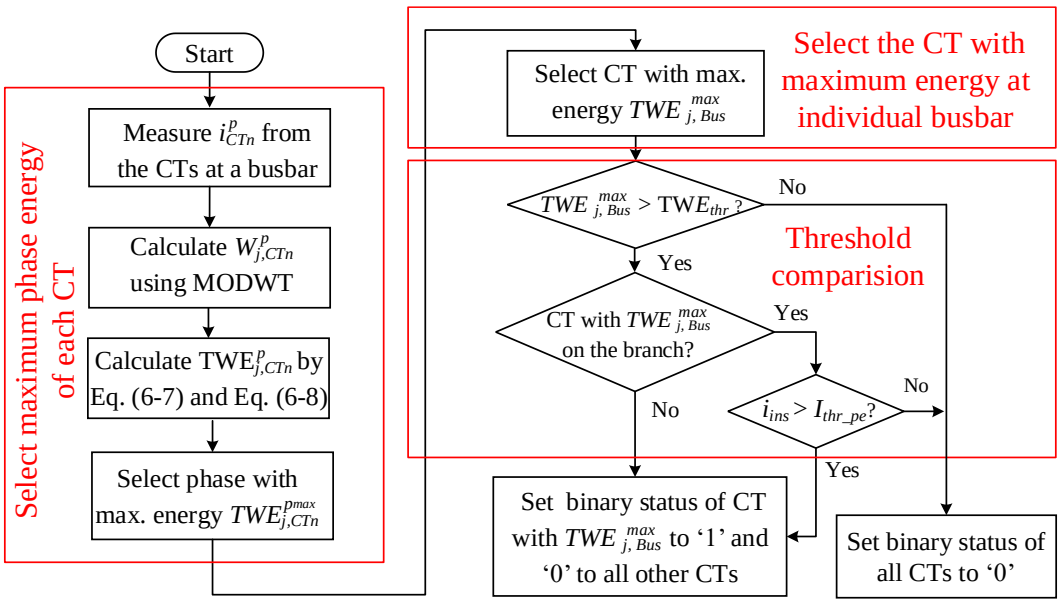

Figure 6-8. Identification of CT binary status of an individual busbar

communication is needed for the developed protection system, unlike differential protection, which requires the communication of sampled current values, the proposed scheme only requires low-cost communication with small bandwidth since it only transmits binary values, i.e., '1' or '0', which is feasible and economical to implement in microgrid [34]. The designed protection has two stages. In stage I, the binary status, i.e., '1' and '0' of all CTs in the microgrid will be identified following the developed identification rule. In stage II, the relays in the microgrid will be coordinated by the newly developed algorithm, which uses the binary status of CTs defined in stage I.

6.3.4.1 Stage I: Binary Status Identification of a Single Busbar

The flowchart to identify the CT binary status of an individual busbar is presented in Figure 6-8. In the following description, the 'main feeder' refers to the feeder connected between two busbars (with relays at both ends) such as the L_1 and L_5 in Figure 6-6 and the 'branch feeder' refer to the feeder connected to a load or a generator only (with no relay on the opposite end) such as the L_6 and L_{12} in Figure 6-6.

Based on the flowchart in Figure 6-8, the three-phase currents measured by all CTs at that busbar are collected by the relay first. Based on the input currents, the wavelet coefficients of the phase currents are calculated by the MODWT algorithm and the three-phase TWEs of different CTs, TWE^{p}_{j,CT_n}, will be calculated by $(6-7)$ and $(6-8)$. As discussed in the previous section, the maximum phase energies, $TWE^{p_{max}}_{j,CT_n}$,

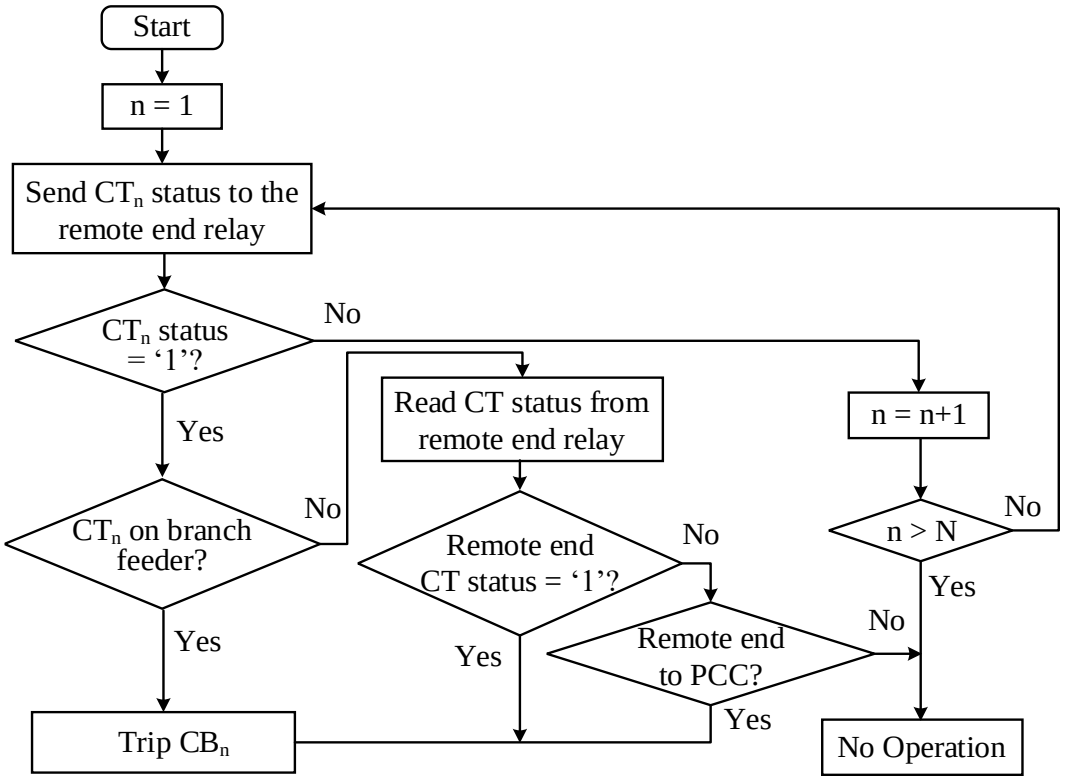

Figure 6-9. Flowchart of the relay coordination algorithm

of all CTs at that busbar are implemented to simplify the design of the real-time implementation of the protection algorithm. In the next step, those CTs in the network will be further grouped based on the connected busbar and the obtained $TWE_{j,CT_n}^{p_{max}}$ will be compared to select the maximum energy, i.e., $TWE_{j,Bus}^{max}$, at the individual busbar, which is then compared against the defined energy threshold, TWE_{thr}, to prevent the unwanted operation during the normal operating state with the likely presence of signal noise. Additionally, considering the potential impact of the non-fault disturbances, i.e., load switching or power variation of the generators, the second threshold, I_{thr_pe}, is applied for the CTs located at the branch feeders. If the CT with the maximum energy is installed on the 'main feeder', the relay will output a binary value of '1' to the CT's side as long as the energy value is above the threshold, but when the CT with the maximum energy is on the 'branch feeder', then both energy and current conditions need to be met as displayed in Figure 6-8, where i_{ins} is the instantaneous current measured by the CT with maximum energy. The process in Figure 6-8 is carried out by all relays in the microgrid and the selection of energy and current thresholds are discussed in Section 6.3.5.

6.3.4.2 Stage II: Coordination of Relays in the Microgrid

From stage I, the binary status of all CTs in the microgrid is identified, which is further used to coordinate the relays in the microgrid. In the developed algorithm, the relays are coordinated based on the fault positions, including 1) the faults on the main feeder connected to the Point of Common Coupling (PCC), 2) the faults on the main feeder not connected to the PCC, and 3) the faults on the branch feeder. The reason for separating the case of the main feeder connected to PCC is that the energy and binary status of CT at PCC, i.e., CT_1 in Figure 6-6, depends on the modes of the microgrid.

Table 6-2. Binary outputs for faults 'F_1', 'F_2' and 'F_3'

Relay/Bus Number	**CT Number**	**Grid-Connected Mode**			**Islanded Mode**		
		F_1	**F_2**	**F_3**	**F_1**	**F_2**	**F_3**
1	1	1	1	1	0	0	0
2	2	1	0	0	1	0	0
	3	0	0	0	0	0	0
	4	0	1	1	0	1	1
3	5	1	0	0	1	0	0
	6	0	0	0	0	0	0
	7	0	0	0	0	0	0
	8	0	1	1	0	1	1
4	9	1	1	0	1	1	0
	10	0	0	0	0	0	0
	11	0	0	1	0	0	1
5	12	1	1	0	1	1	0
	13	0	0	1	0	0	1
	14	0	0	0	0	0	0
6	15	1	1	1	1	1	1
	16	0	0	0	0	0	0
	17	0	0	0	0	0	0

The scheme tripping logic of stage II is shown in Figure 6-9, where the variable n stands for the index of the CTs in the microgrid and N is the total number of CTs. In

that figure, the CTs on both terminals of the main feeder have the neighbouring index number. Three faults named 'F_1', 'F_2' and 'F_3' are applied to the feeders 'L_1', 'L_3' and 'L_{10}' in Figure 6-6 to represent the aforementioned three fault scenarios. According to the identification algorithm in Figure 6-8, the binary outputs from the relays 'R1' to 'R_6' are displayed in Table 6-2, where the relay's number keeps the same as the index of the connected busbar. The thing that needs to be highlighted is that the binary results in Table 6-2 are theoretical values rather than the values from the software simulation.

From the tripping logic in Figure 6-9, for the faults at the feeder L_1, i.e., F_1 scenario, the binary value of CT_2 is always '1' in both grid-connected and islanded modes, while the binary value of CT_1 is '0' in islanded microgrid since the breaker at PCC is open. Based on the coordination strategy in Figure 6-9, for the main feeder connected to PCC, the relays, R_1 and R_2, will send a tripping signal to CB_1 and CB_2 as long as the binary value of CT_2 is '1'. Therefore, fault F_1 can be isolated in both-mode microgrids. Additionally, although the binary values of CT_5, CT_9, CT_{12} and CT_{15} are '1', while the CT_4, CT_8, CT_{11} and CT_{14} sides are always '0' in both modes, the CB_4, CB_5, CB_8, CB_9, CB_{11}, CB_{12}, CB_{14}, CB_{15} will not operate. The other CBs, including CB_3, CB_6, CB_7, CB_{10}, CB_{13}, CB_{16}, CB_{17}, at branch feeders will also maintain stable since the status values of CT_3, CT_6, CT_7, CT_{10}, CT_{13}, CT_{16}, CT_{17} sides are always '0' in the grid-connected and islanded microgrids.

For fault F_2, the fault on the main feeder not connected with PCC, the relays, R_3 and R_4, will trip the CB_8 and CB_9 as the binary status of CT_8 and CT_9 are '1' and since the binary status of CT_2, CT_3, CT_5, CT_6, CT_7, CT_{10}, CT_{11}, CT_{13}, CT_{14}, CT_{16}, CT_{17} are all '0', the other CBs in the network will not operate.

For the fault at the branch feeder, F_3, the CB_{13} will open to isolate the fault on feeder 'L_{10}' since the CT_{13}'s side is marked as '1' by the relay 'R_5' in both modes, while the other CBs in the microgrid will not be tripped as the tripping condition in Figure 6-9 is not satisfied.

In this protection scheme, the under-voltage protection suggested in [35] is used to provide backup in case of the failure of the transient-based protection scheme. The threshold for the under-voltage element is set to 0.9 pu to ensure sensitivity to fault conditions. A time delay of 0.3 s is also implemented, which provides sufficient backup protection grading margin for the transient-based protection and is acceptable

for a 400 V network. This proposed scheme can be extended to protect all feeders in microgrids with high sensitivity, whose performance is evaluated in Section 6.4.

6.3.5 Thresholds Setting

In Section 6.3.4, two thresholds, i.e., TWE_{thr} and I_{thr_pe}, are implemented to avoid the undesired operation caused by non-fault disturbances. The selection of those two values is discussed in this section.

As discussed in [36], high-frequency-based protection is relatively sensitive to noise disturbances and the wavelet transform cannot totally remove the high-frequency noise. Therefore, in the designed protection algorithm, an energy threshold, TWE_{thr}, is introduced, where the white noise with a 40 dB Signal-to-Noise Ratio (SNR) was superimposed on the measured current from the CTs to represent the worst-case noise

$$SNR_{dB} = 10log10^{\frac{P_{Signal}}{P_{Noise}}} \qquad (6-14)$$

pollution scenario. The SNR_{dB} is defined by $(6-14)$, where P_{Signal} and P_{Noise} are the power of the noise [37]. The white noise is injected using the 'White Noise' block provided by SIMULINK, where the injected noise level can be controlled by tuning the 'Noise Power' parameter [38]. After injecting noise with an SNR of 40 dB, the simulation revealed that the maximum energy value of all relays in the network is around 1.3. As in a real power system, the noise level is not a constant value, which varies and might be slightly higher than the assumed maximum tolerable noise level. Therefore, a safety margin of 50 % is adopted in this proposed scheme to avoid a failed trip in the above condition, which provides a good trade-off between protection security and sensitivity. Considering a security margin of 50 %, the energy threshold is set to 2. As the energy threshold is calculated based on the maximum tolerable noise level, the proposed scheme is expected to maintain stability under all noise levels with SNR values down to 40 dB. It should be clarified that the maximum energy related to noise depends on the real network situation. Therefore, the energy threshold can be higher or lower in specific applications.

Additionally, the stability requirements under non-fault disturbances, including load switching and power variation of the generators, should be considered. The second tripping threshold, I_{thr_pe}, is introduced to avoid false tripping caused by

external disturbances. The setting of I_{thr_pe} is based on $(6-15)$.

$$I_{thr\_pe} = \frac{\sqrt{2}s_{Feeder}}{\sqrt{3}v_{LL}} \times 1.5 \qquad (6-15)$$

where the I_{thr_pe} is the peak value of the setting current; s_{Feeder} is the total capacity of the loads and generators connected to the local branch feeder; v_{LL} is the rated line-to-line voltage of the microgrid, i.e., 400 V for the microgrid in Figure 6-6, and 1.5 represents the additional 50% safety margin. One point which needs to be highlighted here is that the additional current threshold is only applied to the branch feeders, as shown in the algorithm in Figure 6-8. This additional condition can prevent the sensitivity of the main feeder protection from being compromised. Additionally, as the energy and current thresholds in this scheme are calculated based on the noise level and loading currents of the investigated microgrid, the change in generation type should have a negligible impact on the selection of protection thresholds.

6.4 Performance Evaluation of the Proposed Protection Scheme

6.4.1 Structure of the Studied Microgrid

A model of 400 V, 50 Hz microgrid has been developed in MATLAB/SIMULINK to evaluate the performance of the proposed scheme, which is designed based on the CIGRE benchmark microgrid model [33]. A single-line diagram of the test network is shown in Figure 6-6. The microgrid connects to a 20-kV distribution network by a step-up transformer and it can operate in both grid-connected and islanded modes by controlling the breaker's status at PCC. The length of lines, L_1 to L_{12}, has been marked in the diagram and the detailed parameters of these feeders can be found in [33]. The CTs are installed at the ends of each feeder. Therefore, the current information on all feeders, including the main and branch feeders, can be monitored. For every busbar, one relay is installed to control the operation of CBs. As shown in Figure 6-6, there are four IIDGs in the microgrid. To eliminate the zero-sequence current on the inverter side, the IIDG is connected to the microgrid by a star-delta connected transformer. In grid-connected mode, all IIDGs operate in active and reactive power (PQ) control mode and only deliver the active power to the grid. When the connection with the utility grid is lost, the microgrid will be connected based on the 'master-slave' strategy,

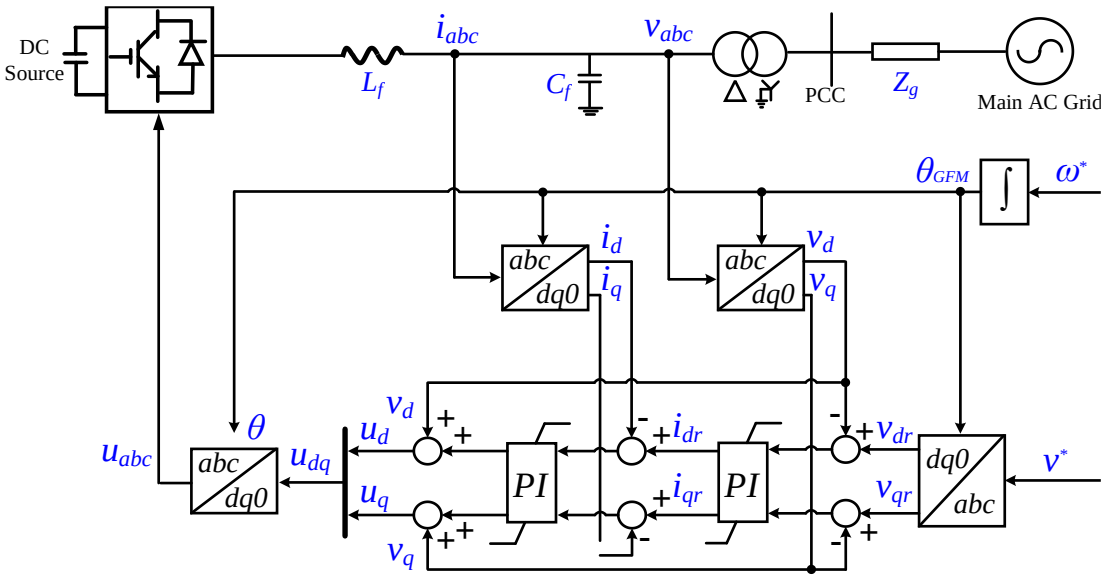

Figure 6-10. Control structure of grid-forming converter [40]

where the control strategy of IIDG 1 will switch to the voltage and frequency (VF) control mode and operate as a grid-forming converter to provide the reference voltage and frequency to the islanded microgrid and the remaining three IIDGs still operate as the grid following converters in the PQ mode. It should be noted that there are a number of ways to maintain the stability of the microgrid energised by multiple IIDGs. For example, a droop-based control strategy can be introduced, where the frequency and voltage are regulated cooperatively by all converters in the grid [39]. However, given the proposed protection scheme relies on the fault-induced high-frequency transients rather than the properties of the generators in the network, the protection response will be unaffected by the voltage and frequency regulation approach in the islanded microgrid. Therefore, the master-slave control approach adopted in the simulation model was considered adequate for the purposes of evaluating the performance of the proposed protection scheme. The structure of the grid-following converter is presented in Figure 2-1 and the grid-forming converter is developed based on [40], whose controller is presented in Figure 6-10. Considering the limited current generating capability of power electronic converters, the fault currents from all IIDGs have been limited to 1.2 pu as suggested in [41]. The parameters of the four IIDGs and loads are presented in Table 6-3.

Table 6-3. Parameters of generators and loads

Equipment Type	Item Name	Controller Type	Rated Power (kVA)	Power Factor
Generators	IIDG 1	PQ/VF	20/50	1/slacking bus
	IIDG 2	PQ	20	1
	IIDG 3	PQ	30	1
	IIDG 4	PQ	40	1
Loads	Load 1		20	0.9
	Load 2		20	0.8
	Load 3		20	0.9
	Load 4		30	0.9

6.4.2 Case Studies to Evaluate Protection Performance

In this section, the performance of the proposed scheme is validated by considering impacts of fault location and type, fault inception angle and fault resistance, non-fault disturbances, measuring noise and IIDG transformer arrangements.

Table 6-4. Scenarios for evaluating the impacts of the fault location and types

Cases	Faulted Feeder	Fault Type	Fault Resistance	Inception Angle of Phase a	Microgrid Mode
1	L_1	AG	1 Ω	30°	Grid-Connected
2	L_3	AB	1 Ω	30°	Grid-Connected
3	L_{10}	ABC	1 Ω	30°	Grid-Connected
4	L_1	AG	1 Ω	30°	Islanded
5	L_3	AB	1 Ω	30°	Islanded
6	L_{10}	ABC	1 Ω	30°	Islanded

6.4.2.1 Impact of Fault Location and Fault Type

The fault scenarios in Table 6-4 are simulated to evaluate the impact of the fault position and type on the protection performance. Three types of faults, including phase-A-to-ground (AG), phase-A-to-phase-B (AB) and three-phase (ABC) faults, are

applied at the midpoint of the feeders L_1, L_3 and L_{10}, firstly in grid-connected and then in the islanded mode. In this initial investigation, both fault resistance and inception angle were fixed, as indicated in the table.

As revealed by Figure 6-4, after the occurrence of the fault, the value of transient wavelet energy, TWE_j, will increase to its peak value and then gradually decrease as the averaging window moves along. The peak energy determines the maximum sensitivity and therefore, the peak value of the maximum phase energy, $TWE_{j,CT_n}^{p_{max}}$, is used in the sensitivity assessment, which is represented as TWE_{j,CT_n}^{Peak}. The results are displayed in Table 6-5 and Table 6-6. It can be seen that regardless of the type or position of the fault, the CT closest to the faults, e.g., CT_2 in Cases 1 and 4, CT_8 and CT_9 in Cases 2 and 5, CT_{13} in Cases 3 and 6, have the highest energy values, and the energies of the CTs at the same busbar confirm the relationship in $(6-13)$.

Table 6-5. Simulation results of the faults with different locations and types (grid-connected mode)

CTs/CBs Number	**Case 1 (L_1)**			**Case 2 (L_2)**			**Case 3 (L_3)**		
	$TWE_{CT_n}^{Peak}$	**Binary Value**	**CB Trips/ Correct?**	$TWE_{CT_n}^{Peak}$	**Binary Value**	**CB Trips/ Correct?**	$TWE_{CT_n}^{Peak}$	**Binary Value**	**CB Trips/ Correct?**
1	26.5	1	Yes/Yes	119.6	1	No/Yes	54.6	1	No/Yes
2	378.1	1	Yes/Yes	119.6	0	No/Yes	54.6	0	No/Yes
3	2.9	0	No/Yes	13.3	0	No/Yes	6.8	0	No/Yes
4	316.4	0	No/Yes	203.1	1	No/Yes	95.3	1	No/Yes
5	316.4	1	No/Yes	203.1	0	No/Yes	95.3	0	No/Yes
6	10.9	0	No/Yes	63.1	0	No/Yes	28.8	0	No/Yes
7	40.8	0	No/Yes	71.0	0	No/Yes	32.5	0	No/Yes
8	66.0	0	No/Yes	862.9	1	Yes/Yes	396.8	1	No/Yes
9	66.0	1	No/Yes	777.5	1	Yes/Yes	396.8	0	No/Yes
10	15.5	0	No/Yes	138.4	0	No/Yes	86.0	0	No/Yes
11	17.6	0	No/Yes	261.8	0	No/Yes	841.7	1	No/Yes
12	17.6	1	No/Yes	261.8	1	No/Yes	841.7	0	No/Yes
13	1.0	0	No/Yes	14.4	0	No/Yes	1831.0	1	Yes/Yes
14	10.3	0	No/Yes	154.8	0	No/Yes	196.5	0	No/Yes
15	10.3	1	No/Yes	154.8	1	No/Yes	196.5	1	No/Yes
16	3.2	0	No/Yes	49.5	0	No/Yes	73.0	0	No/Yes
17	2.1	0	No/Yes	31.4	0	No/Yes	32.2	0	No/Yes

Table 6-6. Simulation results of the faults with different locations and types (islanded mode)

CTs/CBs Number	Case 1 (L_1)			Case 2 (L_2)			Case 3 (L_3)		
	$TWE_{CT_n}^{Peak}$	Binary Value	CB Trips/ Correct?	$TWE_{CT_n}^{Peak}$	Binary Value	CB Trips/ Correct?	$TWE_{CT_n}^{Peak}$	Binary Value	CB Trips/ Correct?
1	0.0	0	Yes/Yes	0.0	0	No/Yes	0.0	1	No/Yes
2	522.6	1	Yes/Yes	0.0	0	No/Yes	0.0	0	No/Yes
3	4.4	0	No/Yes	18.1	0	No/Yes	10.7	0	No/Yes
4	433.9	0	No/Yes	18.1	1	No/Yes	10.7	1	No/Yes
5	433.9	1	No/Yes	18.1	0	No/Yes	10.7	0	No/Yes
6	14.4	0	No/Yes	70.1	0	No/Yes	35.7	0	No/Yes
7	52.9	0	No/Yes	85.0	0	No/Yes	44.1	0	No/Yes
8	96.8	0	No/Yes	464.2	1	Yes/Yes	246.1	1	No/Yes
9	96.8	1	No/Yes	821.8	1	Yes/Yes	246.1	0	No/Yes
10	21.9	0	No/Yes	145.6	0	No/Yes	97.7	0	No/Yes
11	26.7	0	No/Yes	277.7	0	No/Yes	653.5	1	No/Yes
12	26.7	1	No/Yes	277.7	1	No/Yes	653.5	0	No/Yes
13	1.7	0	No/Yes	16.0	0	No/Yes	1560.0	1	Yes/Yes
14	15.1	0	No/Yes	161.8	0	No/Yes	195.8	0	No/Yes
15	15.1	1	No/Yes	161.8	1	No/Yes	195.8	1	No/Yes
16	4.3	0	No/Yes	49.6	0	No/Yes	68.2	0	No/Yes
17	3.6	0	No/Yes	34.8	0	No/Yes	34.9	0	No/Yes

It is worth noting that the magnitude of transient energy generated at the fault position is determined by the instantaneous value of the applied superimposed voltage and the equivalent impedance seen from the fault point. For example, in Case 2 (where the AB fault is triggered in the network), the applied voltage magnitude is equal to the system line voltage, while in Case 1, i.e., AG fault, the applied voltage corresponds to phase a. Additionally, the FIA of line-to-line voltage v_{ab} in Case 2, i.e., 60°, is higher than the inception angle of AG fault, i.e., 30°, in Case 1. Consequently, the fault transient energy for Case 2 is expected to be higher than that observed in Case 1, which can be verified by comparing the energy of CT_1 and CT_2 in Case 1, to the energy of CT_8 and CT_9 in Case 2, as presented in Table 6-5 and Table 6-6. For three-phase faults, the inception angle of phase a, phase b and phase c are 30°, -90° and 150° respectively. As presented in Section 6.3.4.1, the maximum phase energy is implemented in the developed protection algorithm, i.e., the phase b energy is the

highest in Case 3. Therefore, the energy observed in Case 3 will be higher than the energy in Case 1 due to the increased fault inception angle, e.g., comparing the energy of CT_1 and CT_2 in Case 1 (AG fault) to the energy of CT_{13} in Case 3 (ABC fault).

For the fault at different positions, e.g., feeder connected at PCC (Cases 1, 4), main feeders (Cases 2, 5) and branch feeders (Cases 3, 6), the faulted feeder can be selected accurately and the CBs can operate correctly based on the strategy outlined in Figure 6-9. Furthermore, in the proposed protection scheme, the tripping action of CB_1 is governed by the tripping signal from the relay at Bus 2, which ensures that the fault at L_1 in the islanded microgrid can always be isolated. The results confirm that the proposed protection scheme operates correctly in both grid-connected and islanded modes, and its performance is not impacted by the fault location or type.

6.4.2.2 Impact of Fault Inception Angle and Fault Resistance

As reported in [42], the energy of the fault-induced transient depends on the FIA and fault resistance. Given the single-phase-to-ground fault is most frequent, it is used in this section to evaluate the impact of FIA and fault resistance on the TWE. In this test, the AG faults are applied at the midpoint of L_3. The FIA ranges from 0° to 90° and the investigated fault resistances include 0.1 Ω, 1 Ω, 5 Ω and 10 Ω.

The simulation results (a total of 808 cases) are presented in Figure 6-11 and Figure 6-12. Theoretically, in the continuous time domain, the energy of the fault-induced transients should increase with the rise of the FIA for the faults with constant fault resistance, as indicated in [42]. However, in the designed numerical protection, where the current waveform sampling frequency is reduced to 10 kHz, the relay cannot detect all fault inception points with the same sensitivity. For the fault between sampling points, the calculated energy is reduced due to the loss of the high-frequency information at such a low sampling rate. To reveal the negative impact of the low sampling frequency on the measured energy, the faults were applied with an angle increment of 0.9°, i.e., 50 μs, in simulation. This means 2 points are contained between the neighbouring current samples. For these 'blinded' points, the transient wavelet energy will experience a magnitude decay, which results in the periodical fluctuation of the transient wavelet energy as presented in Figure 6-11 and Figure 6-12. The first point with an energy higher than the energy threshold has been highlighted in the zoomed fragment of each figure (in the top-left corner). This point indicates the

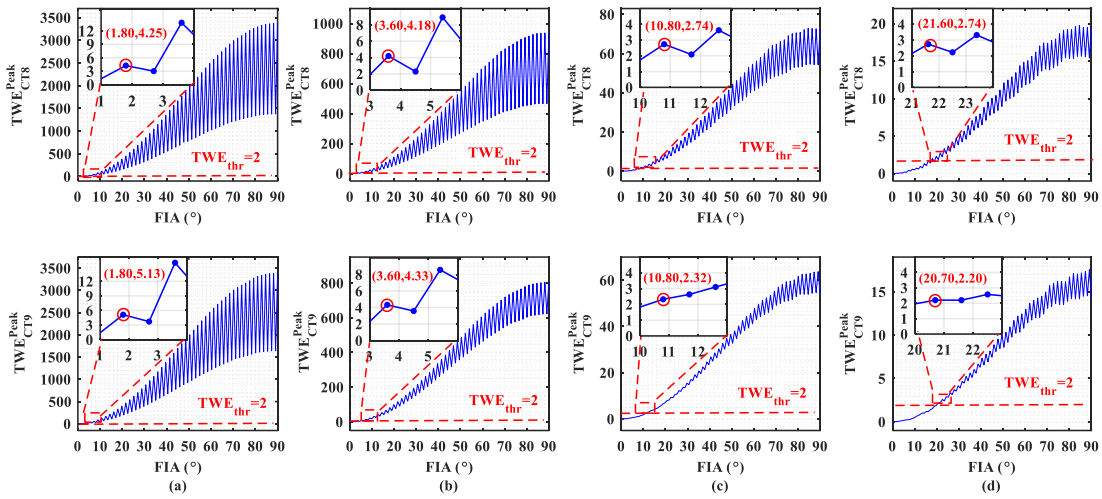

Figure 6-11. The transient wavelet energies of CT_8 and CT_9 for the AG faults in L_3 (Grid-connected microgrid), (a) 0.1 Ω, (b) 1 Ω, (c) 5 Ω, (d) 10 Ω

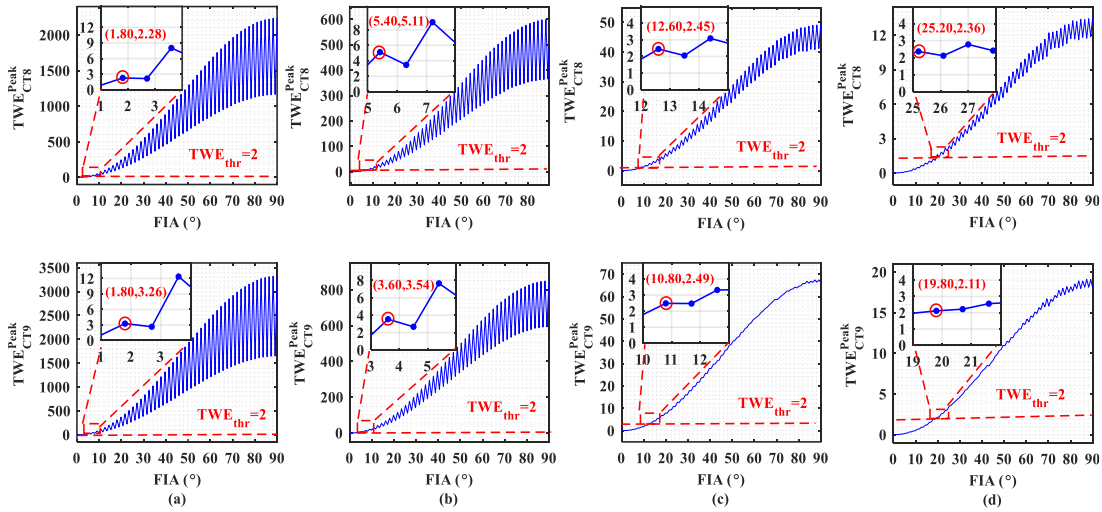

Figure 6-12. The transient wavelet energies of CT_8 and CT_9 for the AG faults in L_3 (islanded microgrid), (a) 0.1 Ω, (b) 1 Ω, (c) 5 Ω, (d) 10 Ω

minimum FIAs detectable by the relay at the assumed sensitivity setting of $TWE_{thr} = 2$. For the FIAs above this point (including the points at the lower boundary), the energy is always higher than TWE_{thr}. In this case, the protection performance under varying fault resistance is summarized in Table 6-7. It can be seen that for the faults with higher resistance, the protection scheme needs higher FIAs.

Table 6-7. Minimum detectable FIAs of the scheme

Microgrid Mode	Fault Resistance			
	0.1 Ω	1 Ω	5 Ω	10 Ω
Grid-Connected	1.8°	3.6°	10.8°	21.6°
Islanded	1.8°	5.4°	12.6°	25.2°

As the nominal voltage of the test system is 400 V, 10 Ω can be regarded as high fault resistance. As reported in [43], the high frequency-based scheme with minimum fault inception angle around 30° is still considered to be effective and reliable under high-impedance fault conditions. It should be noted that the value of 10 Ω is not the maximum detectable fault resistance of the scheme. Through additional simulation studies, it was determined that with 90° FIA, the scheme can detect faults with resistances up to 27 Ω and 25 Ω in the grid-connected and islanded mode respectively. Additionally, it is clear that the values of the minimum detectable FIAs are close in both modes of operation, i.e., the angle difference in the worst-case scenario is less than 3.6°, which further proves that the performance of the proposed scheme is significantly unaffected by the energy sources and the operating modes of microgrids.

6.4.2.3 Impact of Non-Fault Disturbance

In this section, the impacts of typical non-fault transients, including load switching, motor start, and power variation of the IIDGs, are studied. The worst-case scenario in this test is presented by the CT closest to the transient, which has the highest energy. Therefore, the energy and currents of the CT closest to disturbances are displayed only.

The simulation results of the load 3 connection in both operating modes are displayed in Figure 6-13. Although the energy caused by the load connection is higher than the assumed threshold, TWE_{thr}, the current is lower than the defined I_{thr_pe}, and therefore, the protection will maintain stable. To evaluate the motor start impact, a three-phase 10 kVA motor was switched on in parallel with load 4. The results are shown in Figure 6-14. A large starting current is produced by the motor, which is higher than the value of I_{thr_pe}, however, the unwanted tripping is avoided because the wavelet energy caused by the motor start is lower than the assumed threshold TWE_{thr}. Additionally, considering the uncertain nature of the renewable energy-based

generation such as solar and wind, the power generated from the IIDG changes with the variation of the environmental condition. Therefore, the fast variation of the power generation is also considered in this test, where the generation of the IIDG 2 decreases from full loading to half loading in a very short period. The results are presented in Figure 6-15. Both values of energy and current are below the corresponding thresholds. Therefore, the protection scheme remains stable.

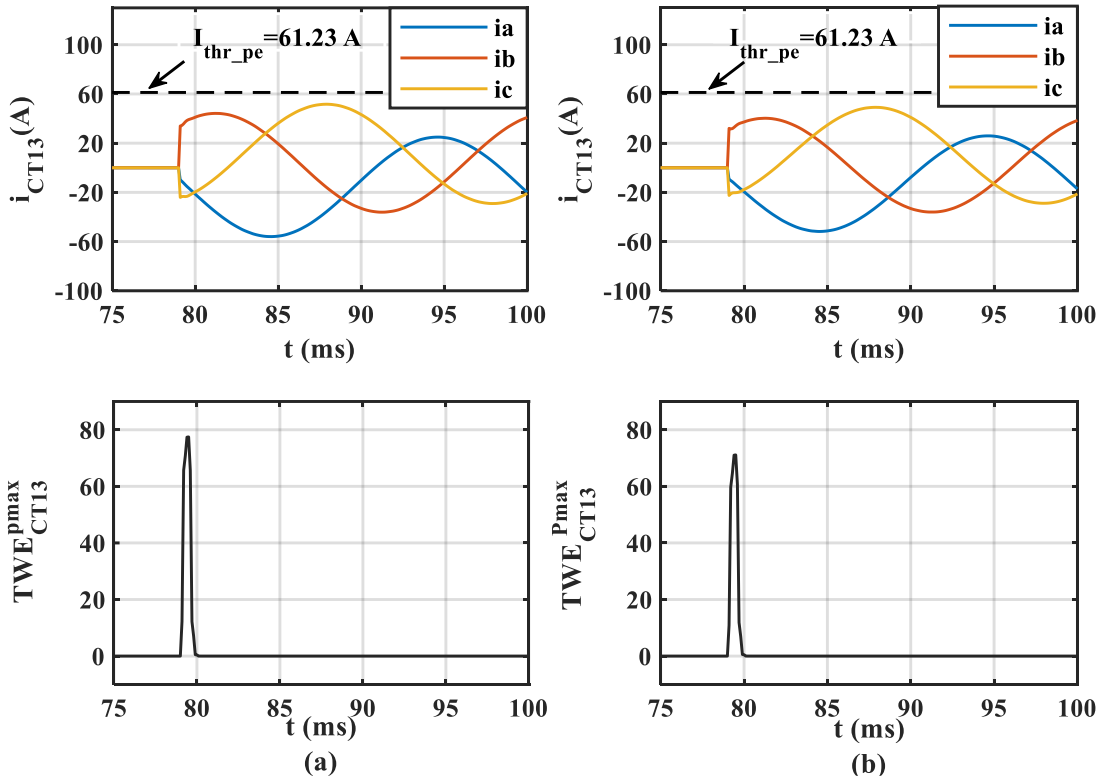

Figure 6-13. Simulation results of load 3 connection, (a) grid-connected mode, (b) islanded mode

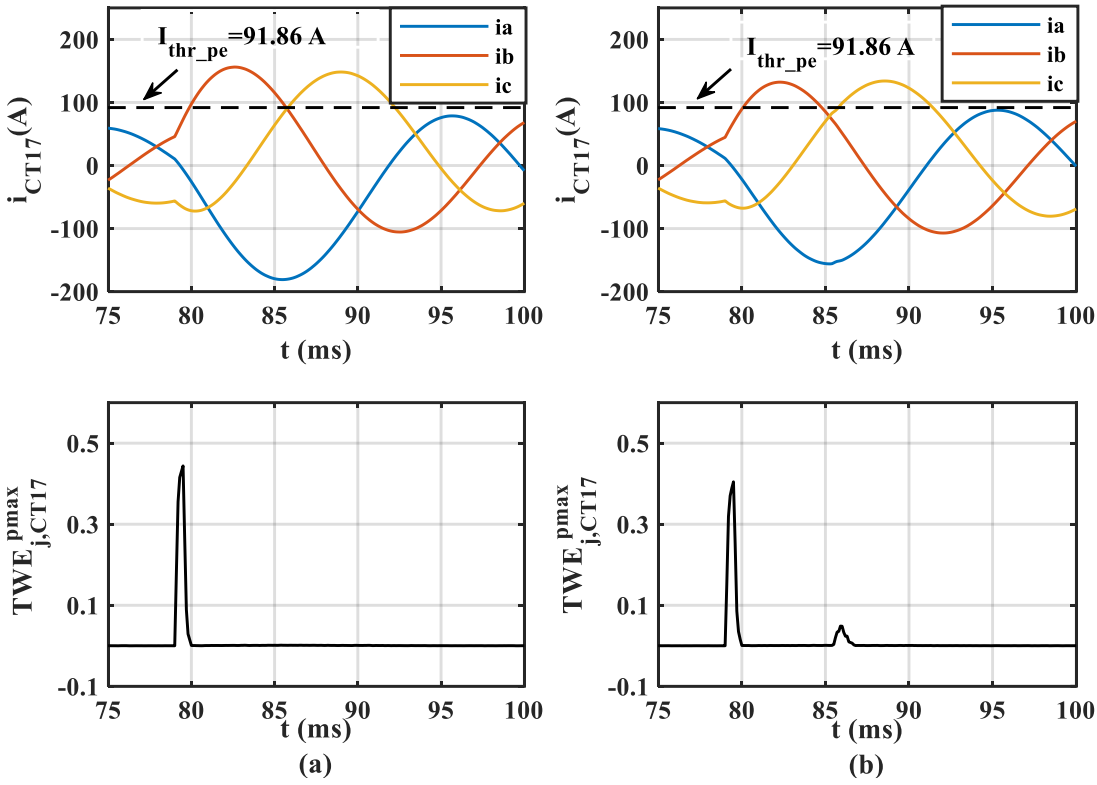

Figure 6-14. Simulation results of three-phase motor start, (a) grid-connected mode, (b) islanded mode

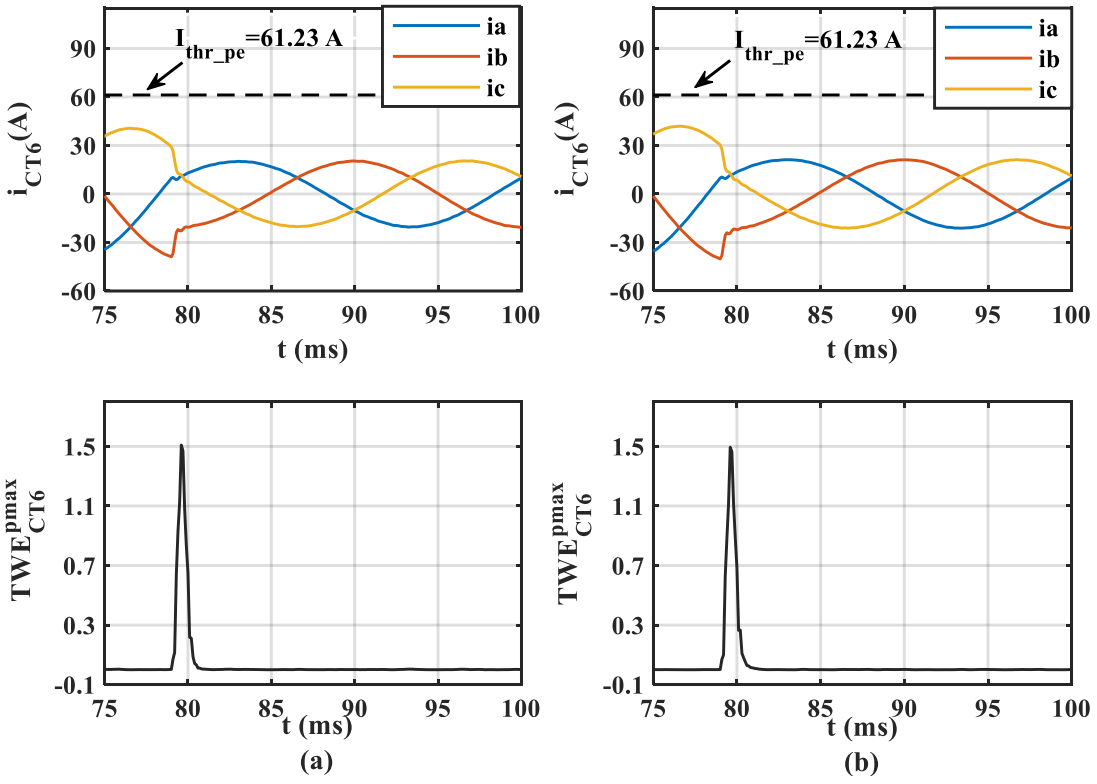

Figure 6-15. Simulation results of power variation of IIDGs, (a) grid-connected mode, (b) islanded mode

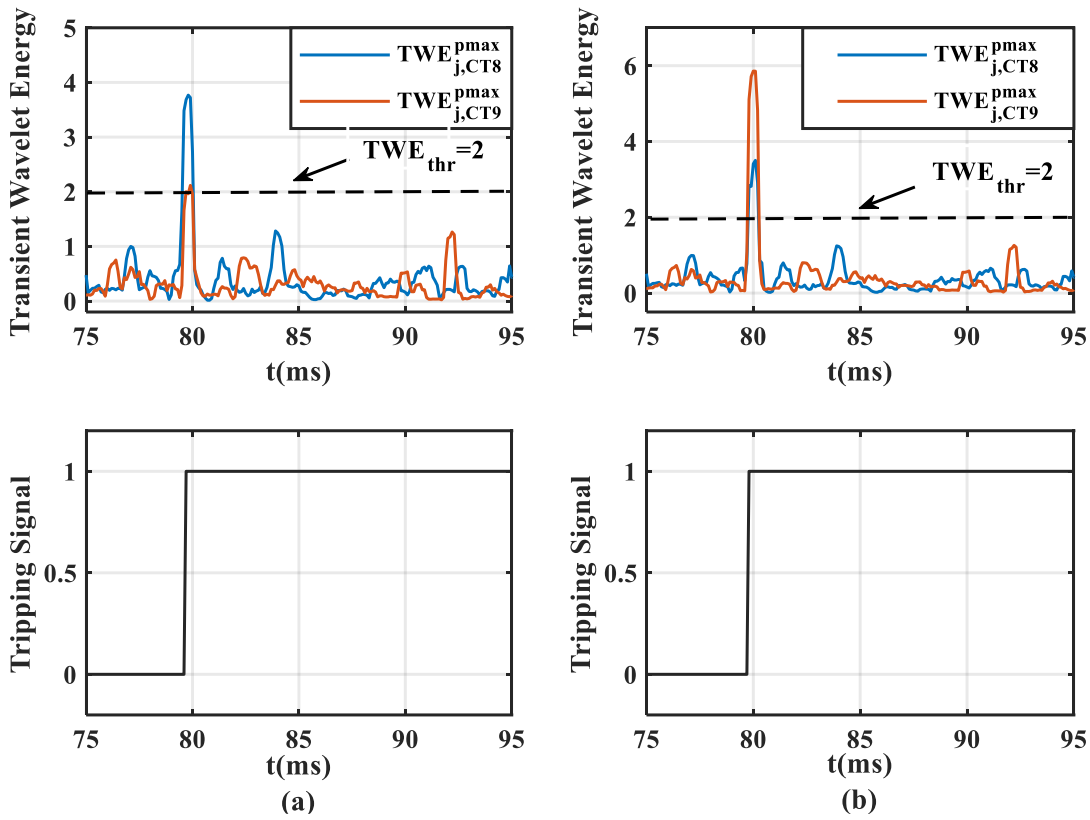

Figure 6-16. Simulation results of 40 dB noise injection, (a) Grid-connected mode, (b) islanded mode

6.4.2.4 Impact of Measuring Noise

In this section, the white noise with 40 dB SNR is superimposed on the current to evaluate the impact of the measurement noise. The energy threshold is maintained as 2, which is 1.5 times the maximum energy in the normal operating condition. The AG fault is applied in the middle of L_3 in both grid-connected and islanded modes of operation. From the energy diagram in Figure 6-11 and Figure 6-12, with the decrease of FIAs and the increase of fault resistance, the magnitude of the energy caused by the fault transients will be reduced. The worst-case scenario from Table 6-7, where the fault resistance is 10 Ω, and the FIA equals the minimum detectable angle, is selected for this test. The simulation results are shown in Figure 6-16, where the tripping signal refers to the signal used to control the operation of CB_8 and CB_9, which is obtained after applying the 'AND' logic to the tripping signals from relays R_3 and R_4. As can be seen in Figure 6-16, the energy of noise is always lower than the energy threshold in the normal state, and the proposed scheme can recognise the faulted feeder and isolate the fault correctly in both microgrid operating modes.

6.4.2.5 Impact of IIDG Transformer Arrangement

The simulation results presented in previous sections were obtained assuming that the IIDG interface transformer windings are star/delta connected with the transformer neutral being solidly earthed. This arrangement is often found in technical literature [34], [44][45] and was also adopted in this thesis. However, some other transformer connection practices, e.g., delta/delta connection or star/delta connection with earthing impedance, can also be adopted in different countries. For example, the UK normally only earths the medium and low-voltage networks via the substation connecting to the main grid [46]. Therefore, in this section, the impact of earthing arrangement of the IIDG transformer is investigated. The studied connections include delta/delta and star/delta with earthing impedance (earthing resistor of 5 Ω was used in this study). The fault scenarios outlined in Table 6-4 are used to evaluate the potential impacts of transformer earthing arrangements on protection performance. The simulation results are presented in Table 6-8, where the energy values of CTs closest to the fault, i.e., energies of CT_1 and CT_2 in Cases 1 and 4, energies of CT_1 and CT_2 in Cases 1 and 4, energies of CT_8 and CT_9 in Cases 2 and 5, and energies of CT_{13} in Cases 3 and 6, are displayed. From those results, we can see that the peak energy values under different transformer arrangements are not affected in any significant way. Only for Cases 1 and 4, there is a noticeable reduction, but the absolute value is still significantly higher than the assumed threshold of 2. Therefore, it can be concluded that the proposed scheme can protect a microgrid where IIDGs adopt different transformer earthing arrangements.

Table 6-8. Simulation results considering transformers with different earthing arrangements

CTs/CBs Number	Grid-Connected						Islanded					
	Case 1 (L_1)		Case 2 (L_3)		Case 3 (L_{10})		Case 4 (L_1)		Case 5 (L_3)		Case 6 (L_{10})	
	$TWE_{CT_n}^{Peak}$ Δ / Δ / Δ (5 Ω) / Δ (0 Ω)	CB Trips/ Correct?	$TWE_{CT_n}^{Peak}$ Δ / Δ / Δ (5 Ω) / Δ (0 Ω)	CB Trips/ Correct?	$TWE_{CT_n}^{Peak}$ Δ / Δ / Δ (5 Ω) / Δ (0 Ω)	CB Trips/ Correct?	$TWE_{CT_n}^{Peak}$ Δ / Δ / Δ (5 Ω) / Δ (0 Ω)	CB Trips/ Correct?	$TWE_{CT_n}^{Peak}$ Δ / Δ / Δ (5 Ω) / Δ (0 Ω)	CB Trips/ Correct?	$TWE_{CT_n}^{Peak}$ Δ / Δ / Δ (5 Ω) / Δ (0 Ω)	CB Trips/ Correct?
1	25.9	Yes/Yes					0	Yes/Yes				
	26.5	Yes/Yes					0	Yes/Yes				
	26.5	Yes/Yes					0	Yes/Yes				
2	195.1	Yes/Yes					243.4	Yes/Yes				
	243.9	Yes/Yes					299.8	Yes/Yes				
	378.1	Yes/Yes					522.6	Yes/Yes				
8			863.1	Yes/Yes					455.2	Yes/Yes		
			862.9	Yes/Yes					448.9	Yes/Yes		
			862.9	Yes/Yes					464.2	Yes/Yes		
9			772.4	Yes/Yes					803.4	Yes/Yes		
			777.6	Yes/Yes					793.9	Yes/Yes		
			777.5	Yes/Yes					821.8	Yes/Yes		
13					1802	Yes/Yes					1566	Yes/Yes
					1830	Yes/Yes					1561	Yes/Yes
					1831	Yes/Yes					1560	Yes/Yes

6.5 Chapter Summary

In this chapter, a transient wavelet energy-based scheme has been developed to protect the microgrids dominated by IIDGs. The MODWT algorithm is implemented in this algorithm to extract the wavelet coefficients of the high-frequency transients resulting from the short-circuit faults. The energy of those transient coefficients is calculated and used to locate the faulted feeder by the derived energy relations and

proposed coordination algorithm. The performance of the proposed scheme is evaluated using comprehensive simulation tests.

Compared to the conventional fundamental phasor-based protection algorithm, its performance is not sensitive to the changes in IIDG's control strategies, fault levels, fault types and positions, system noise and earthing arrangement of interface transformers. Moreover, regarding protection security, it is shown that the protection scheme remains stable under typical non-fault disturbances. The test results also show that the proposed scheme can operate effectively against faults in both grid-connected and islanded modes without adjusting any settings. Unlike differential protection, the proposed scheme only transmits the binary values between relays rather than three-phase currents. Therefore, it only requires a low-cost communication scheme, which is feasible to implement in microgrids. However, similar to other high-frequency components-based protection, the protection sensitivity of the proposed scheme is reduced in faults with small FIAs, where a small-magnitude high-frequency signal will be generated, and it could be failed to detect a fault when the FIA is smaller than the minimum FIA demonstrated in Table 6-7.

Additionally, since the proposed algorithm uses the energy information of the transients resulting from the travelling wave reflection rather than the polarity or magnitude information of initial wavefronts, it uses a much lower sampling rate, i.e., from more than 200 kHz in [1] down to around 10 kHz, while being able to maintain the sensitivity against faults within a wide range of FIAs. Therefore, the proposed scheme offers a practical and economical choice for microgrid protection. Potentially, it could be used as a solution in future distribution systems with high amounts of CBRs, including a possibility of intentional islanding.

6.6 Chapter References

[1] X. Li, A. Dysko and G. Burt, "Traveling Wave-Based Protection Scheme for Inverter-Dominated Microgrid Using Mathematical Morphology", *IEEE Transactions on Smart Grid*, vol. 5, no. 5, pp. 2211-2218, 2014.

[2] X. Dong et al., "Implementation and Application of Practical Traveling-Wave-Based Directional Protection in UHV Transmission Lines," in *IEEE Transactions on Power Delivery*, vol. 31, no. 1, pp. 294-302, Feb. 2016.

[3] Yoo, Y., “Tutorial on Fourier Theory”, March 2001.

[4] D. K. Alves, F. B. Costa, R. Lúcio de Araujo Ribeiro, C. Martins de Sousa Neto and T. de Oliveira Alves Rocha, "Real-Time Power Measurement Using the Maximal Overlap Discrete Wavelet-Packet Transform," in *IEEE Transactions on Industrial Electronics*, vol. 64, no. 4, pp. 3177-3187, April 2017.

[5] Cheng Hong, Chen Xiaojuan, Xiao Wei and Wang Cong, "Short-time fourier transform based analysis to characterization of series arc fault," *2009 2nd International Conference on Power Electronics and Intelligent Transportation System (PEITS)*, 2009, pp. 185-188.

[6] W. Yao, Z. Teng, Q. Tang and Y. Gao, "Measurement of power system harmonic based on adaptive Kaiser self-convolution window", in *IET Generation, Transmission & Distribution*, vol. 10, no. 2, pp. 390-398, 2016.

[7] É. Lima, C. Santos Junqueira, N. Brito, B. Souza, R. Almeida Coelho and H. Gayoso Meira Suassuna de Medeiros, "High impedance fault detection method based on the short-time Fourier transform", in *IET Generation, Transmission & Distribution*, vol. 12, no. 11, pp. 2577-2584, 2018.

[8] M. Sifuzzaman, M.R. Islam, and M.Z. Ali, "Application of Wavelet Transform and its Advantages Compared to Fourier Transform," in *Journal of Physical Sciences*, vol. 13, pp.121-134, 2009.

[9] Shyh-Jier Huang, Cheng-Tao Hsieh and Ching-Lien Huang, "Application of Morlet wavelets to supervise power system disturbances," in *IEEE Transactions on Power Delivery*, vol. 14, no. 1, pp. 235-243, Jan. 1999.

[10] R. Polikar, “The wavelet tutorial,” College Eng. Web Server, Rowan Univ., Glassboro, NJ, USA, 1996.

[11] L. Arts and E. van den Broek, "The fast continuous wavelet transformation (fCWT) for real-time, high-quality, noise-resistant time–frequency analysis", *Nature Computational Science*, vol. 2, no. 1, pp. 47-58, 2022.

[12] Chul-Hwan Kim, Hyun Kim, Young-Hun Ko, Sung-Hyun Byun, R. K. Aggarwal and A. T. Johns, "A novel fault-detection technique of high-impedance arcing faults in transmission lines using the wavelet transform," in *IEEE Transactions on Power Delivery*, vol. 17, no. 4, pp. 921-929, Oct. 2002.

[13] X. Li, "Enhanced Control and Protection for Inverter Dominated Microgrids,"

Ph.D dissertation, Department of Electronic and Electrical Engineering, University of Strathclyde, Glasgow, UK, 2014.

[14] S. G. Mallat, "A theory for multiresolution signal decomposition: the wavelet representation," in *IEEE Transactions on Pattern Analysis and Machine Intelligence*, vol. 11, no. 7, pp. 674-693, July 1989.

[15] Chul Hwan Kim and R. Aggarwal, "Wavelet transforms in power systems. II. Examples of application to actual power system transients," in *Power Engineering Journal*, vol. 15, no. 4, pp. 193-202, Aug. 2001.

[16] "MATLAB wavelet filters", 2022. [Online]. Available: https://uk.mathworks.com/help/wavelet/ref/wfilters.html. [Accessed: 10- Jul- 2022].

[17] S. Kar and S. R. Samantaray, "High impedance fault detection in microgrid using maximal overlapping discrete wavelet transform and decision tree," *2016 International Conference on Electrical Power and Energy Systems (ICEPES)*, 2016, pp. 258-263.

[18] W. G. Morsi and M. E. El-Hawary, "A New Perspective for the IEEE Standard 1459-2000 Via Stationary Wavelet Transform in the Presence of Nonstationary Power Quality Disturbance, " in *IEEE Transactions on Power Delivery*, vol. 23, no. 4, pp. 2356-2365, Oct. 2008.

[19] V. Alarcon-Aquino and J. Barria, "Change detection in time series using the maximal overlap discrete wavelet transform, " *Latin Amer. Appl. Res.*, vol. 39, no. 2, pp. 145–152, 2009.

[20] F. B. Costa, B. A. Souza and N. S. D. Brito, "Real-time classification of transmission line faults based on Maximal Overlap Discrete Wavelet Transform," *PES T&D 2012*, 2012, pp. 1-8.

[21] M. Vitins, "A Fundamental Concept for High Speed Relaying," in *IEEE Transactions on Power Apparatus and Systems*, vol. PAS-100, no. 1, pp. 163-173, Jan. 1981.

[22] G. Benmouy and J. Roberts, Superimposed Quantities: Their True Nature and Application in Relays, vol. 199. Pullman, WA, USA: Schweitzer Eng. Lab., 1999.

[23] T. Hensler, C. Pritchard, N. Fischer, and B. Kasztenny, “Testing superimposed-component and traveling-wave line protection,” in *Locating Faults and*

Protecting Lines at the Speed of Light: Time- Domain Principles Applied. Pullman, WA, USA: Schweitzer Eng. Lab.,2018.

[24] E. O. Schweitzer, B. Kasztenny, A. Guzmán, V. Skendzic, and M. V. Mynam, “Speed of line protection—Can we break free of phasor limitations?” in *Proc. 68th Annu. Conf. Protective Relay Eng.*, 2015, pp. 448–461.

[25] Y. Paithankar and M. Sant, "A new algorithm for relaying and fault location based on autocorrelation of travelling waves", in *Electric Power Systems Research*, vol. 8, no. 2, pp. 179-185, 1985.

[26] N. Fischer, V. Skendzic, R. Moxley, and J. Needs, “Protective relay traveling wave fault location,” in *Proc. 11th IET Int. Conf. Develop. Power Syst. Protect. (DPSP)*, 2012, pp. 1–3.

[27] C. Pang and M. Kezunovic, "Fast Distance Relay Scheme for Detecting Symmetrical Fault During Power Swing," in *IEEE Transactions on Power Delivery*, vol. 25, no. 4, pp. 2205-2212, Oct. 2010.

[28] A. I. Megahed, A. M. Moussa and A. E. Bayoumy, "Usage of wavelet transform in the protection of series-compensated transmission lines," in *IEEE Transactions on Power Delivery*, vol. 21, no. 3, pp. 1213-1221, July 2006.

[29] W. Gao and J. Ning, "Wavelet-Based Disturbance Analysis for Power System Wide-Area Monitoring," in *IEEE Transactions on Smart Grid*, vol. 2, no. 1, pp. 121-130, March 2011.

[30] S. Song and G. Zou, "A Novel Busbar Protection Method Based on Polarity Comparison of Superimposed Current," in *IEEE Transactions on Power Delivery*, vol. 30, no. 4, pp. 1914-1922, Aug. 2015.

[31] "Discrete Filter", 2022. [Online]. Available: https://uk.mathworks.com/help/simulink/slref/discretefirfilter.html. [Accessed: 11- Jul- 2022].

[32] M. Vetterli and C. Herley, "Wavelets and filter banks: theory and design," in *IEEE Trans. on Signal Processing*, vol. 40, no. 9, pp. 2207-2232, Sept. 1992.

[33] S. Papathanassiou, N. Hatziargyriou, and K. Strunz, “A benchmark low voltage microgrid network,” in *Proc. CIGRE Symp. Power Syst. Dispersed Gener.*, 2005, pp. 1–8.

[34] J. Nsengiyaremye, B. C. Pal and M. M. Begovic, "Microgrid Protection Using

Low-Cost Communication Systems," in *IEEE Transactions on Power Delivery*, vol. 35, no. 4, pp. 2011-2020, Aug. 2020.

[35] E. Sortomme, S. S. Venkata and J. Mitra, "Microgrid Protection Using Communication-Assisted Digital Relays," in *IEEE Transactions on Power Delivery*, vol. 25, no. 4, pp. 2789-2796, Oct. 2010.

[36] L. Tang, X. Dong, S. Luo, S. Shi and B. Wang, "A New Differential Protection of Transmission Line Based on Equivalent Travelling Wave," in *IEEE Transactions on Power Delivery*, vol. 32, no. 3, pp. 1359-1369, June 2017.

[37] M. A. Jarrahi, H. Samet and T. Ghanbari, "Fast Current-Only Based Fault Detection Method in Transmission Line," in *IEEE Systems Journal*, vol. 13, no. 2, pp. 1725-1736, June 2019.

[38] 2022. [Online]. Available: https://uk.mathworks.com/help/simulink/slref/bandlimitedwhitenoise.html. [Accessed: 17- Jul- 2022].

[39] U. Tayab, M. Roslan, L. Hwai and M. Kashif, "A review of droop control techniques for microgrid", in *Renewable and Sustainable Energy Reviews*, vol. 76, pp. 717-727, 2017.

[40] J. Rocabert, A. Luna, F. Blaabjerg and P. Rodríguez, "Control of Power Converters in AC Microgrids," in *IEEE Transactions on Power Electronics*, vol. 27, no. 11, pp. 4734-4749, Nov. 2012.

[41] B. Kasztenny, M. V. Mynam, and N. Fischer, “Sequence component applications in protective relays—Advantages, limitations, and solutions,” *Proc. 72nd Annu. Conf. Protective Relay Eng. (CPRE)*, College Station, TX, USA, 2019, pp. 1–23.

[42] F. Costa, B. Souza and N. Brito, "Effects of the fault inception angle in fault-induced transients", in *IET Generation, Transmission & Distribution*, vol. 6, no. 5, pp. 463-471, 2012.

[43] X. Dong, J. Wang, S. Shi, B. Wang, B. Dominik and M. Redefern, "Traveling wave based single-phase-to-ground protection method for power distribution system," in *CSEE Journal of Power and Energy Systems*, vol. 1, no. 2, pp. 75-82, June 2015.

[44] D. P. Mishra, S. R. Samantaray and G. Joos, "A Combined Wavelet and Data-Mining Based Intelligent Protection Scheme for Microgrid," in *IEEE Transactions on Smart Grid*, vol. 7, no. 5, pp. 2295-2304, Sept. 2016.

[45] S. F. Zarei, H. Mokhtari and F. Blaabjerg, "Fault Detection and Protection Strategy for Islanded Inverter-Based Microgrids," in *IEEE Journal of Emerging and Selected Topics in Power Electronics*, vol. 9, no. 1, pp. 472-484, Feb. 2021.

[46] N. Scott, “Microgrids - A guide to their issues and value,” 2016.

Chapter 7

7 Conclusions and Future Works

7.1 Conclusions

Compared to the well-known fault characteristics of SGs, the short-circuit behaviour of CBRs highly depends on their embedded controller and the CBRs cannot generate high-magnitude fault currents owing to the limitation of the thermal capability. To fully understand the challenges of CBRs on power system protection, a representative and flexible converter model is proposed first in this thesis. This presented model can operate in different control modes, including the constant active power, constant reactive power and balanced current mode, inject the reactive currents following the injection curve suggested in the GB Grid Code and limit the fault currents to 1.2 pu. By implementing this model, the performance of two commercially available distance relays is evaluated using a realistic HIL approach under a wide range of system operating scenarios, including different converter operating modes, varied fault levels, different synchronous compensation levels, different fault parameters and different protection characteristics (i.e., MHO and QUAD). From the results, it was found that the connection of the HVDC system could lead to the severe protection issues such as failed tripping, delayed tripping and tripping in the incorrect zone. The reasons behind such compromised distance protection performance, including inaccurate impedance measurement, incorrect faulted phase selection and problematic impedance measurement, are further investigated. Solutions to address the abovementioned issues in the literature are reviewed, which comprise enhanced distance protection, control-assisted protection, travelling wave protection and intelligent techniques-based protection. Unlike conventional distribution systems, the microgrids have bidirectional power flow and can operate in grid-connected and islanded modes. This operating characteristic of microgrids poses serious protection

challenges to the conventional overcurrent relays, which are designed for networks with high-magnitude fault currents and uni-directional current flow. The methods used to address the protection challenges of microgrids are reviewed and their benefits and limitations are compared, which include adaptive protection, differential protection, active protection, intelligent techniques-based protection, and travelling wave protection.

Except for the protection issues of the distance relay at the converter side, the distance relay at the grid side also has the potential for delayed and/or failed operation because of the reduced system fault level in the future. Therefore, a new sequence component-based distance measuring algorithm is proposed for grid-side relays to increase the accuracy of impedance measurement CBRs. Based on the simulation results, the new developed distance measuring approach can detect the fault distance accurately in different fault and system operating conditions, whose performance is not sensitive to the changes in the system fault level, fault resistance, fault location and protected line length, and its operating speed can satisfy the requirements defined in the GB grid code. Additionally, this scheme can be embedded into the existing hardware platform of digital relays. Therefore, it provides an effective and economical way to address the under/over-reach issues of the distance relay at the grid side.

Besides the development of sequence components-based protection for transmission systems, this thesis also presents a transient wavelet energy-based protection algorithm to protect the microgrids dominated by inverter-based resources, where the faulted feeder is located using the energy relations of the CTs in microgrids. Compared to the conventional travelling wave-based approach, where both time and polarity information of travelling waves are required, the proposed scheme has significantly low requirements on the relay's sampling frequency and uses the economic low-bandwidth communication channels. According to the simulation results, it was found that the proposed transients wavelet energy-based protection scheme can detect and isolate faults in microgrids effectively in a wide range of system operation and fault conditions, including varied fault levels, different microgrid operating modes, different fault inception angles, different fault resistance and different fault types. Additionally, the security performance of the developed transient-based protection scheme is verified by applying the non-fault disturbances such as

measuring noise, motor start, load switching and power variation of IIDGs. From the results, it is convinced that the proposed scheme can keep stable in those non-fault disturbances and has a high sensitivity to isolate the faults in microgrids. Since the proposed method can be implemented with low sampling frequency and low-bandwidth communication channels, it also provides an economical solution for future microgrid and distribution system protection.

7.2 Future Work

There are several research questions and technical challenges which still remain and should be considered as guidelines to shape future research activities in this area, such as:

- Testing the performance of the proposed protection methods in Chapters 5 and 6 using a realistic HIL approach.
- Evaluating the performance of the proposed sequence components-based distance measuring algorithm in the event of non-fault disturbances, such as lightning strikes, load switching and power swings.
- Extend the high-frequency transients-based algorithm in Chapter 6 to protect the transmission system with the connection of CBRs.
- Exploring the possibility of expanding the application of the high-frequency transients-based algorithm in Chapter 6 under broader power system scenarios and transient events, such as detecting open circuit faults (a broken conductor) and integrating the algorithm with a self-learning tool for setting the protection threshold adaptively.

Appendix A: Distance Relay Settings Used in Chapter 3

A.1 Line Impedance Calculation

Based on the line parameters in Table 3-4, the positive and zero sequence impedance of the protected line presented on the primary side can be calculated by $(A-3)$ and $(A-6)$:

$$R_L^+ = 12.1 \times 0.0378 = 0.457\ (\Omega) \qquad (A-1)$$

$$jX_L^+ = j12.1 \times (2 \times \pi \times 50 \times 1.324 \times 10^{-3}) = j5.033\ (\Omega) \qquad (A-2)$$

$$Z_L^+ = R_L^+ + jX_L^+ = 0.457 + j5.033 = 5.05\angle 84.81^{\circ}\ (\Omega) \qquad (A-3)$$

$$R_L^0 = 12.1 \times 0.159 = 1.924\ (\Omega) \qquad (A-4)$$

$$jX_L^0 = j12.1 \times (2 \times \pi \times 50 \times 3.202 \times 10^{-3}) = j12.172\ (\Omega) \qquad (A-5)$$

$$Z_L^0 = R_L^0 + jX_L^0 = 1.924 + j12.172 = 12.32\angle 81.02^{\circ}\ (\Omega) \qquad (A-6)$$

The turn ratios of implemented CT and VT are 1200:1 and 275000:110 respectively. Therefore, the gain of $\left(\frac{1200}{1}\right)/\left(\frac{275000}{110}\right) = 0.48$ should be implemented to transfer the primary side impedance (or settings) to the secondary side as presented in $(A-7)$.

$$Z_L^{+\prime} = Z_L^+ \times 0.48 = 2.42\angle 84.81^{\circ}(\Omega) \qquad (A-7)$$

In the tests, the reaches of Zone 1 and Zone 2 are 80% and 120% of the protected line. Therefore, the impedance reaches of the distance relay are calculated by $(A-8)$ and $(A-9)$ and the residual compensation factor is calculated in $(A-10)$.

$$Z_{Zone1} = Z_L^{+\prime} \times 0.8 = 1.94\angle 84.8^{\circ}\ (\Omega) \qquad (A-8)$$

$$Z_{Zone2} = Z_L^{+\prime} \times 1.2 = 2.91\angle 84.8^{\circ}\ (\Omega) \qquad (A-9)$$

$$K_0 = \frac{1}{3} \times \left(\frac{Z_L^0}{Z_L^+} - 1 \right) = 0.48 \angle -6^\circ \qquad (A-10)$$

A.3 Relay Settings in Table 3-6

In addition to the settings in A.2 used for the MHO characteristic, the setting of resistive reach is also implemented in the QUAD characteristic of the distance relay. Based on the GB Grid Code, the maximum loading current of the 275 kV transmission network is 5.2 kA and the 30% safety margin is considered. Therefore, the forwarded resistive reach of Zone 3 (primary side) can be calculated by $(A-11)$.

$$R_{Zone3-for} = \frac{275}{\sqrt{3} \times \left(\frac{5.2}{(1-0.3)} \right)} \times \left(cos\, 30^\circ - \frac{sin\, 30^\circ}{tan\, RCA} \right) = 17.5\ (\Omega) \qquad (A-11)$$

The secondary side of Zone 3 resistive reach is calculated in $(A-12)$. Therefore, the forwarded and reversed resistive reaches of Zone 1 and Zone 2 can be calculated by $(A-13)$ and $(A-14)$.

$$R'_{Zone3-for} = 17.5 \times 0.48 = 8.4\ (\Omega) \qquad (A-12)$$

$$R'_{Zone1-for} = R'_{Zone2-for} = 0.8 \times 8.4 = 6.72\ (\Omega) \qquad (A-13)$$

$$R'_{Zone1-rev} = R'_{Zone2-rev} = 0.25 \times 6.72 = 1.68\ (\Omega) \qquad (A-14)$$

Appendix B: RTDS Script and MATLAB Code for Distance Relay Tests in Chapter 3

B.1 RTDS Script for Distance Relay Tests

The key commands used in the RTDS script for automating the HIL tests are presented below.

❖ Set variables values

This command below is used to set the variable values, which are controlled by the sliders in RSCAD. For example, in the above code, the active power reference of PQ converter is set to the value stored in the matrix 'PQ[p]'. The user can use the following command to control other sliders by replacing the name and values.

```
SetSlider "Subsystem #1 : CTLs : Inputs : PrPQ" = PQ[p];
```

❖ 'Switch' Control

The codes below are used to control the switch operation in RTDS. With the follwing commands, the switch of the AG fault will be on and the switches of the AB and ABCG faults are off.

```
SetSwitch "Subsystem #1 : CTLs : Inputs : AG" = 1;
SetSwitch "Subsystem #1 : CTLs : Inputs : AB" = 0;
SetSwitch "Subsystem #1 : CTLs : Inputs : ABCG" = 0;
```

❖ 'Button' Control

```
ReleaseButton "Subsystem #1 : CTLs : Inputs : FLT";.
```

The above code is used to activate the faults in RTDS by controlling the button named 'FLT'.

❖ Identify the Name and Path of the Saved Data

The 'sprintf' command below is used to set the name and path of the saved data, where '%d' refers to the 'decimal integer' type, which is used to declare the variable

type of ‘loop_counter’; ‘%s’ refers to the ‘string’ type, which is used to declare the variable type of the following string

```
sprintf(name1,"\Plots\Case%d_%s_%s_%s_%s_%s_%s_%s_%s.cfg",loop_counter,RelayA_str[0],FLSG1PPPG_str[g],FLSG2PPPG_str[g],SC_str[h],PQ_str[p],CS_str[i],AG_str[0],res_str[j],FP_str[k]);
```

❖ Save the Comtrade Data

The codes below are used to save the RTDS results as the Comtrade data.

```
ComtradePlotSave"R1_Trip",name1,YEAR,1999,MIN,0,MAX,65535,RATIO_PRIMARY,1.0,RATIO_SECONDARY,1.0,SCALE,P,DIGITAL,0,FREQ,50.0,WRITE_POS,true;
```

B.2 MATLAB Code for Distance Relay Tests

The key commands used in the MATLAB program to automate the analysis of the HIL test results are presented below:

❖ **Comtrade Data to MATLAB Matrix (i.e., mat Data)**

The codes used to transfer the Comtrade data from the RTDS to the matrix data in MATLAB can be found in 'https://uk.mathworks.com/matlabcentral/fileexchange/15619-comtrade-reader?s_tid=mwa_osa_a'.

❖ **Extract the Tripping Time of the Saved Tripping Signal**

The codes below are used to extract the tripping time of the investigated relay.

```
Trip_point=find(diff(R1_Trip)<0); % Search tripping points.
EM=isempty(Trip_point); % Check whether the relay is tripping.
if EM==1;
Trip_time=0; % No tripping.
else
Trip_point=Trip_point;
Trip_time=Trip_point(1)*dt_RTDS; % Save the tripping time of the tripping point.
end
% Calculate and save relay tripping time
t_trip= (Trip_time-t_fault_incep)*1000; % t_trip is the tripping time of the relay (ms) & t_fault inception is the fault inception time (0.2s in this test)
```

❖ **Distinguish Tripping Conditions**

The codes below are used to group the tripping types, such as failed trip, delayed trip, trip in the false zone and healthy trip.

```
for …

loop_counter=loop_counter+1;
if t_trip_overall(loop_counter)<0; %  Failed Tripping
    Trip_Group="Failed Trip";
elseif t_trip_overall(loop_counter)>0 && FP_saved(loop_counter)<80 &&
t_trip_Zone1(loop_counter)> 90;
    Trip_Group="Delayed Trip (Z1)";  % Zone 1 Delay
elseif t_trip_overall(loop_counter)>0 && FP_saved(loop_counter)>= 80 &&
t_trip_Zone2(loop_counter)> 490 && t_trip_Zone1(loop_counter)< 0;
```

```
    Trip_Group="Delayed Trip (Z2)" ; % Zone 2 Delay
elseif t_trip_overall(loop_counter)>0 && FP_saved(loop_counter)<80 && t_trip_Zone1(loop_counter)< 0 && t_trip_Zone2(loop_counter)> 0;
    Trip_Group="False Tripping Zone" ; % Trip in False Zone (Trip in Zone 2 for Zone 1 Fault)
elseif t_trip_overall(loop_counter)>0 && FP_saved(loop_counter)>= 80 && t_trip_Zone1(loop_counter)> 0;
    Trip_Group="False Tripping Zone"; % Trip in False Zone (Trip in Zone 1 for Zone 2 Fault)
else
    Trip_Group="Healthy Trip";
end

…
end
```

❖ Results Table Plot

The codes below are used to plot the table of results.

```
% Create Table and Define the Table's Properties
fig = uifigure('Position',[85,42,1480,720]);
uit = uitable(fig);
uit.Position = [51.4,41.8,1348,675.2];
% Present the Results in the Created Table
uit.Data = dat;
uit.RowName = row_name;
uit.ColumnName = column_name;
```